

Synthesis, crystal structures and characterization of novel alkali-metal containing rare-earth orthoborates

Dissertation

zur Erlangung des Doktorgrades der Naturwissenschaften

-Dr. rer. nat.-

Vorgelegt dem Promotionsausschuss
des Fachbereichs 02 (Biologie/Chemie)
der Universität Bremen



von

Pengyun Chen

Chemische Kristallographie fester Stoffe

Bremen, im DEZ 2020

Erstgutachter: Prof. Dr. Hubert Huppertz, Universität Innsbruck

Zweitgutachter: Prof. Dr. Thomas Schleid, Universität Stuttgart

Tag der mündlichen Prüfung: 03.03.2021

Mitglieder des Prüfungsausschusses:

1. Prof. Dr. Jens Beckmann, Fachbereich 02 Biologie/Chemie, Institut für Anorganische Chemie und Kristallographie, Metallorganische Chemie der Hauptgruppenelemente, Universität Bremen
2. Prof. Dr. Hubert Huppertz, Fakultät für Chemie und Pharmazie, Institut für Allgemeine, Anorganische und Theoretische Chemie, Universität Innsbruck
3. Prof. Dr. Thorsten M. Gesing, Fachbereich 02 Biologie/Chemie, Institut für Anorganische Chemie und Kristallographie, Chemische Kristallographie fester Stoffe, Universität Bremen
4. Dr. Michael Fischer, Fachbereich 05 Geowissenschaften, Kristallographie, Universität Bremen
5. Priv.-Doz. Dr. M. Mangir Murshed, Fachbereich 02 Biologie/Chemie, Institut für Anorganische Chemie und Kristallographie, Chemische Kristallographie fester Stoffe, Universität Bremen
6. Carla Uribe, Fachbereich 02 Biologie/Chemie, Institut für Anorganische Chemie und Kristallographie, Student im Masterstudiengang Chemie, Universität Bremen

Acknowledgments

First of all, I would like to express my gratitude to my Doktorvater, Prof. Dr. Thorsten M. Gesing for allowing me to work in his group, for his continuous support and scholastic advice as well as for his profound insight into solid-state crystallographic chemistry. I deeply enjoy and benefit from his saying, “Do Rietveld refinement and show me, please”.

Many thanks go to my advisor, PD. Dr. M. Mangir Murshed for his guidance and the inspiring discussions as well as for his incredible patience to correct my manuscripts. I am also grateful to Dr. Lars Robben and Mrs. Gabriele Ebert for their kind help during my stay.

I am honored that Prof. Dr. Hubert Huppertz at the University of Innsbruck and Prof. Dr. Thomas Schleid at the University of Stuttgart are willing to serve as the reviewer of my dissertation. I appreciate their time and suggestions for improving my dissertation.

I am indebted to my lovely colleagues, past and present in the AG Gesing group for being good friends to me. Thanks Mathias Gogolin, Julia Butzlaff, Niels Lefeld, Dr. Andera Kirsch, Dr. Hilke Petersen, Dr. Xi Liu, Marius Wolpmann, Kowsik Ghosh, Sarah Wittmann, Dr. Sindu Shree, Christopher Reuter and Selina Schuh. As a german proverb says: „Berg und Tal kommen nicht zusammen, wohl aber die Menschen“.

I am thankful to Dr. Michael Wendschuh, Dr. Iris Spiess and Dr. Johannes Birkenstock in the AG Fischer group at the University of Bremen for the management and training of the X-ray diffractometers. Particular thanks go to Emeritus Prof. Armel Le Bail for his quick reply when I had questions concerning the powder diffraction and crystallography. I am grateful to the JANA workshops organized by the Laboratory of Crystallography, the Czech Academy of Sciences. I also thank the MATRAC summer schools for the theoretical and practical courses at the DESY in Hamburg and at the FRM II in Garching.

I cordially acknowledge the University of Bremen for the administrative support and the China Scholarship Committee (CSC) for the financial support for my doctoral research.

Declaration

I hereby declare that this submission is my own work and that, to the best of my knowledge and belief, it contains no material previously published or written by another person nor material which to a substantial extent has been accepted for the award of any other degree or diploma of the university or other institute of higher learning, except where due acknowledgment has been made in the text.

Signature: _____

Date: _____

Declaration

Versicherung an Eides Statt

Hiermit versichere ich, Pengyun Chen,

an Eides statt durch meine Unterschrift, dass ich die vorstehende Arbeit mit dem Titel „*Synthesis, crystal structures and characterization of novel alkali-metal containing rare-earth orthoborates*“ selbständig und ohne fremde Hilfe angefertigt und alle Stellen, die ich wörtlich dem Sinne nach aus Veröffentlichungen entnommen habe, als solche kenntlich gemacht habe, mich auch keiner anderen als der angegebenen Literatur oder sonstiger Hilfsmittel bedient habe.

Ich versichere an Eides statt, dass ich die vorgenannten Angaben nach bestem Wissen und Gewissen gemacht habe und dass die Angaben der Wahrheit entsprechen und ich nichts verschwiegen habe.

Die Strafbarkeit einer falschen eidesstattlichen Versicherung ist mir bekannt, namentlich die Strafandrohung gemäß § 156 StGB bis zu drei Jahren Freiheitsstrafe oder Geldstrafe bei vorsätzlicher Begehung der Tat bzw. gemäß § 161 Abs. 1 StGB bis zu einem Jahr Freiheitsstrafe oder Geldstrafe bei fahrlässiger Begehung.

(Pengyun Chen)

Bremen, 2020

Contents

Acknowledgement.....	2
Abstract: Thesis structure.....	7
List of Publications.....	8
Chapter 1: Introduction.....	9
Chapter 2: Experimental Methods.....	52
Declaration on own contributions to the publications	59
Chapter 3: $\text{KLi}_2\text{RE}(\text{BO}_3)_2$ (RE = Dy, Ho, Er, Tm, Yb and Y)	61
Chapter 4: $\text{K}_3\text{RE}_3(\text{BO}_3)_4$ (RE = Pr, Nd, Sm, Eu, Gd, Tb, Dy, Ho, Er, Tm, Yb and Lu)	108
Chapter 5: $\text{K}_2\text{Pr}_2\text{O}(\text{BO}_3)_2$	148
Summary and Outlook.....	174
Zusammenfassung und Ausblick.....	176
Appendix.....	178
Curriculum vitae.....	182

Abstract

Inorganic metal borates are of research interest due to their structural diversity, interesting physico-chemical properties and wide applications in optics. To date, several rare-earth borates are developed as laser crystals, nonlinear optical crystals, self-frequency-doubling crystals, fluorescent phosphors and scintillation materials. In addition to these optical applications, rare-earth borates attract intensive attention on fascinating magnetic behaviors arising from their unpaired inner shell 4f electrons. Therefore, the design and search of new rare-earth borates and the investigation of their unique properties are of practical and scientific significance.

This cumulative dissertation involves the use of solid-state synthesis and flux crystal growth methods for exploring the descriptive chemistry of various alkali metal-containing rare-earth borate systems where several new structures were isolated. In **chapter 1**, a series of typical and appealing alkali metal-containing rare-earth borates are reviewed in terms of their crystal structures, structural variation as well as their applications. **Chapter 2** refers to the experimental methods and consists of two parts: synthesis methods of powder and single-crystal samples and multi-tool methods for a variety of characterization. **Chapter 3** introduces a series of rare-earth orthoborates $\text{KLi}_2\text{RE}(\text{BO}_3)_2$ ($\text{RE} = \text{Dy, Ho, Er, Tm, Yb and Y}$) with a new structure-type along with their detailed investigations of the optical, magnetic, vibrational, and thermal properties as well as DFT calculation. In chapter 4, the synthesis and crystal structures of novel alkali rare-earth orthoborates $\text{K}_3\text{RE}_3(\text{BO}_3)_4$ ($\text{RE} = \text{Pr, Nd, Sm, Eu, Gd, Tb, Dy, Ho, Er, Tm, Yb, and Lu}$) along with the structural relationship between the reported $\text{A}_3\text{RE}_3(\text{BO}_3)_4$ ($\text{A} = \text{Na, K, Rb}$) systems are discussed. The following **chapter 5** describes a novel layered potassium praseodymium oxo-orthoborate $\text{K}_2\text{Pr}_2\text{O}(\text{BO}_3)_2$ with crystal structure, optical, magnetic, vibrational, and thermal properties. The last **chapter 6** is the overall summary and the outlook of this cumulative thesis.

This thesis is submitted as cumulative research work, based on three published manuscripts, presented in chapters 3 – 5, and the respective references are given as follows:

KLi₂RE(BO₃)₂ (RE = Dy, Ho, Er, Tm, Yb and Y): structural, spectroscopic and thermogravimetric studies on a series of mixed alkali rare-earth orthoborates.

Pengyun Chen, M. Mangir Murshed*, Michael Fischer, Thomas Frederichs, Thorsten M. Gesing

Published in Inorganic Chemistry, 59, 2020, 18214–18224

DOI: 10.1021/acs.inorgchem.0c02684

Synthesis and crystal structures of novel alkali rare-earth orthoborates K₃RE₃(BO₃)₄ (RE = Pr, Nd, Sm - Lu)

Pengyun Chen, M. Mangir Murshed* and Thorsten M. Gesing

Published in Journal of Materials Science, 56, 2021, 3639–3652

DOI: 10.1007/s10853-020-05506-5

Synthesis and characterization of K₂Pr₂O(BO₃)₂: structural, spectroscopic and thermogravimetric investigations of a novel potassium praseodymium oxoborate structure-type

Pengyun Chen, M. Mangir Murshed* and Thorsten M. Gesing

Published in: Springer Nature Applied Sciences, 2, 2020, 747

DOI: 10.1007/s42452-020-2553-2

Key words: Alkali-metal, Rare-earth borates, vibrational property, optical property, thermal stability, magnetic property

Chapter 1.

The search of new materials with unique properties is always the key to the design of innovative devices and components in advanced technology. The rapid progress of solid-state laser and the nonlinear optics can be attributed to the discovery and the development of borate compounds, such as β -BaB₂O₄ (β -BBO) [1], LiB₃O₅ (LBO) [2] and CsLiB₆O₁₀ (CLBO) [3-5]. The state-of-the-art nonlinear optical crystals used in the range of ultraviolet and deep ultraviolet are mostly inorganic borates [6]. The recent decades have witnessed substantial attention on inorganic borates and their application perspectives including second-harmonic generation (SHG) [5], laser emission [7], photocatalysis [8, 9], phosphors for white light-emitting diodes (wLED) [10], scintillation [11, 12], axial negative thermal expansion [13, 14] and electrolytic capacitors in the nuclear industry [15, 16]. Besides, borates are well-known for their rich structural chemistry as a boron atom can connect either three or four oxygen atoms, forming isolated BO₃³⁻ triangle or BO₄⁵⁻ tetrahedra. Such BO₃³⁻ or/and BO₄⁵⁻ ortho-anions can further be interlinked by corner- or/and edge-sharing to be condensed into complex rings, one-dimensional chains, two-dimensional slabs, and three-dimensional frameworks [17]. To date, nearly 4000 entries for inorganic borates have been indexed in the Inorganic Crystal Structure Database (ICSD) [18].

Structural diversity and practical application of inorganic borates have been significantly expanded in way of incorporating functional ions. The introduction of Be²⁺ into the matrix of borates is beneficial for the largest energy gap, i.e., the shortest absorption wavelength [19, 20]. A typical example is the KBe₂BO₃F₂ (KBBF) crystal that can be used to generate a deep ultraviolet solid-state laser with a wavelength of 177.3 nm [21]. Besides, a variety of 3d-transition metal-containing borates, such as LiMnBO₃ [22], PbMnBO₄ [23], SrCu₂(BO₃)₂ [24], and FeBO₃ [25] are of broad research interest because of their appealing electrochemical and magnetic properties.

A common type of incorporated ions in inorganic borates is the rare-earth cation. Since ionic radii of rare-earth elements are close to each other, these rare-earth borates are favorable to host optically active cations such as Ce^{3+} , Nd^{3+} , Eu^{3+} , and Yb^{3+} [7]. YBO_3 and GdBO_3 doped with Eu^{3+} and Tb^{3+} have been widely used as commercial red- and green-emitting phosphors in the plasma display panels because of their high absorption in the vacuum ultraviolet, efficient light conversion, and thermodynamic stability [26-28]. $\text{LuBO}_3:\text{Ce}^{3+}$ with the calcite structure type is one of the most useful fast-decay scintillators: light yields of the polycrystalline demonstrate around three times than that of the commercial $\text{Bi}_4\text{Ge}_3\text{O}_{12}$ (BGO) scintillators [29]. To date, plenty of acentric rare-earth borates with large SHG coefficients such as $\text{RECa}_4\text{O}(\text{BO}_3)_3$ (RE = La, Gd, Y) [30], $\text{La}_2\text{CaB}_{10}\text{O}_{19}$ [31], $\text{REAl}_3(\text{BO}_3)_4$ (RE = La, Gd, Lu, Y) [32] and $\text{La}_x\text{Y}_y\text{Sc}_{4-x-y}(\text{BO}_3)_4$ [33] can serve as the lasing media. Their bulk single crystals doped with Nd^{3+} and Yb^{3+} are further technically exploited to be self-frequency doubling (SFD) materials. For instance, the continuous wave self-frequency-doubled green laser output power up to 1.1 W was achieved by using $\text{Yb}^{3+}:\text{YAl}_3(\text{BO}_3)_4$ crystal [34].

One fascinating subgroup of rare-earth borates is the alkali metal-containing rare-earth borate, which has been investigated since the 1970s. ^6Li - and ^{10}B -enriched $\text{Li}_6\text{RE}(\text{BO}_3)$ (RE = Gd, Lu, Y) were shown to be promising neutron scintillators [35-37] because of their good energy resolution and fast decay time for thermal neutron detection. A variety of compounds such as $\text{Na}_3\text{RE}_2(\text{BO}_3)_3$ (RE = La, Gd) [38, 39], $\text{Na}_3\text{La}_9\text{O}_3(\text{BO}_3)_8$ [40], and $\text{K}_3\text{REB}_6\text{O}_{12}$ (RE = Gd, Lu, and Y) [41] were reported to be promising NLO materials in the UV/Vis range. Furthermore, a series of near-ultraviolet-excitable emission-tunable phosphors for white light-emitting diodes were designed and developed by doping Ce^{3+} , Eu^{3+} , and Tb^{3+} at the rare-earth sites in the crystal structures [42-44]. Recently, a zeolite-like $\text{Na}_3\text{Y}_3(\text{BO}_3)_4$ [45] featuring an unusual structural motif of hexagonal open-tunnel was reported in the rare-earth borates for the first time. Additionally, the Ab-initio calculation reveals that the distorted coordination polyhedra

of rare-earth atoms, such as Y atom in $\text{Na}_3\text{Y}_3(\text{BO}_3)_4$ and La atom in $\text{Na}_3\text{La}_2(\text{BO}_3)_3$, make a significant contribution to their optical susceptibilities. Very recently, alkali-metal containing rare-earth borates received increasing attraction for their diverse magnetic behaviors. A high terbium content orthoborate, $\text{LiCaTb}_5(\text{BO}_3)_6$ [46] was found to be an excellent Faraday rotator in the Vis-NIR range with a large Verdet constant of $-234 \text{ rad/T}\cdot\text{m}$ at 633 nm, which is 55 % higher than that of the commercial $\text{Tb}_3\text{Ga}_5\text{O}_{12}$ garnet (TGG) crystal. Afterward, $\text{LiCaTb}_5(\text{BO}_3)_6$ [47] and $\text{K}_3\text{Li}_3\text{Gd}_7(\text{BO}_3)_9$ [48] were reported as promising magnetic refrigerator with a profound cooling enhancement over the benchmark medium $\text{Gd}_3\text{Ga}_5\text{O}_{13}$ garnet (GGG) especially above liquid hydrogen temperature. $\text{MBaRE}(\text{BO}_3)_2$ ($\text{M} = \text{Rb}, \text{K}$) [49, 50] with the buetschliite-type structure were attractive models for investigating magnetic frustration in rare-earth-bearing materials due to the triangular rare-earth lattices. For a better understanding, herein, the crystal structures of several typical and technically important alkali-metal containing rare-earth borates are discussed particularly in the viewpoint of rare-earth elements.

Li₆RE(BO₃)₃ (RE = Nd, Sm-Gd, Dy-Lu, Y)

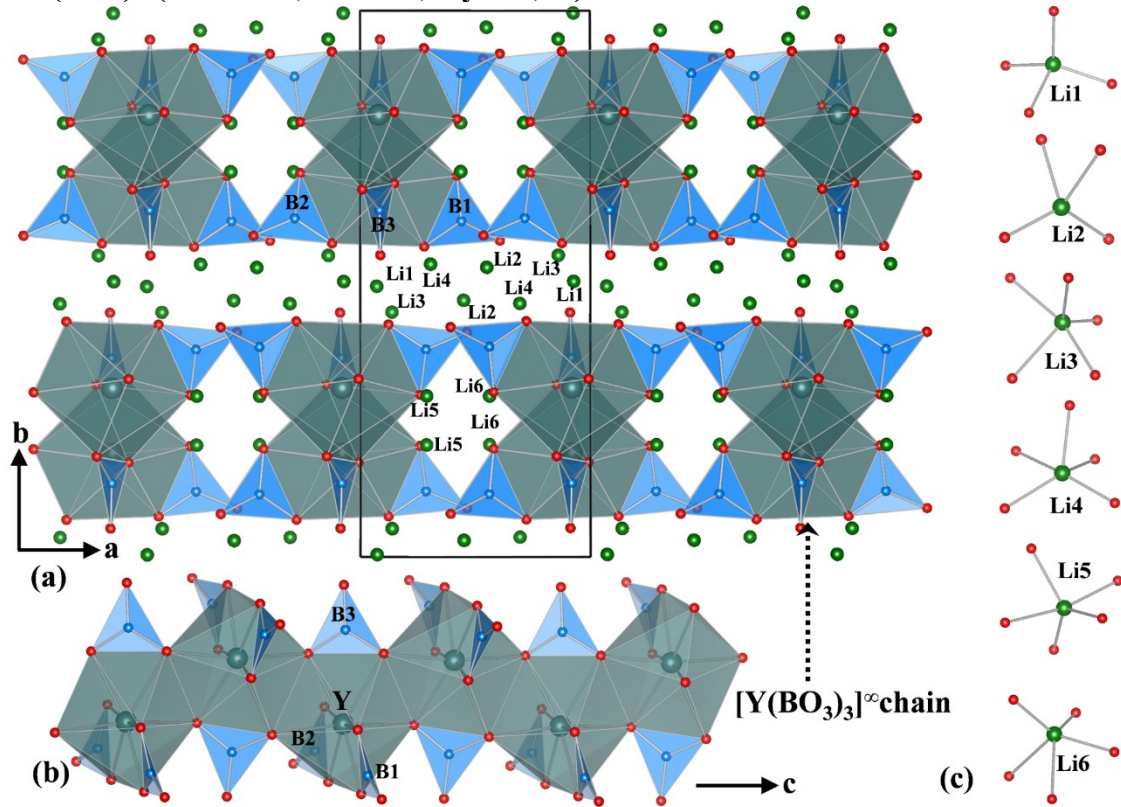


Figure 1.1. (a) crystal structure of the Li₆Y(BO₃)₃ viewed from the **c**-axis; (b) [Y(BO₃)₃][∞] chains running along the **c**-axis in an edge-sharing scheme; (c) coordination sphere of Li atoms.

The lithium-rich Li₆RE(BO₃)₃ family with RE = Nd, Sm-Lu, and Y, was initially demonstrated by Abdullaev et al. [51-54]. Li₆RE(BO₃)₃ (RE = Gd, Lu, and Y) crystals doped with other trivalent rare-earth ions, such as Ce³⁺, Nd³⁺, and Yb³⁺ have been widely studied for thermal neutron scintillation and solid-state laser emission [55, 56]. These compounds crystallize in the monoclinic space group *P*2₁/*c*, with the cell parameters of *a* = 715.7(5) pm, *b* = 1637.8(8) pm, *c* = 662.3(4) pm and $\beta = 105.32(5)^\circ$ and *Z* = 4 in the case of Li₆Y(BO₃)₃.

The asymmetric cell of Li₆Y(BO₃)₃ contains one unique Y atom, three B, nine O, and six Li atoms. The Y atom is eight-coordinated by oxygen atoms to form a YO₈ polyhedron with *C*₁ point symmetry. Each YO₈ polyhedron is interlinked with three BO₃³⁻ groups by sharing common edges, and those YO₈ polyhedra are further interconnected together through edge-sharing, resulting in one-dimensional zigzag [Y(BO₃)₃] chains along the **c**-axis (Figure 1.1(b)).

These $[\text{Y}(\text{BO}_3)_3]$ zigzag chains are separated from each other by six crystallographic-independent Li cations, forming a layered three-dimensional network along the **b**-direction shown in Figure 1.1(a). The separation of zigzag chains can detain the energy migration to one dimension, which may account for the high quenching concentrations of doping optically-active ions at the Y site. Of the six lithium cations, Li(1), Li(2), Li(3), and Li(4) are located between the layers, while Li(5) and Li(6) are situated inside the layers. As displayed in Figure 1.1(c), Li(1) and Li(2) cations are tetrahedrally coordinated, whereas Li(3), Li(4), Li(5), and Li(6) are coordinated by five oxygen atoms to form strongly distorted pyramids. The bond valence sum (BVS) calculation shows the value of 1.25(3), 0.97(2), 0.97(2), 0.92(2), 1.00(2), and 1.04(2) for Li(1), Li(2), Li(3), Li(4), Li(5) and Li(6), respectively, suggesting that all Li cations have normal charge value except Li(1) cation which is over-bonded.

$\text{LiRE}_6\text{O}_5(\text{BO}_3)_3$ (RE = Pr, Nd, Sm-Tm and Y)

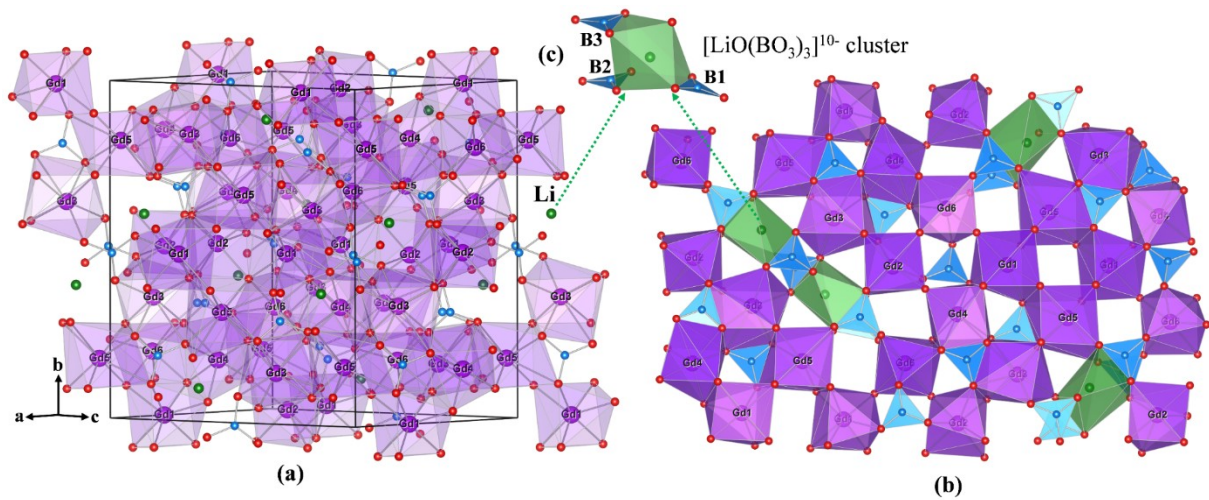


Figure 1.2: (a) three-dimensional framework of $\text{LiGd}_6\text{O}_5(\text{BO}_3)_3$, (b) fluorite-like arrays along the $[102]$ direction, (c) $[\text{LiO}(\text{BO}_3)_3]^{10-}$ cluster

A family of the rare-earth rich lithium-containing oxoborates followed with the formula of $\text{LiRE}_6\text{O}_5(\text{BO}_3)_3$ (RE = Pr, Nd, Sm-Tm and Y) was reported by Chaminade et al. for the first time [57, 58]. Ytterbium-doped $\text{LiGd}_6\text{O}_5(\text{BO}_3)_3$ single-crystals were grown from the high-

temperature flux and were identified as a promising candidate for the ultra-pulsed and continuous-wave laser sources [59]. Moreover, Eu^{3+} , Sm^{3+} co-doped $\text{LiY}_6\text{O}_5(\text{BO}_3)_3$ phosphors [60] were found to be attractive for white LED excited with the near-ultraviolet chips.

The crystal structure of $\text{LiGd}_6\text{O}_5(\text{BO}_3)_3$ was solved by the single-crystal X-ray diffraction, revealing that it belongs to the monoclinic space group $P2_1/c$ with the lattice parameters of $a = 848.9(4)$ pm, $b = 1570.6(3)$ pm, $c = 1211.7(6)$ pm and $\beta = 132.27(2)^\circ$ and $Z = 4$. In the asymmetrical cell of $\text{LiGd}_6\text{O}_5(\text{BO}_3)_3$, there exist six Gd, three B, fourteen O, and one unique Li atoms which are all located on the $4e$ Wyckoff site. As shown in Figure 1.2a, the gadolinium atoms occupy two types of coordination polyhedra: Gd(1), Gd(2), Gd(4), and Gd(6) are in seven-coordination, and Gd(3) and Gd(5) are in eight-coordination. GdO_7 and GdO_8 polyhedra are joined together by sharing common edges and corners to constitute a dense three-dimensional framework of $\text{LiGd}_6\text{O}_5(\text{BO}_3)_3$. Careful inspection of this structure reveals a close relationship to the fluorite-type CaF_2 structure, from both the structure and the composition point of views. If the Li atom is considered as Gd atom and the boron atoms are neglected in the structure, the composition would become exactly “ GdO_2 ” (Gd_7O_{14}). Furthermore, the crystal structure of $\text{LiGd}_6\text{O}_5(\text{BO}_3)_3$ can be interpreted as a distorted fluorite structure, where the vacant Gd cationic site is occupied by $[\text{LiO}(\text{BO}_3)_3]^{10-}$ cluster which comprises one LiO_7 polyhedron and three isolated BO_3^{3-} groups (Figure 1.2(c)). The fluorite-like arrays of $\text{GdO}_{n=7,8}$ polyhedra and $[\text{LiO}(\text{BO}_3)_3]^{10-}$ clusters are displayed along the $[102]$ lattice direction where GdO_8 (strongly distorted cubes), GdO_7 (truncated cubes with one corner missing) and $[\text{LiO}(\text{BO}_3)_3]^{10-}$ clusters share common edges and apices (Figure 1.2(b)). Additionally, each $\text{GdO}_{n=7,8}$ polyhedron is bound to four nearest neighbors, which structurally resembles C-type Gd_2O_3 even though Gd atoms in this cubic sesquioxide phase are all in six-coordination.

$\text{Li}_3\text{RE}(\text{BO}_3)_2$ (RE = Gd, Er-Lu, Y) and $\text{Na}_3\text{RE}(\text{BO}_3)_2$ (RE = La, Pr-Nd, Sm-Gd, Y)

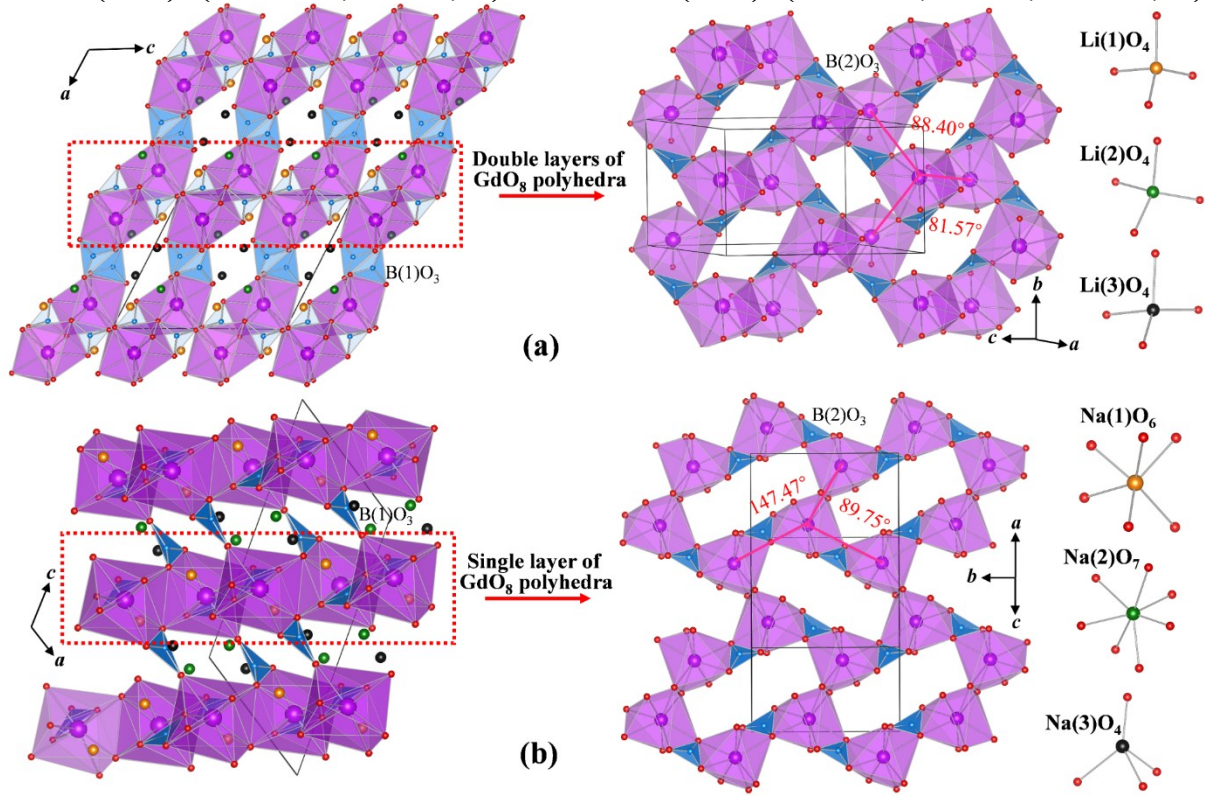


Figure 1.3: (a) crystal structure of $\text{Li}_3\text{Gd}(\text{BO}_3)_2$; double layers of GdO_8 polyhedra; coordination polyhedra of Li cations (b) crystal structure of $\text{Na}_3\text{Gd}(\text{BO}_3)_2$; double layers of GdO_8 polyhedra; coordination polyhedra of Na cations

$\text{Li}_3\text{RE}(\text{BO}_3)_3$ (RE = Gd, Er-Lu, Y) family as well as the single-crystal structure determination of $\text{Li}_3\text{Gd}(\text{BO}_3)_2$ was demonstrated by Jubera et al. [61]. Recently, Huppertz et al. prepared the single crystal of $\text{Li}_3\text{Y}(\text{BO}_3)_2$ and solved the detailed structure [62]. $\text{Na}_3\text{RE}(\text{BO}_3)_2$ (RE = La, Nd) were published by Mascetti et al. [63]. Following La- and Nd-phases, the other members of $\text{Na}_3\text{RE}(\text{BO}_3)_2$ family (RE= Pr, Sm-Gd, Y) [64-66] were synthesized by several different groups. To date, crystal structures of $\text{Na}_3\text{Nd}(\text{BO}_3)_2$ and $\text{Na}_3\text{Sm}(\text{BO}_3)_2$ have been solved by X-ray single-crystal diffraction. Besides, the crystal structures of $\text{Na}_3\text{Gd}(\text{BO}_3)_3$ and $\text{Na}_3\text{Y}(\text{BO}_3)_3$ were identified by X-Ray powder diffraction using Rietveld refinement method. To sum up, the $\text{Na}_3\text{RE}(\text{BO}_3)_3$ family can adapt light rare-earth elements, while the $\text{Li}_3\text{RE}(\text{BO}_3)_3$ family can accommodate heavy rare-earth elements.

Here, $\text{Li}_3\text{Gd}(\text{BO}_3)_2$ and $\text{Na}_3\text{Gd}(\text{BO}_3)_2$ are chosen to represent their respective family to describe their structures. Both $\text{Li}_3\text{Gd}(\text{BO}_3)_3$ and $\text{Na}_3\text{Gd}(\text{BO}_3)_3$ family crystallize into the monoclinic space group $P2_1/c$ with the lattice parameters of $a = 872.4(2)$ pm, $b = 642.5(2)$ pm, $c = 1009.5(2)$ pm, and $\beta = 116.85(2)^\circ$, and $a = 652.297(6)$ pm, $b = 872.831(8)$ pm, $c = 1214.76(1)$ pm and $\beta = 123.3525(5)^\circ$ for $\text{Li}_3\text{Gd}(\text{BO}_3)_2$ and $\text{Na}_3\text{Gd}(\text{BO}_3)_2$, respectively. The asymmetric unit cells of both phases are composed of 12 independent sites: one Gd, two B, six O, and three alkali-metal atoms. It is noteworthy that their crystal structures are not isotypic, although GdO_8 polyhedra and isolated BO_3 groups are present in both phases.

$\text{Li}_3\text{Gd}(\text{BO}_3)_2$ features a double layer of GdO_8 polyhedra parallel to the ac plane (Figure 1.3a). Those double layers of GdO_8 polyhedra are bridged together by $\text{B}(1)\text{O}_3$ groups through the strong B-O covalent bond along the a -direction to constitute the three-dimensional network. By contrast, $\text{Na}_3\text{Gd}(\text{BO}_3)_2$ shows a single layer of GdO_8 polyhedra parallel to the ac plane (Figure 1.3b). The three-dimensional network of $\text{Na}_3\text{Gd}(\text{BO}_3)_2$ can be regarded as single layers of GdO_8 polyhedra joined together by $\text{B}(1)\text{O}_3$ groups through the B-O bond along the a -direction. In both single and double layers, it can be found that $[\text{Gd}_2\text{O}_{14}]$ dimers are formed by edge-shared GdO_8 polyhedra and that two edges of the $\text{B}(2)\text{O}_3$ groups strengthen the connection of these $[\text{Gd}_2\text{O}_{14}]$ dimers. It should be stated that the key difference between the double-layer and the single-layer lies in the orientation of the $[\text{Gd}_2\text{O}_{14}]$ dimers. The two nearest neighboring dimers are arranged at angles of 88.40° and 81.57° in the double layer, whereas 89.75° and 147.47° are found for the same in the single layer, implying that $[\text{Gd}_2\text{O}_{14}]$ dimers pack more tightly in the double layer than in the single layer.

Besides, differences occur in the coordination polyhedra of alkali-metal cations. In $\text{Li}_3\text{Gd}(\text{BO}_3)_3$, Li^+ cations are all coordinated by four oxygen atoms, forming regular tetrahedra. In $\text{Na}_3\text{Gd}(\text{BO}_3)_2$, $\text{Na}(1)$, $\text{Na}(2)$, and $\text{Na}(3)$ cations are located in six, seven, and four coordination polyhedra, respectively. It seems that the size difference between Li^+ and Na^+

cations can markedly influence their crystal structure even though $\text{Li}_3\text{Gd}(\text{BO}_3)_3$ and $\text{Na}_3\text{Gd}(\text{BO}_3)_3$ have a similar formula. Furthermore, it would be interesting to synthesize $\text{LiNa}_2\text{Gd}(\text{BO}_3)_2$ and $\text{Li}_2\text{NaGd}(\text{BO}_3)_2$ to look that either the single layer or the double layer predominately emerges in these compounds.

$\text{K}_3\text{RE}(\text{BO}_3)_2$ (for RE = Pr, Nd, Sm-Gd in *Pnma*; RE = Y, Tb-Lu in *Pnnm*)

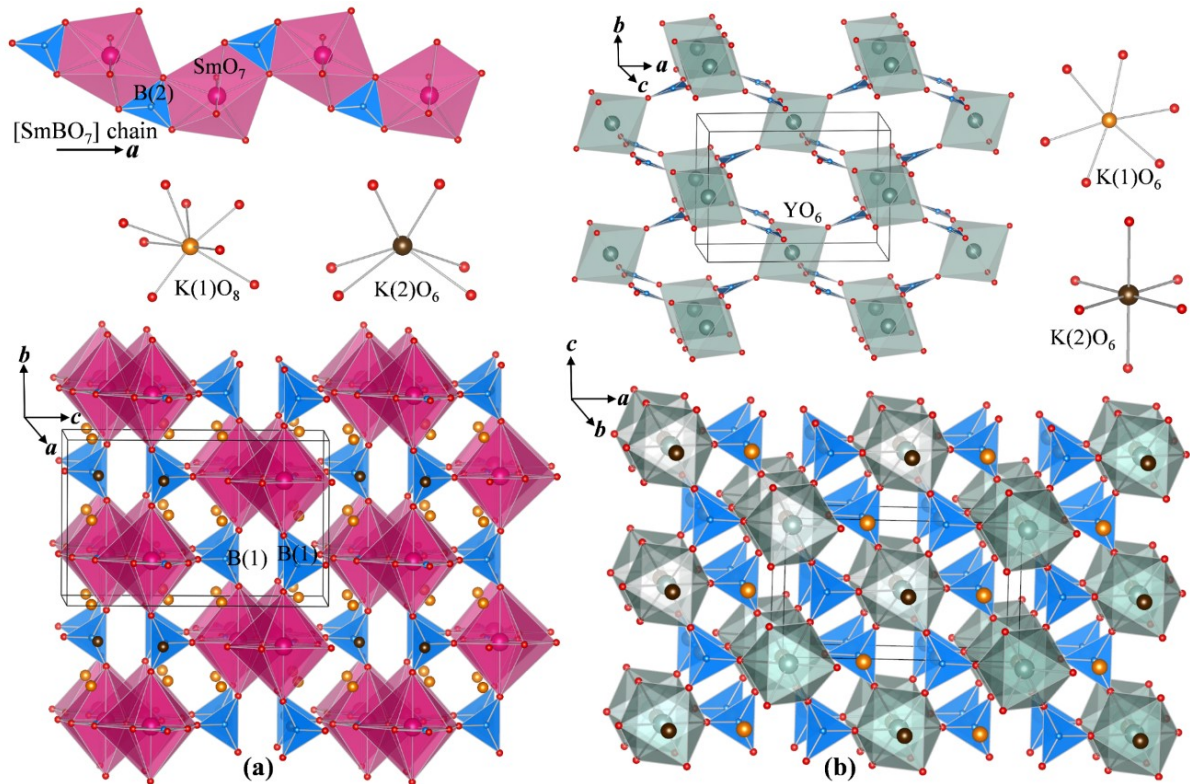


Figure 1.4 (a) $[\text{SmBO}_7]$ zigzag chain and coordination environments of K^+ cations and crystal structure of $\text{K}_3\text{Sm}(\text{BO}_3)_2$ (b) "isolated" YO_6 octahedra bridged by BO_3 groups, chain and coordination environments of K^+ cations and crystal structure of $\text{K}_3\text{Y}(\text{BO}_3)_2$

$\text{K}_3\text{RE}(\text{BO}_3)_2$ family was discovered by Gao et al. [67]. To begin with, $\text{K}_3\text{RE}(\text{BO}_3)_2$ (RE = Nd-Lu) family can be divided into two different structure types. The larger rare-earth cations with RE = Nd-Gd adopt the space group *Pnma*, whereas the smaller rare-earth cations with RE = Tb-Lu and Y belong to the space group *Pnnm*. Here, $\text{K}_3\text{Sm}(\text{BO}_3)_2$ and $\text{K}_3\text{Y}(\text{BO}_3)_2$ were selected

as representative of each group to describe their crystal structures determined by single-crystal X-ray diffraction.

The asymmetric unit cell of $K_3Sm(BO_3)_2$ consists of ten individual sites: one Sm, two K, two B, and five O atoms. Each Sm^{3+} cation is surrounded by seven O atoms, forming a REO_7 pentagonal bipyramid. These REO_7 bipyramids are linked together via corner-sharing along the **a**-direction shown in Figure 1.4(a). Two edges of the $B(2)O_3$ group further reinforce those REO_7 bipyramids in building the $[SmBO_7]$ zigzag chains. All three vertexes of the $B(1)O_3$ group connect three $[SmBO_7]$ zigzag chains, forming a scaffold-like three-dimensional framework. Two types of K cations are located in the interstitial sites: eightfold-coordinated $K(1)^+$ and sixfold-coordinated $K(2)^+$, respectively. Interestingly, $K(1)$ cation is found to be over-bonded with a BVS of 1.37(1) v. u., and $K(2)$ is markedly under-bonded with a BVS of 0.69(1) only.

On the other hand, the asymmetric unit cell of $K_3Y(BO_3)_2$ is made up of six independent sites: one Sm, two K, one B, and two O atoms. In contrast to the sevenfold-coordinated Sm^{3+} in $K_3Sm(BO_3)_2$, Y^{3+} is connected to six O atoms, forming a YO_6 octahedron (Figure 1.4(b)). Unlike the corner-shared SmO_7 pentagonal bipyramid, these YO_6 octahedra are isolated from each other, but every vertex of YO_6 octahedron is connected to one BO_3 groups. The $K(1)$ cation is surrounded by six oxygen atoms that are almost located in the same plane to create an unusual KO_6 hexagon, whereas $K(2)$ cation and six oxygen build up a normal KO_6 octahedron. In contrast to the abnormal BVS values for the K cations in $K_3Sm(BO_3)_2$, the BVS values for K cations in $K_3Y(BO_3)_2$ are within the empirical range: 1.12(1) v. u. and 1.19(1) v. u. for $K(1)$ and $K(2)$, respectively.

Comparing crystal structures of $A_3RE(BO_3)_2$ ($A = Li, Na$ and K), one can reckon that both the alkali-metal and rare-earth cations have a substantial impact on crystal structures of alkali metal-containing rare-earth borates.

LiCaRE₅(BO₃)₆ (RE = Sm-Lu, Y)

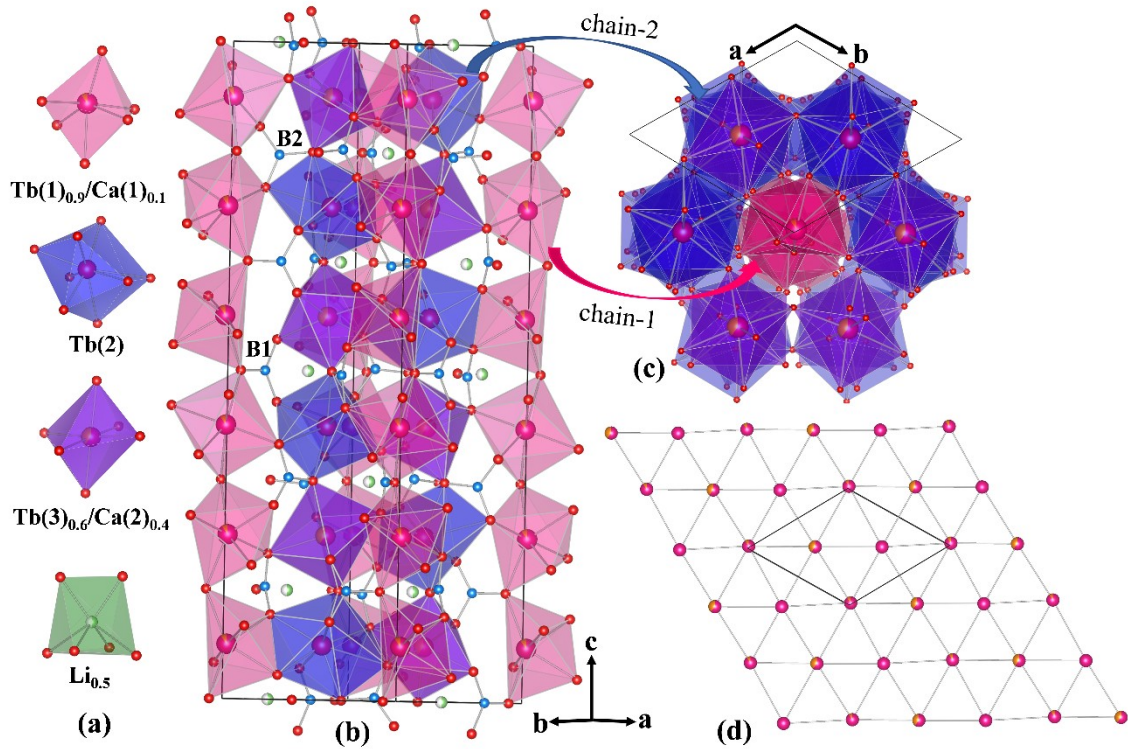


Figure 1.5 (a) coordination environments of Tb, Ca, and Li atom (b) crystal structure of LiCaTb₅(BO₃)₆ (c) chain-1 and chain-2 viewed along the *c*-direction (d) the triangular lattice layer in the *ab* plane.

LiCaTb₅(BO₃)₆ in single crystal form was initially published as a promising Faraday rotator by Li and coauthors [46]. LiCaTb₅(BO₃)₆ crystallizes in the hexagonal space group *P*6₅22 with lattice parameters of *a* = 704.24(4) pm, *c* = 2577.6(2) pm and *Z* = 3. The asymmetric cell of LiCaTb₅(BO₃)₆ contains three Tb, five O, two B, and one Li sites.

Both Tb(1) and Tb(3) atoms are coordinated to six oxygen atoms to form distorted TbO₆ octahedra, while the Tb(2) atom locates at the centroid of a distorted TbO₈ dodecahedron (Figure 1.5 (a)). Interestingly, Ca²⁺ cations tend to merely admix with the 6-coordinated Tb³⁺ cations rather than the 8-coordinated Tb³⁺ cations: the substitutional disorder between Tb³⁺ and Ca²⁺ cations emerges at Tb(1) site and Tb(3) site with ratios of 0.9 and 0.6, respectively. On the contrary, Tb(2) site is solely on its Wyckoff site. As shown in Figure 1.5 (b), [Tb(1)/Ca]O₆ octahedra are joined together by means of corner-sharing to build up the chain-1 along the *c*-direction. Tb(2)O₈ dodecahedra and [Tb(3)/CaO₆] octahedra are alternately stacked along the

c-direction, forming the chain-2. Each chain-1 is surrounded by six nearest neighboring chain-2 to constitute the framework of $\text{LiCaTb}_5(\text{BO}_3)_6$, shown in Figure 1.5 (c). Each $\text{B}(1)\text{O}_3$ shares one vertex with the chain-1 and two vertexes with the chain-2, while each $\text{B}(2)\text{O}_3$ group shares two vertices with the chain-1 and one vertex with the chain-2. Li^+ is octahedrally coordinated but with a half occupancy. Although all Tb^{3+} atoms reside at the same height and form a triangular magnetic lattice in the ab plane, the Tb triangle deviates from an ideal triangular magnetic lattice displayed in Figure 1.5 (d). Nevertheless, such a high terbium content in the uniaxial $\text{LiCaTb}_5(\text{BO}_3)_6$ brings a pronounced Faraday radiation performance over $\text{Tb}_3\text{Ga}_5\text{O}_{12}$ (TGG) in the visible range. Just recently, polycrystalline $\text{LiCaRE}_5(\text{BO}_3)_6$ ($\text{RE} = \text{Sm}, \text{Eu}, \text{Tb}, \text{Dy}, \text{Ho}, \text{Er}, \text{Tm}, \text{Yb}, \text{Lu}, \text{and Y}$) were synthesized by Cong et al. using high-temperature solid-state reactions [68]. The authors also found all $\text{LiCaRE}_5(\text{BO}_3)_6$ members isotypic with $\text{LiCaTb}_5(\text{BO}_3)_6$ by utilizing Rietveld refinement method.

$\text{Li}_3\text{RE}_2(\text{BO}_3)_3$ ($\text{RE} = \text{La}, \text{Pr}, \text{Nd}, \text{Sm-Lu}, \text{Y}$)

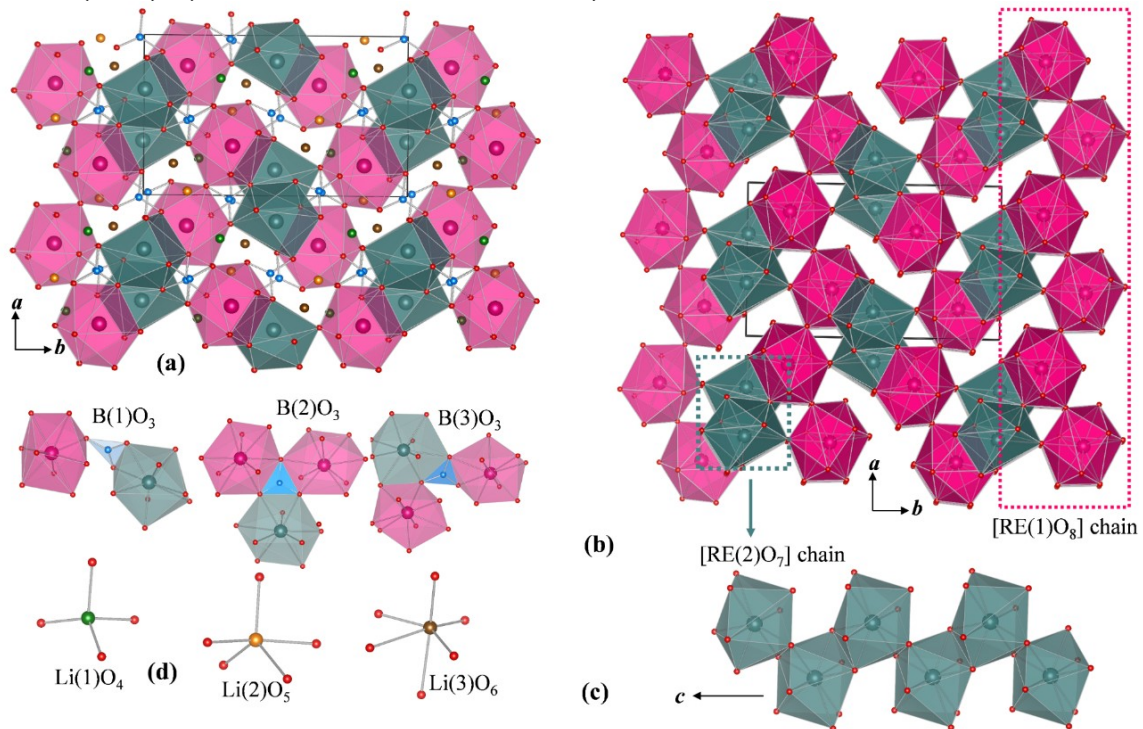


Figure 1.6 (a) crystal structure of $\text{Li}_3\text{RE}_2(\text{BO}_3)_3$ viewed from the c -axis (b) linkage of $[\text{RE}(1)\text{O}_9]$ chain and $[\text{RE}(2)\text{O}_9]$ chain in the ab plane (c) $[\text{RE}(2)\text{O}_9]$ chain (d) coordination environments of B and Li atoms

$\text{Li}_3\text{RE}_2(\text{BO}_3)_3$ family was first reported by Abdullaev et al. in 1977 [69]. In this family, $\text{Li}_3\text{Pr}_2(\text{BO}_3)_3$ is the first published member with the lattice parameters of $a = 881.6(4)$ pm, $b = 1412.7(8)$ pm; $c = 581.2(3)$ pm, and $\beta = 103.72(4)^\circ$. The whole $\text{Li}_3\text{RE}_2(\text{BO}_3)_3$ (RE = La, Pr, Nd, Sm-Lu, and Y) family are isotypic in the space group of $P2_1/n$. To date, crystal structures of only RE = Pr, Nd, Eu members have been solved by single-crystal X-ray diffraction [70].

The asymmetric unit of $\text{Li}_3\text{RE}_2(\text{BO}_3)_3$ contains two RE, three B, three Li, and nine O atoms. Both RE(1) and RE(2) cations are surrounded by nine oxygen atoms. Since Li^+ cation is exceedingly small, $\text{Li}_3\text{RE}_2(\text{BO}_3)_3$ crystallizes into a dense framework mainly made up of REO_9 polyhedra, shown in Figure 1.6(b). RE(1) O_9 polyhedra share common corners to form [RE(1) O_8] zigzag chains along the **a**-direction, while RE(2) O_9 polyhedra are connected via edge-sharing to form [RE(2) O_7] zigzag chains along the **c**-direction. Such [RE(1) O_8] and [RE(2) O_7] zigzag chains are firmly crosslinked together by sharing common edges and corners to construct the dense three-dimensional network of $\text{Li}_3\text{RE}_2(\text{BO}_3)_3$.

All Boron atoms are coordinated by three oxygen atoms to form isolated BO_3 groups. As shown in Figure 1.6(d), the B(1) O_3 group is connected with one RE(1) O_9 and one RE(2) O_9 polyhedra via common vertex and edge, the B(2) O_3 group is connected with two RE(1) O_9 and one RE(2) O_9 polyhedra through sharing all three edges while the B(3) O_3 group is connected with two RE(1) O_9 and one RE(2) O_9 polyhedra by two edges and one vertex. The Li(1), Li(2) and Li(3) are four-, five-, and six-fold coordinated, respectively. The BVS calculation shows the value of 1.12(1), 0.84(1), and 0.91(1) v. u. for Li(1), Li(2), and Li(3), respectively, suggesting that Li(1) is slightly over-bonded while Li(2) and Li(3) are slightly under-bonded.

$\text{Na}_3\text{RE}_2(\text{BO}_3)_3$ (RE=La, Nd, Sm, Gd, Tb)

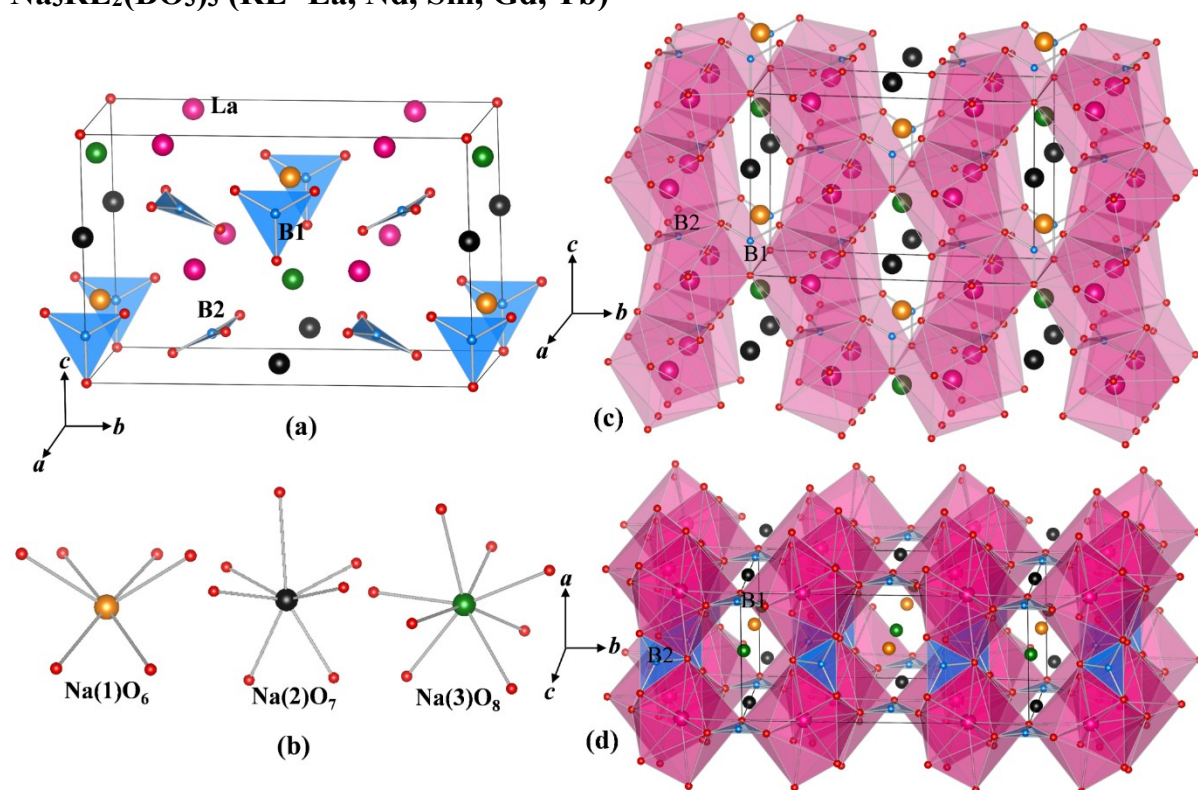


Figure 1.7 (a) the unit cell of $\text{Na}_3\text{La}_2(\text{BO}_3)_3$. (b) coordination spheres of Na atoms (c) crystal structure of $\text{Na}_3\text{La}_2(\text{BO}_3)_3$ viewed along the **a**-axis (d) crystal structure of $\text{Na}_3\text{La}_2(\text{BO}_3)_3$ viewed along the **c**-axis (d)

Early in 1983 two compounds $\text{Na}_3\text{La}_2(\text{BO}_3)_3$ and $\text{Na}_3\text{Nd}_2(\text{BO}_3)_3$ were obtained by Mascetti et al. [71], and only the lattice parameters and space group were given. Afterward, Zhang et al. [72] published the detailed crystal structure of $\text{Na}_3\text{La}_2(\text{BO}_3)_3$ using single-crystal X-ray diffraction. $\text{Na}_3\text{La}_2(\text{BO}_3)_3$ crystallizes in the space group *Amm*2 with the lattice parameters of $a = 5.1580(10)$ pm, $b = 11.350(2)$ pm, $c = 7.3230(15)$ pm, and $Z = 2$. Subsequently, $\text{Na}_3\text{RE}_2(\text{BO}_3)_3$ (RE=La, Sm, Gd) [38, 39, 73] were investigated with aspect to the bulk crystal growth and linear/nonlinear optical properties. Here, it should be stated that the detailed crystallographic data for Sm- and Gd- analogs have not been recorded yet, therefore $\text{Na}_3\text{La}_2(\text{BO}_3)_3$ was chosen to describe the crystal structure of this family.

The asymmetric unit of $\text{Na}_3\text{La}_2(\text{BO}_3)_3$ consists of one La, two B, three Na, and four O independent atoms. La atom is surrounded by 9 oxygen atoms, forming a LaO_9 polyhedron.

LaO₉ polyhedra are connected to each other via face-sharing to build up the [LaO₆]_n zigzag chains along the **c**-direction. Such one chain is further corner shared with four nearest neighboring chains to constitute a three-dimensional framework as shown in Figure 1.7. B(1)O₃ groups are aligned exactly perpendicular to the **a**-direction whereas B(2)O₃ groups are oriented at an angle of approximately 26.5(2)° towards the *ab* plane. Here, it could be considered that B(1)O₃ groups strengthen the connection of [LaO₆]_n chains along the **b**-direction, and B(2)O₃ groups enhance the connection along the **a**-direction.

Three types of Na⁺ ions are found to occupy interstitial voids with three different coordination polyhedra: six-, seven- and eight-fold coordination for Na(1), Na(2), and Na(3), respectively. The BVS calculation reveals that their values are 0.47(1), 1.25(1) and 0.96(1) v. u, for Na(1), Na(2) and Na(3), respectively, suggesting that Na(1)⁺ is seriously under-bonded and Na(2)⁺ is notably over-bonded while Na(3)⁺ is normal as expected. In other words, it can be assumed that Na(1) site is favored for larger monovalent cations while Na(2) site is favored for smaller monovalent cations.

In 2012 a terbium analog Na_{2.67}Tb_{2.11}(BO₃)₃ in single crystal form was reported by Chen et al. [74]. The aliovalent substitution was identified as 11 % of Tb³⁺ cations entered into the Na(3) site, bringing the vacancy of 22 % at the Na(1) site accordingly. Interestingly, the terbium phase with the idealized composition of Na₃Tb₂(BO₃)₃ has not been reported yet.

Later on, a new potassium-containing analog K_{1.34}Na_{1.66}La₂(BO₃)₃ was found by Zeng et al. [75]. Surprisingly, the Na(1) site is co-occupied by 90 % K⁺ and 10 % Na⁺; the Na(2) site is solely occupied by Na⁺ cation; the Na(3) site is co-occupied by 56 % K⁺ and 44 % Na⁺. The authors pointed out that the substitutional disorder between Na and K cations at both Na(1) and Na(3) sites was required judging from the isotropic/anisotropic atom displacement parameters at each site. They also considered that the isovalent substitution would be likely to occur at the Na(3) site instead of the Na(1) site.

Intriguingly, in the course of his Ph.D. studies, the author of this dissertation also found two similar compounds, $\text{Na}_{2.86}\text{Gd}_{2.07}(\text{BO}_3)_3$ and $\text{K}_{1.3(1)}\text{Na}_{1.7(1)}\text{Pr}_2(\text{BO}_3)_3$. Their structures were solved by X-ray single-crystal diffraction. The result of the structure determination is consistent with the previous findings. The crystallographic data for these two compounds are placed in the Appendix part. A concise comparison of cations at the Na sites with their BVS values belonging to members of $\text{Na}_3\text{La}_2(\text{BO}_3)_3$ family is listed in Table 1.1.

Table 1.1 cations at Na sites and the corresponding BVS values

Compounds	Na(1) site	BVS	Na(2) site	BVS	Na(3) site	BVS
$\text{Na}_3\text{La}_2(\text{BO}_3)_3$	Na^+	0.47(1)	Na^+	1.25(1)	Na^+	0.96(1)
$\text{Na}_{2.67}\text{Tb}_{2.11}(\text{BO}_3)_3$	0.78Na^+	0.50(1)	Na^+	1.50(1)	$0.89\text{Na}^+/0.11\text{Tb}^{3+}$	1.45(1)
$\text{K}_{1.34}\text{Na}_{1.66}\text{La}_2(\text{BO}_3)_3$	$0.9\text{K}^+/0.1\text{Na}^+$	0.86(1)	Na^+	1.30(1)	$0.56\text{Na}^+/0.44\text{K}^+$	1.62(1)
$\text{Na}_{2.86}\text{Gd}_{2.07}(\text{BO}_3)_3$	0.86Na^+	0.51(1)	Na^+	1.47(1)	$0.93\text{Na}^+/0.07\text{Gd}^{3+}$	1.42(1)
$\text{K}_{1.3(1)}\text{Li}_{1.7(1)}\text{Pr}_2(\text{BO}_3)_3$	K^+	0.86(1)	Li^+	0.95(1)	$0.7\text{Li}^+/0.3\text{K}^+$	1.17(1)

Note: the origin of the unit cell of $\text{Na}_3\text{La}_2(\text{BO}_3)_3$ has been shifted and the atoms of $\text{Na}_3\text{La}_2(\text{BO}_3)_3$, $\text{Na}_{2.67}\text{Tb}_{2.11}(\text{BO}_3)_3$ and $\text{K}_{1.34}\text{Na}_{1.66}\text{La}_2(\text{BO}_3)_3$ have been uniformly renamed for a straightforward comparison.

However, there are at least two open questions that are worth discussing or answering in the future:

- 1) We can imagine that K^+ , Li^+ , and Na^+ occupy the Na(1), Na(2), and Na(3) sites respectively. As a result, the BVS value for each Na^+ site shall be close to 1. Thus, the question becomes if it is possible to synthesize the $\text{KLiNaRE}_2(\text{BO}_3)_3$ phase.
- 2) What is the reason that the aliovalent substitution at the Na(3) site was observed for Tb^{3+} and Gd^{3+} cations rather than La^{3+} cation?

$\text{Rb}_3\text{RE}_2(\text{BO}_3)_3$ (RE=Y, Ho)

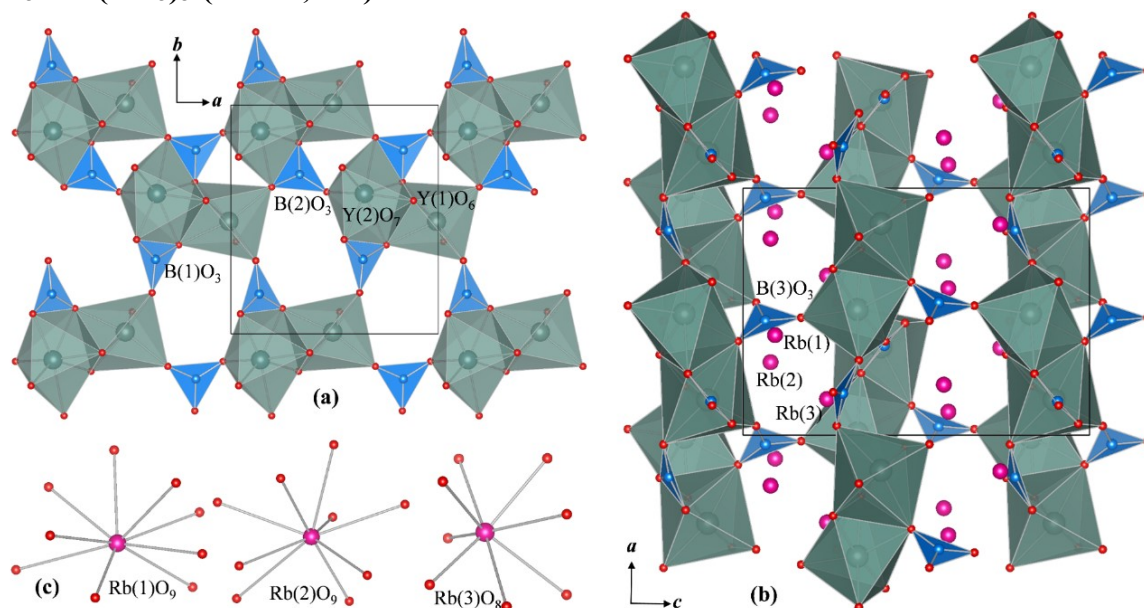


Figure 1.8 (a) [Y₂B₂O₁₀] sheet in the *ab* plane. (b) crystal structure of Rb₃Y₂(BO₃)₃ viewed along the *c*-direction (c) coordination environments of Rb⁺ cations

Rb₃Y₂(BO₃)₃ was reported and structurally characterized by Gao et al. in 2007 [76]. This compound crystallizes into the orthorhombic space group *Pna*2₁ with the lattice parameter of $a = 868.11(4)$ pm, $b = 956.27(4)$ pm, $c = 1219.14(6)$ pm. Comparing with Li₃RE₂(BO₃)₃ and Na₃RE₂(BO₃)₃, Rb₃Y₂(BO₃)₃ has a similar formula, but the crystal structure of Rb₃Y₂(BO₃)₃ distinctly differs from that of either Na₃RE₂(BO₃)₃ or Li₃RE₂(BO₃)₃.

The asymmetric unit of Rb₃Y₂(BO₃)₃ consists of 17 independent sites: two Y, three Rb, three B and nine O atoms. Y(1)³⁺ cation is coordinated to six oxygen atoms, forming a distorted YO₆ octahedron. In contrast, Y(2)³⁺ cation is surrounded by seven oxygen atoms, forming a distorted YO₇ pentagonal bipyramid. YO₆ octahedron and YO₇ pentagonal bipyramid share a common face to build up a Y₂O₁₀ dimer. Such dimers are connected to each other by corner-sharing and firmly bridged by the B(1)O₃ and B(2)O₃ groups, forming a quasi-two-dimensional [Y₂B₂O₁₀] sheet in the *ab* plane (Figure 1.8(a)). Thus, the three-dimensional framework of Rb₃Y₂(BO₃)₃ is built up by those [Y₂B₂O₁₀] sheets bridged by the remaining B(3)O₃ groups along the *c*-direction.

All Rb^+ cations reside between $[\text{Y}_2\text{B}_2\text{O}_{10}]$ sheets (Figure 1.8(c)): both Rb(1) and Rb(2) atoms are nine-fold coordinated while Rb(3) atoms are eight-fold coordinated. The BVS calculation shows the value of 1.12(1) v. u., 0.96(1) v. u. and 1.33(1) v. u. for Rb(1), Rb(2) and Rb(3), respectively, indicating that Rb(1) and Rb(2) are normal as expected while Rb(3) is significantly over-bonded.

Just recently, Subanakov et al. [77] published the synthesis and crystal structure of the $\text{Rb}_3\text{Ho}_2(\text{BO}_3)_3$ compound which is isomorphic with $\text{Rb}_3\text{Y}_2(\text{BO}_3)_3$.

$\text{Na}_3\text{Y}_3(\text{BO}_3)_4$

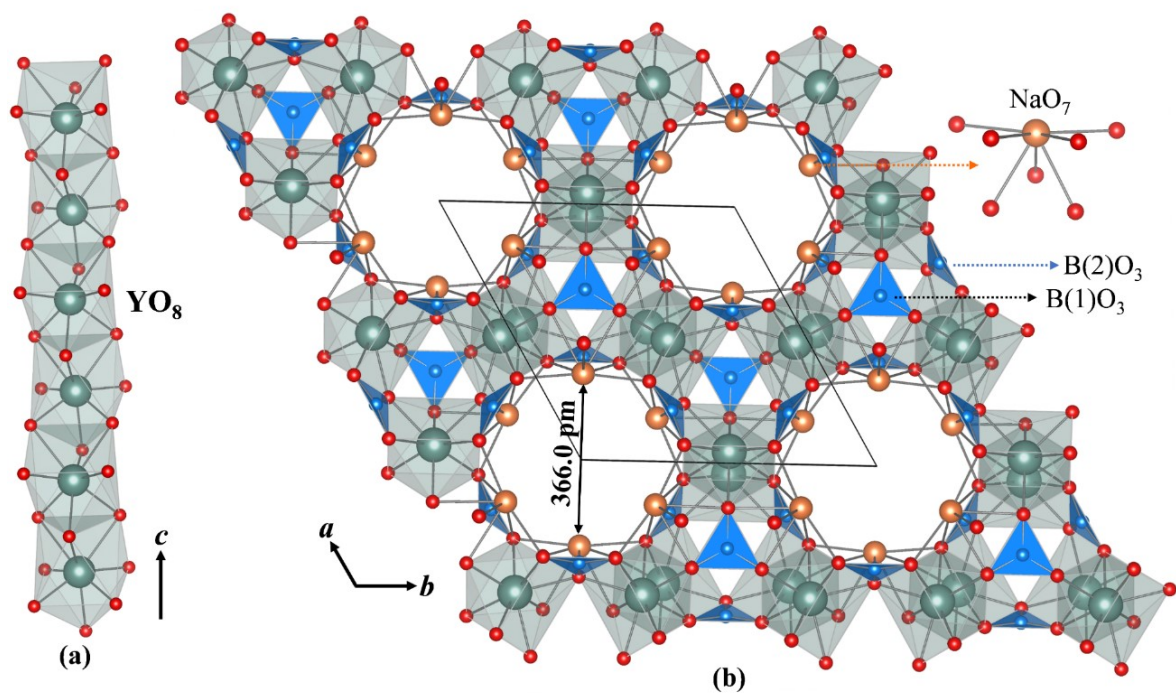


Figure 1.9 (a) one-dimensional YO_8 polyhedra backbone chain along the b -direction. (b) crystal structure of $\text{Na}_3\text{Y}_3(\text{BO}_3)_4$ viewed from the c -axis along with coordination environments of Na and B atom

$\text{Na}_3\text{Y}_3(\text{BO}_3)_4$ single crystal was isolated from the Na_2O - Y_2O_3 - B_2O_3 system by Zhang et al. [45].

This compound features the zeolite-like framework structure with an open hexagonal channel.

It crystallizes in the space group $P6_3mc$ with the lattice parameter of $a = 1011.36(14)$ pm,

$c = 674.85(13)$ pm, and $Z = 2$. The asymmetric unit of $\text{Na}_3\text{Y}_3(\text{BO}_3)_4$ comprises one Na, one Y, two B, and three O atoms.

Y atom is surrounded by eight O atoms to form a distorted YO_8 polyhedron. Every YO_8 polyhedron is connected to their adjacent counterparts via sharing common faces to form a one-dimensional YO_8 polyhedra chain parallel to the c -direction, which serve as the backbone of the open framework (Figure 1.9). Such one-dimensional backbone chains are interlinked with each other through oxygen vertices to form open hexagonal tunnels along the c -direction. The $\text{B}(1)\text{O}_3$ group which is parallel to the ab -plane contributes all three oxygen atoms to linking three backbone chains, whereas the $\text{B}(2)\text{O}_3$ group almost parallel to the c -direction uses two oxygen-oxygen edges to stabilize the connection of its two adjacent backbone chains. Interestingly, Na^+ cation is coordinated by seven oxygen atoms which are all on one side. Such a coordination environment is unusual for the Na^+ cation with the closed electron shell, but it is common for Tl^+ , Pb^{2+} , and Bi^{3+} cations due to the stereochemically active lone electron pairs. Nonetheless, the BVS value of $0.95(1)$ v. u. for Na^+ is pretty close to the theoretical oxidation state.

Of note, the unimpeded diameter of the open hexagonal channel reaches up to 366.0 pm, comparable to that of several 3 Å molecular sieves. That is to say, various molecules such as H_2 , C_2H_2 , NH_3 , NO , and Cl_2 with a kinetic diameter smaller than 366.0 pm can freely move along the open channel. Therefore, $\text{Na}_3\text{Y}_3(\text{BO}_3)_4$ might be applied in the desiccation of petroleum cracking gas and alkenes, selective adsorption of H_2O in insulated glass.

Hitherto, the synthesis of other rare-earth analogs has not been reported yet. If Tb^{3+} can fully substitute Y^{3+} , the bulk single crystal of $\text{Na}_3\text{Tb}_3(\text{BO}_3)_4$ may be a good Faraday rotator in the UV/Vis range because of the uniaxiality and high terbium content.

Na₃RE₉O₃(BO₃)₈ (RE = La, Nd)

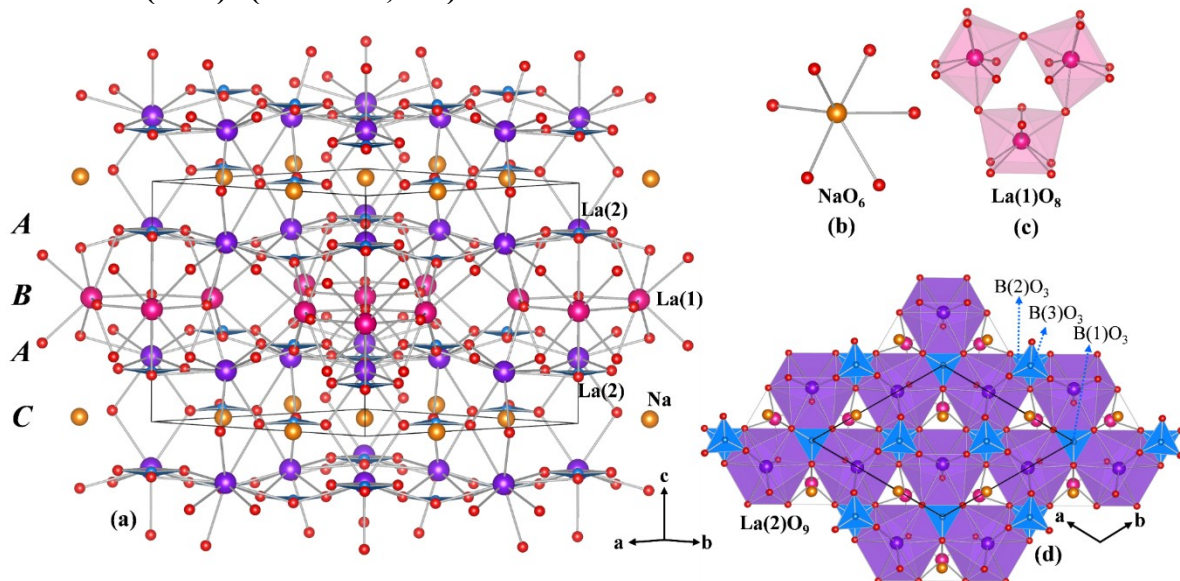


Figure 1.10: (a) Three-dimensional framework of Na₃La₉O₃(BO₃)₈, (b) NaO₆ octahedron (c) trimer of La(1)O₈ polyhedra (d) arrangement of La(2)O₉ and BO₃ groups viewed along the *c*-direction.

Single crystal of Na₃La₉O₃(BO₃)₈ was reported by Wu [78] and Gravereau [79], respectively.

Na₃La₉O₃(BO₃)₈ belongs to the hexagonal $P\bar{6}2m$ space group with the unit cell parameters of $a = 890.33(3)$ pm, $c = 871.31(3)$ pm, and $Z = 1$. The asymmetric cell of Na₃La₉O₃(BO₃)₈ contains two distinct La, one unique Na, three B, and four O atoms.

Na atom at the $3f$ Wyckoff site is surrounded by six oxygen atoms, forming a distorted NaO₆ octahedron. La(1) at the $3g$ site is eight-coordinated while La(2) at the $6i$ site is nine-coordinated. Each La(1)O₈ polyhedron shares common oxygen vertices with the two nearest La(1)O₈ neighbors, forming a trigonal trimer parallel to the *ab*-plane. However, those La(1)₃O₂₁ trigonal trimers are isolated from each other. La(2)O₉ polyhedra are interlinked via corner-sharing to form a hexagonal infinite layer in the *ab* plane. As is shown in Figure 1.10(a), the three-dimensional framework of Na₃La₉O₃(BO₃)₈ can be regarded as a compact sandwich with La(2) layer, La(1) layer, Na layer, La(2) layer stacking along the *c*-direction in the sequence of *ABAC*.... The BVS calculation shows that La(1)³⁺ (3.34(1) v. u.) is over-bonded, while La(2)³⁺ (2.89(1) v. u.) and Na⁺ (0.88(1) v. u.) are slightly under-bonded.

All three types of BO_3 groups are oriented perpendicular to the c -direction. $\text{B}(1)\text{O}_3$ groups are aligned parallel to $\text{B}(3)\text{O}_3$ groups but opposite to $\text{B}(2)\text{O}_3$ groups. From a microscopic viewpoint, such an arrangement of isolated BO_3 groups can still guarantee a large second harmonic generation (SHG) response which Maker fringe experiment using bulk single crystal shows as approximately 2.6 times as that of KH_2PO_4 (KDP). Recently, the synthesis and single-crystal structure of $\text{Na}_3\text{Nd}_9\text{O}_3(\text{BO}_3)_8$ were reported by Shan et al. [80], indicating that La^{3+} can be completely replaced by Nd^{3+} . Owing to the non-centrosymmetric structure and the laser activity of Nd^{3+} cation, $\text{Na}_3(\text{La}_{1-x}\text{Nd}_x)_9\text{O}_3(\text{BO}_3)_8$ ($x = 0-1$) series may be potential self-frequency doubling (SFD) materials.

$\text{K}_3\text{REB}_6\text{O}_{12}$ (RE = Y, Eu-Tb, Yb, Lu)

$\text{K}_3\text{GdB}_6\text{O}_{12}$ discovered by Mutailipu et al. [41] was chosen to elucidate the crystal structure of this family. The Gd-phase crystallizes in the trigonal system with space group $R\bar{3}2$ with the lattice parameter of $a = 1326.5(8)$ pm, $c = 1528.2(14)$ pm, and $Z = 3$. Unlike the isolated orthoborate BO_3 groups that frequently appear in many alkali-metal containing rare-earth borates, $\text{K}_3\text{GdB}_6\text{O}_{12}$ features B_5O_{10} anionic group. In each B_5O_{10} anionic group (Figure 1.11(b)), one BO_4 tetrahedron condenses with four BO_3 triangles via sharing common corners to configure a dual ring. The structure of $\text{K}_3\text{GdB}_6\text{O}_{12}$ consists of two distinct Gd atoms with the Wyckoff position of $6c$ and $3b$ for Gd(1) and Gd(2), respectively. Although both Gd(1) and Gd(2) are surrounded by six oxygen atoms to form GdO_6 octahedra, Gd(2) O_6 octahedron is noticeably more distorted than Gd(1) O_6 octahedron. Additionally, the substitution disorder between Gd and K with a ratio of 0.5:0.5 occurs at the Gd(2) site whereas the Gd(1) site is fully populated by Gd(1) atom. Each $(\text{Gd}_{0.5}\text{K}_{0.5})\text{O}_6$ octahedron shares two common faces with two

neighbor $\text{Gd}(1)\text{O}_6$ octahedra (up and down) to construct $\text{Gd}_2(\text{Gd}_{0.5}\text{K}_{0.5})\text{O}_{12}$ column parallel to the **c**-axis (Figure 1.11(c)).

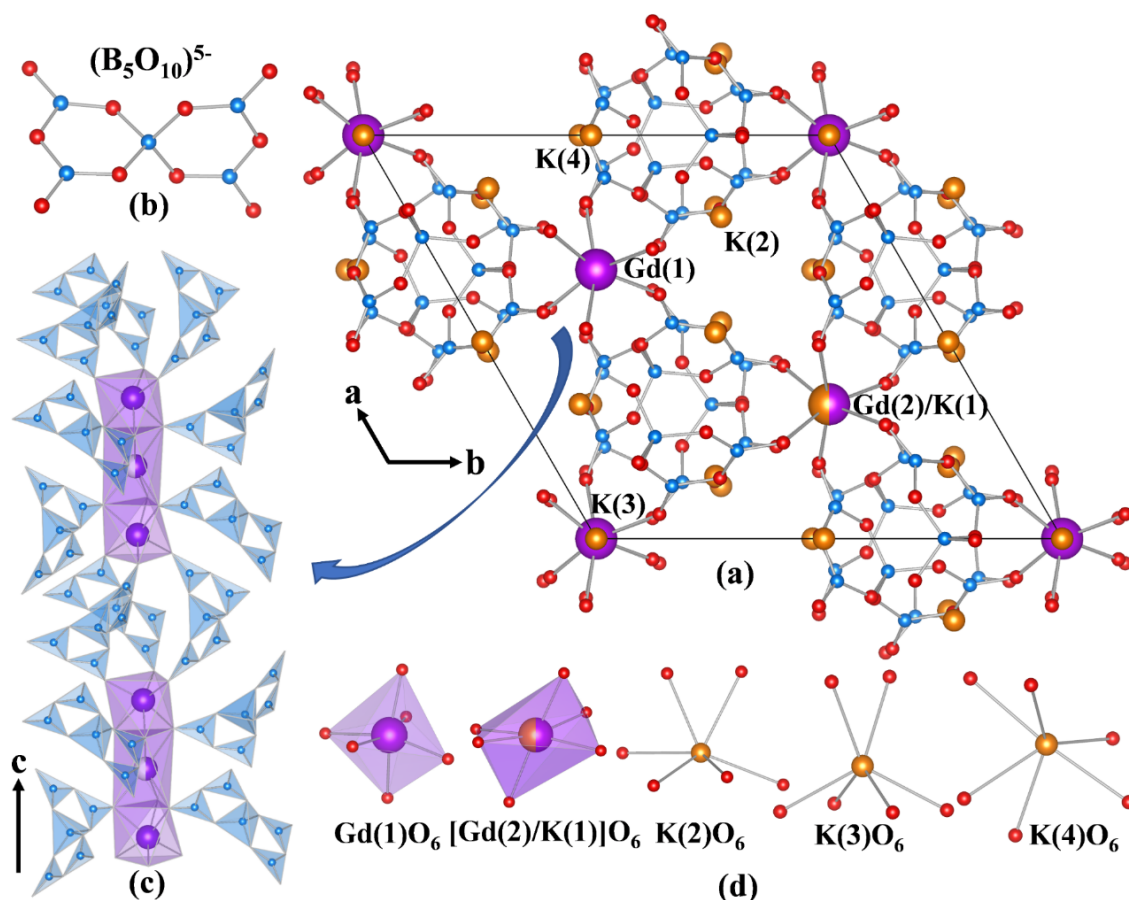


Figure 1.11 (a) The view of the crystal structure of $\text{K}_3\text{GdB}_6\text{O}_{12}$ along the **c**-axis (b) $(\text{B}_5\text{O}_{10})^{5-}$ group (c) connection of B_5O_{10} groups and $\text{Gd}_2(\text{Gd}_{0.5}\text{K}_{0.5})\text{O}_{12}$ columns along the **c**-axis (d) coordination environment of Gd and K cations

Thereby, the structure can be characterized as a three-dimensional framework composed of those $\text{Gd}_2(\text{Gd}_{0.5}\text{K}_{0.5})\text{O}_{12}$ columns bridged by B_5O_{10} anionic groups with the K^+ cations inserted into the interstitial cavities to maintain electrical neutrality. $\text{K}(2)$, $\text{K}(3)$, and $\text{K}(4)$ are all coordinated to six oxygen forming KO_6 prisms. Those distorted KO_6 prisms can be regarded as stitches to support the linkage of $\text{Gd}_2(\text{Gd}_{0.5}\text{K}_{0.5})\text{O}_{12}$ columns and B_5O_{10} anionic groups.

Of note, the structure type of $K_3GdB_6O_{12}$ exhibits a good tolerance for charge balance cation and anion substitutions. To better understand the structural features of $K_3REB_6O_{12}$, $K_3REB_6O_{12}$ is equivalently written as $K_{21}(K_{0.5}RE_{0.5})_3RE_6(B_5O_{10})_9$ or $K_{2.5}RE_{0.8333}B_5O_{10}$ in the following place:

1. RE elements can vary from Eu to Lu and Y, but some subtle differences need to be pointed out:

(1) In the Y-member $K_3YB_6O_{12}$ published by Zhao et al. [81], the substitution disorder at the RE/K site was not observed, suggesting that the RE/K site splits into two distinct crystallographic sites in which RE^{3+} and K^+ populate each. Therefore, a doubled c -parameter was given by Zhao in comparison with the structure information published by Mutailapu [41]. Based on the simulated powder diffraction patterns from Zhao's model, several noticeable diffraction peaks at low angles (Cu $K\alpha$ radiation) can be observed, however these peaks shall be strictly forbidden in Mutailapu's model. Rietveld refinement would be useful to distinguish or verify the two models.

(2) In the case of Yb-member [82], the RE/K site is occupied only by the Yb^{3+} cation but with the occupancy factor of 2/3, thus resulting in the formula of $K_{2.8}Yb_{1.0667}B_6O_{12}$, i.e., $K_{21}Yb_8B_{45}O_{90}$.

2. $Rb_3REB_6O_{12}$ phases [77, 83-85] can be obtained through replacing all K^+ cations by Rb^+ . The RE/Rb disorder was found in $Rb_3YB_6O_{12}$ however not observed in other $Rb_3REB_6O_{12}$ phases with RE = Nd, Eu, and Ho. Accordingly, c -parameters of $Rb_3REB_6O_{12}$ (RE=Nd, Eu and Ho) enlarge by nearly one time compared to that of $Rb_3YB_6O_{12}$.

3. A series of divalent cations can fully occupy the RE/K and RE/Rb site based on the charge balance $M^{2+} = 0.5 A^+ + 0.5 RE^{3+}$ where $A = K, Rb$ and Li ; and $M = Ca, Sr, Ba, Zn, Cd$, and Pb , yielding a rich family of $A_{21}M_3RE_6(B_5O_{10})_9$, i.e., $A_7MRE_2(B_5O_{10})_3$ [86-90]. Since no additional distinct site of M^{2+} are generated, the c -parameters will not be doubled.
4. M^{2+} can further be substituted by two extremely disordered Li^+ ions simultaneously, and then the $K(3)$ cation is replaced with an additional Li^+ cation to form $A_{18}Li_3RE_6(B_5O_{10})_9$, namely $A_6Li_3RE_2(B_5O_{10})_3$ [91].

KBaRE(BO₃)₂ (RE = Pr-Nd, Sm-Lu and Y)

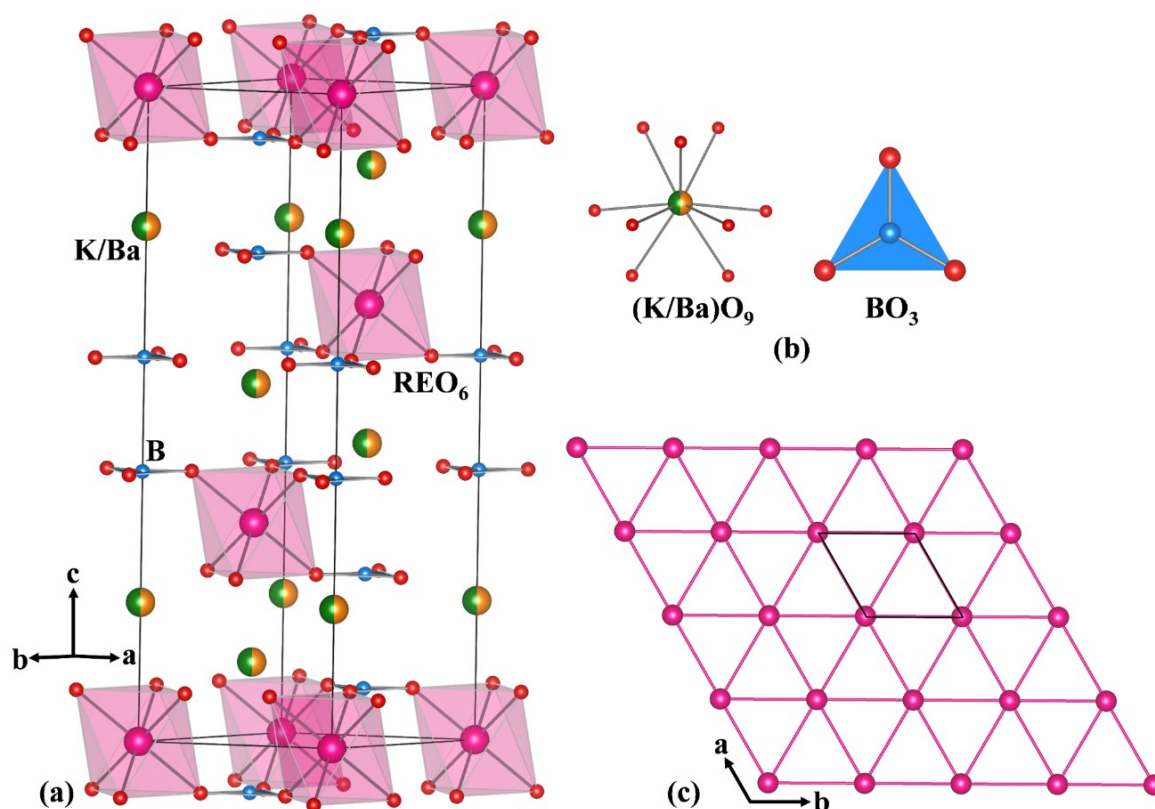


Figure 1.12 (a) the crystal structure of KBaRE(BO₃)₂. (b) coordination environments of K, Ba, and B atoms (c) the ideal two-dimensional rare earth triangular lattice layers, as viewed down the c -axis.

The Y-member, $\text{KBaY}(\text{BO}_3)_2$ was first reported and structurally characterized in 2011 [92]. $\text{KBaRE}(\text{BO}_3)_2$ crystallize into space group $R\bar{3}m$ and this family is isotypic with buetschliite $\text{K}_2\text{Ca}(\text{CO}_3)_2$ [93] through the schematic evolution (Figure 1.13):

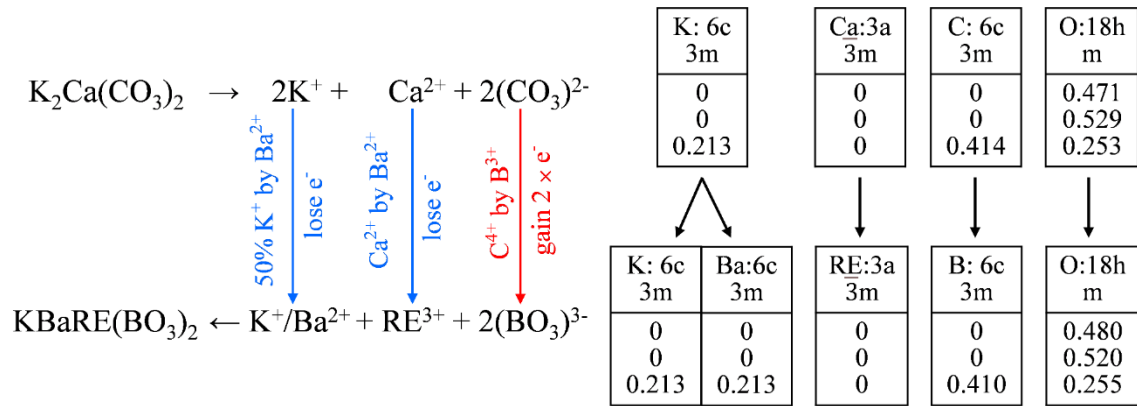


Figure 1.13 schematic evolution from $\text{K}_2\text{Ca}(\text{CO}_3)_2$ to $\text{KBaY}(\text{BO}_3)_2$

In the asymmetric unit, RE (Wyckoff site $3a$), B (Wyckoff site $6c$), and O (Wyckoff site $18h$) are found to fully occupy their unique crystallographic positions. The substitution disorder occurs at the large atom site (Wyckoff site $6c$) where K and Ba are randomly distributed in the proportion of each half. The Ba/K atom is nine-fold coordinated to build up a slightly distorted tricapped trigonal Ba/KO₉ prism in the point group of C_{3v} . The RE atom is surrounded by six O atoms to form a slightly distorted REO₆ octahedron. The B atom is coordinated to three O atoms from three neighboring REO₆ octahedra to form BO₃ triangles. As shown in Figure 1.12(a), those REO₆ octahedra are isolated from each other, and each REO₆ octahedron shares six corners with six BO₃ triangles, which is similarly found in $\text{K}_3\text{Y}(\text{BO}_3)_2$ [67].

In the ab plane, $\text{KBaRE}(\text{BO}_3)_2$ feature the infinite equilateral triangular lattices (Figure 1.12(c)). Such a geometric arrangement of RE^{3+} magnetons is promising to generate geometric magnetic frustration (GFM). Although no indication of magnetic ordering down to 1.8 K could be discovered in a low-spin triangular lattice magnet $\text{KBaYb}(\text{BO}_3)_2$ in single-crystal form, the antiferromagnetic or ferromagnetic ordering might still appear at sufficiently low temperature.

Nevertheless, the coaction of the GFM and rare-earth-dependent crystal field is expected to provoke many fantastic behaviors, for instance, the quantum spin liquid in YbMgGaO₄ [94]. Interestingly, many recently discovered rare-earth borate compounds have a common formula of AAERE(BO₃)₂, where A = alkali metal and AE = alkaline earth metal. The space groups, unit-lattice parameters and fundamental building blocks of the representative members of the AMRE(BO₃)₂ family are briefly summarized in Table 1.2.

Table 1.2 Space group (S. P.), lattice parameters (L. P. in pm) and fundamental building blocks (F.B.B) and the radius ratios (R. R.) of A⁺ and AE²⁺ of the compounds of AAERE(BO₃)₂ family

Compound	S. P.	L. P	F. B. B	R. R
NaBaYb(BO ₃) ₂ [95]	$R\bar{3}m$	$a = 532.95(3), c = 3558.40(17)$	YbO ₆ NaO ₉ BaO ₉ BO ₃	0.84
KBaYb(BO ₃) ₂ [96]	$R\bar{3}m$	$a = 541.59(1), c = 1756.29(3)$	YbO ₆ (K _{0.5} Ba _{0.5})O ₉ BO ₃	1.05
RbBaYb(BO ₃) ₂ [50]	$P2_1/m$	$a = 673.49(2) b = 545.52(2)$ $c = 863.76(3) \beta = 105.5806(17)^\circ$	YbO ₆ RbO ₉ BaO ₉ BO ₃	1.11
KSrYb(BO ₃) ₂ [97]*	$P2_1/m$	$a = 654.10(4), b = 533.80(2)$ $c = 847.40(10), \beta = 105.4280(6)^\circ$	YbO ₆ KO ₉ SrO ₉ BO ₃	1.18
KCaNd(BO ₃) ₂ [98]	$Pbca$	$a = 1020.69(5) b = 902.93(4)$ $c = 1316.34(5)$	(Nd _{0.879} Ca _{0.121})O ₉ BO ₃ (Ca _{0.879} Nd _{0.121})O ₆ KO ₉	1.55

* standardized from the original reported parameters of $a = 926.3(10)$, $b = 533.8(2)$, $c = 654.1(4)$, and $\beta = 117.94(6)^\circ$

Their structures are depicted in Figure 1.14. The common structural feature of the AAERE(BO₃)₂ family is the layer-by-layer distribution of RE³⁺, A⁺ and AE²⁺ cations. NaBaYb(BO₃)₂ and KBaYb(BO₃)₂ both crystallize into the space group $R\bar{3}m$ but the c -parameter of the Na-phase is almost twice as that of the K-phase. This is due to the random disorder of K⁺ and Ba²⁺ over the same site aforementioned. By contrast, Na⁺ and Ba²⁺ occupy different sites probably due to the large size difference, causing the c -parameter to lengthen by one-fold. Thus, NaBaYb(BO₃)₂ can be viewed as the one-dimensional superstructure of KBaYb(BO₃)₂ along the c -direction. Accordingly, the arrangement of Yb³⁺ in NaBaYb(BO₃)₂ remains the ideal triangle magnetic lattice in the ab plane. RbBaYb(BO₃)₂ is free from the disorder of Rb⁺ and Ba²⁺ and is structurally correlated to KBaYb(BO₃)₂: it adopts with

monoclinic $P2_1/m$, a subgroup of $R\bar{3}m$. The monoclinic a -, b - and c -parameters derive from the hexagonal setting by taking the transformation: $(a_m \ b_m \ c_m) = (a_h \ b_h \ c_h) \begin{bmatrix} 1 & 1 & -1/3 \\ -1 & 1 & 1/3 \\ 0 & 0 & 1/3 \end{bmatrix}$. The symmetry reduction of $\text{RbBaYb}(\text{BO}_3)_2$ corresponds to the arrangement of Yb^{3+} cations deviating from the ideal triangle magnetic lattice as well as to the slightly tilted BO_3 triangles. Moreover, one can recognize that $\text{KSrYb}(\text{BO}_3)_2$ is isotypic to $\text{RbBaYb}(\text{BO}_3)_2$ via performing a standardization transformation of the cell parameters. The mild disorder of Ca^{2+} and Nd^{3+} was observed in $\text{KCaNd}(\text{BO}_3)_2$ where the Nd^{3+} cations are arranged in the ripple quasi-two-dimensional (Q2D) plane. Unlike the nearly parallel layout of the borate groups in the other four compounds, two independent BO_3 groups of $\text{KCaNd}(\text{BO}_3)_2$ are oriented perpendicularly to each other,

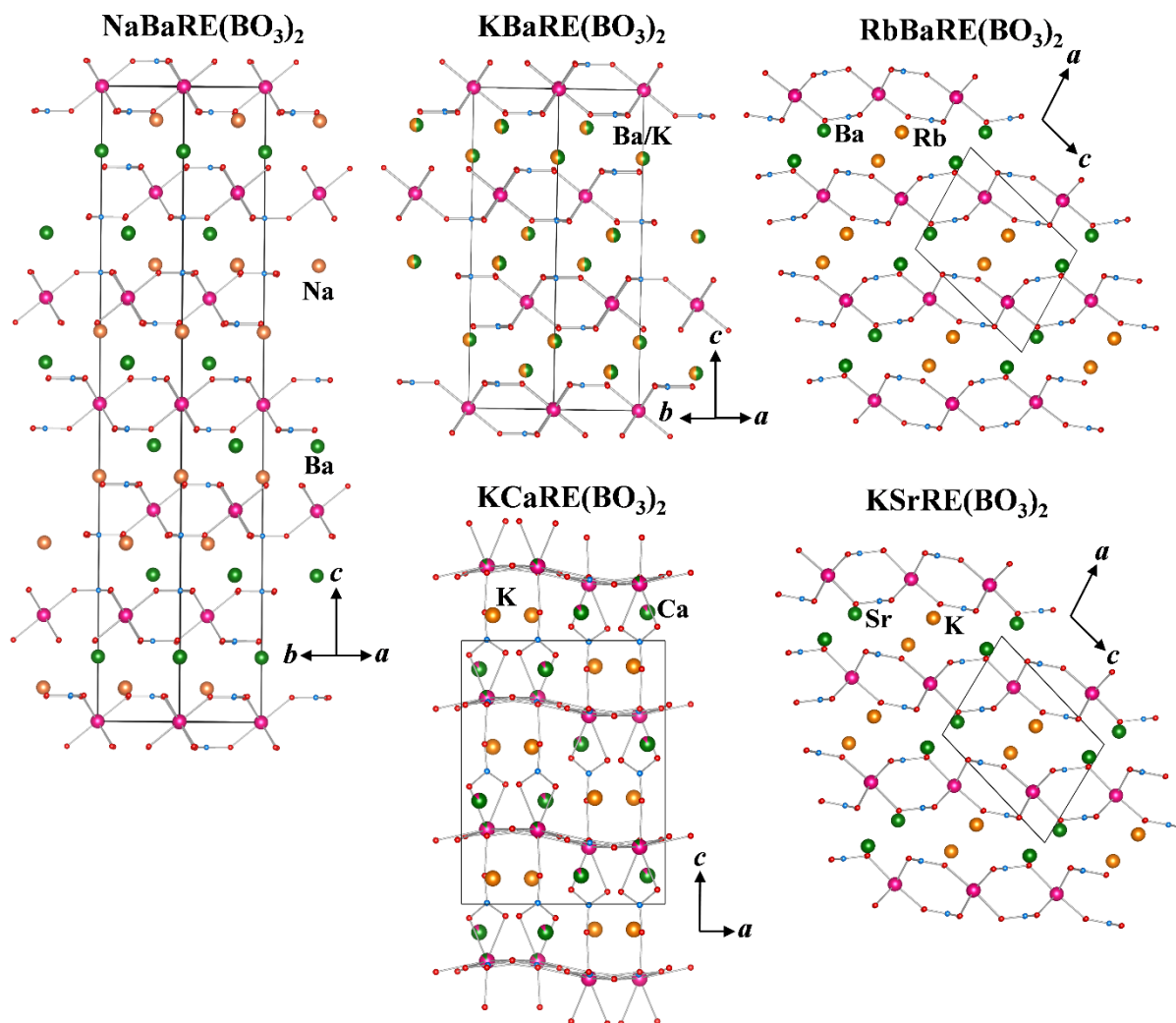


Figure 1.14 Crystal structures of $\text{AAERE}(\text{BO}_3)_2$ family

$\text{K}_9\text{Li}_3\text{RE}_3(\text{BO}_3)_7$ (RE = La, Pr, Nd)

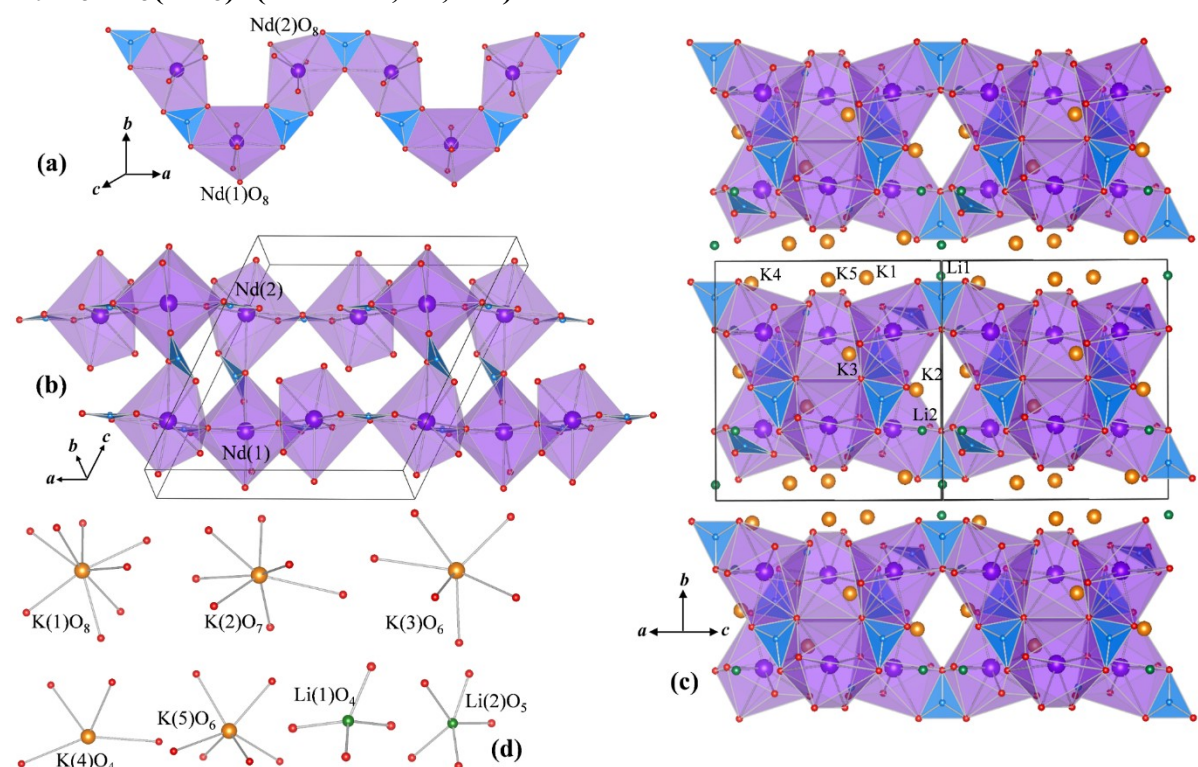


Figure 1.15 (a) [Nd₃B₃O₂₁] chain; (b) [Nd₆B₆O₃₈] double layers consisting of [Nd₃B₃O₂₁] chains. (c) crystal structure of K₉Li₃Nd₃(BO₃)₇ viewed along [101] direction. (d) coordination polyhedra of the Li and K atoms.

K₉Li₃Nd₃(BO₃)₇ is the first reported member of this family [99]. This Nd-phase adopts the monoclinic space group $P2/n$ with lattice parameters of $a = 1145.24(7)$ pm, $b = 1012.66(6)$ pm, $c = 1154.38(7)$ pm, $\beta = 115.263(1)^\circ$. The asymmetric cell of K₉Li₃Nd₃(BO₃) contains 24 crystallographically independent atoms: two Nd, five K, eleven O, four B, and two Li atoms. Most of the atoms are located on the $4g$ Wyckoff sites except Nd(1) and K(5) at the $2f$ sites as well as O(2), B(4), and Li(1) on the $2e$ sites. Nd(1) and Nd(2) atoms are both coordinated by eight oxygen atoms to form NdO₈ polyhedra. Each Nd(1)O₈ polyhedron and two adjacent Nd(2)O₈ polyhedra are joined by three BO₃ groups to constitute [Nd₃B₃O₂₁] chains along the **a**-direction shown in Figure 1.15(a). Such corrugated [Nd₃B₃O₂₁] chains are connected by corner-sharing and further reinforced by the BO₃ groups to build up [Nd₆B₆O₃₈] double layers

in the *ac* plane. Thus, the layered-like network of $\text{K}_9\text{Li}_3\text{Nd}_3(\text{BO}_3)_7$ can be viewed as $[\text{Nd}_6\text{B}_6\text{O}_{38}]$ double layers stacking along the **b**-direction.

K^+ cations are in the eightfold, sevenfold, sixfold, fourfold, and sixfold coordination sphere with the corresponding BVS value of 1.16(1), 1.19(1), 0.91(1), 0.50(1), and 1.39(1) for K(1), K(2), K(3), K(4), and K(5), respectively. $\text{Li}(1)^+$ cation is fourfold coordinated with the BVS value of 1.22(2) whereas $\text{Li}(2)^+$ is fivefold coordinated with the BVS value of 0.97(2). Except that K(4) is significantly under-bonded and K(5) and Li(2) are remarkably over-bonded, the BVS values of other cations are consistent with their respective formal oxidation state.

$\text{K}_3\text{Li}_3\text{RE}_7(\text{BO}_3)_9$ (RE = Y, Sm-Er)

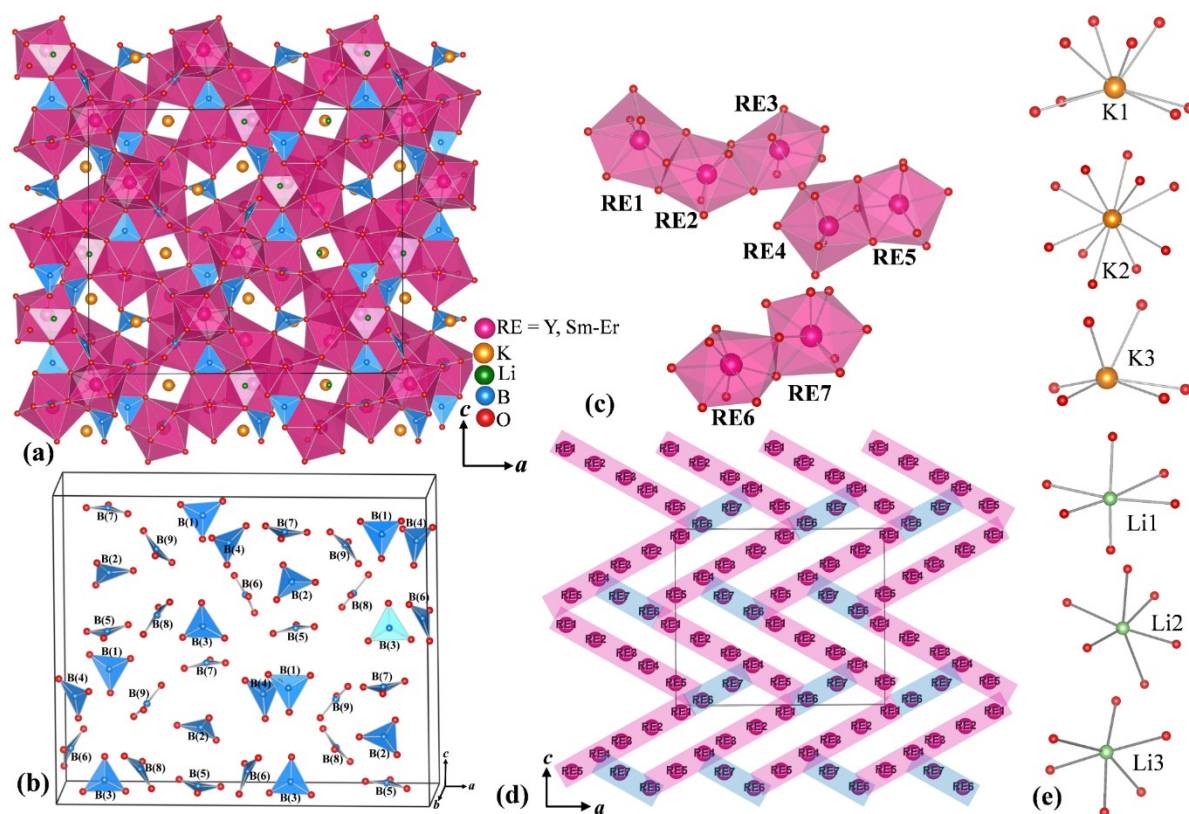


Figure 1.16 (a) crystal structure of $\text{K}_3\text{Li}_3\text{RE}_7(\text{BO}_3)_9$ (b) arrangement of BO_3 groups in the unit cell (c) RE_5O_{32} pentamer and RE_2O_{14} dimer (d) arrangement of RE^{3+} cations viewed along the **b**-direction (e) coordination environments of K and Li cations

$K_3Li_3Y_7(BO_3)_9$ is the first published member in the $K_3Li_3RE_7(BO_3)_9$ family by Huppertz's group [100]. The crystal structure of $K_3Li_3Y_7(BO_3)_9$ solved by single-crystal X-ray diffraction can be described in the polar space group $Pca2_1$ with the lattice parameter of $a = 2074.3(8)$ pm, $b = 638.7(2)$ pm, $c = 1747.4(7)$ pm, and $Z = 4$. Afterward, the Gd-analog was reported as a promising magnetic cryogenic coolant down to 2K due to the high gadolinium content in this structure type [48]. As shown in Figure 1.16 (a) and (c), the crystal structure of the $K_3Li_3RE_7(BO_3)_9$ family features a condensed REO_n polyhedral network where all of RE atoms are 8-fold coordinated, except the RE(4) atom which is nine-fold coordinated. $RE(i)O_n$ ($i = 1-5$) polyhedra subsequently join together via corner-, edge-, face-sharing to form RE_5O_{32} pentamers. These RE_5O_{32} pentamers are further interconnected via edge-sharing to build up infinite triangle wave chains in the ac plane. Each RE_2O_{14} dimer, which is composed of edge-shared $RE(6)O_8$ and $RE(7)O_8$ decahedra, bridges three RE_5O_{32} pentamers to constitute the three-dimensional network.

Of the nine independent BO_3 groups, $B(1)O_3$ and $B(3)O_3$ are almost oppositely oriented to each other. A similar opposite orientation was observed for $B(2)O_3$ and $B(4)O_3$, for $B(5)O_3$ and $B(7)O_3$ as well as for $B(8)O_3$ and $B(9)O_3$ groups (Figure 1.16 (b)). According to the anionic group theory, it can be assumed that such a microscopic arrangement of BO_3 groups may not be in favor of yielding a large macroscopic SHG response even though the whole structure is non-centrosymmetric.

$K(1)$, $K(2)$, and $K(3)$ cations are coordinated to eight, ten, and six oxygen atoms. All Li cations are coordinated to six oxygen atoms. The BVS calculation shows the values of 1.21(1), 1.42(1), 0.85(1), 0.98(1), 0.98(1), and 0.99(1) for $K(1)$, $K(2)$, $K(3)$, $Li(1)$, $Li(2)$ and $Li(3)$ respectively. Except that $K(1)$ and $K(2)$ are highly over-bonded, the BVS values for the other atoms are consistent with their expected formal ionic charge.

Hitherto, considerable efforts have been made to search for novel compounds in the A_2O - RE_2O_3 - B_2O_3 and A_2O - Li_2O - RE_2O_3 - B_2O_3 systems where A are alkali-metal elements.

These discovered compounds are listed in Table 1-3.

Table 1-3. Space groups and fundamental building blocks (F.B. B) of the borate compounds in the A_2O - RE_2O_3 - B_2O_3 and A_2O - Li_2O - RE_2O_3 - B_2O_3 systems (A = Li, Na, K, Rb, Cs)

Systems	Compounds	F. B. B
Li_2O - RE_2O_3 - B_2O_3	$LiRE_6O_5(BO_3)_3$: $P2_1/c$ (RE = Pr-Tm, Y) [57,58]	edge/corner-sharing REO_7 , REO_8 isolated BO_3
	$Li_2RE_5O_4(BO_3)_3$: $P2_1/m$ (RE = Yb, Lu) [101]	edge/corner-sharing REO_7 isolated BO_3
	$Li_3RE_2(BO_3)_3$: $P2_1/n$ (RE = La, Pr, Nd, Sm-Lu, Y) [69]	edge/corner-sharing REO_9 isolated BO_3
	$Li_3RE(BO_3)_2$: $P2_1/c$ (RE = Gd, Er-Lu, Y) [69, 70]	edge/corner-sharing REO_8 isolated BO_3
	$Li_6RE(BO_3)_3$: $P2_1/c$ (RE = Nd, Sm-Gd, Dy-Lu, Y) [51-54]	edge/corner-sharing REO_8 isolated BO_3
Na_2O - RE_2O_3 - B_2O_3	$Na_3RE_9O_3(BO_3)_8$: $P62m$ (RE = La, Nd) [79, 80]	face/edge/corner-sharing REO_8 , REO_9 isolated BO_3
	$Na_2RE_2O(BO_3)_2$: $P2_1/c$ (RE = La, Nd, Sm-Ho, Y) [102-105]	face/edge/corner-sharing REO_8 isolated BO_3
	$Na_3Y_3(BO_3)_4$: $P6_3mc$ [45]	face/corner-sharing REO_8 isolated BO_3
	$Na_3RE_2(BO_3)_3$: $Amm2$ (RE = La, Nd, Sm, Gd, Tb) [38, 71, 73, 74]	face/corner-sharing REO_9 isolated BO_3
	$Na_3RE(BO_3)_2$: $P2_1/c$ (RE = La, Pr-Nd, Sm-Gd, Y) [63-66]	edge/corner-sharing REO_8 isolated BO_3
	$Na_3GdB_8O_{15}$: $P1$ [106]	isolated GdO_8 , 1D- $[B_8O_{15}]$ chain
K_2O - RE_2O_3 - B_2O_3	$K_3Y_3(BO_3)_4$: $P2_1/c$ [107]	face/edge/corner-sharing YO_7 , YO_8 isolated BO_3
	$K_2RE_2(BO_3)_2O$: $P2_1/c$ (RE = La, Nd, Sm, Eu) [108]	face/edge/corner-sharing REO_8 isolated BO_3
	$K_3RE(BO_3)_2$: $Pnma$ (RE = Nd, Sm - Gd) [67]	corner-sharing REO_7 isolated BO_3
	$K_3RE(BO_3)_2$: $Pnnm$ (RE = Tb - Lu, Y) [67]	isolated REO_6 isolated BO_3
	$K_3REB_6O_{12}$, $K_{21}Yb_8B_{45}O_{90}$: $R32$ (RE = Eu - Tb, Lu, Y) [41, 81, 82, 109-111]	face-sharing REO_6 $B_5O_{10}^{5-}$ group
Rb_2O - RE_2O_3 - B_2O_3	$Rb_3La_3(BO_3)_4$: $P2/c$ [112]	face/corner-sharing LaO_7 LaO_8 LaO_{10} isolated BO_3
	$Rb_3RE_2(BO_3)_3$: $Pna2_1$ (RE = Y, Ho) [76, 77]	face/corner-sharing REO_6 REO_7 isolated BO_3
	$Rb_3REB_6O_{12}$: $R32$ (RE = Nd, Eu, Ho, Y) [77, 83-85]	face-sharing REO_6 $B_5O_{10}^{5-}$ group
Cs_2O - RE_2O_3 - B_2O_3	No compounds reported yet	
Na_2O - Li_2O - RE_2O_3 - B_2O_3	No compounds reported yet	
K_2O - Li_2O - RE_2O_3 - B_2O_3	$K_3Li_3RE_7(BO_3)_9$: $Pca2_1$ (RE = Sm-Er, Y) [48, 100, 113, 114]	face/edge/corner-sharing REO_8 , REO_9 isolated BO_3
	$K_9Li_3RE_3(BO_3)_7$: $P2/n$ (RE = La, Pr, Nd) [99, 115]	corner-sharing REO_8 isolated BO_3
Rb_2O - Li_2O - RE_2O_3 - B_2O_3	$Rb_2LiRE(BO_3)_2$: $Pbcm$ (RE = Nd, Tb) [99, 116]	corner-sharing REO_8 isolated BO_3
Cs_2O - Li_2O - RE_2O_3 - B_2O_3	$CsLi_2Gd_4(BO_3)_5$: $P2/n$ [117]	face/edge/corner-sharing GdO_7 , GdO_8 , GdO_9 , isolated BO_3
	$Cs_2LiRE(BO_3)_2$: $Pbcm$ [99, 115] (RE = La, Nd) :	corner-sharing REO_8 isolated BO_3

Comparing the alkali-metal containing rare-earth borates in the $A_2O-RE_2O_3-B_2O_3$ and $A_2O-Li_2O-RE_2O_3-B_2O_3$ systems, it can be reasonably summarized that:

First of all, the coordination number of rare-earth cations ranges from 6 to 10 but the most common coordination numbers are 7, 8, and 9. When the content of alkali-metal cations increases, i.e., the content of rare-earth cations decreases, rare-earth cations tend to adopt the smaller polyhedra environments.

Second, the face-sharing linkage of REO_n polyhedra is more likely to occur in the borates with high rare-earth content, which may be understood in terms of Pauling's third rule [118]. However, several exceptions are found in $K_3REB_6O_{12}$ and $Rb_3REB_6O_{12}$ where the face-sharing connection takes place with the low rare-earth content.

Third, the trigonally coordinated boron atoms and the isolated orthoborate BO_3 groups are predominant in these the alkali-metal containing rare-earth borates. Thus far, the tetrahedral coordination of boron atoms in the alkali-metal containing rare-earth borates has just been found in $B_5O_{10}^{5-}$ group of $K_3REB_6O_{12}$ -type and in $B_8O_{15}^{6-}$ group of $Na_3GdB_8O_{15}$. It shall be noted that these aforementioned compounds were synthesized at ambient pressure. Bearing in mind the pressure-coordination rule [119], the coordination number of boron may increase with rising pressure. Therefore, trigonally coordinated boron atoms, and the BO_4 groups might predominate in the novel alkali-metal containing rare-earth borates when high pressures are applied [120].

Fourth, the BVS values for rare-earth, boron, and oxygen ions in the alkali-metal containing rare-earth borates mostly agree well with their formal ionic charges. However, the pronounced deviations (approx. 40 %) concerning the BVS of alkali-metal cations sometimes occur, such as Na^+ in $Na_3La_2(BO_3)_3$, K^+ in $K_3RE(BO_3)_2$, $K_9Li_3RE_3(BO_3)_7$, and $K_3Li_3RE_7(BO_3)_9$ and Rb^+ in $Rb_3Y_2(BO_3)_3$.

Besides, as is reiterated several times, some of these rare-earth borates have stoichiometric similarity but crystallize in significantly different structures, where the size of the alkali and rare-earth cations is assumed to play an important role. For instance, $\text{Li}_3\text{RE}_2(\text{BO}_3)_3$ crystallize in the space group $P2_1/n$ whereas $\text{Na}_3\text{RE}_2(\text{BO}_3)_3$ crystallizes in the polar $Amm2$ and $\text{Rb}_3\text{RE}_2(\text{BO}_3)_3$ in the polar $Pna2_1$ space groups. Moreover, $\text{K}_3\text{RE}(\text{BO}_3)_2$ with light rare-earth elements (Nd, Sm, Eu and Gd) are to be refined in the orthorhombic space group $Pnma$ whereas the heavy rare-earth elements (Tb, Dy, Ho, Er, Tm, Yb and Lu) are described using $Pnnm$. Besides, those reported alkali rare-earth borates such as $\text{Li}_3\text{Gd}(\text{BO}_3)_2$, $\text{Na}_3\text{Gd}(\text{BO}_3)_2$, $\text{K}_3\text{Sm}(\text{BO}_3)_2$, $\text{K}_3\text{Y}(\text{BO}_3)_2$, $\text{Rb}_2\text{LiNd}(\text{BO}_3)_2$ and $\text{Cs}_2\text{LiNd}(\text{BO}_3)_2$ adopt various structure type even though they possess a common “312” stoichiometric formula where 3, 1, and 2 stands for the number of alkali elements, rare-earth elements, and orthoborate groups, respectively.

The main purpose of this cumulative dissertation is to continue the exploration of new compounds in the $\text{K}_2\text{O-Li}_2\text{O-RE}_2\text{O}_3\text{-B}_2\text{O}_3$ and $\text{K}_2\text{O-RE}_2\text{O}_3\text{-B}_2\text{O}_3$ systems and to further investigate their optical, magnetic, thermal, and vibrational properties. In general, this dissertation is composed of three parts:

In the $\text{K}_2\text{O-Li}_2\text{O-RE}_2\text{O}_3\text{-B}_2\text{O}_3$ systems, six new compounds $\text{KLi}_2\text{RE}(\text{BO}_3)_2$ ($\text{RE} = \text{Dy, Ho, Er, Tm, Yb and Y}$) were obtained. Single crystal X-ray diffraction and Rietveld refinement of powder X-ray diffraction together confirm these six isotypic rare-earth borates crystallize into a new structure type, which is distinctly different from other previously known compounds.

In the $\text{K}_2\text{O-RE}_2\text{O}_3\text{-B}_2\text{O}_3$ systems, a series of novel potassium rare-earth borates $\text{K}_3\text{RE}_3(\text{BO}_3)_4$ ($\text{RE} = \text{Pr, Nd, Sm, Eu, Gd, Tb, Dy, Ho, Er, Tm, Yb and Lu}$) was synthesized using solid-state reaction as well as spontaneous crystallization from high-temperature flux. Combined X-ray single crystal and powder diffraction reveal the monoclinic space group $P2_1/c$ for $\text{K}_3\text{RE}_3(\text{BO}_3)_4$ ($\text{RE} = \text{Sm-Lu}$) and the triclinic space group $P\bar{1}$ for $\text{K}_3\text{RE}_3(\text{BO}_3)_4$ ($\text{RE} = \text{Pr, Nd}$). Amid differences in the space groups, each member of the series keeps close structural correlations

in their motif and connectivity. In addition, a potassium-containing praseodymium oxo-orthoborate, $\text{K}_2\text{Pr}_2\text{O}(\text{BO}_3)_2$ was isolated and belong to the $\text{K}_2\text{La}_2(\text{BO}_3)_2\text{O}$ family. A comparative view finds that $\text{K}_2\text{RE}_2(\text{BO}_3)_2\text{O}$ borates have many common structural features with the known KREOCO_3 carbonates

Reference

- [1] C. Chuangtian, W. Bochang, J. Aidong, Y. Guiming, A new-type ultraviolet SHG crystal— $\beta\text{-BaB}_2\text{O}_4$, *Sci. Sin. Ser. B*, 28 (**1985**) 235-243.
- [2] Y.W. Chuangtian Chen, Aidong Jiang, Bochang Wu, Guiming You, Rukang Li, and Shujie Lin, New nonlinear-optical crystal: LiB_3O_5 , *J. Opt. Soc. Am. B*, 6 (**1989**) 616-621.
- [3] Y. Mori, I. Kuroda, S. Nakajima, T. Sasaki, S. Nakai, New nonlinear optical crystal: Cesium lithium borate, *Appl. Phys. Lett.*, 67 (1995) 1818-1820.
- [4] P. Becker, Borate Materials in Nonlinear Optics, *Adv. Mater.*, 10 (**1998**) 979-992.
- [5] C. Chen, T. Sasaki, R. Li, Y. Wu, Z. Lin, Y. Mori, Z. Hu, J. Wang, G. Aka, M. Yoshimura, Nonlinear optical borate crystals: Principals and applications, John Wiley & Sons**2012**.
- [6] M. Mutailipu, S. Pan, Emergent Deep-Ultraviolet Nonlinear Optical Candidates, *Angew. Chem. Int. Ed.*, 59 (**2020**) 20302-20317.
- [7] R. Arun Kumar, M. Arivanandhan, Y. Hayakawa, Recent advances in rare earth-based borate single crystals: Potential materials for nonlinear optical and laser applications, *Prog. Cryst. Growth Charact. Mater.*, 59 (**2013**) 113-132.
- [8] H. Huang, Y. He, Z. Lin, L. Kang, Y. Zhang, Two Novel Bi-Based Borate Photocatalysts: Crystal Structure, Electronic Structure, Photoelectrochemical Properties, and Photocatalytic Activity under Simulated Solar Light Irradiation, *J. Phys. Chem. C*, 117 (**2013**) 22986-22994.
- [9] W. Gao, Y. Jing, J. Yang, Z. Zhou, D. Yang, J. Sun, J. Lin, R. Cong, T. Yang, Open-Framework Gallium Borate with Boric and Metaboric Acid Molecules inside Structural Channels Showing Photocatalysis to Water Splitting, *Inorg. Chem.*, 53 (**2014**) 2364-2366.
- [10] Z. Xia, Q. Liu, Progress in discovery and structural design of color conversion phosphors for LEDs, *Prog. Mater Sci.*, 84 (**2016**) 59-117.
- [11] J.B. Czirr, Low-energy neutron detector based upon lithium lanthanide borate scintillators, US Patents, **1998**.

- [12] M. Balcerzyk, Z. Gontarz, M. Moszynski, M. Kapusta, Future hosts for fast and high light output cerium-doped scintillator, *J. Lumin.*, 87-89 (2000) 963-966.
- [13] R.S. Bubnova, S.K. Filatov, Strong anisotropic thermal expansion in borates, *Phys. Status Solidi B*, 245 (2008) 2469-2476.
- [14] M. Gogolin, M.M. Murshed, M. Ende, R. Miletich, T.M. Gesing, Uniaxial negative thermal expansion in the mullite-and borax-type PbAlBO_4 polymorphs, *J. Mater. Sci.*, 55 (2020) 177-190.
- [15] R.A. Smith, R.B. McBroom, Boron oxides, boric acid, and borates, *Kirk-Othmer Encycl. Chem. Technol.*, (2000).
- [16] H. Huppertz, D.A. Keszler, Borates: Solid-State Chemistry, *Encycl. Inorg. Chem. Bioinorg. Chem.*, (2011) 1-12.
- [17] P.C. Burns, J.D. Grice, F.C. Hawthorne, Borate minerals; I, Polyhedral clusters and fundamental building blocks, *Can. Mineral.*, 33 (1995) 1131-1151.
- [18] D. Zagorac, H. Müller, S. Ruehl, J. Zagorac, S. Rehme, Recent developments in the Inorganic Crystal Structure Database: theoretical crystal structure data and related features, *J. Appl. Crystallogr.*, 52 (2019).
- [19] R.K. Li, The interpretation of UV absorption of borate glasses and crystals, *J. Non-Cryst. Solids*, 111 (1989) 199-204.
- [20] C. Chen, Y. Wang, B. Wu, K. Wu, W. Zeng, L. Yu, Design and synthesis of an ultraviolet-transparent nonlinear optical crystal $\text{Sr}_2\text{Be}_2\text{B}_2\text{O}_7$, *Nat.*, 373 (1995) 322-324.
- [21] Z. Wang, J.-y. Zhang, F. Yang, X. Cheng, Y. Zhou, J. Xu, Y. Xu, Y. Bo, Q. Peng, D. Cui, Stable operation of 4 mW nanoseconds radiation at 177.3 nm by second harmonic generation in $\text{KBe}_2\text{BO}_3\text{F}_2$ crystals, *Opt. Express*, 17 (2009) 20021-20032.
- [22] V. Legagneur, Y. An, A. Mosbah, R. Portal, A.L.G. La Salle, A. Verbaere, D. Guyomard, Y. Piffard, LiMBO_3 (M= Mn, Fe, Co): synthesis, crystal structure and lithium deinsertion/insertion properties, *Solid State Ionics*, 139 (2001) 37-46.
- [23] H. Park, R. Lam, J.E. Greedan, J. Barbier, Synthesis, crystal structure, crystal chemistry, and magnetic properties of PbMBO_4 (M= Cr, Mn, Fe): a new structure type exhibiting one-dimensional magnetism, *Chem. Mater.*, 15 (2003) 1703-1712.
- [24] H. Kageyama, K. Yoshimura, R. Stern, N.V. Mushnikov, K. Onizuka, M. Kato, K. Kosuge, C.P. Slichter, T. Goto, Y. Ueda, Exact dimer ground state and quantized magnetization plateaus in the two-dimensional spin system $\text{SrCu}_2(\text{BO}_3)_2$, *Phys. Rev. Lett.*, 82 (1999) 3168.
- [25] A.J. Kurtzig, R. Wolfe, R.C. LeCraw, J.W. Nielsen, Magneto-optical properties of a green room-temperature ferromagnet: FeBO_3 , *Appl. Phys. Lett.*, 14 (1969) 350-352.

- [26] R.P. Rao, Tb³⁺ activated green phosphors for plasma display panel applications, J. Electrochem. Soc., 150 (2003) H165.
- [27] R.P. Rao, D.J. Devine, RE-activated lanthanide phosphate phosphors for PDP applications, J. Lumin., 87 (2000) 1260-1263.
- [28] R.P. Rao, D.J. Devine, Method of making green emitting alkaline earth aluminate phosphor for VUV excited light emitting device, US Patents, 2002.
- [29] L. Zhang, C. Pédrini, C. Madej, C. Dujardin, J.C. Gcon, B. Moine, I. Kamenskikh, A. Belsky, D.A. Shaw, M.A. MacDonald, P. Mesnard, C. Fouassier, J.C. Van't Spijker, C.W.E. Van Eijk, Fast fluorescence and scintillation properties of cerium and praseodymium doped lutetium orthoborates, Radiat Eff. Defects Solids, 150 (1999) 47-52.
- [30] G. Aka, E. Reino, P. Loiseau, D. Vivien, B. Ferrand, L. Fulbert, D. Pelenc, G. Lucas-Leclin, P. Georges, Ca₄REO(BO₃)₃ crystals for green and blue microchip laser generation: from crystal growth to laser and nonlinear optical properties, Opt. Mater., 26 (2004) 431-436.
- [31] G. Wang, J. Lu, D. Cui, Z. Xu, Y. Wu, P. Fu, X. Guan, C. Chen, Efficient second harmonic generation in a new nonlinear La₂CaB₁₀O₁₉ crystal, Opt. Commun., 209 (2002) 481-484.
- [32] N.I. Leonyuk, Half a century of progress in crystal growth of multifunctional borates RAl₃(BO₃)₄ (R=Y, Pr, Sm–Lu), J. Cryst. Growth, 476 (2017) 69-77.
- [33] L. Gheorghe, M. Greculeasa, A. Broasca, F. Voicu, G. Stanciu, K.N. Belikov, E.Y. Bryleva, O. Gaiduk, Incongruent Melting La_xY_ySc_{4-x-y}(BO₃)₄: LYSB Nonlinear Optical Crystal Grown by the Czochralski Method, ACS Appl. Mater. Interfaces, 11 (2019) 20987-20994.
- [34] P. Dekker, J.M. Dawes, J.A. Piper, Y. Liu, J. Wang, 1.1 W CW self-frequency-doubled diode-pumped Yb:YAl₃(BO₃)₄ laser, Opt. Commun., 195 (2001) 431-436.
- [35] C.W.E. van Eijk, Inorganic scintillators for thermal neutron detection, Radiat. Meas., 38 (2004) 337-342.
- [36] Z. Fu, S. Pan, F. Yang, S. Gu, X. Lei, Y. Heng, G. Ren, M. Qi, Neutron detection properties of Li₆Y(BO₃)₃:Ce crystal, Radiat. Meas., 72 (2015) 39-43.
- [37] J. Yin, J. Zhang, J. Wang, F. Du, R. Li, S. Pan, J. Pan, Growth and scintillation properties of Ce:Li₆Y(BO₃)₃ crystal enriched with ¹⁰B isotopes, Radiat. Meas., 113 (2018) 20-24.
- [38] W.W. Zhou, R.Z. Zhuang, W. Zhao, G.F. Wang, L.Z. Zhang, J.G. Ma, X. Bao, F.W. Wang, Y.H. Chen, Second harmonic generation in Na₃Gd₂(BO₃)₃ crystals, Cryst. Res. Technol., 46 (2011) 926-930.
- [39] K. Li, G. Zhang, S. Guo, X. Zhang, R. He, J. Zhang, Z. Lin, Y. Wu, Linear and nonlinear optical properties of Na₃La₂(BO₃)₃ crystal, Opt. Laser Technol., 54 (2013) 407-412.

- [40] A.H. Reshak, S. Auluck, I.V. Kityk, Optical susceptibilities of $\text{Na}_3\text{La}_9\text{O}_3(\text{BO}_3)_8$, ternary oxyborate nonlinear single crystal: theory and experiment, *J. Phys.: Condens. Matter*, 20 (2008) 145209.
- [41] M. Mutailipu, Z. Xie, X. Su, M. Zhang, Y. Wang, Z. Yang, M.R.S.A. Janjua, S. Pan, Chemical Cosubstitution-Oriented Design of Rare-Earth Borates as Potential Ultraviolet Nonlinear Optical Materials, *J. Am. Chem. Soc.*, 139 (2017) 18397-18405.
- [42] B. Han, B. Liu, J. Du, Y. Dai, J. Zhang, H. Shi, $\text{K}_3\text{YB}_6\text{O}_{12}:\text{Ce}^{3+}, \text{Tb}^{3+}$: A near-ultraviolet-excitable emission-tunable phosphor for white light-emitting diodes, *Opt. Laser Technol.*, 113 (2019) 211-216.
- [43] Y. Fu, Z. Zhang, F. Zhang, C. Li, B. Liu, G. Li, Electronic structure, energy transfer mechanism and thermal quenching behavior of $\text{K}_3\text{YB}_6\text{O}_{12}:\text{Dy}^{3+}, \text{Eu}^{3+}$ phosphor, *Opt. Mater.*, 99 (2020) 109519.
- [44] I.V.B. Maggay, P.-C. Lin, W.-R. Liu, Investigation of luminescence properties and the energy transfer mechanism of $\text{Li}_6\text{Lu}(\text{BO}_3)_3:\text{Ce}^{3+}, \text{Tb}^{3+}$ green-emitting phosphors, *RSC Adv.*, 5 (2015) 5591-5597.
- [45] F. Shan, L. Kang, G. Zhang, J. Yao, Z. Lin, M. Xia, X. Zhang, Y. Fu, Y. Wu, $\text{Na}_3\text{Y}_3(\text{BO}_3)_4$: a new noncentrosymmetric borate with an open-framework structure, *Dalton Trans.*, 45 (2016) 7205-7208.
- [46] R.K. Li, C.C. Wu, M.J. Xia, $\text{LiCaTb}_5(\text{BO}_3)_6$: A new magneto-optical crystal promising as Faraday rotator, *Opt. Mater.*, 62 (2016) 452-457.
- [47] R. Li, Enhancing the Magnetocaloric Effect of a Paramagnet to above Liquid Hydrogen Temperature, *Energy Technol.*, 7 (2019) 1801070.
- [48] M. Xia, S. Shen, J. Lu, Y. Sun, R. Li, $\text{K}_3\text{Li}_3\text{Gd}_7(\text{BO}_3)_9$: A New Gadolinium-Rich Orthoborate for Cryogenic Magnetic Cooling, *Chem. Eur. J.*, 24 (2018) 3147-3150.
- [49] M.B. Sanders, F.A. Cevallos, R.J. Cava, Magnetism in the $\text{KBaRE}(\text{BO}_3)_2$ (RE = Sm, Eu, Gd, Tb, Dy, Ho, Er, Tm, Yb, Lu) series: materials with a triangular rare earth lattice, *Mater. Res. Express*, 4 (2017) 036102.
- [50] S. Guo, T. Kong, W. Xie, L. Nguyen, K. Stolze, F.A. Cevallos, R.J. Cava, Triangular Rare-Earth Lattice Materials $\text{RbBaR}(\text{BO}_3)_2$ (R = Y, Gd–Yb) and Comparison to the $\text{KBaR}(\text{BO}_3)_2$ Analogs, *Inorg. Chem.*, 58 (2019) 3308-3315.
- [51] G.K. Abdullaev, K.S. Mamedov, Crystal structure of double ortho-borate of lithium and ytterbium $\text{Li}_6\text{Yb}(\text{BO}_3)_3$, *Kristallografiya*, 22 (1977) 389-392.

- [52] G.K. Abdullaev, K.S. Mamedov, P.F. Rzazade, S.A. Guseinova, G.G. Dzhaferov, Synthesis and x-ray-diffraction study of double orthoborate crystals of lithium and holmium, *Zh. Neorg. Khim.*, 22 (1977) 3239-3242.
- [53] Y.F. Lou, W.Y. Wang, G.M. Cai, Y.P. Sun, C. Wang, Crystal structure determination of new compounds $\text{Li}_6\text{MB}_3\text{O}_9$ (M=Nd, Sm, Eu, Tm, Er), *Powder Diff.*, 23 (2008) 3-9.
- [54] H. Chen, P. Loiseau, G. Aka, B. Baptiste, P. Veber, Crystal Growth and Characterization of Terbium-Based Borate Crystals of $\text{Sr}_3\text{Tb}(\text{BO}_3)_3$, $\text{Li}_6\text{Tb}(\text{BO}_3)_3$, and $\text{TbCa}_4\text{O}(\text{BO}_3)_3$: Color Centers, Spectroscopic Properties, and Optical Gain, *Cryst. Growth Des.*, 20 (2020) 1905-1919.
- [55] Y. Huang, C. Tu, Z. Luo, G. Chen, Spectra and intensity parameters of $\text{Li}_6\text{Y}(\text{BO}_3)_3\text{:Nd}^{3+}$ laser crystal, *Opt. Commun.*, 92 (1992) 57-60.
- [56] J. Sablayrolles, V. Jubera, J.-P. Chaminade, I. Manek-Hönniger, S. Murugan, T. Cardinal, R. Olazcuaga, A. Garcia, F. Salin, Crystal growth, luminescent and lasing properties of the ytterbium doped $\text{Li}_6\text{Y}(\text{BO}_3)_3$ compound, *Opt. Mater.*, 27 (2005) 1681-1685.
- [57] J.-P. Chaminade, P. Gravereau, V. Jubera, C. Fouassier, A New Family of Lithium Rare-Earth Oxyborates, $\text{LiLn}_6\text{O}_5(\text{BO}_3)_3$ (Ln=Pr–Tm): Crystal Structure of the Gadolinium Phase $\text{LiGd}_6\text{O}_5(\text{BO}_3)_3$, *J. Solid State Chem.*, 146 (1999) 189-196.
- [58] J.H. Gao, Crystal structure of lithium yttrium borate $\text{LiY}_6\text{O}_5(\text{BO}_3)_3$, *Chin. J. Struct. Chem.*, 25 (2006) 1175-1178.
- [59] V. Jubera, P. Veber, M. Chavoutier, A. Garcia, F. Adamietz, V. Rodriguez, J.-P. Chaminade, M. Velázquez, Crystal growth and optical characterizations of Yb^{3+} -doped $\text{LiGd}_6\text{O}_5(\text{BO}_3)_3$ single crystal: a new promising laser material, *CrystEngComm*, 12 (2010) 355-357.
- [60] Q. Wen, Z. Xiang, X. Gao, X. Yang, S. Xiao, Luminescence properties of $\text{LiY}_6\text{O}_5(\text{BO}_3)_3\text{:Eu}^{3+}/\text{Sm}^{3+}$ phosphor, *Mater Sci Eng, B*, 197 (2015) 82-86.
- [61] V. Jubera, P. Gravereau, J.P. Chaminade, Crystal structure of the new borate $\text{Li}_3\text{Gd}(\text{BO}_3)_2$: Comparison with the homologous $\text{Na}_3\text{Ln}(\text{BO}_3)_2$ (Ln: La, Nd) compounds, *Solid State Sci.*, 3 (2001) 469-475.
- [62] S. Bräuchle, H. Huppertz, Synthesis and structural characterization of $\text{Li}_3\text{Y}(\text{BO}_3)_2$, *Z. Naturforsch., B*, 72 (2017) 153-158.
- [63] J. Mascetti, M. Vlasse, C. Fouassier, The crystal chemistry of the new rare-earth sodium borates $\text{Na}_3\text{Ln}(\text{BO}_3)_2$ (Ln = La, Nd), *J. Solid State Chem.*, 39 (1981) 288-293.
- [64] S. Asiri Naidu, S. Boudin, U.V. Varadaraju, B. Raveau, Influence of structural distortions upon photoluminescence properties of Eu^{3+} and Tb^{3+} activated $\text{Na}_3\text{Ln}(\text{BO}_3)_2$ (Ln=Y, Gd) borates, *J. Solid State Chem.*, 190 (2012) 186-190.

- [65] Z.X. Wang, H.K. Li, G.M. Cai, Z.P. Jin, Synthesis, crystal structure, and thermal stability of new borates $\text{Na}_3\text{REB}_2\text{O}_6$ (RE = Pr, Sm, Eu), Powder Diffr., 31 (2016) 110-117.
- [66] D. Zhao, F.X. Ma, C.K. Nie, J. Wang, L. Zhang, Y.C. Fan, Structure Determination and Luminescent Property Studies of the Single Crystal $\text{Na}_3\text{Sm}(\text{BO}_3)_2$, Crystals, 7 (2017).
- [67] J.H. Gao, R.K. Li, Potassium rich rare earth (RE) borates $\text{K}_3\text{RE}(\text{BO}_3)_2$, Solid State Sci., 10 (2008) 26-30.
- [68] Y. Gao, C. Yin, P. Jiang, W. Gao, R. Cong, T. Yang, Synthesis, crystal structure of $\text{LiCaRE}_5(\text{BO}_3)_6$ (RE = Sm, Eu, Gd, Tb, Dy, Ho, Er, Tm, Yb, Lu, Y) and Eu^{3+} luminescence in $\text{LiCaRE}_5(\text{BO}_3)_6$ (RE = Gd, Y, Lu), J. Solid State Chem., 293 (2021) 121821.
- [69] G.K. Abdullaev, K.S. Mamedov, I.R. Amiraslanov, A.I. Magerramov, Crystal-structure of lithium praseodymium orthoborate $\text{Li}_3\text{Pr}_2(\text{BO}_3)_3$, J. Struct. Chem., 18 (1977) 331-333.
- [70] S.A. Gamidova, Triangulation in the $\text{Li}_2\text{O}-\text{Ln}_2\text{O}_3-\text{B}_2\text{O}_3$ (Ln = Nd, Eu, Dy, Yb, and Y) systems and the melting character of ternary compounds, Russ. J. Inorg. Chem., 54 (2009) 141-144.
- [71] J. Mascetti, C. Fouassier, P. Hagenmuller, Concentration quenching of the Nd^{3+} emission in alkali rare earth borates, J. Solid State Chem., 50 (1983) 204-212.
- [72] G. Zhang, Y. Wu, P. Fu, G. Wang, S. Pan, C. Chen, A New Nonlinear Optical Borate Crystal $\text{Na}_3\text{La}_2(\text{BO}_3)_3$, Chem. Lett., 30 (2001) 456-457.
- [73] G. Zhang, Y. Wu, P. Fu, G. Wang, H. Liu, G. Fan, C. Chen, A new sodium samarium borate $\text{Na}_3\text{Sm}_2(\text{BO}_3)_3$, J. Phys. Chem. Solids, 63 (2002) 145-149.
- [74] Z.H. Cui, W. Liu, L.Z. Zhang, F.Y. Guo, C.C. Huang, J.Z. Chen, Crystal Structure and Properties of a Sodium Terbium Borate $\text{Na}_{2.67}\text{Tb}_{2.11}\text{B}_3\text{O}_9$, Chin. J. Struct. Chem., 31 (2012) 1823-1828.
- [75] Q. Zeng, R.K. Li, Crystals Structure of $(\text{K},\text{Na})_3\text{La}_2(\text{BO}_3)_3$ Solid Solution System, Rengong Jingti Xuebao, 42 (2013) 815-818.
- [76] J.H. Gao, R.K. Li, $\text{Rb}_3\text{Y}_2(\text{BO}_3)_3$ with a noncentrosymmetric structure, Acta Crystallogr., Sect. C, 63 (2007) I112-I114.
- [77] A.K. Subanakov, E.V. Kovtunets, B.G. Bazarov, S.G. Dorzhieva, J.G. Bazarova, New double holmium borates: $\text{Rb}_3\text{HoB}_6\text{O}_{12}$ and $\text{Rb}_3\text{Ho}_2\text{B}_3\text{O}_9$, Solid State Sci., 105 (2020) 106231.
- [78] Y. Wu, G. Zhang, P. Fu, C. Chen, Nonlinear optical crystals of compound $\text{Na}_3\text{La}_9\text{B}_8\text{O}_{27}$ and producing method and uses thereof, US Patents, 2005.
- [79] P. Gravereau, J.-P. Chaminade, S. Pechev, V. Nikolov, D. Ivanova, P. Peshev, $\text{Na}_3\text{La}_9\text{O}_3(\text{BO}_3)_8$, a new oxyborate in the ternary system $\text{Na}_2\text{O}-\text{La}_2\text{O}_3-\text{B}_2\text{O}_3$: preparation and crystal structure, Solid State Sci., 4 (2002) 993-998.

- [80] F. Shan, M. Xia, G. Zhang, J. Yao, X. Zhang, T. Xu, Y. Wu, Growth, structure, and optical properties of a self-activated crystal: $\text{Na}_3\text{Nd}_9\text{O}_3(\text{BO}_3)_8$, *Solid State Sci.*, 41 (2015) 31-35.
- [81] S. Zhao, G. Zhang, J. Yao, Y. Wu, $\text{K}_3\text{Yb}_6\text{O}_{12}$: A new nonlinear optical crystal with a short UV cutoff edge, *Mater. Res. Bull.*, 47 (2012) 3810-3813.
- [82] K. Feng, W. Yin, W. Hao, J. Yao, Y. Wu, A novel UV nonlinear optical crystal material: $\text{K}_{21}\text{Yb}_8\text{B}_{45}\text{O}_{90}$, *CrystEngComm*, 15 (2013) 5064-5069.
- [83] Z. Jia, Q. Zeng, P. Gong, Y. Dong, X. Zhang, B. Xin, Z. Lin, M. Xia, Nonlinear-Optical Crystal $\text{Rb}_3\text{YB}_6\text{O}_{12}$ with Condensed B_5O_{10} Blocks That Exhibits an Intriguing Structural Arrangement and a Short Ultraviolet Absorption Edge, *Inorg. Chem.*, 59 (2020) 13029-13033.
- [84] V.V. Atuchin, A.K. Subanakov, A.S. Aleksandrovsky, B.G. Bazarov, J.G. Bazarova, S.G. Dorzhieva, T.A. Gavrilova, A.S. Krylov, M.S. Molokeev, A.S. Oreshonkov, A.M. Pugachev, Y.L. Tushinova, A.P. Yelisseyev, Exploration of structural, thermal, vibrational and spectroscopic properties of new noncentrosymmetric double borate $\text{Rb}_3\text{NdB}_6\text{O}_{12}$, *Adv. Powder Technol.*, 28 (2017) 1309-1315.
- [85] V.V. Atuchin, A.K. Subanakov, A.S. Aleksandrovsky, B.G. Bazarov, J.G. Bazarova, T.A. Gavrilova, A.S. Krylov, M.S. Molokeev, A.S. Oreshonkov, S.Y. Stefanovich, Structural and spectroscopic properties of new noncentrosymmetric self-activated borate $\text{Rb}_3\text{EuB}_6\text{O}_{12}$ with B_5O_{10} units, *Mater. Des.*, 140 (2018) 488-494.
- [86] Z. Xie, Y. Wang, S. Cheng, G. Han, Z. Yang, S. Pan, Synthesis, characterization, and theoretical analysis of three new nonlinear optical materials $\text{K}_7\text{MRE}_2\text{B}_{15}\text{O}_{30}$ ($\text{M} = \text{Ca}$ and Ba , $\text{RE} = \text{La}$ and Bi), *Sci. China Mater.*, 62 (2019) 1151-1161.
- [87] Z. Xie, M. Mutailipu, G. He, G. Han, Y. Wang, Z. Yang, M. Zhang, S. Pan, A Series of Rare-Earth Borates $\text{K}_7\text{MRE}_2\text{B}_{15}\text{O}_{30}$ ($\text{M} = \text{Zn}, \text{Cd}, \text{Pb}$; $\text{RE} = \text{Sc}, \text{Y}, \text{Gd}, \text{Lu}$) with Large Second Harmonic Generation Responses, *Chem. Mater.*, 30 (2018) 2414-2423.
- [88] Y. Li, F. Liang, H. Song, W. Liu, Z. Lin, G. Zhang, Y. Wu, $\text{Rb}_7\text{SrY}_2(\text{B}_5\text{O}_{10})_3$: A Rare-Earth Pentaborate with Moderate Second-Harmonic Response and Interesting Phase-Matching Behavior, *Inorg. Chem.*, 58 (2019) 8943-8947.
- [89] W. Liu, X. Liu, J. Shen, Y. Li, H. Song, J. Feng, Z. Lin, G. Zhang, A new non-centrosymmetric Gd-based borate crystal $\text{Rb}_7\text{SrGd}_2(\text{B}_5\text{O}_{10})_3$: growth, structure, and nonlinear optical and magnetic properties, *Dalton Trans.*, 49 (2020) 9355-9361.
- [90] J. Feng, X. Xu, C.-L. Hu, J.-G. Mao, $\text{K}_6\text{ACaSc}_2(\text{B}_5\text{O}_{10})_3$ ($\text{A} = \text{Li}, \text{Na}, \text{Li}_{0.7}\text{Na}_{0.3}$): Nonlinear-Optical Materials with Short UV Cutoff Edges, *Inorg. Chem.*, 58 (2019) 2833-2839.
- [91] S. Zhao, G. Zhang, J. Yao, Y. Wu, $\text{K}_6\text{Li}_3\text{Sc}_2\text{B}_{15}\text{O}_{30}$: A new nonlinear optical crystal with a short absorption edge, *CrystEngComm*, 14 (2012) 5209-5214.

- [92] J. Gao, L. Song, X. Hu, D. Zhang, A buetschliite-type rare-earth borate, $\text{KBaY}(\text{BO}_3)_2$, *Solid State Sci.*, 13 (2011) 115-119.
- [93] A. Pabst, Synthesis, properties, and structure of $\text{K}_2\text{Ca}(\text{CO}_3)_2$, buetschliite, *Am. Mineral.*, 59 (1974) 353-358.
- [94] J.A.M. Paddison, M. Daum, Z. Dun, G. Ehlers, Y. Liu, Matthew B. Stone, H. Zhou, M. Mourigal, Continuous excitations of the triangular-lattice quantum spin liquid YbMgGaO_4 , *Nat. Phys.*, 13 (2017) 117-122.
- [95] S. Guo, A. Ghasemi, C.L. Broholm, R.J. Cava, Magnetism on ideal triangular lattices in $\text{NaBaYb}(\text{BO}_3)_2$, *Phys. Rev. Mater.*, 3 (2019) 094404.
- [96] S. Guo, T. Kong, F.A. Cevallos, K. Stolze, R.J. Cava, Crystal growth, crystal structure and anisotropic magnetic properties of $\text{KBaR}(\text{BO}_3)_2$ ($\text{R} = \text{Y, Gd, Tb, Dy, Ho, Tm, Yb and Lu}$) triangular lattice materials, *J. Magn. Magn. Mater.*, 472 (2019) 104-110.
- [97] A.E. Kokh, N.G. Kononova, V.S. Shevchenko, Y.V. Seryotkin, A.K. Bolatov, K.A. Abdullin, B.M. Uralbekov, M. Burkitbayev, Syntheses, crystal structure and luminescence properties of the novel isostructural $\text{KSrR}(\text{BO}_3)_2$ with $\text{R} = \text{Y, Yb, Tb}$, *J. Alloys Compd.*, 711 (2017) 440-445.
- [98] A.B. Kuznetsov, K.A. Kokh, N.G. Kononova, V.S. Shevchenko, E.V. Kaneva, B. Uralbekov, V.A. Svetlichnyi, A.E. Kokh, Synthesis and growth of new rare earth borates $\text{KCaR}(\text{BO}_3)_2$ ($\text{R} = \text{La, Pr and Nd}$), *J. Solid State Chem.*, 282 (2020) 121091.
- [99] P. Chen, M. Xia, R. Li, Mixed Alkali Neodymium Orthoborates: $\text{K}_9\text{Li}_3\text{Nd}_3(\text{BO}_3)_7$ and $\text{A}_2\text{LiNd}(\text{BO}_3)_2$ ($\text{A} = \text{Rb, Cs}$), *Z. Anorg. Allg. Chem.*, 642 (2016) 424-430.
- [100] S. Bräuchle, H. Huppertz, Synthesis and structural characterization of $\text{Li}_3\text{K}_3\text{Y}_7(\text{BO}_3)_9$, *J. Solid State Chem.*, 253 (2017) 242-248.
- [101] V. Jubera, P. Gravereau, J.-P. Chaminade, C. Fouassier, A New Oxyborate in the Ternary Phase Diagrams $\text{Li}_2\text{O}-\text{Ln}_2\text{O}_3-\text{B}_2\text{O}_3$: $\text{Li}_2\text{Ln}_5\text{O}_4(\text{BO}_3)_3$ ($\text{Ln} = \text{Yb, Lu}$): Crystal Structure of the Ytterbium Phase, *J. Solid State Chem.*, 156 (2001) 161-167.
- [102] G. Corbel, M. Leblanc, E. Antic-Fidancev, M. Lemaître-Blaise, Crystal Structure of Sodium Rare Earth Oxyborates $\text{Na}_2\text{Ln}_2(\text{BO}_3)_2\text{O}$ ($\text{Ln} = \text{Sm, Eu, and Gd}$) and Optical Analysis of $\text{Na}_2\text{Gd}_2(\text{BO}_3)_2\text{O}:\text{Eu}^{3+}$, *J. Solid State Chem.*, 144 (1999) 35-44.
- [103] G. Heymann, K. Beyer, H. Huppertz, High-Temperature Synthesis, Crystal Structure, and Properties of the New Sodium Rare-Earth Oxide Borates $\text{Na}_2\text{Ln}_2(\text{BO}_3)_2\text{O}$ ($\text{Ln} = \text{Dy, Ho}$), *Z. Naturforsch., B: Chem. Sci.*, 50 (2004) 11-12.

- [104] P. Peshev, S. Pechev, V. Nikolov, P. Gravereau, J.P. Chaminade, D. Binev, D. Ivanova, Studies on some ternary oxyborates of the $\text{Na}_2\text{O}-\text{Me}_2\text{O}_3-\text{B}_2\text{O}_3$ (Me=rare earth or aluminum) systems: Synthesis, structure and crystal growth, *J. Solid State Chem.*, 179 (2006) 2834-2849.
- [105] Z. Jia, M. Xia, Congruent melt terbium-rich borate $\text{Na}_2\text{Tb}_2\text{B}_2\text{O}_7$: Synthesis, crystal structure, optical and magnetic properties, *J. Alloys Compd.*, 743 (2018) 537-542.
- [106] D. Zhao, Y.-N. Li, Y.-P. Fan, B.-Z. Liu, S.-R. Zhang, R.-J. Zhang, Crystal structure, theoretical studies and luminescent properties of a new borate $\text{Na}_3\text{GdB}_8\text{O}_{15}$ with one-dimensional broad-banded anionic framework, *Dalton Trans.*, 49 (2020) 13167-13175.
- [107] J.H. Gao, R.K. Li, Preparation, structure and luminescent properties of a new potassium yttrium borate $\text{K}_3\text{Y}_3(\text{BO}_3)_4$, *Mater. Res. Bull.*, 43 (2008) 882-888.
- [108] Q.D. Zeng, R.K. Li, A new potassium rare earth oxyborate $\text{K}_2\text{La}_2(\text{BO}_3)_2\text{O}$, *Solid State Sci.*, 12 (2010) 2144-2147.
- [109] D. Zhao, F.-X. Ma, Z.-Q. Wu, L. Zhang, W. Wei, J. Yang, R.-H. Zhang, P.-F. Chen, S.-X. Wu, Synthesis, crystal structure and characterizations of a new red phosphor $\text{K}_3\text{EuB}_6\text{O}_{12}$, *Mater. Chem. Phys.*, 182 (2016) 231-236.
- [110] D. Zhao, F.-X. Ma, R.-J. Zhang, W. Wei, J. Yang, Y.-J. Li, A new rare-earth borate $\text{K}_3\text{LuB}_6\text{O}_{12}$: crystal and electronic structure, and luminescent properties activated by Eu^{3+} , *J. Mater. Sci.: Mater. Electron.*, 28 (2017) 129-136.
- [111] D. Zhao, F.-X. Ma, R.-J. Zhang, M. Huang, P.-F. Chen, R.-H. Zhang, W. Wei, Substitution disorder and photoluminescent property of a new rare-earth borate: $\text{K}_3\text{TbB}_6\text{O}_{12}$, *Z. Kristallogr. Cryst. Mater.*, 231 (2016) 525-530.
- [112] J.H. Gao, M.S. Zheng, Synthesis and Crystal Structure of a Rubidium Lanthanum Borate $\text{Rb}_3\text{La}_3(\text{BO}_3)_4$, *Chin. J. Struct. Chem.*, 28 (2009) 82-86.
- [113] S. Bräuchle, M. Seibald, H. Huppertz, Synthesis and structural characterization of $\text{Li}_3\text{K}_3\text{Eu}_7(\text{BO}_3)_9$, *Z. Naturforsch., B: Chem. Sci.*, 72 (2017) 959-965.
- [114] P.Y. Chen, G. Wang, Syntheses, structure determination and characterization of two novel non-centrosymmetric mixed alkali rare-earth orthoborates: $\text{K}_3\text{Li}_3\text{RE}_7(\text{BO}_3)_9$ (RE=Dy, Tb), *Solid State Sci.*, 108 (2020) 106442.
- [115] R. Ma, Y. Yang, C. Hu, X. Dong, Z. Yang, S. Pan, $\text{LiCs}_2\text{La}(\text{BO}_3)_2$ and $\text{Li}_3\text{K}_9\text{La}_3(\text{BO}_3)_7$: new mixed alkali metal lanthanum borates with three-dimensional open frameworks and short cut-off edges, *Dalton Trans.*, 47 (2018) 3512-3520.
- [116] Z. Jia, D. Wang, Q. Huang, B. Xu, X. Zhang, M. Xia, Synthesis, single crystal structure, optical, and magnetic properties of mixed-alkali-metal terbium borate $\text{Rb}_2\text{LiTbB}_2\text{O}_6$, *J. Mater. Sci.: Mater. Electron.*, 31 (2020) 6288-6294.

- [117] M.J. Xia, R.K. Li, A new quaternary rare earth borate, $\text{CsLi}_2\text{Gd}_4(\text{BO}_3)_5$, *Acta Crystallogr., Sect. E*, 63 (2007) I173-U160.
- [118] L. Pauling, The principles determining the structure of complex ionic crystals, *J. Am. Chem. Soc.*, 51 (1929) 1010-1026.
- [119] W. Schreyer, B. Stöckhert, High-pressure metamorphism in nature and experiment, *Lithos*, 41 (1997) 1-4.
- [120] H. Emme, M. Valldor, R. Pöttgen, H. Huppertz, Associating Borate and Silicate Chemistry by Extreme Conditions: High-Pressure Synthesis, Crystal Structure, and Properties of the New Borates $\text{RE}_3\text{B}_5\text{O}_{12}$ (RE = Er–Lu), *Chem. Mater.*, 17 (2005) 2707-2715.

Chapter 2. Experimental Methods

2.1 Synthesis of rare-earth borate compounds

Series of samples were synthesized using the conventional solid-state reaction. This method ensures all the chemicals react together at the same time. Stoichiometric amounts of raw materials were thoroughly mixed in an agate mortar. The mixtures were put in covered platinum or corundum crucibles and typically heated in the Muffle furnaces (CAROLITE – CWF) with a heating rate (usually 100 K/ hour). The reaction temperatures and the dwelling time depend on the compounds themselves. During the heating process, intermediate grindings are usually carried out to ensure the mixtures with a homogenous reaction.

In this dissertation, single crystals were obtained by spontaneous crystallization using self-flux from the high-temperature solution. The educts are dissolved in platinum crucibles at high temperature, and then the melting slowly cools down (usually around 3K /hour) until the single crystal forms.

2.2 Single crystal X-ray diffractometer

A Single crystal with suitable size and high quality was picked under the microscope and was mounted on a glass fiber using epoxy glue, and then was placed on a KAPPA geometry goniometer. The single crystal X-ray diffraction (SCXRD) data were recorded at room temperature on a D8 Venture diffractometer (Bruker AXS GmbH, Karlsruhe, Germany) diffractometer equipped with the PHOTON 100 CMOS (Complementary Metal Oxide Sensor) detector where the active area is up to 100 cm². The Mo K α radiation was monochromated by the curved graphite single crystals with the wavelength of $\lambda_{\alpha_1} = 70.9300(3)$ pm and $\lambda_{\alpha_2} = 71.3574(2)$ pm, treated as average $\lambda = 71.073(1)$ pm.

The collected data was integrated, merged, averaged to create an HKL file using APEX 3 software [1]. The numerical absorption correction was also carried out within APEX 3 software.

Afterward, the HKL data file was transferred to the SHELXT software [2] where the structure was initially solved by the intrinsic phasing method. Finally, the crystal structure was refined by least-squares on the SHELXLE software [3]. All of the figures of the crystal structures displayed throughout the following chapters were created using the VESTA software program [4] (JP-Mineral, Tokyo, Japan).

2.3 Powder X-ray Diffraction

X-ray powder-diffraction experiments were carried out using two instruments:

- 1) on a Panalytical X'Pert Pro powder diffractometer in Bragg–Brentano geometry with $\text{CuK}\alpha_{1,2}$ ($\lambda_{\text{K}\alpha 1} = 154.05929(5)$ pm, $\lambda_{\text{K}\alpha 2} = 154.4414(2)$ pm) radiation. This instrument is equipped with a divergence slit (0.25°), an anti-scatter slit (0.5°), a soller slit (0.04 rad) and a mask (10 mm) in the primary beam. A soller slit (0.04 rad), a Ni-filter, and a X'Celerator detector system are used in the secondary beam.
- 2) on a Bruker D8 Discover diffractometer (Bruker AXS GmbH, Karlsruhe, Germany) in Bragg–Brentano geometry with $\text{CuK}\alpha_{1,2}$ ($\lambda_{\text{K}\alpha 1} = 154.0598(1)$ pm, $\lambda_{\text{K}\alpha 2} = 154.4439(1)$ pm) radiation. This instrument is equipped with a divergence slit (0.25°), a mask (10.5 mm), and an axial soller slit (2.5°) in the primary beam. A soller slit (2.5°), and an energy-sensitive detector (LynxEye XE) are provided in the secondary beam.

The Rietveld refinement of all recorded PXRD data was performed using “DiffracPlus Topas 6 software” (Bruker AXS GmbH, Karlsruhe, Germany) [5]. The instrument profiles were determined by the fundamental parameter approach, where the fundamental parameters were fitted against a LaB_6 standard reference sample.

2.4 Bond Valence Sum (BVS) method

Bond Valence Sum [6] is an approach based on Pauling second rule with summarizing a large number of crystal structures and considering the basic laws of structural chemistry. According to the Bond Valence theory, the valence of an atom is distributed on each bond it participates in, that is, each chemical bond has a bond valence S_i , which is determined by the bond length with the following equation

$$S_i = \exp \frac{(R_0 - R_i)}{B}$$

where R_i is the observed bond length, R_0 is an empirical parameter expressing the ideal bond length when the element has exactly valence, and B is an empirical constant, typically 37.0 pm. R_0 and B usually can be consulted in the relevant literature. Thereby, if the coordination environment of an atom is known, its Bond Valence Sum V can be calculated:

$$V = \sum_i S_i$$

The *Bondstr* software within the FullProf suite was utilized to perform the BVS calculation throughout this dissertation.

2.5 Scanning electron microscope (SEM) and Energy dispersive X-ray spectroscopy (EDX)

Energy dispersive X-ray spectroscopy (EDX) data were collected in a JSM-6510 (JEOL Ltd, Tokyo, Japan) scanning electron microscope (SEM) equipped with an XFlash Detector 410-M with an accelerating voltage of 20 kV. Prior to the EDX measurement, the gold coating process was performed via argon plasma discharge to improve the samples' conductivity. The elemental analysis offered the constituent metals ratio in atom-% in the compound. The whole spectra were used for the quantification of the component elements.

2.6 UV/Vis diffuse reflectance spectroscopy

Optical diffuse reflectance spectra were recorded at room temperature on a Shimadzu UV-2600 (Shimadzu, Kyoto, Japan) spectrophotometer equipped with an ISR-2600 plus two-detector integrating sphere (Pike Technologies, USA). Data were collected in the range of 200 to 850 nm with a step of 1 nm. A standard BaSO₄ sample was used as reference for the baseline correction.

The diffuse reflectance spectra of samples were converted to F(R) spectra according to the Kubelka-Munk function [9]:

$$F(R) = \frac{(1 - R)^2}{2R}$$

where R is reflectance. The Tauc's method [10] followed by the Kubelka-Munk function are commonly used to estimate the bandgap energy by finding the intercept of the abscissa from the following relations:

$$F(R)(h\nu) = B(h\nu - E_g)^n$$

Where h is the Planck's constant, ν the frequency of light, E_g the bandgap in eV and n the type of optical transition. That is, for $n = 2$ and $\frac{1}{2}$ refers to direct and indirect transition, respectively. Recently, the derivation of absorption spectrum fitting (DASF) method [11] was proposed for thin films to calculate the bandgap energies without any presumption of the nature of the transition. Based on this, the DASF can also be expressed as follows proposed by Kirsch et al. [12, 13] for powder samples:

$$\frac{d \ln F(R)}{d h \nu} = \frac{n}{h \nu - E_g}$$

Combining the results of the absolute bandgap width determination using the DASF method with the values for a direct or indirect transition obtained by the Tauc method, type, and width of the bandgap could be experimentally identified.

2.7 Fourier transform infrared (IR)-spectroscopy

Fourier transform infrared (FTIR) spectra were recorded on a Bruker IFS66v/S spectrometer (Bruker Optik GmbH, Ettlingen, Germany) using the standard KBr method. Approx. 2 mg sample was mixed with 200 mg dried KBr and pressed at 100 kN, forming disks of 12 mm in diameter. The reference pellet consists of 200 mg dried KBr only. Measurements were carried out between 370 and 4000 cm^{-1} with a total acquisition of 128 spectra, leading to a spectral resolution of 1.0 cm^{-1} .

2.8 Raman Spectroscopy

Temperature-dependent Raman spectra were recorded on a LabRam ARAMIS (Horiba Jobin Yvon) Micro-Raman spectrometer equipped with a laser working at 785 nm and less than 5 mW. The use of a 50x long working distance objective (Olympus) with a numerical aperture of 0.55 provides a focus spot of about 2 μm diameter when closing the confocal hole to 200 μm . Raman spectra were collected in the range 85 cm^{-1} to 1700 cm^{-1} with a spectral resolution of approximately 1.2 cm^{-1} using a grating of 1800 grooves/mm and a thermoelectrically cooled CCD detector (Synapse, 1024 x 256 pixels). The spectral positions were calibrated against the Raman mode of Si before and after the sample measurements. The position of the Si peak was repeatedly measured against the Rayleigh line (0.0 cm^{-1}) yielding a value of $520.7 \pm 0.1 \text{ cm}^{-1}$. The linearity of the spectrometer was calibrated against the emission lines of a neon lamp. For the low-temperature measurements, a pressed pellet of powder sample was placed on a Linkam cooling stage (THMS600) attached to a pump (LNP95 Cooling Pump) that provides a continuous flow of liquid nitrogen. The measurements were carried out between 78 K and 300 K. A ramp rate of 5 K/min and a holding time of 5 min were followed to properly equilibrate the temperature. For the spectrum at the ambient condition, the baseline was corrected and fitted with Pseudo-Voigt line shape.

2.9 Thermal analysis

Simultaneous thermogravimetric analysis and differential scanning calorimetry (TGA/DSC) measurements were performed on a simultaneous TGA/DSC 3+ STAR e system (Mettler Toledo, Schwerzenbach, Switzerland). Approx. 10 mg of each polycrystalline samples were measured with a heating rate of 10 K/min and a continuous N₂ flow of 20 mL/min from room temperature to the destination temperature. Afterward, the data were normalized to the respective mass. An empty corundum crucible was used as a reference. A drift correction was applied based on the empty crucible data.

2.10 Magnetic susceptibility

Temperature-dependent DC magnetic susceptibility measurements were carried out with a Magnetic Property Measurement System MPMS-XL7 (Quantum Design, San Diego, USA) using the field-cooling process in the range from 1.9 K to 300 K at a magnetic field of 0.01 T. Polycrystalline samples were sealed in a gel capsule and attached to a nonmagnetic sample holder.

Reference

- [1] Bruker: APEX3, SAINT, SADABS and XP. Bruker AXS Inc., Madison, Wisconsin, USA.
- [2] G. M. Sheldrick, SHELXT - Integrated space-group and crystal-structure determination, *Acta Cryst. A* 71 (2015), 3-8
- [3] C. B. Hübschle, G. M. Sheldrick and B. Dittrich, ShelXle: a Qt graphical user interface for SHELXL, *J. Appl. Cryst.* 44, (2011), 1281-1284
- [4] K. Momma and F. Izumi, VESTA 3 for three-dimensional visualization of crystal, volumetric and morphology data, *J. Appl. Cryst.*, 44 (2011), 1272-1276
- [5] A. A. Coelho, TOPAS and TOPAS-Academic: an optimization program integrating computer algebra and crystallographic objects written in C++, *J. Appl. Cryst.*, 51 (2018), 210-218
- [6] Brown, I. D, *The Chemical Bond in Inorganic Chemistry*, (2002), the Oxford University Press.
- [7] L. Pauling, The principles determining the structure of complex ionic crystals, *J. Am. Chem. Soc.*, 51 (1929) 1010-1026.
- [8] Rodriguez-Carvajal J, Roisnel T, WinPLOTR: A windows tool for powder diffraction pattern analysis, *Mater. Sci. Forum*, proceedings of the seventh European powder diffraction conference (2000), Barcelona, Spain, pp. 378–381.
- [9] P. Kubelka, Ein Beitrag zur Optik der Farbanstriche, *Z. Tech. Phys.*, 12 (1931) 593-601.
- [10] J. Tauc, R. Grigorovici, A. Vancu, Optical properties and electronic structure of amorphous germanium, *Phys. Status Solidi B*, 15 (1966) 627-637.
- [11] D. Souri, Z. E. Tahan, A new method for the determination of optical band gap and the nature of optical transitions in semiconductors, *Appl. Phys. B*, 119 (2015) 273-279.
- [12] A. Kirsch, M. M. Murshed, M. Schowalter, A. Rosenauer, T. M. Gesing, Nanoparticle precursor into polycrystalline $\text{Bi}_2\text{Fe}_4\text{O}_9$: an evolutionary investigation of structural, morphological, optical, and vibrational properties, *J. Phys. Chem. C*, 120 (2016) 18831-18840.
- [13] A. Kirsch, M. M. Murshed, F. J. Litterst, T. M. Gesing, Structural, spectroscopic, and thermoanalytic studies on $\text{Bi}_2\text{Fe}_4\text{O}_9$: tunable properties driven by nano-and poly-crystalline states, *J. Phys. Chem. C*, 123 (2019) 3161-3171.

Declaration on own contributions to the publications

The results presented in this cumulative dissertation were obtained in collaborations with several other groups. In this section, I specifically announce my own contributions to the individual publications.

The work presented in **chapter 3** is based on a previously published, Pengyun Chen, M. Mangir Murshed, Michael Fischer, Thomas Frederichs, Thorsten M. Gesing; $\text{KLi}_2\text{RE}(\text{BO}_3)_2$ (RE = Dy, Ho, Er, Tm, Yb, and Y): Structural, Spectroscopic, And Thermogravimetric Studies on a Series of Mixed-Alkali Rare-Earth Orthoborates, *Inorganic Chemistry*, 59, (2020), 18214–18224

I conducted the following tasks:

- Writing of the main manuscript
- Generation of the figures
- Solid state synthesis and single-crystal growth of the samples
- Perform the measurements of powder and single-crystal XRD, SEM-EDX, UV/Vis, IR, Raman as well as their evaluation and interpretation including the single-crystal structure determination, and Rietveld refinements.
- Evaluation of magnetic susceptibility data and their interpretation
- DFT calculation of the electronic bandgap
- Evaluation of DSC/TG data and their interpretation

I did not conduct the following tasks:

- DFT calculation of the vibrational properties (carried out by Dr. Michael Fischer)
- Magnetic Measurements (done by Dr. Thomas Frederichs)
- DSC/TG measurements (carried out by Julia Butzlaff)

The work presented in **chapter 4** is based on a previously published, Pengyun Chen, M. M. Murshed, Thorsten. M. Gesing; Synthesis and crystal structures of novel alkali rare-earth orthoborates $\text{K}_3\text{RE}_3(\text{BO}_3)_4$ (RE = Pr, Nd, Sm - Lu), *Journal of Material Science*, 56 (2021) 3639-3652.

I conducted the following tasks:

- Writing of the main manuscript

- Generation of the figures
- Solid state synthesis and single-crystal growth of the samples
- Perform the measurements of powder and single-crystal XRD, UV/Vis, IR, Raman as well as their evaluation and interpretation including the single-crystal structure determination, and Rietveld refinements.

The work presented in **chapter 5** is based on a previously published, Pengyun Chen, M. M. Murshed, Thorsten. M. Gesing; Synthesis and characterization of $K_2Pr_2O(BO_3)_2$: structural, spectroscopic and thermogravimetric investigations of a novel potassium praseodymium oxoborate structure-type, *SN Applied Sciences* 2, (2020), 747.

I conducted the following tasks:

- Writing of the main manuscript
- Generation of the figures
- Solid state synthesis and single-crystal growth of the sample
- Perform the measurements of powder and single-crystal XRD, UV/Vis, IR, Raman as well as their evaluation and interpretation including the single-crystal structure determination, and Rietveld refinement.
- Evaluation of magnetic susceptibility data and their interpretation
- Evaluation of DSC/TG data and their interpretation

I did not conduct the following tasks:

- Magnetic Measurements (done by Dr. Thomas Frederichs)
- DSC/TG measurement (carried out by Julia Butzlaff)

Chapter 3

KLi₂RE(BO₃)₂ (RE = Dy, Ho, Er, Tm, Yb and Y): structural, spectroscopic and thermogravimetric studies on a series of mixed alkali rare-earth orthoborates

Pengyun Chen¹, M. Mangir Murshed^{1,4*}, Michael Fischer^{2,4}, Thomas Frederichs³,

Thorsten M. Gesing^{1,4}

¹University of Bremen, Institute of Inorganic Chemistry and Crystallography, Faculty of Biology and Chemistry, Leobener Straße 7, D-28359 Bremen, Germany

²University of Bremen, Crystallography, Faculty of Geosciences, Klagenfurter Straße 2-4, D-28359 Bremen, Germany

³University of Bremen, Faculty of Geosciences, Klagenfurter Straße 2-4, D-28359 Bremen, Germany

⁴ University of Bremen, MAPEX Center for Materials and Processes, Bibliothekstraße 1, D-28359 Bremen, Germany

*Corresponding author: e-mail address: murshed@uni-bremen.de, phone: +49 (0)421 218 63144, fax: +49 421 218 63145.

Abstract

We report a detailed structural, spectroscopic, and thermogravimetric investigation of a new series of mixed alkali rare-earth orthoborates $\text{KLi}_2\text{RE}(\text{BO}_3)_2$ ($\text{RE} = \text{Dy, Ho, Er, Tm, Yb and Y}$). Single crystals are directly prepared by a flux method, as well as mechanically separated from the polycrystalline powder obtained from the conventional solid-state reactions. All $\text{KLi}_2\text{RE}(\text{BO}_3)_2$ members are isotypic and crystallize in the space group $P2_1/n$. The novel structure type comprises of $[\text{RE}_2(\text{BO}_3)_4\text{O}_4]^{14-}$ anionic clusters where the edge-sharing REO_7 pentagonal bipyramids are connected by BO_3 groups, and both K^+ and Li^+ cations are located at the interstitial voids of the 3D network. The metric parameters and crystal structural features obtained from single crystal data are in excellent agreement with those refined from powder data. The change of the lattice parameters and unit cell volumes can be explained in terms of lanthanide contraction effect. A comparison between $\text{KLi}_2\text{RE}(\text{BO}_3)_2$ and other rare-earth borates with similar chemical composition indicates that the sum of the ionic radii of the alkali-metal cations governs the symmetry of the crystals. Diffuse reflectance UV/Vis spectra display the characteristic absorption behaviors of the RE^{3+} cations and the fundamental absorption edge. Both Tauc's and derivation of absorption spectrum fitting (DASF) methods are used to identify the magnitude and the type of bandgap, respectively, which is compared with those obtained from density functional theory (DFT) calculations. The calculated phonon density of states and vibrational frequency at the gamma-point helps understand the Fourier-transform infrared and Raman spectra of $\text{KLi}_2\text{RE}(\text{BO}_3)_2$. The incongruent melting behavior and the thermal stability of each member of the $\text{KLi}_2\text{RE}(\text{BO}_3)_2$ series are also studied by thermogravimetric analyses.

Keywords: Rare-earth borate, Crystal structure, Vibrational property, Optical property, Thermal stability, DFT

1. Introduction

Inorganic metal borates are of research interests due to their structural diversity, interesting physico-chemical properties and wide applications especially in nonlinear optics (NLO). [1-3] To date, many acentric rare-earth borates such as $\text{La}_2\text{CaB}_{10}\text{O}_{19}$ [4], $\text{Na}_3\text{La}_9\text{O}_3(\text{BO}_3)_8$ [5], $\text{YAl}_3(\text{BO}_3)_4$ [6], $\text{GdAl}_3(\text{BO}_3)_4$ [7], $\text{YCa}_4\text{O}(\text{BO}_3)_3$ [8] and $\text{K}_7\text{MRE}_2(\text{B}_5\text{O}_{10})_3$ ($\text{M} = \text{Zn, Cd, Pb}$; $\text{RE} = \text{Sc, Y, Gd, Lu}$) [9-10] have been widely explored as NLO crystals due to their large optical second-harmonic (SHG) coefficients, suitable birefringence, high laser damage threshold, good crystal growth habit, mechanical strength and excellent hygroscopic resistance [4-12]. Moreover, rare-earth borates doped with other optically-active rare-earth cations (e.g., Er^{3+} and Yb^{3+}) have as well received vast attentions as they are able to generate efficient radiation of solid-state lasers [13]. The continuous wave self-frequency-doubled green laser output powder up to 1.1 W has been achieved in $\text{Yb}^{3+}:\text{YAl}_3(\text{BO}_3)_4$ crystals [14]. Of notes, $(\text{Er}^{3+}, \text{Yb}^{3+}):\text{GdAl}_3(\text{BO}_3)_4$ and $(\text{Er}^{3+}, \text{Yb}^{3+}):\text{GdMgB}_5\text{O}_{10}$ crystals were demonstrated producing human eye-safe 1.5- μm laser and their slope efficiencies lie close to that of Er - Yb: commercial glass [15-16]. $\text{YGa}_3(\text{BO}_3)_4$ activated by Dy^{3+} , Tm^{3+} [17] and $\text{Ca}_4\text{LaO}(\text{BO}_3)_3$ [18] co-doped with Dy^{3+} and Eu^{3+} are developed as single-phase phosphors, emitting white light under the excitation of near UV light. ^6Li - and ^{10}B -enriched $\text{Li}_6\text{RE}(\text{BO}_3)_3$ ($\text{RE} = \text{Gd, Lu, Y}$) crystals [19-20] were shown to be promising neutron scintillators because of their high yields for thermal neutron irradiation. Recently, rare-earth borates containing alkali elements have received increasing attractions for their diverse magnetic behaviors such as $\text{K}_3\text{Li}_3\text{Gd}_7(\text{BO}_3)_9$ [21] for cryogenic magnetic cooling, $\text{LiCaTb}_5(\text{BO}_3)_6$ [22] for Faraday rotation in the visible range, and $\text{ABaRE}(\text{BO}_3)_2$ ($\text{A} = \text{K, Rb}$, $\text{RE} = \text{Gd - Yb}$) [23-24] for the triangular rare-earth lattices. In search of novel phases in quasi-ternary alkali-rare-earth borate systems ($\text{A}_2\text{O}-\text{RE}_2\text{O}_3-\text{B}_2\text{O}_3$) compounds like $\text{Li}_3\text{RE}(\text{BO}_3)_2$ [25], $\text{LiRE}_6\text{O}_5(\text{BO}_3)_3$ [26], $\text{Na}_3\text{RE}_2(\text{BO}_3)_3$ [27], $\text{Na}_3\text{RE}_9\text{O}_3(\text{BO}_3)_8$ [11], $\text{K}_2\text{RE}_2\text{O}(\text{BO}_3)_2$ [28] and $\text{K}_3\text{RE}(\text{BO}_3)_2$ [29] were reported. In the present study, we

particularly focus on mixed alkali rare-earth borates $\text{KLi}_2\text{RE}(\text{BO}_3)_2$. To the best of our knowledge, six structure types of rare-earth borates were reported in quasi-quaternary $\text{A}_2\text{O}-\text{Li}_2\text{O}-\text{RE}_2\text{O}_3-\text{B}_2\text{O}_3$ system: $\text{CsLi}_2\text{Gd}_4(\text{BO}_3)_5$ [30], $\text{K}_6\text{Li}_3\text{Sc}_2\text{B}_{15}\text{O}_{30}$ [31], $\text{A}_2\text{LiNd}(\text{BO}_3)_2$ ($\text{A} = \text{Rb}$, Cs) [32], $\text{K}_9\text{Li}_3\text{Nd}_3(\text{BO}_3)_7$ [32] and $\text{K}_3\text{Li}_3\text{Gd}_7(\text{BO}_3)_9$ [21]. The crystal structure of each compound of the series $\text{KLi}_2\text{RE}(\text{BO}_3)_2$ ($\text{RE} = \text{Dy}$, Ho , Er , Tm , Yb and Y) determined by single crystal X-ray diffraction data analysis is found to be a new structure type, which are distinctly different from other known compounds mentioned above. This study includes the syntheses and thermal stability of the $\text{KLi}_2\text{RE}(\text{BO}_3)_2$ compounds along with their detailed structural and spectroscopic features.

2. Experimental

2.1. Synthesis

Polycrystalline

Polycrystalline samples of $\text{KLi}_2\text{RE}(\text{BO}_3)_2$ ($\text{RE} = \text{Dy}$, Ho , Er , Tm , Yb and Y) were synthesized using conventional solid-state reaction methods. K_2CO_3 , Li_2CO_3 , RE_2O_3 ($\text{RE} = \text{Dy}$, Ho , Er , Tm , Yb , Y) and H_3BO_3 (analytical grade) were used as the starting materials. Stoichiometric mixtures of the educts were mixed, intensively ground in an agate mortar and loaded into alumina crucibles. The mixtures were preheated at 773 K for 24 h to decompose the carbonates. The products were again thoroughly ground, followed by heating at 898 K. Afterward, the samples were held at this temperature for 72 hours with several intermediate grindings and mixings till the X-ray diffraction patterns did not change. Several micrometre-sized single crystals could be observed in the $\text{KLi}_2\text{Y}(\text{BO}_3)_2$, $\text{KLi}_2\text{Dy}(\text{BO}_3)_2$ and $\text{KLi}_2\text{Ho}(\text{BO}_3)_2$ polycrystalline samples under the microscope.

Table 1: Crystallographic data and crystal structure refinements of $\text{KLi}_2\text{RE}(\text{BO}_3)_2$ (RE = Dy, Ho, Er, Tm, Yb and Y)

Formula	$\text{KLi}_2\text{Dy}(\text{BO}_3)_2$	$\text{KLi}_2\text{Ho}(\text{BO}_3)_2$	$\text{KLi}_2\text{Er}(\text{BO}_3)_2$	$\text{KLi}_2\text{Tm}(\text{BO}_3)_2$	$\text{KLi}_2\text{Yb}(\text{BO}_3)_2$	$\text{KLi}_2\text{Y}(\text{BO}_3)_2$
Weight	333.1	335.53	337.86	339.53	343.64	259.51
Space group	$P2_1/n$	$P2_1/n$	$P2_1/n$	$P2_1/n$	$P2_1/n$	$P2_1/n$
a /pm	672.257(10)	671.112(5)	669.887(5)	668.034(8)	668.262(4)	671.322(6)
b /pm	934.586(15)	931.737(6)	928.866(6)	925.845(1)	922.959(5)	930.571(8)
c /pm	900.894(13)	899.091(6)	897.274(7)	894.919(12)	893.478(6)	898.650(8)
β /°	102.8828(13)	102.8257(6)	102.7513(6)	102.6660(10)	102.5922(5)	102.8351(8)
V / $10^6 \times \text{pm}^3$	551.768(15)	548.174(7)	544.546(7)	540.034(10)	537.822(6)	547.371(9)
Z	4	4	4	4	4	4
Density / g cm^{-3}	4.010(1)	4.066(1)	4.121(1)	4.176(1)	4.244(1)	3.149(1)
Temperature /K	300(2)	300(2)	301(2)	301(2)	300(2)	301(2)
Wavelength /pm	71.0747(6)	71.0747(6)	71.0747(6)	71.0747(6)	71.0747(6)	71.0747(6)
Crystal Size / mm^3	$0.070 \times 0.086 \times 0.105$	$0.033 \times 0.071 \times 0.074$	$0.108 \times 0.122 \times 0.181$	$0.043 \times 0.054 \times 0.065$	$0.079 \times 0.123 \times 0.124$	$0.054 \times 0.061 \times 0.103$
Absorption coefficient / mm^{-1}	14.254	15.150	16.133	17.157	18.120	11.373
$F(000)$ / e^-	596	600	604	608	612	488
θ range /°	3.18 - 43.54	3.19 - 33.21	3.20 - 33.27	3.21 - 33.23	3.21 - 33.30	3.20 - 33.22
Range in hkl	$-11 \leq h \leq 12,$ $-18 \leq k \leq 17,$ $-17 \leq l \leq 15$	$-10 \leq h \leq 10,$ $-14 \leq k \leq 14,$ $-13 \leq l \leq 13$	$-10 \leq h \leq 10,$ $-14 \leq k \leq 14,$ $-13 \leq l \leq 13$	$-10 \leq h \leq 10,$ $-14 \leq k \leq 14,$ $-13 \leq l \leq 13$	$-10 \leq h \leq 10,$ $-14 \leq k \leq 14,$ $-13 \leq l \leq 13$	$-10 \leq h \leq 10,$ $-14 \leq k \leq 14,$ $-13 \leq l \leq 12$
Reflections collected	45894	19650	67326	31050	35921	18713
Data/Restraints/Parameters	4106/0/110	2096/0/110	1676/0/110	2068/0/110	2072/0/110	2101/0/110
Goodness-of-Fit on F^2	1.048	1.053	1.074	1.042	1.054	1.005
$R1$ (all data)	0.0443	0.0299	0.0143	0.0287	0.0125	0.0640
$wR2$ (all data)	0.0348	0.0319	0.0246	0.0310	0.0321	0.0559
CSD-number ^a	1984916	1984917	1984918	1984919	1984920	1984921

^aFurther details can be obtained from Fachinformationszentrum Karlsruhe (Germany) referring to the respective CSD number.

Single crystal

Single crystals of $\text{KLi}_2\text{RE}(\text{BO}_3)_2$ (RE = Er, Tm and Yb) were obtained by high-temperature solution through spontaneous crystallization using the self-flux method. The mixture of samples with a molar ratio of $\text{K}_2\text{CO}_3 : \text{Li}_2\text{CO}_3 : \text{RE}_2\text{O}_3$ (RE = Er, and Yb) : $\text{H}_3\text{BO}_3 = 3 : 3 : 1 : 1 : 8$ were transferred into platinum crucibles and heated to 1123 K with a heating rate of 100 K/h in a muffle furnace and hold at this temperature for 2 hours. Afterward, the melt was cooled down to 773 K at a cooling rate of 3 K/h followed by rapid cooling to room temperature by taking the crucible out of the furnace. Transparent millimetre sized reddish $\text{KLi}_2\text{Er}(\text{BO}_3)_2$ and colourless $\text{KLi}_2\text{Tm}(\text{BO}_3)_2$ and $\text{KLi}_2\text{Yb}(\text{BO}_3)_2$ single crystals were obtained.

2.2. X-ray diffraction

Single crystal

Selected single crystals of $\text{KLi}_2\text{RE}(\text{BO}_3)_2$ were mounted on a glass fibre with epoxy for structure determination. At ambient condition the single crystal X-ray diffraction were performed using a D8 Venture diffractometer (Bruker AXS GmbH, Karlsruhe, Germany) devised with molybdenum radiation and a pyrolytic graphite monochromator, providing bichromatic $\text{MoK}\alpha_{1,2}$ ($\lambda_1 = 70.93171(4)$ pm, $\lambda_2 = 71.3607(12)$ pm treated as average $\lambda = 71.073(1)$ pm). Numerical absorption corrections were carried out using the SCALE program in the APEX III software (Bruker AXS GmbH, Karlsruhe, Germany). The initial structures were solved by ShelxT [33] using the intrinsic phasing method, suggesting $P2_1/n$ space group. It is worth mentioning that space group $P2_1/n$ ($P2_1/c$, unique axis b , cell choice 2) [34] was chosen as the β -angle is closer to 90° compared to those values using other possible unique axis or cell choice settings for space group number 14. All associated coordinates were

refined using full matrix least-squares techniques with anisotropic displacement parameters and the final least-squares refinement on F_o^2 with $F_o^2 \geq 2\sigma(F_o^2)$ data in the Shelxle packages [35]. The crystal structures of $\text{KLi}_2\text{RE}(\text{BO}_3)_2$ were further checked for missing symmetry elements using PLATON [36] and additional symmetries could not be found. Relevant crystallographic data, atomic coordinates, equivalent isotropic displacement parameters, bond valence sum (BVS) and select interatomic distances are listed in **Table 1**, **Table 2**, **Table 3** and **Table S1** (Supplementary Information), respectively.

Table 2: Atomic coordinates, equivalent isotropic displacement parameters ($U_{\text{eq}}/10^4 \times \text{pm}^2$), and bond valence sum (BVS /v.u.) of $\text{KLi}_2\text{Ho}(\text{BO}_3)_2$. U_{eq} is defined as one-third of the trace of the orthogonalized U_{ij} tensor components. All atoms are in the $4e$ Wyckoff site.

Atoms	<i>x</i>	<i>y</i>	<i>z</i>	U_{eq}	BVS
Ho	0.53732(2)	0.88288(2)	0.34214(2)	0.00490(4)	3.18(1)
K	0.57442(9)	0.37574(6)	0.41377(7)	0.01071(11)	1.49(1)
B1	0.6489(5)	0.8589(3)	0.7626(4)	0.0071(5)	2.87(2)
B2	0.6314(4)	0.6300(3)	0.2151(3)	0.0065(5)	2.93(2)
Li1	0.4176(8)	0.8833(6)	0.9949(6)	0.0132(10)	1.14(1)
Li2	0.4179(8)	0.3848(6)	0.0505(6)	0.0145(10)	0.94(1)
O1	0.7233(3)	0.72717(19)	0.8172(2)	0.0075(4)	-2.06(1)
O2	0.6006(3)	0.9643(2)	0.8586(2)	0.0083(4)	-2.04(1)
O3	0.6021(3)	0.8943(2)	0.6075(2)	0.0099(4)	-1.95(1)
O4	0.6579(3)	0.4983(2)	0.1496(2)	0.0078(4)	-2.06(1)
O5	0.5740(3)	0.7480(2)	0.1239(2)	0.0090(4)	-2.14(1)
O6	0.6593(3)	0.6505(2)	0.3700(2)	0.0090(4)	-2.20(1)

Powder

X-ray powder diffraction (XRPD) pattern were recorded on a Panalytical X'Pert powder diffractometer (Panalytical, Almelo, The Netherlands) using Bragg-Brentano geometry with

CuK $\alpha_{1,2}$ ($\lambda_{k\alpha 1} = 154.05929(5)$ pm, $\lambda_{k\alpha 2} = 154.4414(2)$ pm) radiation and an X'Cellerator detector system. Each measurement was carried out at ambient conditions in a range between 5° and 130° 2θ with a step size of 0.0167° and a data collection time of 30 s/step. The fundamental parameter approach, where the fundamental parameters were fitted against a LaB₆ standard material, was applied for the Rietveld refinement using “DiffracPlus Topas 6” software (Bruker AXS GmbH, Karlsruhe, Germany). The starting lattice parameters and atomic coordinates were taken from the results of the single crystal structure determination.

2.3. UV/Vis diffuse reflectance spectroscopy

UV/Vis diffuse reflectance spectra were recorded at room temperature on a Shimadzu UV-2600 (Shimadzu, Kyoto, Japan) spectrophotometer equipped with an ISR-2600 plus two-detector integrating sphere (Pike Technologies, USA). Data were collected in the range between 200 nm and 850 nm with a step size of 1 nm. Powder BaSO₄ sample was used as reference standard for baseline correction.

The diffuse reflectance spectra of KLi₂RE(BO₃)₂ were converted to $F(R)$ spectra using the following Kubelka-Munk expression [37]:

$$F(R) = \frac{(1 - R)^2}{2R} \quad (1)$$

where R refers to reflectance. In the Tauc's method [38], the Kubelka-Munk function is commonly used to estimate the bandgap energy by using the intercept of the abscissa from the following relations:

$$F(R)(h\nu) = B(h\nu - E_g)^n \quad (2)$$

Where h is the Planck's constant, ν the frequency of light, E_g the bandgap [eV] and n -the type (direct or indirect) of optical transition. That is, for $n = 2$ and $\frac{1}{2}$ refers to direct and indirect transition, respectively. The derivation of absorption spectrum fitting

(DASF) method [39] was proposed for the optical absorption spectra of thin films to calculate the bandgap energies. DASF offers peak-shape spectra, leading to a single bandgap value without any presumption of the nature of the transition. Recently, Kirsch et al. [40-41] proposed that the DASF can also be expressed as follows for powder samples:

$$\frac{d\ln F(R)}{dh\nu} = \frac{n}{h\nu - E_g} \quad (3)$$

Comparing the bandgap obtained from the DASF method with that of Tauc's direct or indirect transition, both the type and the width of the band gap can be better explained.

2.4. Infrared and Raman spectroscopy

Fourier transform infrared (FTIR) spectra were recorded on a Bruker IFS66v/S spectrometer (Bruker Optik GmbH, Ettlingen, Germany). As a standard KBr procedure, 2 mg borate sample was mixed with 200 mg dried KBr followed by exerting hydrostatic pressure of about 100 kN to make of pellet of 12 mm in diameter. Using the same procedure, the reference pellet comprises of 200 mg dried KBr only. FTIR spectra were collected in the mid-infrared range between 370 and 4000 cm^{-1} . A total of 128 acquisitions were counted, providing a spectral resolution of about 1.0 cm^{-1} .

Since rare-earth cations are susceptible to photon induced 4f-electronic transitions, Raman spectra were measured at ambient condition using available three lasers of 532 nm, 633 nm and 785 nm. In this regard, the UV/Vis spectra (see below) helped to choose the laser wavelength to avoid possible fluorescence emissions from the 4f-4f transitions. That is, laser wavelength of 532 nm for $\text{KLi}_2\text{Dy}(\text{BO}_3)_2$, $\text{KLi}_2\text{Tm}(\text{BO}_3)_2$ and $\text{KLi}_2\text{Y}(\text{BO}_3)_2$, 633 nm for $\text{KLi}_2\text{Yb}(\text{BO}_3)_2$ and 785 nm for $\text{KLi}_2\text{Ho}(\text{BO}_3)_2$ and $\text{KLi}_2\text{Er}(\text{BO}_3)_2$ were chosen. Raman spectra were collected from 85 cm^{-1} to 1700 cm^{-1} . The 50x objective, the moving grating of 1800 grooves/mm and a thermoelectrically cooled CCD detector (Synapse, 1024×256 pixels) provides the spectral resolution of

approximately 1.1 cm^{-1} . The spectral positions were calibrated against the Raman mode of silicon before and after the sample measurements.

2.5. Scanning electron microscope investigations

Energy dispersive X-ray spectroscopy (EDX) data were collected on a JSM-6510 (JEOL Ltd, Tokyo, Japan) scanning electron microscope (SEM) equipped with an XFlash Detector 410-M. Prior to the EDX measurement, the gold coating process was performed via argon plasma discharge to improve the samples' conductivity. The atomic ratio of K : RE for each $\text{KLi}_2\text{RE}(\text{BO}_3)_2$ analogue was analysed using measurements of three different single crystal each with an accelerating voltage of 20 kV. The individual result of the EDX measurements are displayed in **Table S2**.

2.6. Thermal analysis

Simultaneous thermogravimetric analysis and differential scanning calorimetry (TGA/DSC) measurements were performed on a simultaneous TGA/DSC 3+ STAR e system (Mettler Toledo, Schwerzenbach, Switzerland). Approx. 10 mg of each polycrystalline samples of $\text{KLi}_2\text{RE}(\text{BO}_3)_2$ was measured with a heating rate of 10 K/min and a continuous N_2 flow of 20 mL/min from 300 K to 1073 K. Afterward, the data were normalized to the respective mass. An empty corundum crucible served as reference, and a drift correction was applied based on the empty crucible data.

2.7. Magnetic susceptibility

Temperature-dependent DC magnetic susceptibility measurements were carried out with a Magnetic Property Measurement System MPMS-XL7 (Quantum Design, San Diego, USA) using the field-cooling process in the range from 1.9 K to 300 K at a magnetic field of 0.01 T. Polycrystalline $\text{KLi}_2\text{Dy}(\text{BO}_3)_2$ (72.0 mg), $\text{KLi}_2\text{Ho}(\text{BO}_3)_2$ (41.1

mg), $\text{KLi}_2\text{Ho}(\text{BO}_3)_2$ (56.2 mg), $\text{KLi}_2\text{Tm}(\text{BO}_3)_2$ (55.6 mg) and $\text{KLi}_2\text{Yb}(\text{BO}_3)_2$ (46.0 mg) samples were sealed in a gel capsule and attached to a nonmagnetic sample holder.

2.8. Theoretical calculations

To avoid the strongly correlated behavior of the f-elements, DFT calculations were performed for electronic and vibrational properties of the compound $\text{KLi}_2\text{Y}(\text{BO}_3)_2$. The crystallographic data of $\text{KLi}_2\text{Y}(\text{BO}_3)_2$ determined by single-crystal X-ray diffraction were used for the DFT calculations. The electronic band structure was calculated using the Quantum Espresso Burai1.3 software [42], which employs pseudopotentials to describe electron–ion interactions and represents electronic wave functions using a plane-wave basis set. The generalized gradient approximation (GGA) with the Perdew–Burke–Ernzerhof (PBE) functional was employed for the exchange–correlation potential [43]. The plane-wave energy cutoff was 676.9 eV using the projector augmented wave (PAW) pseudopotentials. The total energy and the force convergence thresholds were $1.0 \cdot 10^{-6}$ eV/atom and 0.5 eV/nm, respectively. A $5 \times 3 \times 3$ mesh of k-points was set to define the number of integration points in reciprocal space.

The vibrational properties of the representative $\text{KLi}_2\text{Y}(\text{BO}_3)_2$ were also calculated using the plane-wave DFT code CASTEP [44]. The calculations used a plane-wave energy cutoff of 1200 eV and on-the-fly generated norm-conserving pseudo-potentials. The PBE for solids and surfaces (PBEsol) exchange-correlation functional was used [43] and a $3 \times 2 \times 2$ mesh of k -points (three irreducible points) was employed in the sampling of the first Brillouin zone. The structure of $\text{KLi}_2\text{Y}(\text{BO}_3)_2$ was optimized, relaxing all atomic coordinates, but fixing the lattice parameters to the experimental values measured at 300 K. The convergence criteria for the total energy and the largest residual force were $1.0 \cdot 10^{-8}$ eV/atom and 0.01 eV/nm, respectively. Variational density functional perturbation theory [45] was used for the subsequent calculations of the phonon density of states (PDOS) and of the IR- and Raman-active modes (including intensities). These calculations used a $3 \times 2 \times 2$ mesh of q -points in reciprocal space. The total PDOS and the partial contribution of each non-equivalent atom were plotted using a smearing of 0.1 THz.

3. Results and discussion

3.1. Crystal structure

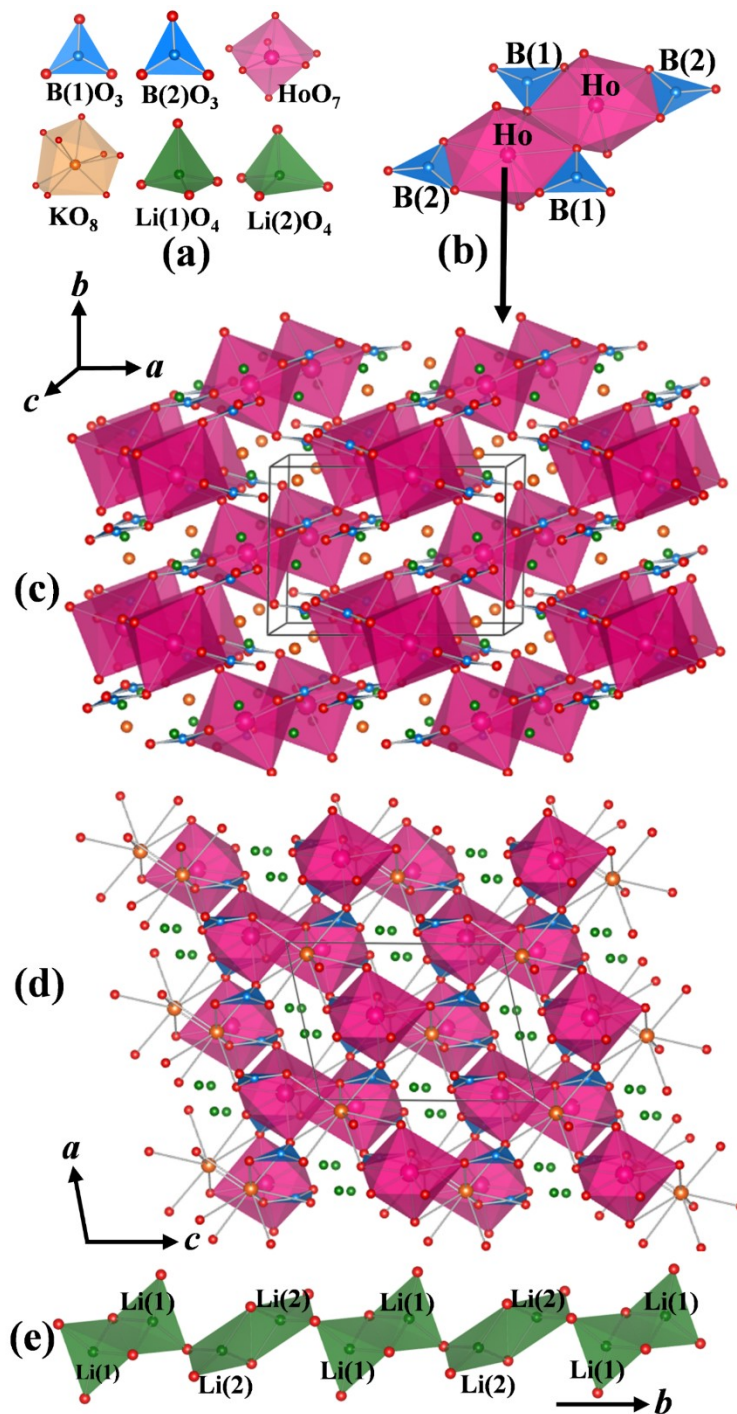


Figure 1: Crystal structure of $\text{KLi}_2\text{Ho}(\text{BO}_3)_2$, showing polyhedral structural units (a) $[\text{Ho}_2(\text{BO}_3)_4\text{O}_4]^{14-}$ anionic clusters (b), 3D structure of $\text{KLi}_2\text{Ho}(\text{BO}_3)_2$ (c), view of the structure of $\text{KLi}_2\text{Ho}(\text{BO}_3)_2$ along the b -axis (d), and the infinite $[\text{LiO}_1\text{O}_{3/2}]^\infty$ in the b -direction (e).

Both the single crystal diffraction data analysis and PXRD data Rietveld refinement results show that each member of the series $\text{KLi}_2\text{RE}(\text{BO}_3)_2$ ($\text{RE} = \text{Y}, \text{Dy}, \text{Ho}, \text{Er}, \text{Tm}, \text{Yb}$) crystallizes isotypically in the space group $P2_1/n$. As a representative member of the series we choose $\text{KLi}_2\text{Ho}(\text{BO}_3)_2$ to describe the detailed crystal structural features. The structure contains twelve crystallographic independent atoms in the asymmetric unit cell, located all at the $4e$ Wyckoff position (**Tab. 2**). HoO_7 pentagonal bipyramid, KO_8 dodecahedra, LiO_4 tetrahedra and trigonal planar BO_3 groups can be regarded as building units as shown in **Figure 1**. The mean B-O bond length of 138.8(4) pm and 138.0(3) pm, as given in **Table 3**, have been obtained from the isolated $\text{B}(1)\text{O}_3$ and $\text{B}(2)\text{O}_3$ groups, respectively. Both these values lie close to those of other alkali-metal rare-earth borate-containing isolated BO_3 groups, for instance, 137.4 pm in $\text{Li}_3\text{K}_3\text{Y}_7(\text{BO}_3)_9$ [46] and 137.6 pm in $\text{K}_9\text{Li}_3\text{Nd}_3(\text{BO}_3)_7$ [32]. The Ho^{3+} cations are found at the centroid of a slightly distorted pentagonal bipyramid, where the Ho-O bond distances vary from 229.8(2) pm to 238.8(2) pm with an average value of 233.1(2) pm; the values well fit for seven-coordinated Ho^{3+} cations [47-48]. Sharing the equatorial oxygen atoms two HoO_7 bipyramids are edge-shared and connected with four BO_3 groups, forming the $[\text{Ho}_2(\text{BO}_3)_4\text{O}_4]^{14-}$ anionic cluster which is regulated by the inversion centre (**Fig. 1b**). Each $[\text{Ho}_2(\text{BO}_3)_4\text{O}_4]^{14-}$ anionic cluster is further bridged by eight neighbouring counterparts via corner-sharing four apical oxygen atoms (**Fig. 1c and 1d**). Hence, the 3D network of $\text{KLi}_2\text{Ho}(\text{BO}_3)_2$ is composed of $[\text{Ho}_2(\text{BO}_3)_4\text{O}_4]^{14-}$ anionic cluster and interstitial K^+ and Li^+ cations. In the distorted KO_8 dodecahedron the interatomic distances of K-O range from 267.1(2) pm to 285.5(2) pm with a mean value of 276.3(2) pm, which is slightly shorter than 289.0 pm for the ideal K-O bond length. Bond valence sum (BVS) calculation performed in the *BondSTR* program within the

scope of *FullProf* suite [49], gave a positive charge of 1.49(1) v.u. for K^+ , which is at least surprisingly high.

Table 3. Interatomic bond distances/pm and the arithmetic mean in $KLi_2Ho(BO_3)_2$.

Bond	Bond dist.	Bond	Bond dist.
B1O ₃		B2O ₃	
B1-O1	137.4(3)	B2-O5	137.4(3)
B1-O2	139.2(4)	B2-O6	137.7(4)
B1-O3	139.9(4)	B2-O4	139.0(3)
Mean	138.8(4)		138.0(3)
HoO ₇		KO ₈	
Ho-O4	229.8(2)	K-O6	267.1(2)
Ho-O6	230.9(2)	K-O1	271.7(2)
Ho-O1	231.0(2)	K-O5	273.0(2)
Ho-O2	232.3(2)	K-O2	276.5(2)
Ho-O3	233.1(2)	K-O6	276.7(2)
Ho-O3	236.2(2)	K-O3	276.9(2)
Ho-O5	238.8(2)	K-O4	280.1(2)
		K-O1	285.5(2)
Mean	233.1(2)		276.3(2)
Li1O ₄		Li2O ₄	
Li1-O5	187.0(6)	Li2-O4	196.7(6)
Li1-O6	187.1(5)	Li2-O1	197.5(6)
Li1-O2	195.9(6)	Li2-O5	200.8(6)
Li1-O2	206.1(6)	Li2-O4	206.8(6)
Mean	194.0(6)		200.5(6)

The KO₈ dodecahedra can be regarded to serve as stitches to reinforce connection among $[Ho_2(BO_3)_4O_4]^{14-}$ anionic clusters in the *ac*-plane. Both $Li(1)^+$ and $Li(2)^+$ are tetrahedrally coordinated with oxygen atoms. The Li(1)-O distances range from 187.0(6) pm to 206.1(6) pm with a mean value of 194.0(6) pm, while 196.7(6) pm to

206.1(6) pm with a mean value of 200.5(6) pm are found for the Li(2)-O distances. The BVS of lithium was found to be 1.14(1), and 0.94(1) v.u., respectively, for the Li(1)O₄ and Li(2)O₄ tetrahedra which are interlinked by both corner- and edge-sharing, building an infinite [LiO₁O_{3/2}][∞] chain parallel to the **b**-direction (**Fig. 1e**). The shortest observed Li-Li interatomic distance (Li(1)-Li(1)) in the [LiO₁O_{3/2}][∞] chain is 243(1) pm. Such a Li-Li distance is smaller than those in some well-known lithium ion solid-state electrolytes, for instance, 276.4(1) pm in anti-perovskite Li₃OCl [50], 252.4(1) pm in garnet-like Li₇La₃Zr₂O₁₂ [51], and 302.2(2) pm in NASICON-type Li_{1.4}Ti_{1.6}Al_{0.6}(PO₄)₃ [52]. The bond valence sums of the framework cations Ho, B(1), B(2) show 3.08(1), 2.87(2), and 2.93(2) v.u., respectively. The calculated structural BVS of the cations correspond well to their theoretical oxidation state except that the K⁺ cation is highly over-bonded. Although the K⁺ cation is shown with a large isotropic atomic displacement parameter, the substitutional or positional disorder at K⁺ cation can be thoroughly ruled out by the structure refinement and no significant electronic holes and peaks could be observed at the same time. The EDX (**Tab. S2**) shows the K : RE ratio close to 1 : 1 is in good agreement with the values obtained from the structure determination. Additional to the over-bonding of the K cations surprisingly short K-K distances of 307.25(9) pm are found for KLi₂Ho(BO₃)₂. While searching for comparable cases we found 9051 crystal structure reports in the ICSD data base (FIZ Karlsruhe, Germany) containing K and O. Out of these structures 37 are reported with K-K distances of less than 310 pm. Out of these 6 structures, KCrO₂ (304.3(1) pm, 1.56(1) v.u.) [53], KAlO₂ (304(17) pm, 1.4(2) v.u.) [54], KAuO₂ (300.5(1) pm, 1.44(1) v.u.) [55], KMo₄O₈ (296.4(9) pm, 1.47(2) v.u.) [56] K₂Mg₂Si₂O₇ (293.0(1) pm, 1.52(1) v.u.) [57] and KAlSi₃O₈ (272.3(1) pm, 1.58(6) v.u.) [58] provide at least one comparable BVS as calculated for the reported structures here. This did not really explain why the structures

provide short K-K distances together with higher BVS, but shows that this phenomenon is not unique, although rare. Further detailed investigations should in future be carried out on these structures to probably find a common explanation.

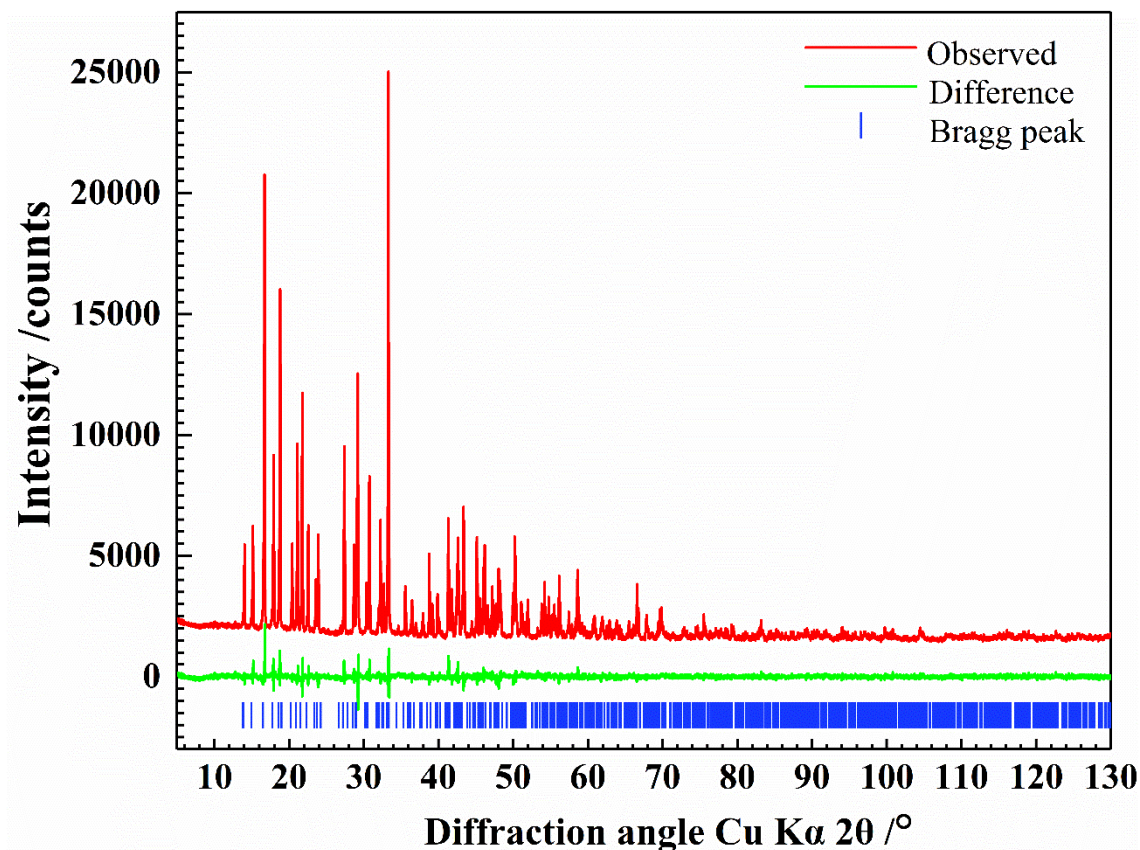


Figure 2: X-ray powder data Rietveld plots of $\text{KLi}_2\text{Ho}(\text{BO}_3)_2$.

To cross-check the accuracy of the crystal structures obtained from X-ray single crystal data analysis complementary Rietveld refinements were performed on PXRD data of $\text{KLi}_2\text{RE}(\text{BO}_3)_2$. **Figure 2** depicts a representative Rietveld plot of $\text{KLi}_2\text{Ho}(\text{BO}_3)_2$; the other Rietveld plots ($\text{RE} = \text{Dy}, \text{Er}, \text{Tm}, \text{Yb}$ and Y) are shown in **Figure S1 - S5**. The evolution of the metric parameters obtained from the PXRD data Rietveld refinement are shown in **Figure 3**, which are in excellent agreement with those obtained from the single crystal structure determination (**Tab. 1**). The lanthanide contraction effect could be observed in the series of $\text{KLi}_2\text{RE}(\text{BO}_3)_2$. That is, the a -, b - and c -lattice parameters

as well as the unit cell volumes decrease upon increasing the atomic numbers with smaller (decreasing) ionic radii. As a geometric consequence, the respective β -angle also contracts.

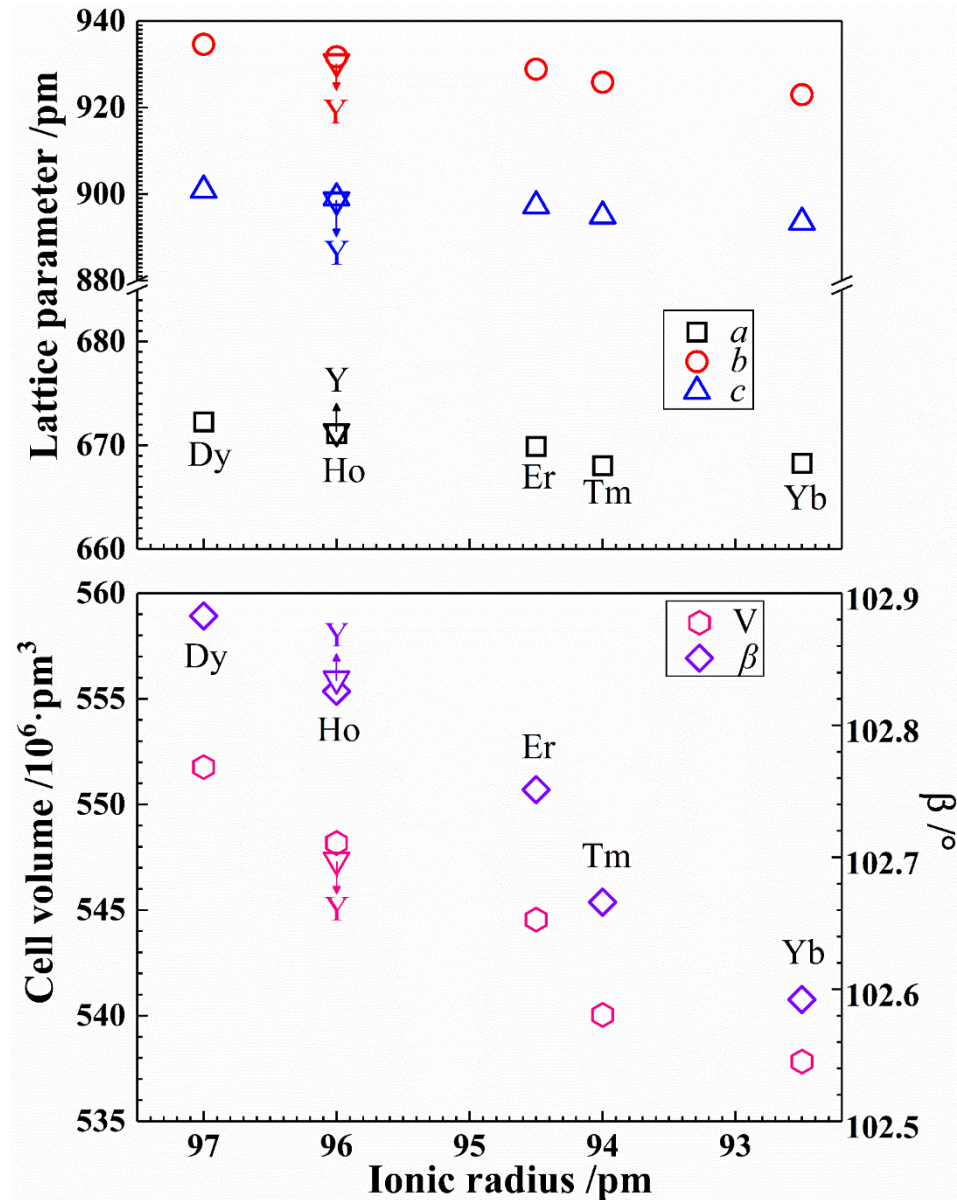


Figure 3: Evolution of the metric parameters of $\text{KLi}_2\text{RE}(\text{BO}_3)_2$ (RE= Dy-Yb, and Y) with respect to the ionic radii of the rare-earth cation.

Of notes, alike reported alkali rare-earth borates such as $\text{Li}_3\text{Sc}(\text{BO}_3)_2$ [59], $\text{Li}_3\text{Gd}(\text{BO}_3)_2$ [25], $\text{Na}_3\text{Gd}(\text{BO}_3)_2$ [60], $\text{K}_3\text{Sm}(\text{BO}_3)_2$ [29], $\text{K}_3\text{Y}(\text{BO}_3)_2$ [29], $\text{Rb}_2\text{LiNd}(\text{BO}_3)_2$ [32] and $\text{Cs}_2\text{LiNd}(\text{BO}_3)_2$ [32] the here reported $\text{KLi}_2\text{RE}(\text{BO}_3)_2$ phases also possess a “312”

stoichiometric formulae where 3, 1, and 2 stands for the number of alkali elements, rare-earth elements and orthoborate groups, respectively. **Table S3** presents a comparative feature between $\text{KLi}_2\text{RE}(\text{BO}_3)_2$ and other “312” type rare-earth borates with respect to space group, unit cell dimension, sum of alkali-metal ionic radii, cationic coordination, and structural construction. To provide a more straightforward comparison, we transformed the space group settings of $\text{Li}_3\text{Gd}(\text{BO}_3)_2$ and $\text{Na}_3\text{Gd}(\text{BO}_3)_2$ from $P2_1/c$ into $P2_1/n$ taking a $[1\ 0\ 1; 0\ 1\ 0; -1\ 0\ 0]$ transformation matrix using the *Jana2006* software [61]. The comparative view clearly reveals that $\text{KLi}_2\text{RE}(\text{BO}_3)_2$ comprises of a novel structural type although it crystallizes in the same $P2_1/n$ space group as $\text{Li}_3\text{Sc}(\text{BO}_3)_2$, $\text{Li}_3\text{Gd}(\text{BO}_3)_2$ and $\text{Na}_3\text{Gd}(\text{BO}_3)_2$. The phases having average cationic radii of the alkali-metal smaller than 313 pm crystallizes monoclinically, while a larger value (> 313 pm) lead to orthorhombic phases (**Tab. S3**).

3.2. TGA/DSC investigation

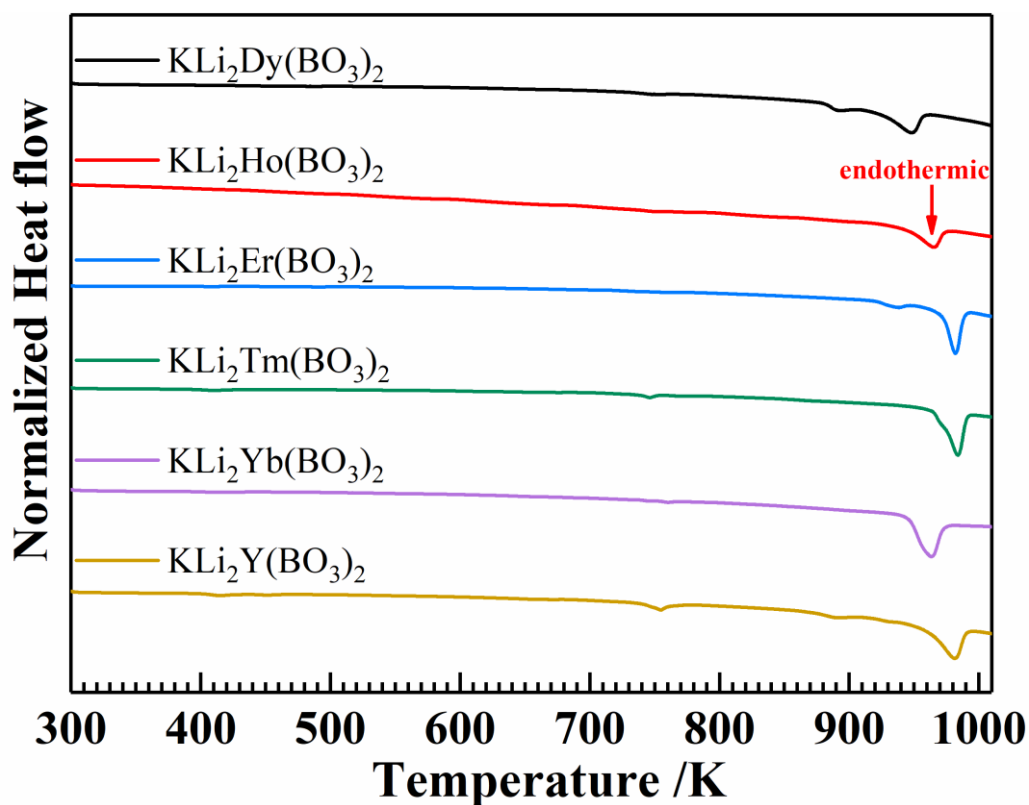


Figure 4: Differential scanning calorimetry (DSC) curves of $\text{KLi}_2\text{RE}(\text{BO}_3)_2$.

All DSC curves contain pronounced endothermic peaks in the range from 945 K to 985 K, however, with no noticeable change of mass during the heating process, as shown in **Figure 4 and Figure S6**. Thermal decomposition starts at approximately 948 (1) K in $\text{KLi}_2\text{Dy}(\text{BO}_3)_2$ and at around 963(1) K in $\text{KLi}_2\text{Yb}(\text{BO}_3)_2$ and $\text{KLi}_2\text{Ho}(\text{BO}_3)_2$, whereas $\text{KLi}_2\text{Er}(\text{BO}_3)_2$, $\text{KLi}_2\text{Tm}(\text{BO}_3)_2$ and $\text{KLi}_2\text{Y}(\text{BO}_3)_2$ decompose unanimously at 982(1) K, indicating that the Er-, Tm-, Y-containing compounds are slightly more stable than Dy-, Ho-, and Yb-containing analogues. X-ray diffraction patterns of the residuals after TGA/DSC (**Figure. S7**) reveal that the final residuals contain $\text{Li}_6\text{Ho}(\text{BO}_3)_3$ and some other unindexed compounds. Thermal analyses followed by X-ray diffraction suggests an incongruent nature of $\text{KLi}_2\text{Ho}(\text{BO}_3)_2$, indicating that a flux method would be necessary for the growth of bulk crystals.

3.3. UV/Vis spectra

Beside the fundamental absorption edge, the UV/Vis spectra are dominated by characteristic electron transitions. According to the energy diagrams proposed by Dieke and Carnall [62, 63], the intra- (f–f) and inter-(f–d) orbital transitions of the RE^{3+} cations exhibit characteristic absorption peaks between 200 nm and 850 nm, shown in **Figure 5 and Figure S7 - S12**. $\text{KLi}_2\text{Dy}(\text{BO}_3)_2$ shows sharp absorption bands at 209(1) and 809(1) nm, which correspond to $4f^9 \rightarrow 4f^85d^1$ and ${}^6\text{H}_{15/2} \rightarrow {}^6\text{F}_{5/2}$ 1094, respectively. $\text{KLi}_2\text{Ho}(\text{BO}_3)_2$ exhibits strong absorption bands at 361(1), 420(1), 448(1), 539(1) and 644(1) nm. $\text{KLi}_2\text{Er}(\text{BO}_3)_2$ also displays absorption bands at 255(1) 388(1), 489(1), 522(1), 652(1) and 800(1) nm. The absorption spectra of $\text{KLi}_2\text{Tm}(\text{BO}_3)_2$ emerges strong absorption bands at 262(1), 359(1), 686(1) and 791 nm. $\text{KLi}_2\text{Yb}(\text{BO}_3)_2$ and $\text{KLi}_2\text{Dy}(\text{BO}_3)_2$ do not contain any obvious absorption bands above 400 nm, which correspond well to their colourlessness in daylight. The characteristic electronic

transition of RE^{3+} cations are labelled (**Fig. 5, Fig. S8 – S12**). To determine the type and width of the bandgap, a combination of Tauc and DASF method was used. The combined approach suggests that each member of the $\text{KLi}_2\text{RE}(\text{BO}_3)_2$ series exhibits direct transition with high bandgaps (insulator) of 5.85(1), 5.39(1), 5.37(1), 5.61(1), 5.08(1) and 5.76(1) eV for the Dy-, Ho-, Er-, Tm-, Yb- and Y- containing compound, respectively. These values are comparable to those of the other rare-earth sesquioxides and borates such as Y_2O_3 (5.6 eV) [64] and $\text{Na}_3\text{La}_2(\text{BO}_3)_3$ (5.82 eV) [65].

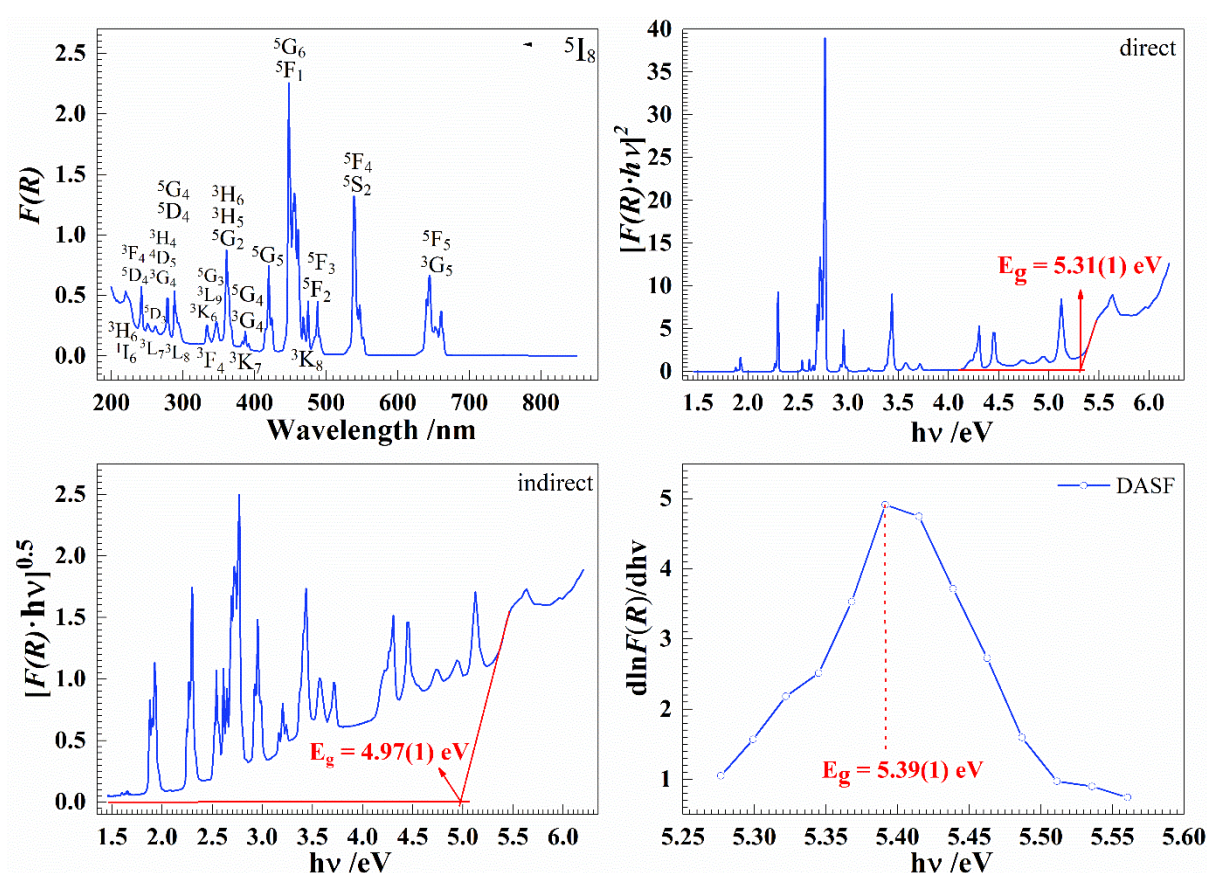


Figure 5: Kubelka-Munk transformed UV/Vis diffuse reflectance spectra of $\text{KLi}_2\text{Ho}(\text{BO}_3)_2$ (top left), Tauc plots for indirect (bottom left) and direct (top right) optical transitions, and DASF plot (bottom right).

3.4. FTIR and Raman

The measured FTIR and Raman spectra along with the fitted compound and component models are shown in **Figure 6**. Since the crystal structure of $\text{KLi}_2\text{RE}(\text{BO}_3)_2$ adopt $P2_1/n$ space group, factor group analysis predicts 156 vibrational modes at the zone center ($39\text{A}_g + 39\text{A}_u + 39\text{B}_g$

+ 39B_u), of which 75 modes (38A_u + 37B_u) are IR active, 78 modes (39A_g+39B_g) are Raman active and three modes are acoustic modes (A_u + 2B_u). The Raman spectra of KLi₂RE(BO₃)₂ are shown in **Figure 6b**. From the UV/Vis spectrum of KLi₂Er(BO₃)₂ (**Fig. S9**) the strong photoluminescence peaks of Er³⁺ hardly leaves any transparent (absorption) region to irradiate the sample with available lasers. Therefore, the Raman spectrum of KLi₂Er(BO₃)₂ under irradiation of the 785 nm laser contains several non-phononic peaks, originating from the photoluminescence of Er³⁺. For instance, the sharp bands centered at around 323 cm⁻¹ (805 nm in wavelength) could be attributed to ⁴I_{9/2} → ⁴I_{15/2} of Er³⁺ cation. The vibrational features of each KLi₂RE(BO₃)₂ sample looks similar with a slight global shift due to different metric parameters. The representative Raman spectrum of KLi₂Ho(BO₃)₂ at ambient condition could be fitted with 56 component peaks (**Fig. 6d**). Several intense bands below 600 cm⁻¹ can be ascribed to the bending and stretching vibrations associated with the heavy cations such as K-O and Ho-O bonds. The bands in the range of 600 - 700 cm⁻¹ and 700 - 800 cm⁻¹ correspond to ν₄ and ν₂ modes, respectively. The bands between 600 cm⁻¹ and 1600 cm⁻¹ owing to vibration of planar BO₃³⁻ groups, can be classified into four types [46, 66]: (I) in-plane bending (ν₄; 600 - 700 cm⁻¹), (II) out-of-plane bending (ν₂; 750 cm⁻¹ - 770 cm⁻¹), (III) B-O symmetric stretching (ν₁; ~ 905 cm⁻¹) and (IV) B-O asymmetric stretching (ν₃; 1000 cm⁻¹ and 1600 cm⁻¹). Clearly, the intense band at about 928 cm⁻¹ can be assigned to ν₁ mode of BO₃ group, which is also a common feature to other rare-earth orthoborates such as Li₂Ca₅Tb(BO₃)₅ [67] and KCaLa(BO₃)₂ [68]. Alike Raman, the IR bands of KLi₂RE(BO₃)₂ (**Fig. 6a**) also show global shifts due to varying size of the RE-cations. The IR spectrum of KLi₂Ho(BO₃)₂ at ambient conditions requires 50 component peaks (**Fig. 6b**). The resolved frequencies between 400 cm⁻¹ and 600 cm⁻¹ can be compared to those of the RE-O vibrational bands [69] in some C-type [70] rare-earth sesquioxides. Clearly, the ν₂ and ν₃ modes are more intense than that of ν₁. Group analysis of an ideal planar BO₃ group possesses D_{3h} symmetry, where ν₂ and ν₃ are IR

active, whereas the ν_1 is IR inactive. Therefore, the clear appearance of ν_1 in the IR spectrum indicates that the BO_3 groups in some $\text{KLi}_2\text{RE}(\text{BO}_3)_2$ crystallites are distorted from an ideal symmetry, comparable to PbMBO_4 ($\text{M} = \text{Cr}, \text{Mn}, \text{Fe}$) phases [71] where the boron distance to the oxygen plain was evaluated by neutron diffraction data analysis.

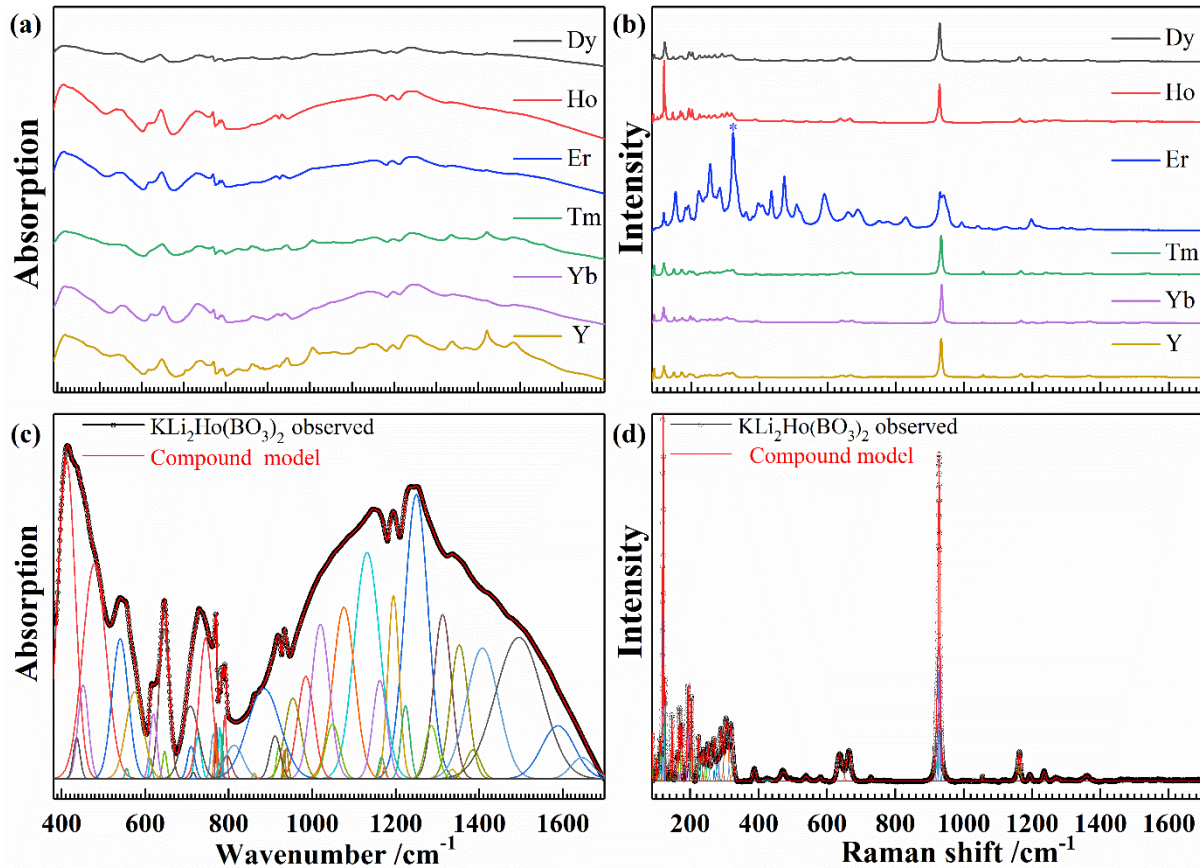


Figure 6: Infrared (left-top), Raman (right-top) spectra of $\text{KLi}_2\text{Ho}(\text{BO}_3)_2$ along with their respective fittings (bottom), showing the fitted component and compound models.

3.5. Magnetic properties

Temperature-dependent DC magnetic susceptibility, $\chi(T)$ of $\text{KLi}_2\text{RE}(\text{BO}_3)_2$ ($\text{RE} = \text{Dy} - \text{Yb}$) and the corresponding inverse susceptibility (χ^{-1}) are displayed in **Figure 7**. Of them, only $\text{KLi}_2\text{Dy}(\text{BO}_3)_2$ shows a clear antiferromagnetic peak-shape behaviour at 5(1) K in the susceptibility curve. Fitting the inverse susceptibility using Curie–Weiss law ($\chi = C/(T - \theta_{\text{cw}})$) where C and θ_{cw} are the Curie constant and the Curie–Weiss temperature, respectively, the negative θ_{cw} values of -3.4(1) K, -5.5(1) K and -32.9(1) K for

$\text{KLi}_2\text{Ho}(\text{BO}_3)_2$, $\text{KLi}_2\text{Er}(\text{BO}_3)_2$ and $\text{KLi}_2\text{Yb}(\text{BO}_3)_2$, respectively, correlate these phases exhibiting antiferromagnetic ordering. Both $\text{KLi}_2\text{Dy}(\text{BO}_3)_2$ and $\text{KLi}_2\text{Tm}(\text{BO}_3)_2$ are of weakly ferromagnetic nature with small positive θ_{cw} values of 6.1(1) K and 0.6(1) K, respectively. In $\text{KLi}_2\text{Yb}(\text{BO}_3)_2$, although no long-range ordering is observed down to 2 K, a pronounced deviation from the Curie-Weiss behaviour starts around 125 K, indicating that crystal field effects (CFEs) of Yb^{3+} cations should be considered [72]. The effective magnetic moments were obtained as 10.47(1) [10.63] μ_{B} , 10.50(1) [10.58] μ_{B} , 9.47(1) [9.59] μ_{B} , 7.16(1) [7.54] μ_{B} and 4.41(1) [4.54] μ_{B} calculated for Dy^{3+} , Ho^{3+} , Er^{3+} , Tm^{3+} and Yb^{3+} cations in $\text{KLi}_2\text{Dy}(\text{BO}_3)_2$, $\text{KLi}_2\text{Ho}(\text{BO}_3)_2$, $\text{KLi}_2\text{Er}(\text{BO}_3)_2$, $\text{KLi}_2\text{Tm}(\text{BO}_3)_2$ and $\text{KLi}_2\text{Yb}(\text{BO}_3)_2$ compounds, respectively, which are in good agreement with the respective theoretical values given in the square brackets.

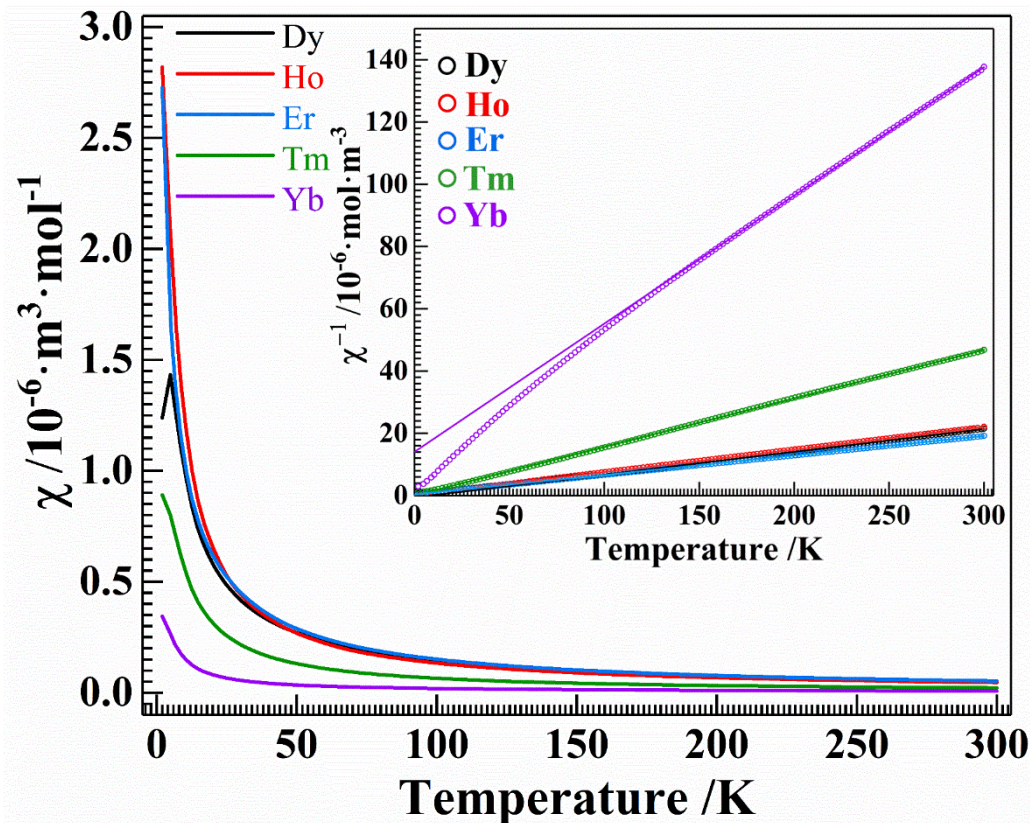


Figure 7: Temperature-dependent field-cooling DC magnetic susceptibilities and respective inverse magnetic susceptibilities (inset) of $\text{KLi}_2\text{RE}(\text{BO}_3)_2$.

3.6 Theoretical calculations

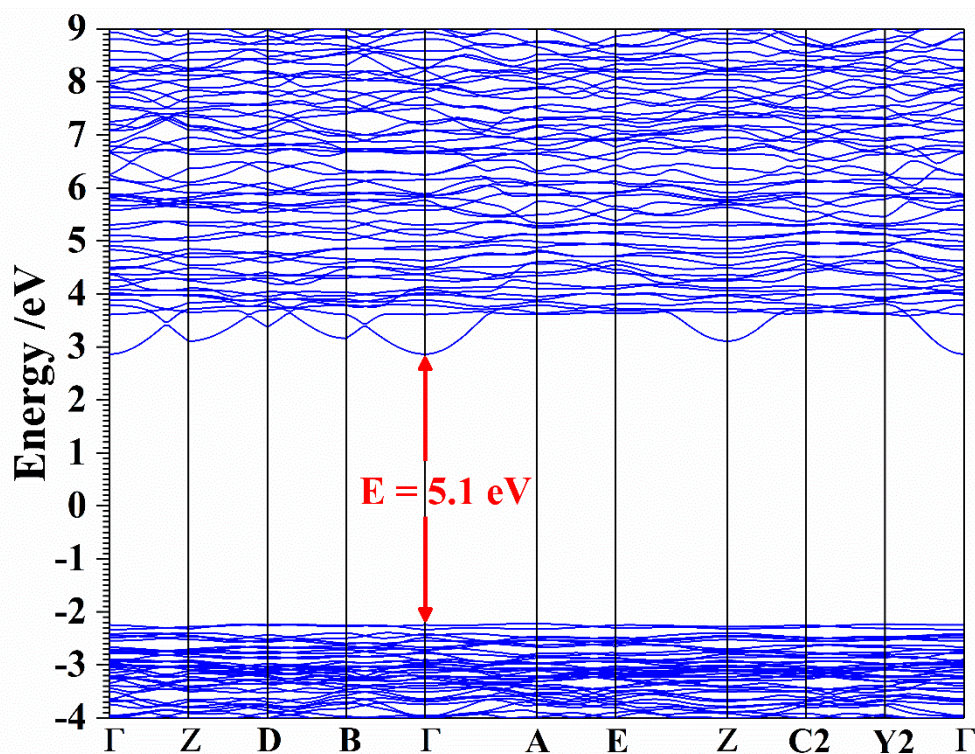


Figure 8: Calculated electronic band structure of $\text{KLi}_2\text{Y}(\text{BO}_3)_2$ in some high symmetry directions.

The electronic band structures and the electronic density of states (EDOS) of $\text{KLi}_2\text{Y}(\text{BO}_3)_2$ was obtained using the generalized gradient approximation (GGA) with the Perdew–Burke–Ernzerhof (PBE) functional, as shown in **Figure 8**. The calculated direct bandgap of 5.1 eV for $\text{KLi}_2\text{Y}(\text{BO}_3)_2$ would well agree to the experimental direct bandgap of 5.05(1) eV (**Fig. S12**). But one has to consider that in most cases the GGA method underestimates the bandgap energy by around 0.5 eV as the unoccupied eigenvalues of the electronic states cannot not be accurately described. Therefore, the direct band gap of 5.7(1) eV obtained using the direct Tauc plot analysis and the DASF method seems to be more reliable. Nevertheless, both the calculated and the experiment value unanimously confirm $\text{KLi}_2\text{Y}(\text{BO}_3)_2$ as an insulator.

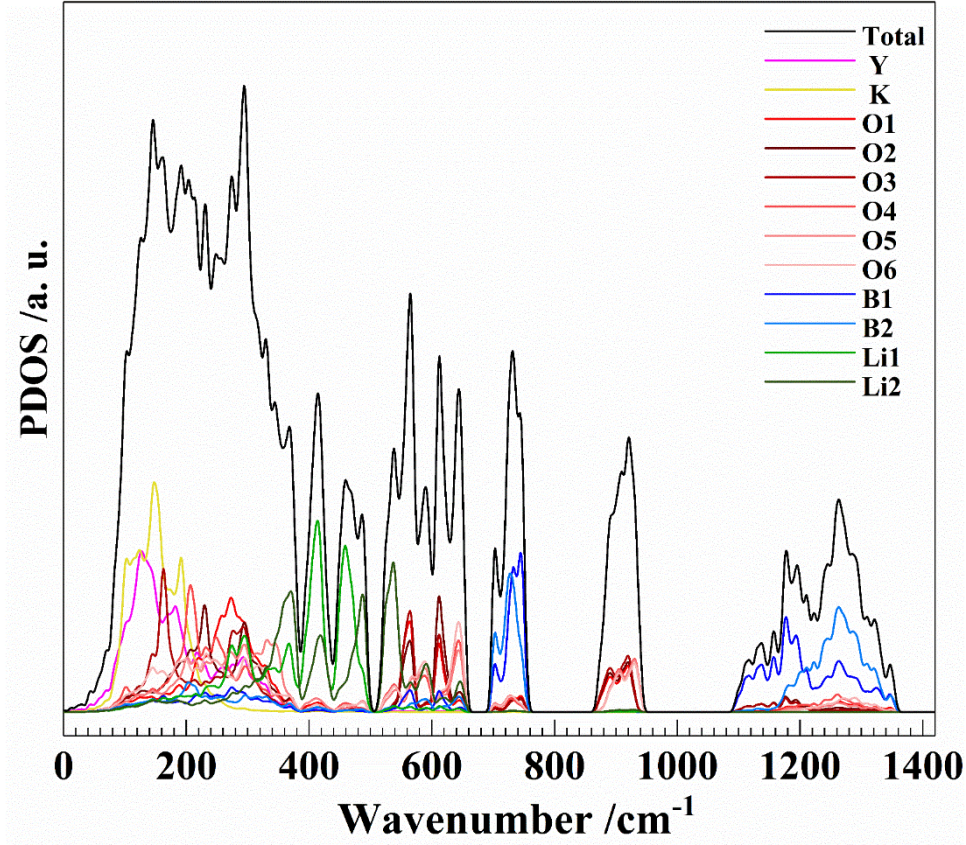


Figure 9: Phonon density of states (PDOS) of $\text{KLi}_2\text{Y}(\text{BO}_3)_2$ along with the constituent atoms.

The phonon density of states (PDOS) of $\text{KLi}_2\text{Y}(\text{BO}_3)_2$ along with the respective atomic contributions are plotted in **Figure 9**. The heavy atoms (Y and K) and the light boron dominate the low (200 cm^{-1}) and high ($> 600 \text{ cm}^{-1}$) frequency regions of the PDOS, respectively. Since for each vibrational feature an oxygen atom is a common neighbor, contributions of oxygen atoms are present spreading the whole PDOS. Of particular notes, although lithium is a light atom, its spectral feature is seen below $\sim 500 \text{ cm}^{-1}$, which can be associate with rather longer Li-O interatomic distances (**Tab. 3**). The PDOS can be described using two continua: the low-frequency region ($0 - 760 \text{ cm}^{-1}$) is composed of two discrete optical modes and the high-frequency region spreads between 1080 and 1360 cm^{-1} . The isolated sharp band feature centered at 920 cm^{-1} is exclusively contributed by oxygen, that is, the symmetric stretching of

B(1)O₃ and B(2)O₃ groups. The high-frequency spectral region ($> 1080\text{ cm}^{-1}$) is also mainly due to the rigid BO₃ groups, where B(1) is coordinated with O1, O2 and O3, and B(2) with O4, O5 and O6 atoms. **Figure S13** shows a comparative view between the PDOS, Raman and IR spectra, where the calculated Raman spectrum shows an excellent agreement with that of the experimental one, especially when taking the temperature difference from 0 K for the calculations and 298 K for the measurement into account.

4. Conclusion

Complementary results from single crystal and powder X-ray diffraction revealed that KLi₂RE(BO₃)₂ (RE = Dy, Ho, Er, Tm, Yb and Y) belong to a novel structure type of rare-earth borates, where the void of the anionic cluster [RE₂(BO₃)₄O₄]¹⁴⁻ is filled with interstitial K⁺ and Li⁺ cations. From our experimental trials it seems that this new structure type is somehow governed by the selective size of the RE- and alkali-cations. For instance, trials using RE-cation with either larger (Eu³⁺, Gd³⁺ and Tb³⁺) or smaller (Lu³⁺, Sc³⁺ and In³⁺) radii could not produce the phase (**Table S4**). Moreover, trials to replace K⁺ with larger alkali cations such as Rb⁺ and Cs⁺ did not work either. Based on these exercises, we can safely conclude that the structure type of KLi₂RE(BO₃)₂ crystallizes by adjusting the suitable cationic sizes. Due to the incongruent nature of KLi₂RE(BO₃)₂ a high-temperature flux method seems to be promising to grow bulk crystals. The characteristic absorption behaviors in the visible range owing to the inner 4fⁿ-configuration of the observed trivalent rare-earth cations, calculation of band gaps from the UV/Vis diffuse reflectance spectra is challenging, which may additionally complicate the Raman data analysis. The effective magnetic moment of the RE-cations obtained from the

DC magnetic susceptibility excludes the possible RE-RE coupling at the investigated temperature range. Since $\text{KLi}_2\text{Y}(\text{BO}_3)_2$ with high lithium and boron content is of high transparency and has no fundamental absorption in the visible range (insulator), investigations such as lithium ion conductivity, photoluminescence and neutron scintillation etc. may be some attractive avenues for future investigations.

Acknowledgement

PYC gratefully thanks the China Scholarship Council for the financial support to carry out this work. The scientific and technical support from the University of Bremen is acknowledged with high appreciation. MF is indebted to Andreas Lüttge and Rolf Arvidson for generous access to the Asgard cluster for CASTEP calculations.

Supporting Information

X-ray crystallographic data of $\text{KLi}_2\text{RE}(\text{BO}_3)_2$ (RE= Dy, Ho, Er, Tm, Yb and Y) in CIF format;
Atomic coordinates, Wyckoff sites, isotropic displacement parameters of $\text{KLi}_2\text{RE}(\text{BO}_3)_2$;
Structural comparison between “312”-type rare-earth borates;
Phases or compounds emerged in the process of the trials of $\text{ALi}_2\text{RE}(\text{BO}_3)_2$ (A = Rb and Cs, RE = Eu, Gd, Tb, Lu, Sc and In)
EDX analysis results, X-ray powder data Rietveld plots, Thermal gravimetric analysis and Kubelka-Munk transformed diffuse reflectance spectra of $\text{KLi}_2\text{RE}(\text{BO}_3)_2$;
Powder XRD patterns of $\text{KLi}_2\text{Ho}(\text{BO}_3)_2$ before and after the TG/DSC;
Calculated PDOS, Raman and IR spectra of $\text{KLi}_2\text{Y}(\text{BO}_3)_2$;

Reference

- [1] Tran, T.; Yu, H.; Rondinelli, J.; Poeppelmeier, K.; Halasyamani, P.; Deep ultraviolet nonlinear optical materials, *Chem. Mater.*, **2016**, 28, 5238-5258.
- [2] Mutailipu, M.; Pan, S.; Emergent Deep-Ultraviolet Nonlinear Optical Candidates, *Angew. Chem. Int. Ed.*, **2020**, 59, 20302-20317
- [3] Becker, P., Borate materials in nonlinear optics, *Adv. Mater.*, **1998**, 10, 979-992.
- [4] Yan, C.; Wang, Y.; Xu, D.; Zhang, L.; Li, K.; Li, Z.; Li, J.; Liu, P.; Yu, H.; Zhang, G.; Wang, L.; Shan, F.; Wang, N.; Wang, B.; Yang, Y.; Lin, X.; Wu, Y.; Yao, J., High-power high-efficiency picosecond 355nm ultraviolet laser based on $\text{La}_2\text{CaB}_{10}\text{O}_{19}$ crystal, *Proc. SPIE, High-Power Lasers and Applications VII*, **2014**, 9266, 92661G-1-5.
- [5] Zhang, J.; Wang, L. Li, Y.; Wang, G.; Zhang, G.; Wu, Y.; 355nm laser generation based on $\text{Na}_3\text{La}_9\text{O}_3[\text{BO}_3]_8$ crystal, *Opt. Express*, **2012**, 20, 16490-16493.
- [6] Rytz, D.; Gross, A.; Vernay, S.; Wesemann, V., $\text{YAl}_3(\text{BO}_3)_4$: a novel NLO crystal for frequency conversion to UV wavelengths, *Solid State Lasers and Amplifiers III*, International Society for Optics and Photonics, **2008**, 699814.
- [7] Yue, Y.; Zhu, Y.; Zhao, Y.; Tu, H.; Hu, Z., Design, Growth and nonlinear optical properties of $\text{GdAl}_3(\text{BO}_3)_4$ in a flux without molybdate, *Cryst. Growth Des.*, **2016**, 16, 347-350.
- [8] Tu, X.; Wang, S.; Xiong, K.; Zheng, Y.; Shi, E., Growth and properties of large aperture YCOB crystal for NLO application, *J. Cryst. Growth*, **2020**, 535, 125527.
- [9] Xie, Z.; Mutailipu, M.; He, G.; Han, G.; Wang, Y.; Yang, Z.; Zhang, M.; Pan, S., A series of rare-earth borates $\text{K}_7\text{MRE}_2\text{B}_{15}\text{O}_{30}$ ($\text{M} = \text{Zn, Cd, Pb}$; $\text{RE} = \text{Sc, Y, Gd, Lu}$) with large second harmonic generation responses, *Chem. Mater.*, **2018**, 30, 2414-2423.
- [10] Mutailipu, M.; Xie, Z.; Su, X.; Zhang, M.; Wang, Y.; Yang, Z.; Janjua, M.; Pan, S., Chemical cosubstitution-oriented design of rare-earth borates as potential ultraviolet nonlinear optical materials, *J. Am. Chem. Soc.*, **2017**, 139, 18397-18405.
- [11] Gravereau, P.; Chaminade, J.; Pechev, S.; Nikolov, V.; Ivanova, D.; Peshev, P., $\text{Na}_3\text{La}_9\text{O}_3(\text{BO}_3)_8$, a new oxyborate in the ternary system $\text{Na}_2\text{O-La}_2\text{O}_3\text{-B}_2\text{O}_3$: preparation and crystal structure, *Solid State Sci*, **2002**, 4, 993-998.
- [12] Chen, C.; Sasaki, T.; Li, R.; Wu, Y.; Lin, Z.; Mori, Y.; Hu, Z.; Wang, J.; Aka, G.; Yoshimura, M., Nonlinear optical borate crystals: Principals and applications, John Wiley & Sons **2012**.
- [13] Tu, C.; Wang, Y.; Al-Khursan, A., Ed.; INTECH Open Access Publisher: Rijeka, Croatia, The Recent Development of Rare Earth-Doped Borate Laser Crystals, *Solid State Laser*; **2012**, 63-118.
- [14] Dekker, P.; Dawes, J.; Piper, J.; Liu, Y.; Wang, J., 1.1 W CW self-frequency-doubled diode-pumped Yb: $\text{YAl}_3(\text{BO}_3)_4$ laser, *Opt. Commun.*, **2001**, 195, 431-436.
- [15] Gorbachenya, K.; Kisel, V.; Yasukevich, A.; Maltsev, V.; Leonyuk, N.; Kuleshov, N., Eye-safe 1.55 μm passively Q-switched Er,Yb:GdAl₃(BO₃)₄ diode-pumped laser, *Opt. Lett.*, **2016**, 41, 918-921.

- [16] Chen, Y.; Huang, Y.; Lin, Z.; Huang, Y., Passively Q-switched Er:Yb:GdMgB₅O₁₀ pulse laser at 1567 nm, *OSA Continuum*, **2019**, 2, 3598-3603.
- [17] Yin, C.; Wang, R.; Jiang, P.; Cong, R.; Yang, T., Dy³⁺ and Tm³⁺ doped YGa₃(BO₃)₄ for near ultraviolet excited white phosphors, *J. Solid State Chem.*, **2019**, 269, 30-35
- [18] Wu, X.; Yin, B.; Ren, Q.; Ren, Y.; Hai, O., Compounds, Structure, luminescence, properties and energy transfer of Dy³⁺ and Eu³⁺ codoped Ca₄LaO(BO₃)₃ phosphor, *J. Alloys Compd.*, **2020**, 822, 153562.
- [19] Singh, A. K.; Tyagi, M.; Desai, D. G.; Singh, S. G.; Sen, S.; Gadkari, S. C., A Comparative Study of Li₆R(BO₃)₃ (R= Gd, Lu, and Y) Single Crystals for Thermal Neutron Detection, *Phys. Status Solidi A*, **2018**, 215, 1800224.
- [20] Yin, J.; Zhang, J.; Wang, J.; Du, F.; Li, R.; Pan, S.; Pan, J., Growth and scintillation properties of Ce:Li₆Y(BO₃)₃ crystal enriched with ¹⁰B isotopes, *Radiat. Meas.*, **2018**, 113, 20-24.
- [21] Xia, M.; Shen, S.; Lu, J.; Sun, Y.; Li, R., K₃Li₃Gd₇(BO₃)₉: A New Gadolinium-Rich Orthoborate for Cryogenic Magnetic Cooling, *Chem. Eur. J.*, **2018**, 24, 3147-3150.
- [22] Li, R.; Wu, C.; Xia, M., LiCaTb₅(BO₃)₆: A new magneto-optical crystal promising as Faraday rotator, *Opt. Mater.*, **2016**, 62, 452-457.
- [23] Guo, S.; Kong, T.; Xie, W.; Nguyen, L.; Stolze, K.; Cevallos, F. A.; Cava, R., Triangular Rare-Earth Lattice Materials RbBaR(BO₃)₂ (R = Y, Gd–Yb) and Comparison to the KBaR(BO₃)₂ Analogs, *Inorg. Chem.*, **2019**, 58, 3308-3315.
- [24] Guo, S.; Kong, T.; Cevallos, F. A.; Stolze, K.; Cava, R., M. Materials, Crystal growth, crystal structure and anisotropic magnetic properties of KBaR(BO₃)₂ (R = Y, Gd, Tb, Dy, Ho, Tm, Yb and Lu) triangular lattice materials, *J. Magn. Magn. Mater.*, **2019**, 472, 104-110.
- [25] Jubera, V.; Gravereau, P.; Chaminade, J. P., Crystal structure of the new borate Li₃Gd(BO₃)₂: Comparison with the homologous Na₃Ln(BO₃)₂ (Ln: La, Nd) compounds, *Solid State Sci.*, **2001**, 3, 469-475.
- [26] Chaminade, J.-P.; Gravereau, P.; Jubera, V.; Fouassier, C., A New Family of Lithium Rare-Earth Oxyborates, LiLn₆O₅(BO₃)₃ (Ln = Pr–Tm): Crystal Structure of the Gadolinium Phase LiGd₆O₅(BO₃)₃, *J. Solid State Chem.*, **1999**, 146, 189-196.
- [27] Mascetti, J.; Fouassier, C.; Hagenmuller, P. Concentration quenching of the Nd³⁺ emission in alkali rare earth borates, *J. Solid State Chem.*, **1983**, 50, 204-212.
- [28] Zeng, Q.; Li, R., A new potassium rare earth oxyborate K₂La₂(BO₃)₂O, *Solid State Sci.*, **2010**, 12, 2144-2147.
- [29] Gao, J.; Li, R., Potassium rich rare earth (RE) borates K₃RE(BO₃)₂, *Solid State Sci.*, **2008**, 10, 26-30.
- [30] Xia, M.-J.; Li, R., A new quaternary rare earth borate, CsLi₂Gd₄(BO₃)₅, *Acta Crystallogr. Sect. E*, **2007**, 63, i173-i173.
- [31] Zhao, S.; Zhang, G.; Yao, J.; Wu, Y. J., K₆Li₃Sc₂B₁₅O₃₀: A new nonlinear optical crystal with a short absorption edge, *Cryst. Eng. Comm.*, **2012**, 14, 5209-5214.

- [32] Chen, P.; Xia, M.; Li, R., Mixed Alkali Neodymium Orthoborates: $\text{K}_9\text{Li}_3\text{Nd}_3(\text{BO}_3)_7$ and $\text{A}_2\text{LiNd}(\text{BO}_3)_2$ ($\text{A} = \text{Rb}, \text{Cs}$), *Z. Anorg. Allg. Chem.*, **2016**, *642*, 424-430.
- [33] Sheldrick, G. M., SHELXT–Integrated space-group and crystal-structure determination, *Acta Crystallogr., Sect. A: Found. Crystallogr.* **2015**, *71*, 3-8.
- [34] *International Tables for Crystallography* Vol. A, **2006**, Space group 14, 184–191.
- [35] Hübschle, C. B.; Sheldrick, G. M.; Dittrich, B., ShelXle: a Qt graphical user interface for SHELXL, *J. Appl. Crystallogr.*, **2011**, *44*, 1281-1284.
- [36] Spek, A. L., checkCIF validation ALERTS: what they mean and how to respond, *Acta Crystallogr., Sect. E*, **2020**, *76*, 1-11.
- [37] Kubelka, P., Ein Beitrag zur Optik der Farbanstriche, *Z. Tech. Phys.*, **1931**, *12*, 593-601.
- [38] Tauc, J.; Grigorovici, R.; Vancu, A., Optical properties and electronic structure of amorphous germanium, *Phys. Status Solidi B*, **1966**, *15*, 627-637.
- [39] Souri, D.; Tahan, Z. E., A new method for the determination of optical band gap and the nature of optical transitions in semiconductors, *Appl. Phys. B*, **2015**, *119*, 273-279.
- [40] Kirsch, A.; Murshed, M. M.; Schowalter, M.; Rosenauer, A.; Gesing, T. M., Nanoparticle precursor into polycrystalline $\text{Bi}_2\text{Fe}_4\text{O}_9$: an evolutionary investigation of structural, morphological, optical, and vibrational properties, *J. Phys. Chem. C*, **2016**, *120*, 18831-18840.
- [41] Kirsch, A.; Murshed, M. M.; Litterst, F. J.; Gesing, T. M., Structural, spectroscopic, and thermoanalytic studies on $\text{Bi}_2\text{Fe}_4\text{O}_9$: tunable properties driven by nano-and poly-crystalline states, *J. Phys. Chem. C*, **2019**, *123*, 3161-3171.
- [42] Giannozzi, P.; Andreussi, O.; Brumme, T.; Bunau, O.; Nardelli, M. B.; Calandra, M.; Car, R.; Cavazzoni, C.; Ceresoli, D.; Cococcioni, M., Advanced capabilities for materials modelling with Quantum ESPRESSO, *J. Phys.: Condens. Matter*, **2017**, *29*, 465901.
- [43] Perdew, J. P.; Ruzsinszky, A.; Csonka, G. I.; Vydrov, O. A.; Scuseria, G. E.; Constantin, L. A.; Zhou, X.; Burke, K., Restoring the density-gradient expansion for exchange in solids and surfaces, *Phys. Rev. Lett.*, **2008**, *100*, 136406
- [44] Clark, S. J.; Segall, M. D.; Pickard, C. J.; Hasnip, P. J.; Probert, M. I.; Refson, K.; Payne, M. C., First principles methods using CASTEP, *Z. Kristallogr.-Cryst. Mater.*, **2005**, *220*, 567-570.
- [45] Refson, K.; Tulip, P. R.; Clark, S. J., Variational density-functional perturbation theory for dielectrics and lattice dynamics, *Phys. Rev. B*, **2006**, *73*, 155114.
- [46] Bräuchle, S.; Huppertz, H., Synthesis and structural characterization of $\text{Li}_3\text{K}_3\text{Y}_7(\text{BO}_3)_9$, *J. Solid State Chem.*, **2017**, *253*, 242-248.
- [47] Shannon, R. D., Revised effective ionic radii and systematic studies of interatomic distances in halides and chalcogenides, *Acta Crystallogr., Sect. A: Found. Crystallogr.*, **1976**, *32*, 751-767.
- [48] Jia, Y. J., Crystal radii and effective ionic radii of the rare earth ions, *J. Solid State Chem.*, **1991**, *95*, 184-187.

- [49] Rodriguez-Carvajal, J.; Roisnel, T., WinPLOTR: A windows tool for powder diffraction pattern analysis, *Mater. Sci. Forum, Proceedings of the Seventh European Powder Diffraction Conference*, Barcelona, Spain, **2000**, pp. 378-381.
- [50] Emly, A.; Kioupakis, E.; Van der Ven, A., Phase stability and transport mechanisms in antiperovskite Li_3OCl and Li_3OBr superionic conductors, *Chem. Mater.*, **2013**, *25*, 4663-4670.
- [51] Murugan, R.; Thangadurai, V.; Weppner, W., Fast lithium ion conduction in garnet-type $\text{Li}_7\text{La}_3\text{Zr}_2\text{O}_{12}$, *Angew. Chem. Int. Ed.*, **2007**, *46*, 7778-7781.
- [52] Pérez-Estébanez, M.; Isasi-Marín, J.; Többs, D.; Rivera-Calzada, A.; León, C., A systematic study of Nasicon-type $\text{Li}_{1+x}\text{M}_x\text{Ti}_{2-x}(\text{PO}_4)_3$ (M: Cr, Al, Fe) by neutron diffraction and impedance spectroscopy, *Solid State Sci.*, **2014**, *266*, 1-8.
- [53] Scheld, W.; Hoppe, R., Über den α - NaFeO_2 -Typ: Zur Kenntnis von NaCrO_2 und KCrO_2 , *Z. Anorg. Allg. Chem.*, **1989**, *568*, 151-156.
- [54] Husheer, S. L. G.; Thompson, J. G.; Melnitchenko, A., Cristobalite-Related Phases in the KAlO_2 – KAlSiO_4 System, *J. Solid State Chem.*, **1999**, *147*, 624-630.
- [55] Wasel-Nielen, H.-D.; Hoppe, R., Zur Kristallstruktur von Li_3AuO_3 , Li_5AuO_4 , KAuO_2 und RbAuO_2 , *Z. Anorg. Allg. Chem.*, **1970**, *375*, 43-54.
- [56] Torardi, C. C.; Calabrese, J. C., Hydrothermal synthesis of a new molybdenum hollandite containing tetranuclear metal-atom clusters. X-ray crystal structure of $\text{K}_2\text{Mo}_8\text{O}_{16}$, *Inorg. Chem.*, **1984**, *23*, 3281-3284.
- [57] Matsuzaki, T.; Hagiya, K.; Shatskiy, A.; Katsura, T.; Matsui, M., Crystal structure of anhydrous phase X, $\text{K}_{1.93}(\text{Mg}_{2.02}\text{Cr}_{0.02})\text{Si}_{2.00}\text{O}_7$, *J. Mineral. Petrol. Sci.*, **2010**, *105*, 303-308.
- [58] Yamada, H.; Matsui, Y.; Ito, E., Crystal-chemical characterization of KAlSi_3O_8 with the hollandite structure, *Mineral. J.*, **1984**, *12*, 29-34.
- [59] Mao, L.; Zhou, T.; Ye, N., Trilithium scandium bis (orthoborate), *Acta Crystallogr., Sect. E*, **2008**, *64*, i38-i38.
- [60] Naidu, S. A.; Boudin, S.; Varadaraju, U.; Raveau, B., Influence of structural distortions upon photoluminescence properties of Eu^{3+} and Tb^{3+} activated $\text{Na}_3\text{Ln}(\text{BO}_3)_2$ (Ln = Y, Gd) borates, *J. Solid State Chem.*, **2012**, *190*, 186-190.
- [61] Petříček, V.; Dušek, M.; Palatinus, L., Crystallographic Computing System JANA2006: General features, *Z. Kristallogr.-Cryst. Mater.*, **2014**, *229*, 345–352.
- [62] Dieke, G. H.; Crosswhite, H. M., The Spectra of the Doubly and Triply Ionized Rare Earths, *Appl. Opt.*, **1963**, *2*, 675-686.
- [63] Carnall, W.; Fields, P.; Rajnak, K., Electronic energy levels in the trivalent lanthanide aquo ions. I. Pr^{3+} , Nd^{3+} , Pm^{3+} , Sm^{3+} , Dy^{3+} , Ho^{3+} , Er^{3+} , and Tm^{3+} , *J. Chem. Phys.*, **1968**, *49*, 4424-4442.
- [64] Som, S.; Sharma, S., $\text{Eu}^{3+}/\text{Tb}^{3+}$ -codoped Y_2O_3 nanophosphors: Rietveld refinement, bandgap and photoluminescence optimization, *J. Phys. D: Appl. Phys.*, **2012**, *45*, 415102.
- [65] Zhang, G.; Wu, Y.; Fu, P.; Wang, G.; Pan, S.; Chen, C., A new nonlinear optical borate

crystal $\text{Na}_3\text{La}_2(\text{BO}_3)_3$, *Chem. Lett.*, **2001**, 30, 456-457.

[66] Steele, W.; Decius, J., Infrared absorption of lanthanum, scandium, and indium borate and the force constants of borate ion, *J. Chem. Phys.*, **1956**, 25, 1184-1188.

[67] Tao, C.; Wu, C.; Xia, M.; Li, R., $\text{Li}_2\text{Ca}_5\text{Tb}(\text{BO}_3)_5$: An orthoborate with large spherical hollow cages, *Opt. Mater.*, **2019**, 96, 109358.

[68] Kuznetsov, A.; Kokh, K.; Kononova, N.; Shevchenko, V.; Kaneva, E.; Uralbekov, B.; Svetlichnyi, V.; Kokh, A., Synthesis and growth of new rare earth borates $\text{KCaR}(\text{BO}_3)_2$ (R= La, Pr and Nd), *J. Solid State Chem.*, **2020**, 282, 121091.

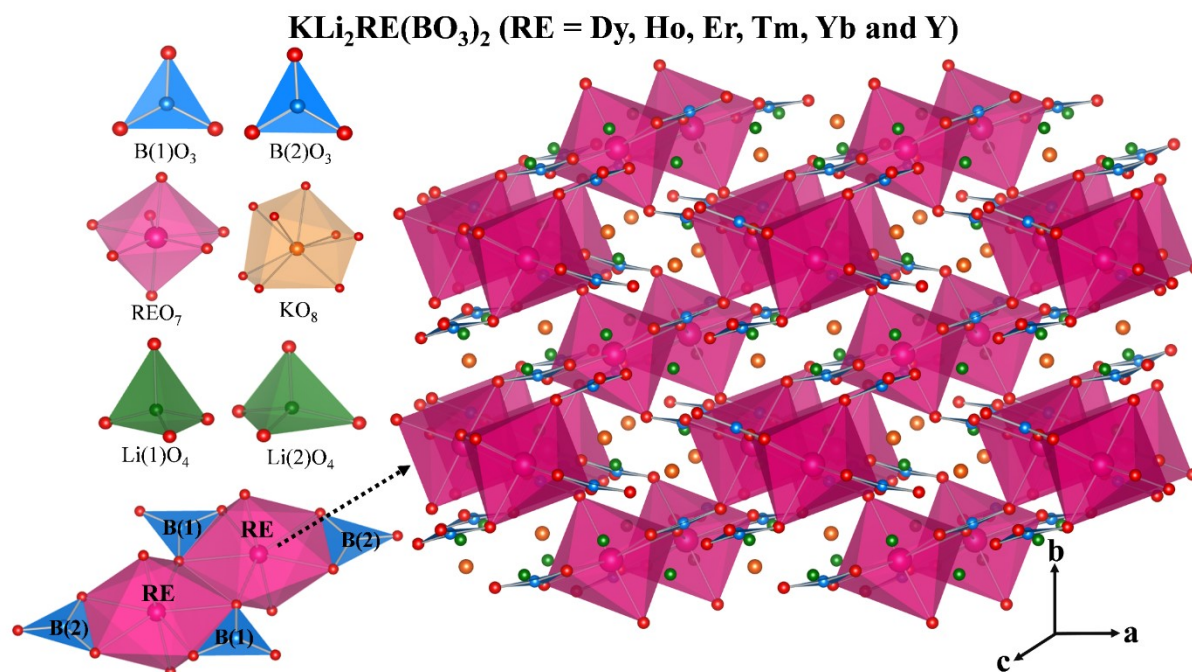
[69] Dilawar, N.; Mehrotra, S.; Varandani, D.; Kumaraswamy, B.; Haldar, S.; Bandyopadhyay, A., A Raman spectroscopic study of C-type rare earth sesquioxides, *Mater. Charact.*, **2008**, 59, 462-467.

[70] Abrashev, M. V.; Todorov, N. D.; Geshev, J., Raman spectra of R_2O_3 (R-rare earth) sesquioxides with C-type bixbyite crystal structure: A comparative study, *J. Appl. Phys.*, **2014**, 116, 103508.

[71] Park, H.; Lam, R.; Greedan J. E.; Barbier, J., Synthesis, Crystal Structure, Crystal Chemistry, and Magnetic Properties of PbMBO_4 (M = Cr, Mn, Fe): A New Structure Type Exhibiting One- Dimensional Magnetism, *Chem. Mater.*, **2003**, 15, 1703–1712

[72] Besara, T.; Lundberg, M. S.; Sun, J.; Ramirez, D.; Dong, L.; Whalen, J. B.; Vasquez, R.; Herrera, F.; Allen, J. R.; Davidson, M. W.; Siegrist, T., Single crystal synthesis and magnetism of the BaLn_2O_4 family (Ln = lanthanide), *Prog. Solid State Chem.*, **2014**, 42, 23-36.

For Table of Contents Only



Synopsis

A series of mixed alkali rare-earth orthoborates with novel structure types, $\text{KLi}_2\text{RE}(\text{BO}_3)_2$ (RE = Dy, Ho, Er, Tm, Yb and Y), comprise $[\text{RE}_2(\text{BO}_3)_4\text{O}_4]^{14-}$ anionic clusters where the edge-sharing REO_7 pentagonal bipyramids are connected by BO_3 groups, and both KO_8 dodecahedra and LiO_4 tetrahedra are located at the interstitial voids of the three-dimensional network.

Supplementary Information

KLi₂RE(BO₃)₂ (RE = Dy, Ho, Er, Tm, Yb and Y): structural, spectroscopic and thermogravimetric studies on a series of mixed alkali rare-earth orthoborates

Pengyun Chen¹, M. Mangir Murshed^{1,4*}, Michael Fischer^{2,4}, Thomas Frederichs³,

Thorsten M. Gesing^{1,4}

¹University of Bremen, Institute of Inorganic Chemistry and Crystallography, Faculty of Biology and Chemistry, Leobener Straße 7, D-28359 Bremen, Germany

²University of Bremen, Crystallography, Faculty of Geosciences, Klagenfurter Straße 2-4, D-28359 Bremen, Germany

³University of Bremen, Faculty of Geosciences, Klagenfurter Straße 2-4, D-28359 Bremen, Germany

⁴University of Bremen, MAPEX Center for Materials and Processes, Bibliothekstraße 1, D-28359 Bremen, Germany

*Corresponding author: e-mail address: murshed@uni-bremen.de, phone: +49 (0)421 218 63144, fax: +49 421 218 63145.

Table S1: Atomic coordinates, equivalent isotropic displacement parameters ($U_{eq} / 10^4 \text{pm}^2$), and bond valence sum (BVS /v.u.) of $\text{KLi}_2\text{RE}(\text{BO}_3)_2$. U_{eq} is defined as one-third of the trace of the U_{ij} tensor components. All atoms are in the $4e$ Wyckoff.

Atom	x	y	z	U_{eq}	BVS
$\text{KLi}_2\text{Dy}(\text{BO}_3)_2$					
Dy	0.53708(2)	0.88265(2)	0.34218(2)	0.00483(2)	2.81(1)
K	0.57478(7)	0.37572(5)	0.41357(4)	0.01071(7)	1.46(1)
B1	0.6471(3)	0.8590(2)	0.7634(2)	0.0068(3)	2.86(1)
B2	0.6301(3)	0.6296(2)	0.2148(2)	0.0061(3)	2.93(1)
Li1	0.4182(6)	0.8835(4)	0.9944(4)	0.0120(6)	1.13(1)
Li2	0.4174(6)	0.3842(4)	0.0495(4)	0.0132(7)	0.95(1)
O1	0.7220(2)	0.72711(14)	0.81783(15)	0.0075(2)	-2.00(1)
O2	0.6002(2)	0.96401(14)	0.85915(15)	0.0081(2)	-2.01(1)
O3	0.6014(2)	0.89412(15)	0.60856(15)	0.0095(2)	-1.88(1)
O4	0.6565(2)	0.49831(14)	0.14945(15)	0.0074(2)	-2.00(1)
O5	0.5732(2)	0.74754(14)	0.12375(15)	0.0089(2)	-2.10(1)
O6	0.6594(2)	0.65034(15)	0.36933(15)	0.0091(2)	-2.15(1)
$\text{KLi}_2\text{Er}(\text{BO}_3)_2$					
Er	0.53739(2)	0.88315(2)	0.34192(2)	0.00536(4)	2.87(1)
K	0.57422(7)	0.37571(4)	0.41403(5)	0.01082(8)	1.50(1)
B1	0.6491(3)	0.8593(2)	0.7621(2)	0.0069(3)	2.86(1)
B2	0.6320(3)	0.6298(2)	0.2153(2)	0.0068(3)	2.93(1)
Li1	0.4171(7)	0.8826(4)	0.9945(5)	0.0132(7)	1.15(1)
Li2	0.4167(7)	0.3853(4)	0.0502(5)	0.0132(7)	0.94(1)
O1	0.7253(2)	0.72683(15)	0.81675(17)	0.0080(2)	-2.02(1)
O2	0.6001(2)	0.96430(16)	0.85810(16)	0.0089(2)	-2.02(1)
O3	0.6028(3)	0.89482(16)	0.60672(17)	0.0103(3)	-1.89(1)
O4	0.6584(2)	0.49800(15)	0.14996(17)	0.0077(2)	-2.03(1)
O5	0.5746(2)	0.74868(16)	0.12402(17)	0.0092(2)	-2.11(1)
O6	0.6600(2)	0.65146(16)	0.37052(17)	0.0093(2)	-2.18(1)
$\text{KLi}_2\text{Tm}(\text{BO}_3)_2$					
Tm	0.53721(2)	0.88334(2)	0.34175(2)	0.00472(4)	3.06(1)

K	0.57512(10)	0.37571(7)	0.41441(7)	0.01183(12)	1.54(1)
B1	0.6485(5)	0.8591(3)	0.7612(4)	0.0062(5)	2.86(2)
B2	0.6323(5)	0.6300(3)	0.2155(4)	0.0071(5)	2.95(2)
Li1	0.4179(8)	0.8835(6)	0.9950(6)	0.0136(10)	1.16(1)
Li2	0.4146(8)	0.3857(6)	0.0501(6)	0.0136(10)	0.95(1)
O1	0.7257(3)	0.7260(2)	0.8159(2)	0.0074(4)	-2.05(1)
O2	0.5992(3)	0.9639(2)	0.8575(2)	0.0076(4)	-2.07(1)
O3	0.6016(3)	0.8952(2)	0.6054(2)	0.0097(4)	-1.95(1)
O4	0.6592(3)	0.4975(2)	0.1501(2)	0.0071(4)	-2.07(1)
O5	0.5756(3)	0.7489(2)	0.1242(2)	0.0091(4)	-2.16(1)
O6	0.6589(3)	0.6517(2)	0.3706(2)	0.0094(4)	-2.22(1)
KL₂Yb(BO₃)₂					
Yb	0.53733(2)	0.88369(2)	0.34144(2)	0.00474(3)	2.85(1)
K	0.57460(8)	0.37563(5)	0.41460(5)	0.01035(8)	1.54(1)
B1	0.6501(3)	0.8593(2)	0.7609(2)	0.0058(3)	2.87(1)
B2	0.6323(3)	0.6305(2)	0.2155(3)	0.0062(3)	2.94(2)
Li1	0.4191(8)	0.8830(5)	0.9952(5)	0.0154(8)	1.17(1)
Li2	0.4152(7)	0.3859(5)	0.0508(5)	0.0134(8)	0.94(1)
O1	0.7268(2)	0.72642(16)	0.81537(17)	0.0074(2)	-2.03(1)
O2	0.5993(2)	0.96458(17)	0.85708(17)	0.0083(3)	-2.04(1)
O3	0.6031(3)	0.89628(17)	0.60504(18)	0.0096(3)	-1.88(1)
O4	0.6599(2)	0.49777(16)	0.15072(18)	0.0072(2)	-2.04(1)
O5	0.5754(2)	0.74960(17)	0.12390(17)	0.0089(3)	-2.14(1)
O6	0.6598(2)	0.65330(17)	0.37112(17)	0.0087(3)	-2.18(1)
KL₂Y(BO₃)₂					
Y	0.53708(4)	0.88293(3)	0.34189(3)	0.00516(7)	3.04(1)
K	0.57467(9)	0.37586(7)	0.41398(6)	0.01089(12)	1.47(1)
B1	0.6480(4)	0.8591(3)	0.7628(3)	0.0066(5)	2.85(2)
B2	0.6319(4)	0.6296(3)	0.2146(3)	0.0072(5)	2.93(2)
Li1	0.4171(7)	0.8831(6)	0.9934(5)	0.0125(9)	1.13(1)
Li2	0.4172(8)	0.3851(6)	0.0502(5)	0.0142(10)	0.93(1)
O1	0.7239(3)	0.72693(19)	0.8169(2)	0.0073(4)	-2.04(1)
O2	0.6000(3)	0.9640(2)	0.8587(2)	0.0084(4)	-2.04(1)

O3	0.6014(3)	0.8945(2)	0.6074(2)	0.0098(4)	-1.93(1)
O4	0.6584(3)	0.4983(2)	0.1495(2)	0.0074(4)	-2.05(1)
O5	0.5739(3)	0.7481(2)	0.1238(2)	0.0092(4)	-2.11(1)
O6	0.6597(3)	0.65126(19)	0.3696(2)	0.0088(4)	-2.19(1)

Table S2. Energy dispersive X-ray (EDX) analysis results on three different single crystals of each $\text{KLi}_2\text{RE}(\text{BO}_3)_2$ (RE = Dy, Ho, Er, Tm, Yb and Y) compound, showing the K:RE atomic ratio.

Compound	K : RE		
	Crystal-1	Crystal-2	Crystal-3
$\text{KLi}_2\text{Dy}(\text{BO}_3)_2$	1.03(3) : 1.00(10)	1.00(3) : 1.00(10)	1.04(2) : 1.00(6)
$\text{KLi}_2\text{Ho}(\text{BO}_3)_2$	1.11(3) : 1.00(9)	1.06(3) : 1.00(9)	1.03(3) : 1.00(9)
$\text{KLi}_2\text{Er}(\text{BO}_3)_2$	1.05(4) : 1.00(13)	1.03(2) : 1.00(8)	1.00(3) : 1.00(10)
$\text{KLi}_2\text{Tm}(\text{BO}_3)_2$	1.01(2) : 1.00(9)	1.06(2) : 1.00(7)	1.08(2) : 1.00(7)
$\text{KLi}_2\text{Yb}(\text{BO}_3)_2$	1.01(2) : 1.00(8)	1.17(3) : 1.00(9)	1.13(2) : 1.00(7)
$\text{KLi}_2\text{Y}(\text{BO}_3)_2$	1.12(3) : 1.00(8)	0.91(2) : 1.00(7)	1.05(3) : 1.00(8)

Table S3: Structural comparison between “312”-type rare-earth borates in terms of space group (*SG*), sum of ionic radii of alkali-metals (Σ in units of pm), metric parameter (*a*, *b* and *c* in units of pm and β in degree), coordination and their connectivity.

Formula	<i>SG</i>	Σ	Metric	Coordination	Structural details	Reference
Li ₃ Sc(BO ₃) ₂	<i>P2₁/n</i>	177	<i>a</i> = 478.3(2) <i>b</i> = 595.4(2) <i>c</i> = 816.3(3) β = 90.70(1)	ScO ₆ octahedra BO ₃ triangle LiO ₄ tetrahedra LiO ₄ rectangle	Isolated ScO ₆ octahedra are linked via LiO ₄ rectangles along the <i>b</i> axis, further bridged by LiO ₄ tetrahedra and BO ₃ triangles	[1]
Li ₃ Gd(BO ₃) ₂	<i>P2₁/n</i>	177	<i>a</i> = 992.3 <i>b</i> = 642.5 <i>c</i> = 872.4 β = 114.815	GdO ₈ dodecahedra BO ₃ triangle LiO ₄ tetrahedra	Double layers of [Gd ₂ O ₁₄] dimer connected by BO ₃ triangles with LiO ₄ tetrahedra inserted into the cavity.	[2]
KLi ₂ Ho(BO ₃) ₂	<i>P2₁/n</i>	269	<i>a</i> = 671.112(5) <i>b</i> = 931.737(6) <i>c</i> = 899.091(6) β = 102.8257(6)	HoO ₇ pentagonal bipyramid BO ₃ triangle KO ₈ dodecahedra LiO ₄ tetrahedra	[Ho ₂ (BO ₃) ₄ O ₄] ¹⁴⁻ anionic clusters connected to each other by corner-sharing, with KO ₈ dodecahedra and LiO ₄ tetrahedra filled into the voids	This work
Na ₃ Gd(BO ₃) ₂	<i>P2₁/n</i>	313	<i>a</i> = 1014.8 <i>b</i> = 872.83 <i>c</i> = 652.3 β = 89.12	GdO ₈ dodecahedra BO ₃ triangles NaO ₇ monocapped octahedra NaO ₆ triangle prism, NaO ₄ tetrahedra	Single layers of [Gd ₂ O ₁₄] dimer are further bridged by the BO ₃ triangles and NaO _x polyhedra.	[3]
Rb ₂ LiNd(BO ₃) ₂	<i>Pbcm</i>	363	<i>a</i> = 711.3(2) <i>b</i> = 969.1(3) <i>c</i> = 1013.5(3)	NdO ₈ dodecahedra BO ₃ triangle RbO ₅ pentagonal pyramid LiO ₄ tetrahedra	Corner-shared [NdO ₅ B(1)O ₃] chains are reinforced by B(2)O ₃ groups to build up [Nd ₄ B ₄ O ₂₄] _n layers in the <i>bc</i> plane.	[4]
K ₃ Sm(BO ₃) ₂	<i>Pnma</i>	414	<i>a</i> = 904.6(3) <i>b</i> = 710.0(2) <i>c</i> = 1118.6(3)	SmO ₇ pentagonal bipyramid KO ₆ octahedra KO ₆ triangle prism	B(1)O ₃ triangle bridges three [SmO ₄ B(2)O ₃] chains in a scaffolding-like way with KO ₆ residing the interstitials	[5]
K ₃ Y(BO ₃) ₂	<i>Pnnm</i>	414	<i>a</i> = 933.77(9) <i>b</i> = 677.01(6) <i>c</i> = 550.58(4)	YO ₆ octahedra BO ₃ triangle KO ₆ octahedra KO ₆ hexagons	Isolated YO ₆ octahedra use all oxygen atoms sharing with BO ₃ groups to form a 3-dimensional framework.	[5]
Cs ₂ LiNd(BO ₃) ₂	<i>Pbcm</i>	446	<i>a</i> = 721.13(3) <i>b</i> = 996.21(4) <i>c</i> = 1033.47(4)	NdO ₈ dodecahedra BO ₃ triangle CsO ₅ pentagonal pyramid LiO ₄ tetrahedra	Isostructural to Rb ₂ LiNd(BO ₃) ₂	[4]

Table S4: Phases identified from the X-ray powder data Rietveld refinement during the synthesis trials of $ALi_2RE(BO_3)_2$ (A = Rb and Cs, RE = Eu, Gd, Tb, Lu, Sc and In) compounds.

Target compound	Observed phase/phases
$KLi_2Eu(BO_3)_2$	$Li_6Eu(BO_3)_3$
$KLi_2Gd(BO_3)_2$	$Li_6Gd(BO_3)_3$
$KLi_2Tb(BO_3)_2$	$Li_6Tb(BO_3)_3$
$KLi_2Lu(BO_3)_2$	$K_3Lu(BO_3)_2$ and $LuBO_3$
$KLi_2Sc(BO_3)_2$	$Li_3Sc(BO_3)_2$, $LiScO_2$ and KBO_2
$KLi_2In(BO_3)_2$	In_2O_3
$RbLi_2Er(BO_3)_2$	$Li_6Er(BO_3)_3$ and $ErBO_3$
$RbLi_2Yb(BO_3)_2$	$Li_6Yb(BO_3)_2$ and $YbBO_3$
$CsLi_2Er(BO_3)_2$	$Li_6Er(BO_3)_3$ and $ErBO_3$
$CsLi_2Yb(BO_3)_2$	$Li_6Yb(BO_3)_2$ and $YbBO_3$

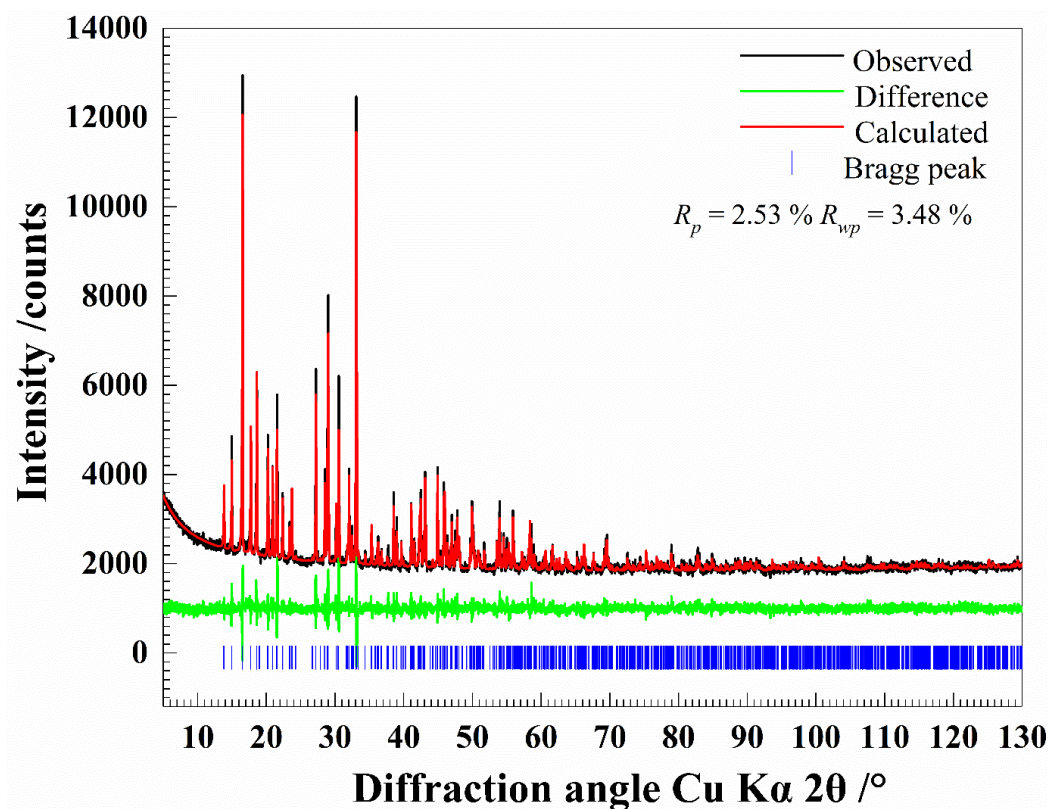


Figure S1: X-ray powder data Rietveld plot of KLi₂Dy(BO₃)₂.

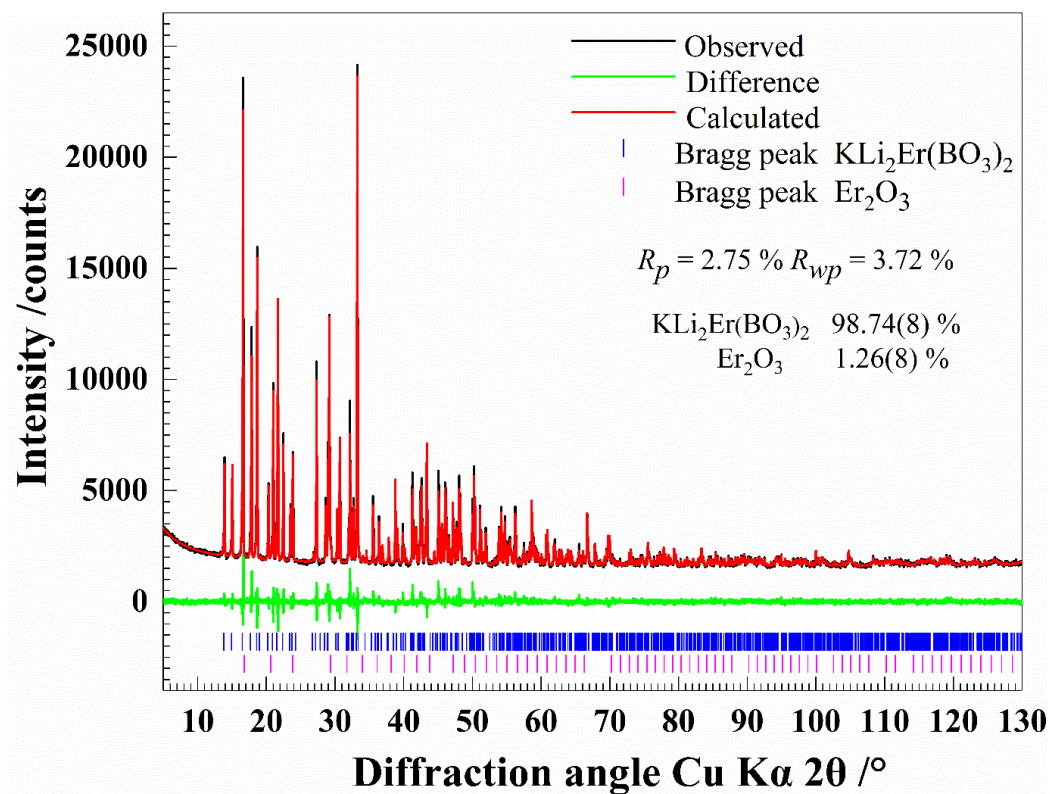


Figure S2: X-ray powder data Rietveld plot of KLi₂Er(BO₃)₂.

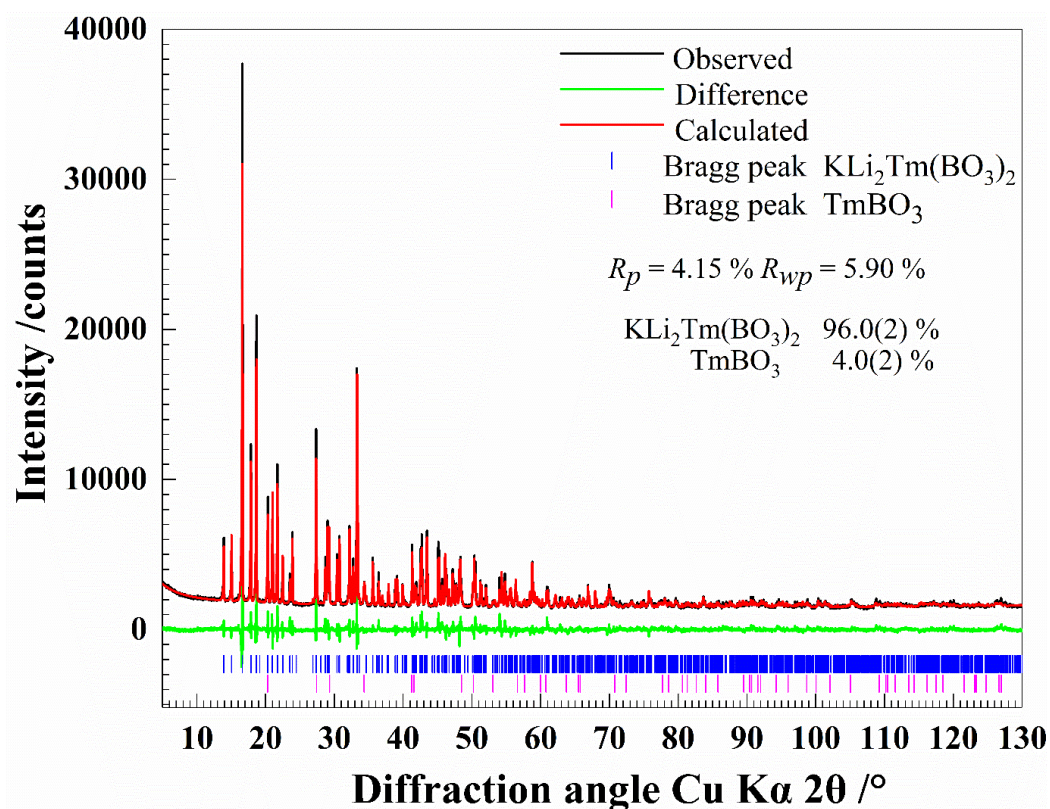


Figure S3: X-ray powder data Rietveld plots of KLi₂Tm(BO₃)₂

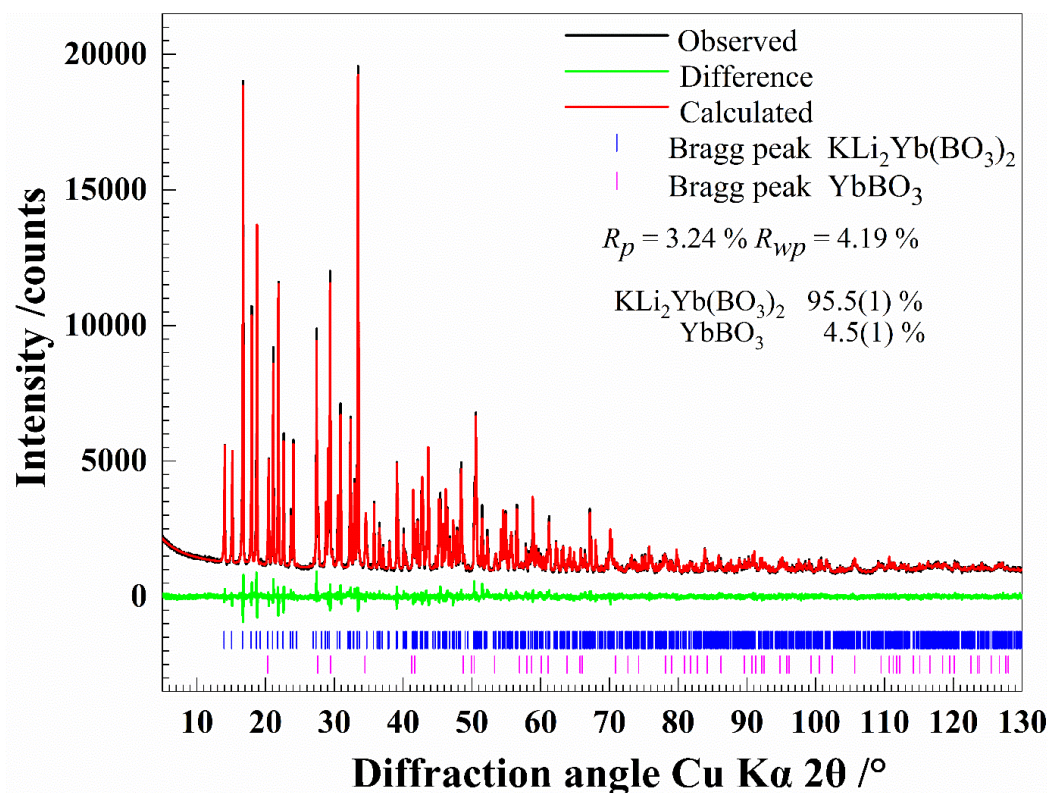


Figure S4: X-ray powder data Rietveld plot of KLi₂Yb(BO₃)₂.

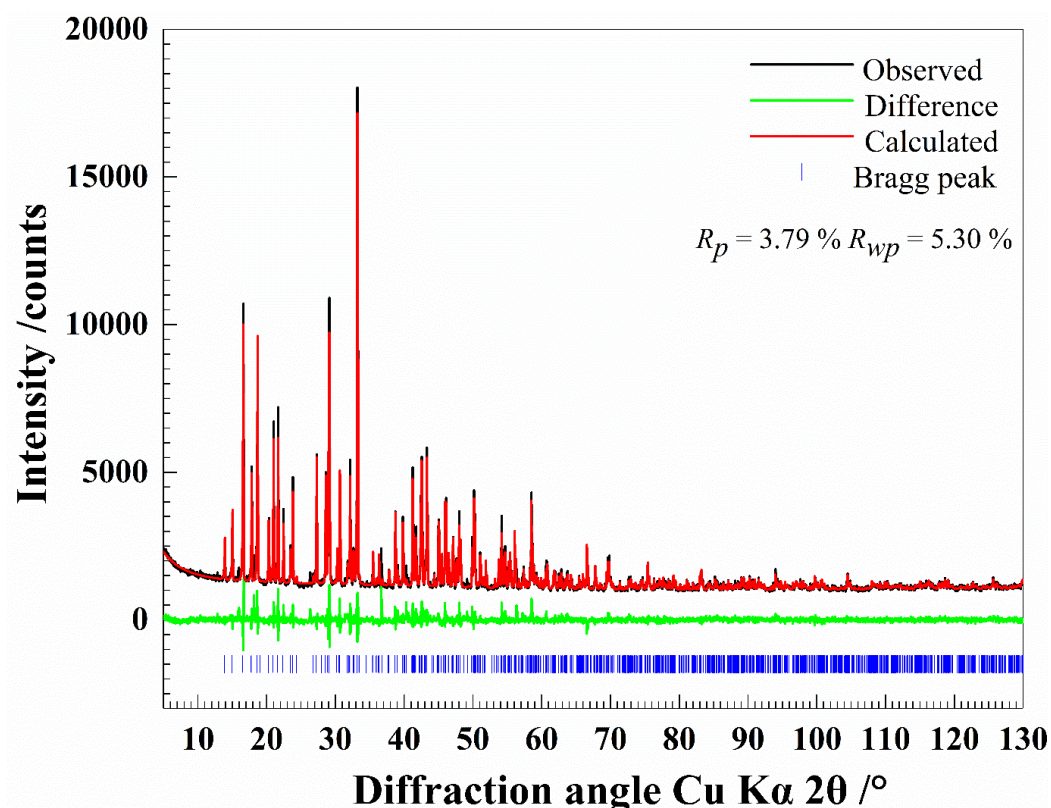


Figure S5: X-ray powder data Rietveld plots of $\text{KLi}_2\text{Y}(\text{BO}_3)_2$.

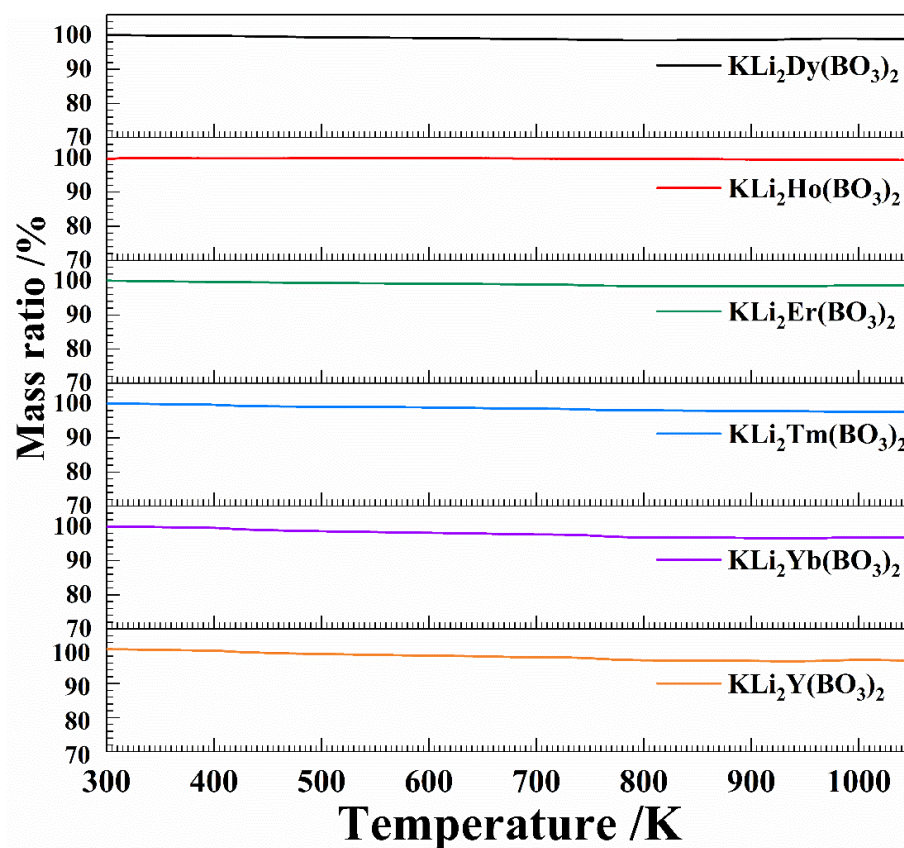


Figure S6: Thermal gravimetric analysis (TGA) curves of $\text{KLi}_2\text{RE}(\text{BO}_3)_2$.

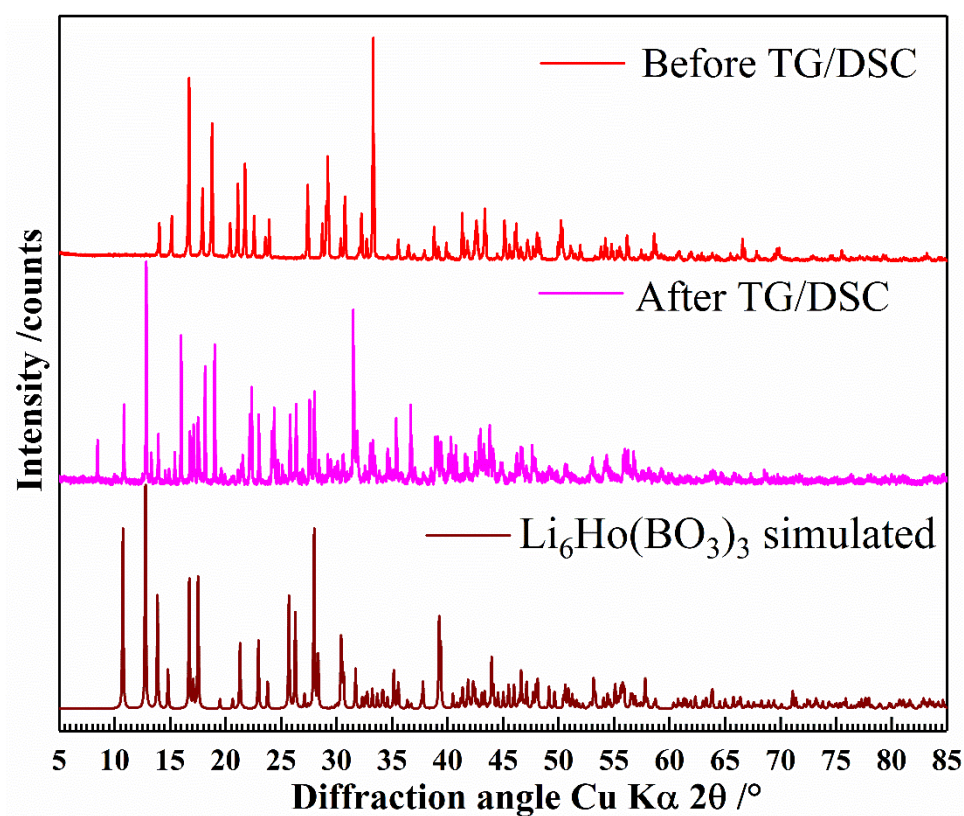


Figure S7: Powder XRD patterns of $\text{KLi}_2\text{Ho}(\text{BO}_3)_2$ before and after the TG/DSC. The simulated XRD pattern of $\text{Li}_6\text{Ho}(\text{BO}_3)_3$ is only for comparison.

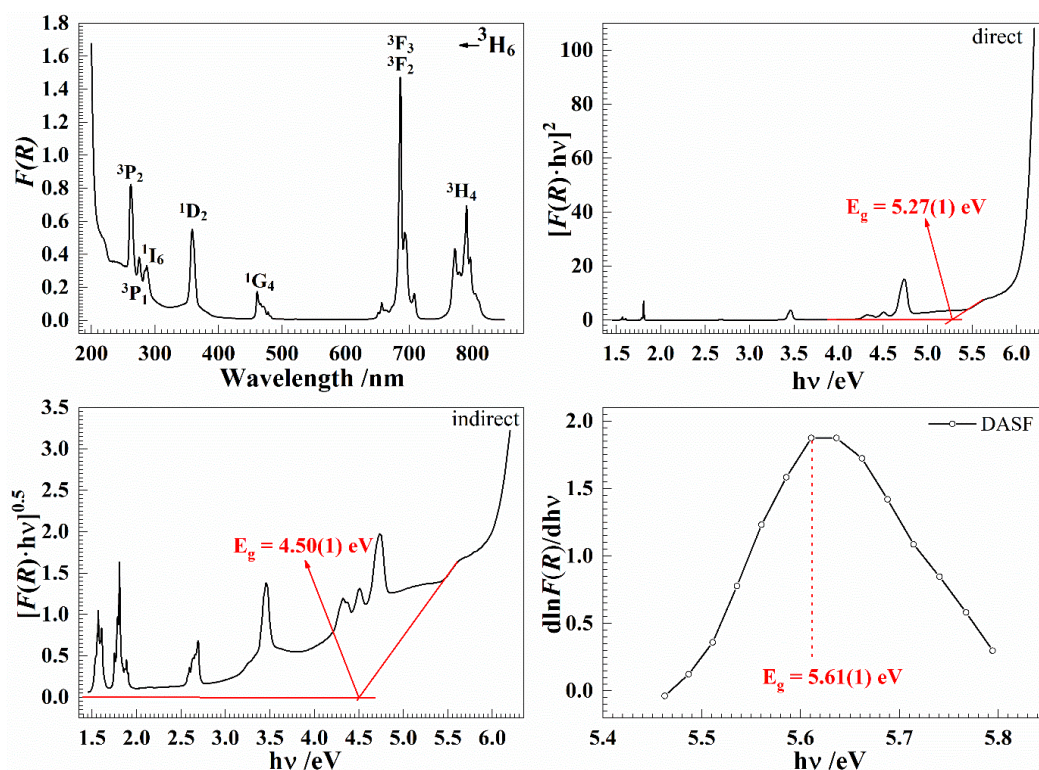


Figure S10: Kubelka-Munk transformed diffuse reflectance spectrum of $\text{KLi}_2\text{Tm}(\text{BO}_3)$ (top left), Tauc plots for indirect (bottom left) and direct (top right) optical transitions, and DASF plot (bottom right).

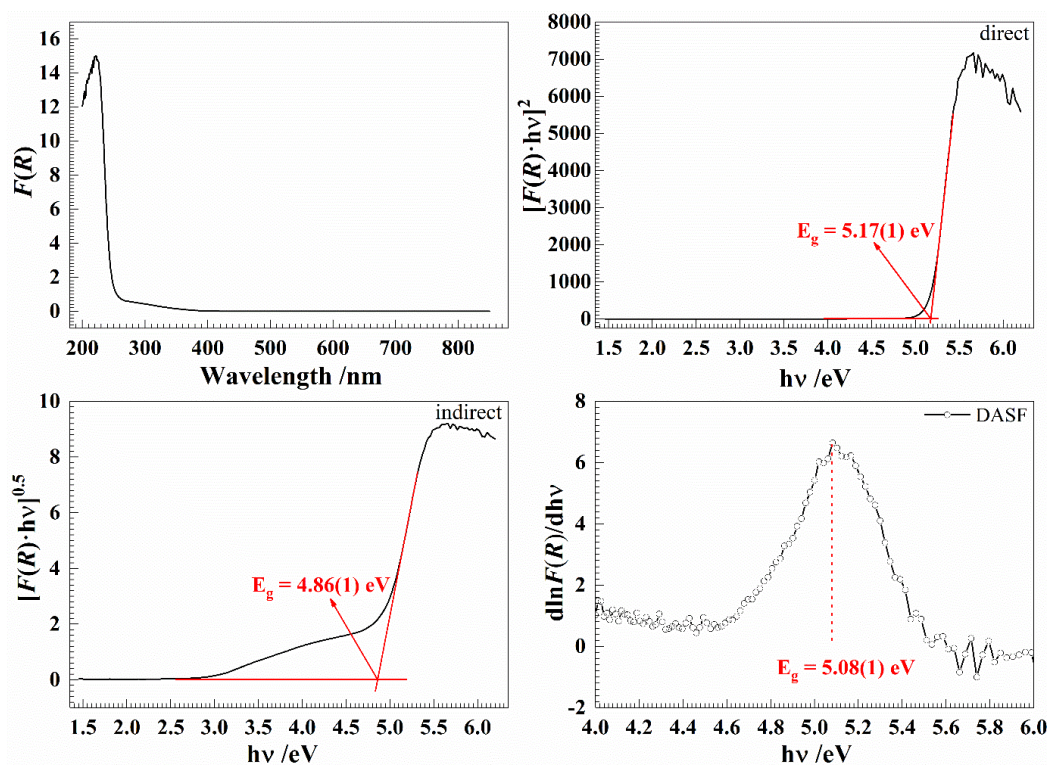


Figure S11: Kubelka-Munk transformed diffuse reflectance spectrum of $\text{KLi}_2\text{Yb}(\text{BO}_3)$ (top left), Tauc plots for indirect (bottom left) and direct (top right) optical transitions, and DASF plot (bottom right).

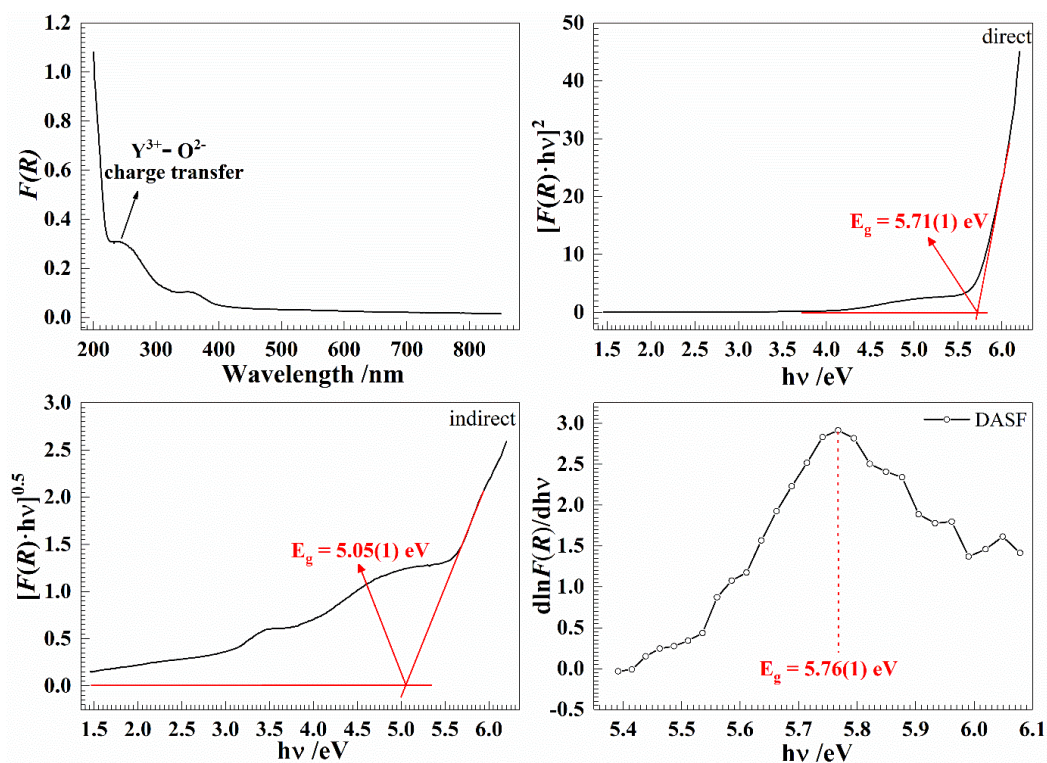


Figure S12: Kubelka-Munk transformed diffuse reflectance spectrum of $\text{KLi}_2\text{Y}(\text{BO}_3)$ (top left), Tauc plots for indirect (bottom left) and direct (top right) optical transitions, and DASF plot (bottom right).

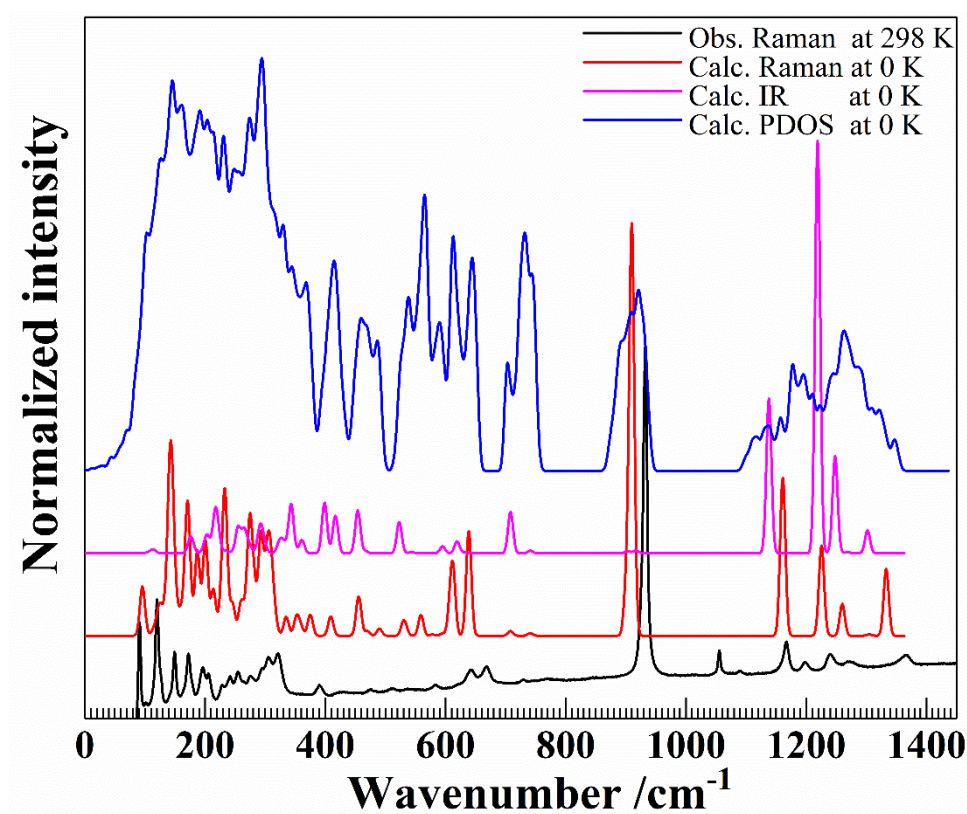


Figure S13: Comparative view between the phonon density of states (PDOS), Raman and infrared (IR) spectra of $\text{KLi}_2\text{Y}(\text{BO}_3)_2$.

References

- [1] Mao, L.; Zhou, T.; Ye, N., Trilithium scandium bis (orthoborate), *Acta Crystallogr., Sect. E*, **2008**, 64, i38-i38.
- [2] Jubera, V.; Gravereau, P.; Chaminade, J. P., Crystal structure of the new borate $\text{Li}_3\text{Gd}(\text{BO}_3)_2$: Comparison with the homologous $\text{Na}_3\text{Ln}(\text{BO}_3)_2$ (Ln: La, Nd) compounds, *Solid State Sci.*, **2001**, 3, 469-475.
- [3] Naidu, S. A.; Boudin, S.; Varadaraju, U.; Raveau, B., Influence of structural distortions upon photoluminescence properties of Eu^{3+} and Tb^{3+} activated $\text{Na}_3\text{Ln}(\text{BO}_3)_2$ (Ln = Y, Gd) borates, *J. Solid State Chem.*, **2012**, 190, 186-190.
- [4] Chen, P.; Xia, M.; Li, R., Mixed Alkali Neodymium Orthoborates: $\text{K}_9\text{Li}_3\text{Nd}_3(\text{BO}_3)_7$ and $\text{A}_2\text{LiNd}(\text{BO}_3)_2$ (A = Rb, Cs), *Z. Anorg. Allg. Chem.*, **2016**, 642, 424-430.
- [5] Gao, J.; Li, R., Potassium rich rare earth (RE) borates $\text{K}_3\text{RE}(\text{BO}_3)_2$, *Solid State Sci.*, **2008**, 10, 26-30.

Chapter 4

Synthesis and crystal structures of novel alkali rare-earth orthoborates $K_3RE_3(BO_3)_4$ (RE = Pr, Nd, Sm - Lu)

Pengyun Chen¹, M. Mangir Murshed^{1,2*}, Thorsten M. Gesing^{1,2}

¹University of Bremen, Institute of Inorganic Chemistry and Crystallography, Faculty of Biology and Chemistry, Leobener Straße 7, D-28359 Bremen, Germany

²University of Bremen, MAPEX Center for Materials and Processes, Bibliothekstraße 1, D-28359 Bremen, Germany

*Corresponding author: e-mail address: murshed@uni-bremen.de, phone: +49 (0)421 218 63144, fax: +49 421 218 63145.

Abstract

We report a series of novel alkali rare-earth orthoborates $K_3RE_3(BO_3)_4$ ($RE = Pr, Nd, Sm, Eu, Gd, Tb, Dy, Ho, Er, Tm, Yb$ and Lu) prepared by high-temperature solid state syntheses. Single crystals of $K_3Pr_3(BO_3)_4$, $K_3Er_3(BO_3)_4$, $K_3Tm_3(BO_3)_4$, $K_3Yb_3(BO_3)_4$ and $K_3Lu_3(BO_3)_4$ are obtained by spontaneous crystallization using a flux. Complementary single crystal and powder X-ray diffraction measurements followed by structure refinements reveal that both Pr- and Nd-containing phases crystallize in the space group $P\bar{1}$ ($Z = 4$), whereas the other $K_3RE_3(BO_3)_4$ members with higher atomic number ($RE = Sm$ to Lu) crystallize in the higher symmetry space group $P2_1/c$ ($Z = 8$). Amid differences in the space groups each member of the series keeps close structural correlations in their motif and connectivity. The crystal structures of $K_3RE_3(BO_3)_4$ ($RE = Sm - Lu$) consists of quasi-two-dimensional $[RE_8(BO_3)_8]$ layers parallel to the ab -plane which are connected by out-of-layer RE_2O_{12} and RE_2O_{14} dimers as well as BO_3 groups in the c -direction, forming a 3D framework. On the other hand, both $K_3Pr_3(BO_3)_4$ and $K_3Nd_3(BO_3)_4$ phases are comprised of the $[RE_4(BO_3)_4]$ layers, indicating to the absence of 2_1 screw axis along the b -axis. The K^+ cations are located between the $[RE_8(BO_3)_8]$ and $[RE_4(BO_3)_4]$ layers, occupying the interstitial voids. All samples exhibit characteristic absorption features in the UV/Vis range relevant to the rare-earth cations, and their optical bandgaps are evaluated by both conventional Tauc plot and derivation of absorption spectrum fitting (DASF) methods. The geometric deviations away from the D_{3h} symmetry of the BO_3 planar groups are verified using Fourier transformed infrared and Raman spectra, and supported by the X-ray diffraction results.

Keywords: rare-earth borate, crystal structure; UV-Vis, infrared, Raman

1. Introduction

Inorganic rare-earth borates are of growing interest owing to their diverse structural motifs and wide applications in particular in optics. (Y, Gd)BO₃ doped with Eu³⁺ and Tb³⁺ have been widely used as commercial red- and green-emitting phosphors in the plasma displays panels for their high vacuum ultraviolet absorption, efficient light conversion and thermodynamic stability [1, 2]. The calcite structure type Lu_{1-x}Sc_xBO₃:Ce³⁺ [3, 4] is one of the most useful orthoborates as a fast-decay scintillator; light yields of the polycrystalline presents around three times than that of the commercial Bi₄Ge₃O₁₂ (BGO) scintillators. Some rare-earth borates exhibit promising nonlinear optical (NLO) properties such as La_xY_ySc_{4-x-y}(BO₃)₄ [5], Ca₄REO(BO₃)₃ (RE = La, Gd, Y) [6], Cd₄REO(BO₃)₃ (RE = La, Gd and Y) [7], REAl₃(BO₃)₄ (RE = Y, Gd, Lu) [8-10] and K₇MRE₂(B₅O₁₀)₃ (M = Ca, Sr, Ba, Zn, Cd, Pb; RE = Sc, Y, Gd, Lu) [11, 12]. Rare-earth borates are also suitable candidates to host optically-active Er³⁺ and Yb³⁺ cations to serve as laser crystals [13, 14] and self-frequency doubling crystals [15, 16]. A high terbium content borate, LiCaTb₅(BO₃)₆ was found to be a promising Faraday rotator [17] possessing 55 % higher Verdet constant in the Vis-NIR range than that of commercial Tb₃Ga₅O₁₂ (TGG) crystal. Recently, LiCaTb₅(BO₃)₆ was further reported as a novel magnetic refrigerator [18] with a profound cooling enhancement over the benchmark medium Gd₃Ga₅O₁₃ (GGG) for the cryogenic temperatures especially above liquid hydrogen temperature.

A fascinating subgroup of the rare-earth borates is the quaternary A₂O-RE₂O₃-B₂O₃ (A = alkali metals, RE = rare earth) system, which attracts intensive research attention in recent years particularly due to its structural richness. To date, a vast array of novel alkali metal rare-earth borates with various structural motifs have been reported, such as Li₃RE₂(BO₃)₃[19],

$\text{Li}_3\text{RE}(\text{BO}_3)_2$ [20, 21], $\text{Na}_3\text{RE}(\text{BO}_3)_2$ [22-24], $\text{Na}_3\text{Y}_3(\text{BO}_3)_4$ [25], $\text{K}_3\text{RE}(\text{BO}_3)_2$ [26], $\text{K}_3\text{REB}_6\text{O}_{12}$ [12, 27], $\text{K}_3\text{Y}_3(\text{BO}_3)_4$ [28], $\text{Rb}_3\text{REB}_6\text{O}_{12}$ [29-31] and $\text{Rb}_3\text{La}_3(\text{BO}_3)_4$ [32]. Some of these compounds have stoichiometric similarity but crystallize in significantly different structures, where the size of the alkali and rare-earth cations is assumed to play an important role. For instance, $\text{Li}_3\text{RE}_2(\text{BO}_3)_3$ crystallize in the space group $P2_1/n$ whereas $\text{Na}_3\text{RE}_2(\text{BO}_3)_3$ crystallizes in the polar $Amm2$ and $\text{Rb}_3\text{RE}_2(\text{BO}_3)_3$ in the polar $Pna2_1$ space groups. Moreover, $\text{K}_3\text{RE}(\text{BO}_3)_2$ with light rare-earth elements (Nd, Sm, Eu and Gd) are to be refined in the orthorhombic space group $Pnma$ whereas the heavy rare-earth elements (Tb, Dy, Ho, Er, Tm, Yb and Lu) are described using $Pnnm$. In search of new compounds in the quaternary systems we obtained a series of potassium rare-earth borates $\text{K}_3\text{RE}_3(\text{BO}_3)_4$ (RE = Pr, Nd, Sm, Eu, Gd, Tb, Dy, Ho, Er, Tm, Yb and Lu) with novel structure types using solid-state synthesis as well as spontaneous crystallization methods. Herein, we described their comparative structural and spectroscopic features using single crystal and powder X-ray diffractions, FTIR, Raman and UV/Vis spectroscopy.

2. Experimental

2.1. Synthesis

Single crystals of $\text{K}_3\text{RE}_3(\text{BO}_3)_4$ (RE = Er, Tm and Yb) were obtained by spontaneous crystallization from high-temperature flux. The starting materials K_2CO_3 , Li_2CO_3 , RE_2O_3 (RE = Er, Tm and Yb) and H_3BO_3 with a molar ratio of 3: 3: 1: 8, were thoroughly ground in an agate mortar, and transferred to platinum crucibles. The mixtures in the crucibles were heated up to 1193 K in a muffle furnace with a heating rate of 100 K/h and maintained at that

temperature for 2 h to be thoroughly molten, then slowly cooled down to 773 at 3 K/h. Transparent millimeter-sized reddish $\text{K}_3\text{Er}_3(\text{BO}_3)_4$ and, colorless $\text{K}_3\text{Tm}_3(\text{BO}_3)_4$ and $\text{K}_3\text{Yb}_3(\text{BO}_3)_4$ single crystals were obtained. Single crystals of $\text{K}_3\text{RE}_3(\text{BO}_3)_4$ (RE = Pr and Lu) were prepared by flux-assisted syntheses. For $\text{K}_3\text{Pr}_3(\text{BO}_3)_4$, the starting materials K_2CO_3 , PrO_2 and H_3BO_3 with a molar ratio of 2: 3: 5, and for $\text{K}_3\text{Lu}_3(\text{BO}_3)_4$, K_2CO_3 , Lu_2O_3 and H_3BO_3 with a molar ratio of 2: 1.5: 5 were thoroughly mixed and ground in an agate mortar. The mixtures were transferred to platinum crucibles followed by heating up to 1223 K in a muffle furnace with a heating rate of 100 K/h and kept at that temperature for 24 h. The sample were then cooled down to room temperature, followed with power off. Transparent submillimeter-sized yellowish $\text{K}_3\text{Pr}_3(\text{BO}_3)_4$ and, colorless $\text{K}_3\text{Lu}_3(\text{BO}_3)_4$ single crystals were mechanically separated under the microscope.

The polycrystalline samples of $\text{K}_3\text{RE}_3(\text{BO}_3)_4$ (RE = Pr, Nd, Sm - Lu) were synthesized by solid-state reactions in alumina crucibles with analytically pure starting materials K_2CO_3 , H_3BO_3 and rare-earth oxides PrO_2 , Nd_2O_3 , Sm_2O_3 , Eu_2O_3 , Gd_2O_3 , Tb_4O_7 , Dy_2O_3 , Ho_2O_3 , Er_2O_3 , Tm_2O_3 , Yb_2O_3 and Lu_2O_3 . The stoichiometric mixtures were thoroughly ground, then heated at 773 K for 24 h, 973 K for another 24 h, finally sintered at 1173 K for another 24 h with intermediate grindings between the heating steps.

2.2. X-ray diffraction

Single crystal X-ray diffraction were performed at room temperature using a D8 Venture diffractometer (Bruker AXS GmbH, Karlsruhe, Germany) with molybdenum target using a pyrolytic graphite monochromator providing dichromatic $\text{MoK}\alpha_{1,2}$ ($\lambda_1 = 70.93171(4)$ pm, $\lambda_2 =$

71.3607(12) pm treated as average $\lambda = 71.073(1)$ pm) radiation. The numerical absorption correction was applied to the intensity data sets. The systematic extinctions and $|E^2-1|$ statistics suggested the monoclinic space group $P2_1/c$ for $K_3Er_3(BO_3)_4$, $K_3Tm_3(BO_3)_4$, $K_3Yb_3(BO_3)_4$ and $K_3Lu_3(BO_3)_4$; therefore, the structure determination was performed in this space group. Their structures were finely solved via the intrinsic phasing method and successfully refined on F^2 by full-matrix least-square methods with the ShelxT [33] and Shelxle [34] program packages. All atoms were refined with anisotropic displacement parameters and the final difference Fourier synthesis did not reveal any significant residual electron density. However, although the monoclinic space group $P2/c$ for $K_3Pr_3(BO_3)_4$ was initially suggested, the subsequent structure solution and refinement could not be successfully performed in the $P2/c$, Pc , $P2$ and even in any monoclinic space groups. Nevertheless, remarkable residual electron peaks and holes, high R -values, low $|E^2-1|$ value (~ 0.8), plenty of non-positive definite (NPD) atoms and significantly long interatomic B-O distances, suggested to conjecture the occurrence of a pseudo-merohedral twinning in $K_3Pr_3(BO_3)_4$, namely the metric parameters of α and γ happen to be very close to 90° . Thus, a triclinic space group $P\bar{1}$ was used to solve the structure by intrinsic phasing method, resulting to a starting R_1 value of 13 %. Afterward, a twin law $(-1\ 0\ 0\ 0\ 1\ 0\ 0\ 0\ -1)$ and an initial BASF value of 0.45, as suggested by the PLATON software [35], was introduced into the refinement. As a consequence, the R_1 factor converged down to 4.66 %. After all atoms were anisotropically refined, the final circle converges with $R_1 = 2.69\%$, $wR_2 = 3.03\%$ and BASF value of 0.4963(5), indicating a nearly “perfect twin” of $K_3Pr_3(BO_3)_4$. Meanwhile, neither non-positive definite atoms nor obvious residual electron densities were present in the final refinement, and none of constraint and restraint were used during the whole

refinement process. Relevant crystallographic data are listed in **table 1**. The bond valence sum (BVS) calculations were performed by the *Bondstr* software within the scope of the *FullProf* Suite [36].

Table 1: Crystallographic data and single crystal structural refinement for $K_3RE_3(BO_3)_4$ (RE = Pr, Er, Tm, Yb and Lu).

Formula	$K_3Pr_3(BO_3)_4$	$K_3Er_3(BO_3)_4$	$K_3Tm_3(BO_3)_4$	$K_3Yb_3(BO_3)_4$	$K_3Lu_3(BO_3)_4$
Weight	775.27	854.31	859.33	871.65	877.45
Space group	$P\bar{1}$	$P2_1/c$	$P2_1/c$	$P2_1/c$	$P2_1/c$
a / pm	1081.67(10)	1051.89(2)	1049.94(5)	1045.92(2)	10.4282(3)
b / pm	907.76(9)	1743.22(4)	1738.14(8)	1735.19(4)	17.3029(6)
c / pm	1410.14(16)	1383.05(3)	1379.29(6)	1376.14(3)	13.7515(4)
α /°	90.051(6)	90	90	90	90
β /°	110.257(6)	110.5210(10)	110.514(2)	110.329(1)	110.286(1)
γ /°	89.901(6)	90	90	90	90
$V / 10^6 \times \text{pm}^3$	1299.0(2)	2375.14(9)	2357.50(19)	2341.95(9)	2327.39(13)
Z	4	8	8	8	8
Temperature /K	303(2)	303(2)	302(2)	301(2)	303(2)
Wavelength /pm	71.0747(6)	71.0747(6)	71.0747(6)	71.0747(6)	71.0747(6)
Crystal Size /mm ³	0.141 × 0.124 × 0.092	0.059 × 0.058 × 0.054	0.214 × 0.184 × 0.093	0.147 × 0.107 × 0.091	0.108 × 0.093 × 0.075
Abs. coeff. / mm ⁻¹	12.092	22.118	23.525	24.883	26.387
$F(000) / e$	1400	3016	3040	3064	3088
θ range /°	2.06–30.578	1.96 – 28.37	1.96 – 30.60	1.97 – 28.36	1.97 – 30.59
Range in hkl	$-15 \leq h \leq 15,$ $-12 \leq k \leq 12,$ $-20 \leq l \leq 20$	$-14 \leq h \leq 14,$ $-23 \leq k \leq 23,$ $-18 \leq l \leq 18$	$-15 \leq h \leq 15,$ $-24 \leq k \leq 24,$ $-19 \leq l \leq 19$	$-13 \leq h \leq 13,$ $-23 \leq k \leq 23,$ $-18 \leq l \leq 18$	$-14 \leq h \leq 14,$ $-24 \leq k \leq 24,$ $-19 \leq l \leq 19$
No. of reflections	74731	149449	135682	155507	155571
Data/ Parameters	7319/399	5931/398	7232/398	5848/398	7135/398
GOF (F^2)	1.055	1.072	1.109	1.131	1.086
R_1 ($I > 2 \sigma(I)$)	0.0206	0.0218	0.0191	0.0224	0.0295
R_1 (all data)	0.0269	0.0333	0.0266	0.0316	0.0493
wR_2 (all data)	0.0303	0.0353	0.0356	0.0395	0.0381

The X-ray powder diffraction (XRPD) pattern were recorded on a Bruker D8 Discover powder diffractometer using Bragg-Brentano geometry with $\text{CuK}\alpha_{1,2}$ ($\lambda_{\text{K}\alpha 1} = 154.05929(5)$ pm, $\lambda_{\text{K}\alpha 2} = 154.4414(2)$ pm) radiation. The measurements were carried out at ambient condition

with a step size of 0.0149° and a data collection time of 1 s/step. The fundamental parameter approach, where the fundamental parameters were fitted against a LaB_6 standard material, was applied for the Rietveld refinement using “Diffrac^{Plus} Topas 6” software (Bruker AXS GmbH, Karlsruhe, Germany). The starting lattice parameters and atomic coordinates were taken from the results of the single crystal structure determinations. In some cases, small amount of REBO_3 phase was identified and the associated spectroscopic analyses shall be considered.

2.2. Spectroscopy

Fourier transform infrared (FTIR) spectroscopy

The FTIR spectra were recorded on a Bruker IFS66v/S spectrometer (Bruker Optik GmbH, Ettlingen, Germany) using the standard KBr method for the data collection in the mid infrared range (MIR). 2 mg sample was mixed with 200 mg dried KBr and pressed at 10 kN, forming disks of 12 mm in diameter. The reference pellet consists of 200 mg dried KBr only. Measurements were carried out between 370 and 4000 cm^{-1} with a total acquisition of 128 spectra, leading to a spectral resolution of about 1.0 cm^{-1} .

Raman spectroscopy

Due to laser induced susceptibility of the 4f-electronic transitions of the rare-earth cations, Raman spectra were measured at ambient condition using at least three lasers (532 nm, 633 nm and 785 nm). To avoid the fluorescence emissions arising from 4f-4f transitions of $\text{K}_3\text{RE}_3(\text{BO}_3)_4$ (see also UV/Vis spectra below) laser wavelengths of 532 nm was chosen for RE = Yb, 633 nm for RE = Nd, Sm, Gd, Tb, Dy, Tm and Lu, and 785 nm for RE = Pr, Ho and Er. Raman spectra were collected in the range between 85 cm^{-1} and 1700 cm^{-1} with a moving

grating of 1800 grooves/mm and a thermoelectrically cooled CCD detector (Synapse, 1024 × 256 pixels). The spectral positions were calibrated against the Raman mode of silicon before and after the sample measurements.

UV/Vis diffuse reflectance spectroscopy

Optical diffuse reflectance spectra were recorded at room temperature on a Shimadzu UV-2600 (Shimadzu, Kyoto, Japan) spectrophotometer equipped with an ISR-2600 plus two-detector integrating sphere (Pike Technologies, USA). Data were collected in the range of 200 to 850 nm with a step of 1.0 nm. A standard BaSO₄ sample was used as reference for the baseline correction.

The diffuse reflectance data were converted to F(R) spectra according to the Kubelka-Munk function [37]

$$F(R) = \frac{(1 - R)^2}{2R}$$

where R is the reflectance. The Tauc's method [38] followed by the Kubelka-Munk function are commonly used to estimate the bandgap energy by finding the intercept of the abscissa from the following relations:

$$F(R)(h\nu) = B(h\nu - E_g)^n$$

where h is the Planck's constant, ν the frequency of light, E_g the bandgap in eV and n - the type of optical transition. That is, for $n = 2$ and $\frac{1}{2}$ refers to direct and indirect transition, respectively. Recently, the derivation of absorption spectrum fitting (DASF) method [39] was proposed for thin films to calculate the bandgap energies without any presumption of the nature of the transition. Based on this, the DASF can also be expressed as follows proposed by Kirsch et al. [40, 41] for powder samples:

$$\frac{d\ln F(R)}{dh\nu} = \frac{n}{h\nu - E_g}$$

Combining the results of the absolute bandgap width determination using the DASf method with the values for a direct or indirect transition obtained by the Tauc method, type and width of the band gap could be experimentally identified.

3. Results and discussion

Crystal structure

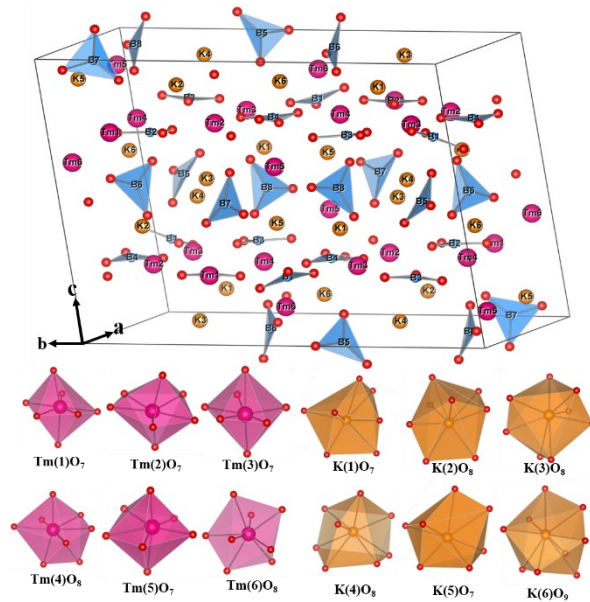


Figure 1: Representative crystal structure of $K_3Tm_3(BO_3)_4$, showing the building blocks.

Single crystal diffraction data analysis reveals that each member of $K_3RE_3(BO_3)_4$ (RE = Er - Lu) is isotypic and can be described in the space group $P2_1/c$ whereas both $K_3Pr_3(BO_3)_4$ and $K_3Nd_3(BO_3)_4$ are as well isotypic to each other but must be described in space group $P\bar{1}$. Herein we choose representative $K_3Tm_3(BO_3)_4$ and $K_3Pr_3(BO_3)_4$ to describe the detailed crystal structural features. The metric parameters of the monoclinic phase $K_3Tm_3(BO_3)_4$ were obtained as $a = 1049.94(5)$ pm, $b = 1738.14(8)$ pm, $c = 1379.29(6)$ pm and $\beta = 110.514(1)^\circ$. As shown in **figure 1**, the crystallographic asymmetric unit of $K_3Tm_3(BO_3)_4$ comprises six unique thulium,

six potassium, eight boron and twenty-four oxygen atoms. Each boron atom is bound to three oxygen atoms, building an isolated BO_3 triangular anionic group. Interestingly, four of the BO_3 groups, namely, $(\text{B}(1)\text{O}_3, \text{B}(2)\text{O}_3, \text{B}(3)\text{O}_3 \text{ and } \text{B}(4)\text{O}_3)$ are almost parallel to the ab plane, whereas the other four $(\text{B}(5)\text{O}_3, \text{B}(6)\text{O}_3, \text{B}(7)\text{O}_3 \text{ and } \text{B}(8)\text{O}_3)$ groups are oriented parallel to the c -direction. The thulium atoms adopt two types of coordination: $\text{Tm}(1)$, $\text{Tm}(2)$, $\text{Tm}(3)$ and $\text{Tm}(5)$ are located at the centroid of a slightly distorted TmO_7 pentagonal bipyramid while $\text{Tm}(4)$ and $\text{Tm}(6)$ are surrounded by eight oxygen atoms forming a distorted TmO_8 dodecahedra. The $\text{Tm}(1)\text{O}_7$, $\text{Tm}(2)\text{O}_7$, $\text{Tm}(3)\text{O}_7$, $\text{Tm}(4)\text{O}_8$ polyhedra are linked with each other via corner-sharing and are further joined by $\text{B}(1)\text{O}_3$, $\text{B}(2)\text{O}_3$, $\text{B}(3)\text{O}_3$ and $\text{B}(4)\text{O}_3$ groups to generate a quasi-two-dimensional (Q2D) $[\text{Tm}_8(\text{BO}_3)_8]^\infty$ layer in the ab plane, as displayed in **figure 2**. This Q2D $[\text{Tm}_8(\text{BO}_3)_8]^\infty$ layer is regulated by the 2_1 screw axis along the b -direction, where every BO_3 group reinforces three $\text{TmO}_{7/8}$ polyhedra. The $\text{B}(1)\text{O}_3$ trigonal group is linked via three oxygen vertices of the $\text{Tm}(1)\text{O}_7$, $\text{Tm}(2)\text{O}_7$ and $\text{Tm}(3)\text{O}_7$ polyhedral units. Opposite, the $\text{B}(2)\text{O}_3$ and $\text{B}(4)\text{O}_3$ groups share the edges with $\text{Tm}(1)\text{O}_7$, $\text{Tm}(2)\text{O}_7$, $\text{Tm}(4)\text{O}_8$, and $\text{Tm}(2)\text{O}_7$, $\text{Tm}(3)\text{O}_7$ $\text{Tm}(4)\text{O}_8$ polyhedra, respectively. Moreover, the $\text{B}(3)\text{O}_3$ groups share two edges with $\text{Tm}(1)\text{O}_7$ and $\text{Tm}(3)\text{O}_7$ and one vertex with $\text{Tm}(4)\text{O}_8$. Between the $[\text{Tm}_8(\text{BO}_3)_8]^\infty$ layers, $\text{Tm}(5)_2\text{O}_{12}$ and $\text{Tm}(6)_2\text{O}_{14}$ dimers are linked via single edge-sharing (**figure 2b**). Two adjacent $[\text{Tm}_8(\text{BO}_3)_8]^\infty$ layers are interconnected along the c -direction alternately by $\text{Tm}(5)_2\text{O}_{12}$ and $\text{Tm}(6)_2\text{O}_{14}$ dimers through face/edge-sharing. The $\text{B}(5)\text{O}_3$, $\text{B}(6)\text{O}_3$, $\text{B}(7)\text{O}_3$ and $\text{B}(8)\text{O}_3$ groups additionally strengthen the linkage among these Q2D $[\text{Tm}_8(\text{BO}_3)_8]^\infty$ layers by the contributions of the strong covalent B-O bonds along the c -direction, forming a 3D framework. The $\text{K}(1)$,

K(2), K(3) and K(4) cations are located in a channel along the **a**-direction while K(5) and K(6) are located at interstitial voids of the 3D framework.

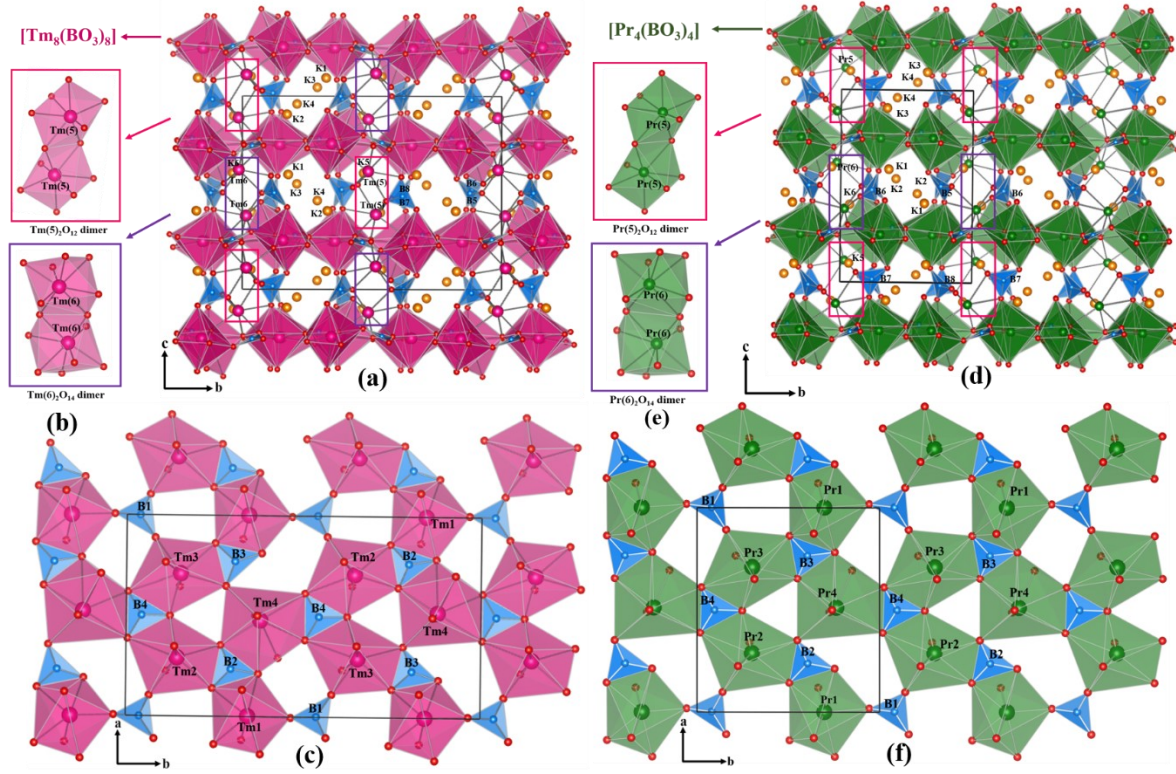


Figure 2: Crystal structures of $K_3Tm_3(BO_3)_4$ (a) and $K_3Pr_3(BO_3)_4$ (d) along the **a**-axis. The quasi-two-dimensional $[Tm_8(BO_3)_8]$ (c) $[Pr_4(BO_3)_4]$ (f) layers show the connectivity of $Tm(5)_2O_{12}$ and $Tm(6)_2O_{14}$ (b), and $Pr(5)_2O_{12}$ and $Pr(6)_2O_{14}$ dimers (e), respectively.

Table 2: Average bond length (M-O /pm) of the MO_x coordination spheres for Tm, K and B atoms together with their bond valence sum (BVS /v.u.) of $K_3Tm(BO_3)_4$.

Polyhedra	M-O	BVS	Polyhedra	M-O	BVS
Tm(1)O ₇	229.9(3)	3.17(1)	K(1)O ₇	281.9(3)	1.13(1)
Tm(2)O ₇	231.3(3)	3.19(1)	K(2)O ₈	285.02(3)	1.26(1)
Tm(3)O ₇	233.0(3)	3.17(1)	K(3)O ₈	285.5(3)	1.23(1)
Tm(4)O ₈	246.0(3)	2.68(1)	K(4)O ₈	286.8(3)	1.16(1)
Tm(5)O ₇	230.4(3)	3.19(1)	K(5)O ₇	284.7(3)	1.14(1)
Tm(6)O ₈	237.1(3)	3.05(1)	K(6)O ₉	292.0(3)	1.17(1)
B(1)O ₃	137.7(5)	2.95(1)	B(5)O ₃	137.4(5)	2.98(1)
B(2)O ₃	137.1(5)	3.00(1)	B(6)O ₃	137.0(5)	3.01(1)
B(3)O ₃	137.9(5)	2.94(1)	B(7)O ₃	136.7(5)	3.04(1)
B(4)O ₃	137.5(5)	2.97(1)	B(8)O ₃	137.7(5)	2.95(1)

The average B-O bond distances range from 136.7(5) to 137.9(5) pm with the bond valence sums (BVS) from 2.94(1) to 3.01(1) v.u. (table 2). The average Tm-O distances vary from 229.9(3) to 246.0(3) pm. As could be seen, most of the Tm cations are slightly over bonded, except Tm(4) which is strongly under bonded and Tm(6), which has a normal charge value. Here, it shall be mentioned that those oxygen atoms with the interatomic distances to K cations below 320.0 pm will be considered to participate the coordination spheres of central K cations. As a consequence, K(1) and K(5) locate at the centroid of KO_7 polyhedra, K(2), K(3) and K(4) of KO_8 polyhedra, K(6) of a KO_9 polyhedron, respectively. The average interatomic distances and BVS of K-O are between 280.50(5) pm / 1.26(1) v.u. to 281.9(3) pm / 1.13(1) v.u. (**table 2**). All the bond lengths fall in the normal range of the sum of effective ionic radii [42, 43] with the corresponding coordination number (CN): 138.0 pm of O^{2-} ; 94.0 pm and 99.4 pm of Tm^{3+} with CN = 7, 8; 146.0 pm, 151.0 pm and 155.0 pm of K^+ with CN = 7, 8, 9, respectively. The calculated BVS value of each atom lies close to their respective integer oxidation state (Table 4). 3): 3.07(1), 1.18(1) and 2.98(1) v.u. for Tm^{3+} , K^+ and B^{3+} , respectively. A slightly higher BSV of K^+ indicates to tight K-O bonding to the channels, where the charge difference could be compensated by the available framework cations. This leads to the assumption that the K^+ cations may hardly be replaced by ion exchange. Similar results are found for $\text{K}_3\text{Er}_3(\text{BO}_3)_4$ and for $\text{K}_3\text{Yb}_3(\text{BO}_3)_4$ as well as for $\text{K}_3\text{Lu}_3(\text{BO}_3)_4$ (**table 3**).

The crystal structure of $\text{K}_3\text{Pr}_3(\text{BO}_3)_4$ is described using the triclinic space group $P\bar{1}$ with metric parameters of $a = 1081.67(10)$ pm, $b = 907.76(9)$ pm, $c = 1410.14(16)$ pm, $\alpha = 90.051(6)^\circ$, $\beta = 110.257(6)^\circ$ and $\gamma = 89.901(6)^\circ$ (**table 1**). The structure is highly correlated to that of $\text{K}_3\text{Tm}_3(\text{BO}_3)_4$. Each of the boron atoms is triangularly coordinated by oxygen atoms, forming

BO₃ group. Pr(1), Pr(2), Pr(3) and Pr(5) are located at the centroid of a slightly distorted PrO₇ pentagonal bipyramids and, Pr(4) and Pr(6) of PrO₈ dodecahedra. Pr(1)O₇, Pr(2)O₇, Pr(3)O₇ and PrO₈ polyhedra are further interlinked with four BO₃ groups, building the Q2D [Pr₄(BO₃)₄][∞] layers. The length of the [Pr₄(BO₃)₄][∞] layer is nearly half of the length of the [Tm₈(BO₃)₈][∞], corresponding to the *b*-parameter of K₃Pr₃(BO₃)₄ approximately half of that of K₃Tm₃(BO₃)₄. Those Q2D [Pr₄(BO₃)₄][∞] layers are alternatively connected by Pr(5)₂O₁₂ or Pr(6)₂O₁₄ dimers almost along the *c*-direction, unlike Tm(5)₂O₁₂ and Tm(6)₂O₁₄ dimers along the *c*- and *b*-direction. A different arrangement of K⁺ and BO₃ groups could also be observed, arising from the absence of the 2₁-screw axis along the *b*-direction in K₃Pr₃(BO₃)₄. The symmetry reduction from *P*2₁/*c* for K₃Tm₃(BO₃)₄ to *P* $\bar{1}$ for K₃Pr₃(BO₃)₄ may result from the size effect, where the Pr³⁺ cation possesses a larger radius than that of the Tm³⁺ cation. All the bond lengths in K₃Pr₃(BO₃)₄ results in BVS values close to the respective integer ones, as given in **table 3**.

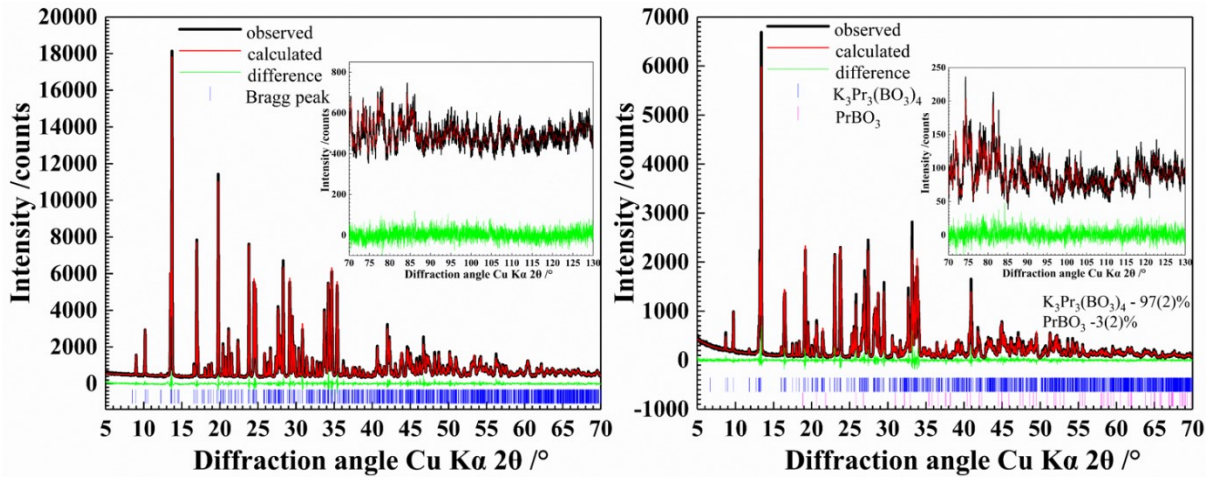


Figure 3: X-ray powder data Rietveld plots of K₃Tm₃(BO₃)₄ (left) and K₃Pr₃(BO₃)₄ (right), showing the high angle region as insets.

Table 3: Average bond length (M-O /pm) and bond valence sums (BVS /v. u.) of the cations (M) of $K_3RE_3(BO_3)_4$ (RE = Pr, Nd, Sm-Lu).

Compound	RE-O	K-O	B-O	BVS (B)	BVS (K)	BVS (RE)
$K_3Pr_3(BO_3)_4$	247.4(3)	296.8(3)	137.8(5)	3.19(1)	0.99(1)	2.95(1)
$K_3Nd_3(BO_3)_4$	246.1(3)	296.8(5)	137.2(5)	3.03(1)	1.03(1)	3.00(1)
$K_3Sm_3(BO_3)_4$	242.2(3)	295.9(5)	137.9(8)	3.28(1)	1.07(1)	2.94(1)
$K_3Eu_3(BO_3)_4$	242.0(3)	291.7(5)	138.9(8)	3.23(1)	1.10(1)	2.86(1)
$K_3Gd_3(BO_3)_4$	240.7(3)	288.5(5)	138.2(8)	3.23(1)	1.09(1)	2.93(1)
$K_3Tb_3(BO_3)_4$	239.4(3)	286.1(5)	138.0(8)	3.03(1)	1.11(1)	2.93(1)
$K_3Dy_3(BO_3)_4$	237.4(3)	287.9(5)	138.6(8)	2.88(1)	1.12(1)	2.88(1)
$K_3Ho_3(BO_3)_4$	236.8(3)	287.3(5)	138.1(8)	3.12(1)	1.14(1)	2.93(1)
$K_3Er_3(BO_3)_4$	235.8(3)	286.3(4)	137.4(6)	2.89(1)	1.15(1)	2.98(1)
$K_3Tm_3(BO_3)_4$	234.9(3)	286.2(3)	137.4(5)	3.07(1)	1.18(1)	2.98(1)
$K_3Yb_3(BO_3)_4$	234.3(4)	285.9(4)	137.4(7)	2.88(1)	1.19(1)	2.98(1)
$K_3Lu_3(BO_3)_4$	233.6(4)	285.5(5)	137.3(7)	2.99(1)	1.21(1)	2.99(1)

To further cross-check the accuracy of crystal structure obtained from the X-ray single crystal diffraction data, complementary Rietveld refinements were performed on X-ray powder diffraction data of $K_3RE_3(BO_3)_4$ (RE = Pr, Nd, Sm - Lu). The representative Rietveld plots of $K_3Tm_3(BO_3)_4$ and $K_3Pr_3(BO_3)_4$ are depicted in **figure 3**, and the other Rietveld plots are shown in **figure S1 – S10**. (Supplementary Information). Although the powder diffraction pattern of all $K_3RE_3(BO_3)_4$ members look similar to each other, the results of Rietveld refinement reveal that $K_3RE_3(BO_3)_4$ (RE = Sm - Lu) are isotypic to be described in the monoclinic $P2_1/c$ space group except the Pr- and Nd-analogues which crystallize in the triclinic space group $P\bar{1}$. Of notes, we also attempt to use the starting model with the space group $P2_1/c$ and $P2/c$ to refine the powder diffraction patterns of $K_3Pr_3(BO_3)_4$ and $K_3Nd_3(BO_3)_4$, leading to poor refinement

results (e.g., **figure S11**). A similar pseudo-monoclinic symmetry was observed in the oxygen-deficient distorted fluorite-type rare-earth borates $\text{RE}_{26}\text{O}_{27}\square(\text{BO}_3)_8$, for instance, $P2_1/c$ for $\text{La}_{26}\text{O}_{27}\square(\text{BO}_3)_8$ and $P\bar{1}$ for $\text{Nd}_{26}\text{O}_{27}\square(\text{BO}_3)_8$, where the α and γ angles slightly deviate from 90, unveiled by the combined X-ray single crystal analyses and Rietveld refinement of the powder diffraction data [44-46].

Table 4: Comparison of the space group (SG), lattice parameters (/pm), β -angle ($^\circ$) and unit cell volumes ($/10^4 \text{ pm}^3$) between the present and reported alkali rare-earth borates $\text{A}_3\text{RE}_3(\text{BO}_3)_4$ for $\text{A} = \text{Na}, \text{K}, \text{Rb}$.

Compound	SG	<i>a</i>	<i>b</i>	<i>c</i>	β	<i>V</i>	Sample	CSD/Ref.
$\text{K}_3\text{Pr}_3(\text{BO}_3)_4$	$P\bar{1}$	1081.67(10)	907.76(9)	1410.14(16)	110.257(6)	1299.0(2)	Single crystal	2034347
$\text{K}_3\text{Pr}_3(\text{BO}_3)_4$	$P\bar{1}$	1079.873(10)	908.101(9)	1408.573(14)	110.193(1)	1296.36(29)	powder	-
$\text{K}_3\text{Nd}_3(\text{BO}_3)_4$	$P\bar{1}$	1075.98(2)	903.140(19)	1406.27(3)	110.2693(16)	1281.90(5)	powder	2034350
$\text{K}_3\text{Sm}_3(\text{BO}_3)_4$	$P2_1/c$	1070.484(17)	1786.10(3)	1400.94(2)	110.4510(10)	2509.76(7)	powder	2034349
$\text{K}_3\text{Eu}_3(\text{BO}_3)_4$	$P2_1/c$	1067.682(19)	1779.76(3)	1397.72(3)	110.4574(11)	2488.46(8)	powder	2034351
$\text{K}_3\text{Gd}_3(\text{BO}_3)_4$	$P2_1/c$	1064.37(2)	1773.32(4)	1396.09(3)	110.4400(15)	2469.17(10)	powder	2034410
$\text{K}_3\text{Tb}_3(\text{BO}_3)_4$	$P2_1/c$	1061.574(14)	1763.58(2)	1392.425(19)	110.5702(8)	2440.65(6)	powder	2034353
$\text{K}_3\text{Dy}_3(\text{BO}_3)_4$	$P2_1/c$	1058.688(12)	1757.482(19)	1388.286(16)	110.5317(7)	2419.00(5)	powder	2034354
$\text{K}_3\text{Ho}_3(\text{BO}_3)_4$	$P2_1/c$	1055.028(15)	1752.58(2)	1385.81(2)	110.4841(9)	2400.37(6)	powder	2034355
$\text{K}_3\text{Er}_3(\text{BO}_3)_4$	$P2_1/c$	1051.46(3)	1741.61(5)	1382.37(4)	110.544(1)	2370.45(12)	Single crystal	2034356
$\text{K}_3\text{Er}_3(\text{BO}_3)_4$	$P2_1/c$	1052.391(6)	1745.265(11)	1383.500(9)	110.4914(4)	2380.29(3)	powder	-
$\text{K}_3\text{Tm}_3(\text{BO}_3)_4$	$P2_1/c$	1049.94(5)	1738.14(8)	1379.29(6)	110.514(2)	2357.50(19)	Single crystal	2034357
$\text{K}_3\text{Tm}_3(\text{BO}_3)_4$	$P2_1/c$	1048.289(8)	1738.862(13)	1376.936(11)	110.4031(5)	2352.46(3)	powder	-
$\text{K}_3\text{Yb}_3(\text{BO}_3)_4$	$P2_1/c$	1045.92(2)	1735.19(4)	1376.14(3)	110.329(1)	2341.95(9)	Single crystal	2034376
$\text{K}_3\text{Yb}_3(\text{BO}_3)_4$	$P2_1/c$	1046.216(8)	1737.961(12)	1376.727(10)	110.3269(5)	2347.39(5)	powder	-
$\text{K}_3\text{Lu}_3(\text{BO}_3)_4$	$P2_1/c$	1042.82(3)	1730.29(6)	1375.15(4)	110.2860(10)	2327.39(13)	Single crystal	2034358
$\text{K}_3\text{Lu}_3(\text{BO}_3)_4$	$P2_1/c$	1043.461(5)	1731.655(8)	1375.873(6)	110.2734(3)	2332.071(19)	powder	-
$\text{K}_3\text{Y}_3(\text{BO}_3)_4$	$P2_1/c$	1046.67(16)	1736.1(3)	1378.1(2)	110.548(8)	2344.8(7)	Single crystal	[28]
$\text{Na}_3\text{Y}_3(\text{BO}_3)_4$	$P6_3mc$	1011.36(14)	1011.36(14)	674.85(13)	90.0	597.79(16)	Single crystal	[25]
$\text{Rb}_3\text{La}_3(\text{BO}_3)_4$	$P2/c$	1100.24(17)	929.79(14)	1450.0(2)	110.879(2)	1385.9(4)	Single crystal	[32]

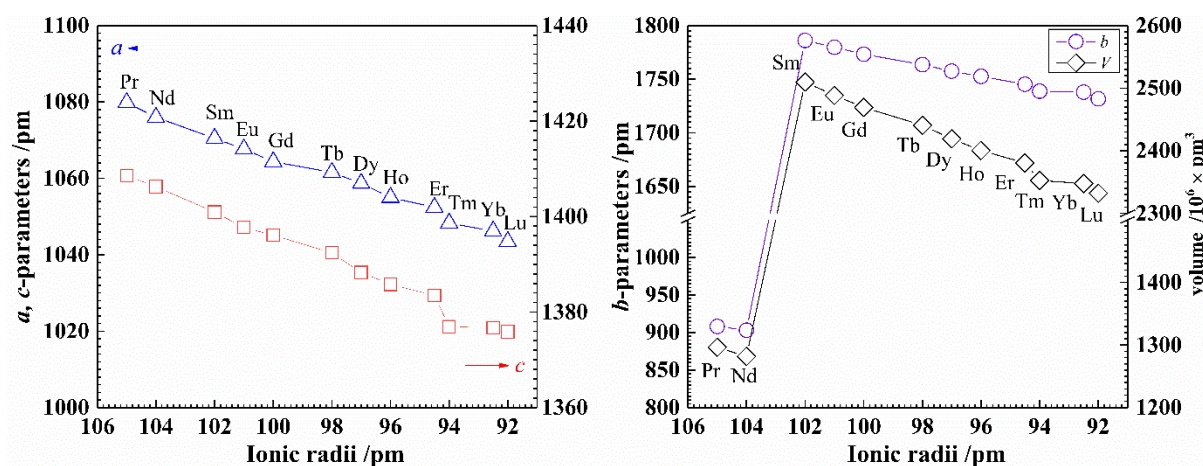


Figure 4: Lattice parameters as well as unit cell volumes of $K_3RE_3(BO_3)_4$ (RE = Pr, Nd, Sm - Lu)

The structural parameters are in excellent agreement with those of the results obtained from the single crystal data analyses. The evolution of the metric parameters obtained from the XRPD data Rietveld refinement are shown in **figure 4** and **table 4**. The *a*- and *c*-parameters of $K_3RE_3(BO_3)_4$ (RE= Pr, Nd, Sm-Lu) decrease with an increase of the atomic number with the shrinking radius of the RE^{3+} cations, known as the lanthanide contraction. Due to the absence of the 2_1 -screw axis running along the **b**-direction, the *b*-parameters of Pr and Nd-containing phases are approximately half of those of the other rare-earth analogues. Nevertheless, the *b*-parameters and cell volumes of $K_3RE_3(BO_3)_4$ (RE = Sm-Lu) comply with the lanthanide contraction. A detailed comparison between the previously reported $A_3RE_3(BO_3)_4$ phases (A = Na, K, Rb) and the present $K_3RE_3(BO_3)_4$ (RE = Pr, Nd, Sm - Lu) phases are summarized (**table 4**). Despite similar chemical formulae, structural variation occur in $Na_3Y_3(BO_3)_4$ ($P6_3mc$) [25], $K_3RE_3(BO_3)_4$ (Pr, Nd in $P\bar{1}$, Sm-Lu and Y in $P2_1/c$) and $Rb_3La_3(BO_3)_4$ ($P2/c$) [32]. As the asymmetric units of $K_3Y_3(BO_3)_4$ [28] $K_3Tm_3(BO_3)_4$ contain similar Wyckoff sites, it can be safely concluded that $K_3Y_3(BO_3)_4$ is isostructural to the $K_3RE_3(BO_3)_4$ (RE = Sm - Lu). Due to

the size of Y^{3+} cations, close to that of Dy^{3+} and Ho^{3+} cations, this isomorphism is expected. The lattice parameters of $Rb_3La_3(BO_3)_4$ is comparable to those of $K_3RE_3(BO_3)_4$ ($RE = Pr, Nd$), which implies that $Rb_3La_3(BO_3)_4$ to be structurally correlated to $K_3RE_3(BO_3)_4$ family. In the unit cell of $Rb_3La_3(BO_3)_4$ [32], two La-, two B- and two O-atoms are found to occupy the two-fold special sites whereas the whole of crystallographic independent sites in the asymmetric unit of $K_3RE_3(BO_3)_4$ ($Pr, Nd, Sm - Lu$) are general sites, indicating that the symmetry of 2-fold rotation axis along the **b**-direction breaks in all of $K_3RE_3(BO_3)_4$ members. As a result, $K_3RE_3(BO_3)_4$ ($RE = Pr - Nd$) could be regarded as a pseudo-monoclinic archetype of $Rb_3La_3(BO_3)_4$ while $K_3RE_3(BO_3)_4$ ($RE = Sm - Lu$) can be viewed as a one-dimensional superstructure of $Rb_3La_3(BO_3)_4$ along the **b**-axis. It is worthwhile to mention that we also tried to solve the structure of $K_3Tm_3(BO_3)_4$, $K_3Er_3(BO_3)_4$, $K_3Yb_3(BO_3)_4$ and $K_3Lu_3(BO_3)_4$ with the $P2/c$ space group and $b/2$ -parameters of $Rb_3La_3(BO_3)_4$. However, the respective structure refinements presented four positional disorder O-atoms and several much too long B-O bonds (bond lengths approach to around 144.5 pm for trigonal BO_3 group). Therefore, it can be concluded that the structures of $K_3RE_3(BO_3)_4$ ($RE = Sm - Lu$) crystallize in space group $P2_1/c$ and not in the $P2/c$ symmetry of $Rb_3La_3(BO_3)_4$. In comparison to $Na_3Y_3(BO_3)_4$ with a hexagonal open framework, much more close-packed arrangements are found in $K_3RE_3(BO_3)_4$ and $Rb_3La_3(BO_3)_4$ probably owing to the larger ionic radii of K^+ and Rb^+ than Na^+ . Furthermore, attempts to synthesize $K_3La_3(BO_3)_4$ and $K_3Ce_3(BO_3)_4$ was not successful, suggesting that both La^{3+} or Ce^{3+} cations may be too large for the structure of $K_3RE_3(BO_3)_4$ family.

UV/Vis spectra

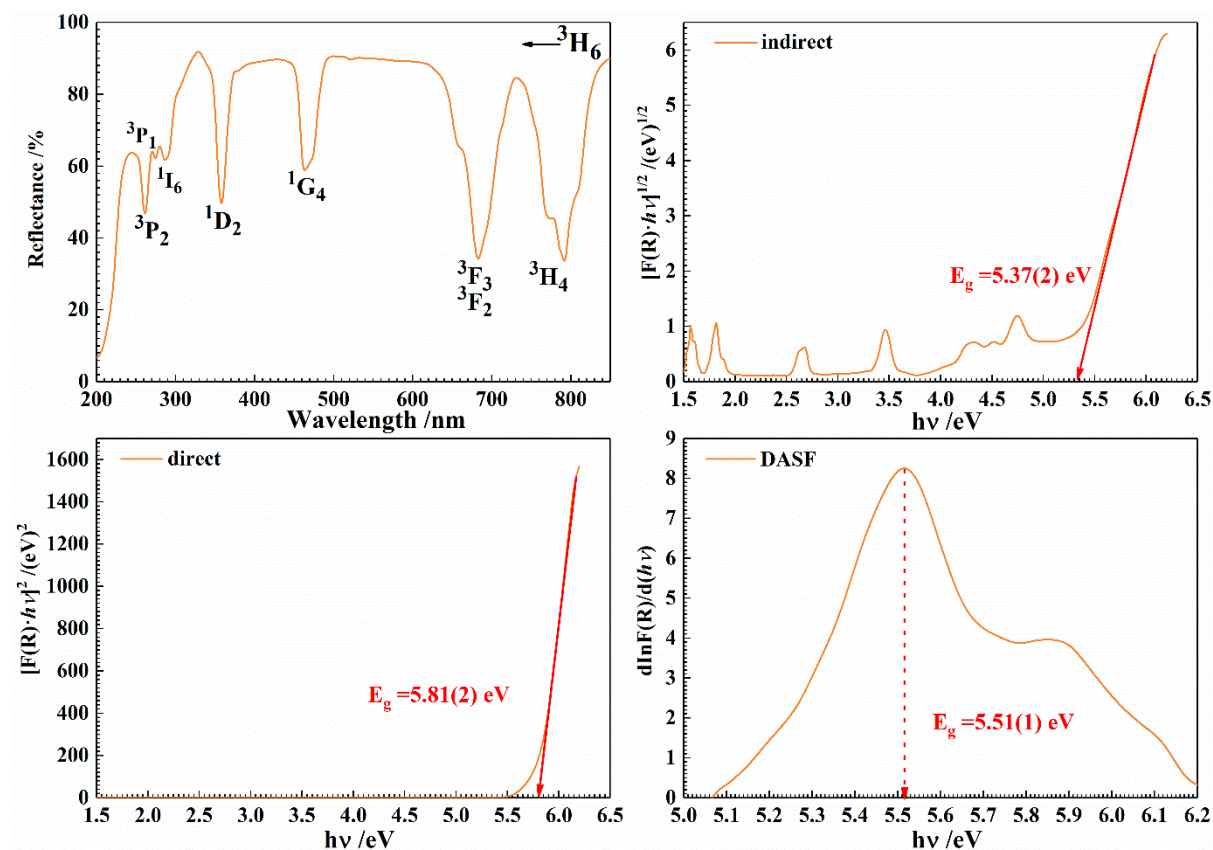


Figure 5: UV/Vis diffuse reflectance spectrum of $K_3Tm_3(BO_3)_4$ (top left), Tauc plots for indirect (bottom left) and direct (top right) optical transitions, and DASf plot (bottom right).

Beside the fundamental band gap absorption edge, the UV/Vis spectra are dominated by characteristic electron transitions. According to the energy diagrams proposed by Dieke and Carnall [47, 48] the intra- (f–f) and inter-(f–d) orbital transitions of the RE^{3+} cations exhibit characteristic absorption peaks between 200 nm and 850 nm, as shown in **figure 5** and **figure S12 – S22**. Among them, $K_3Tm_3(BO_3)_4$ exhibits strong absorption bands at 255(2), 360(2), 455(2), 680(2) and 790(2) nm, which usually correspond to the intra f-f transitions: $^3H_6 \rightarrow ^3P_2$, 1D_2 , 1G_4 , $^3F_{n=2,3}$ and 3H_4 , respectively. The characteristic absorption bands of other rare-earth cations in the visible range are observed at 445(2),

471(2), 487(2) and 590(2) nm for $K_3Pr_3(BO_3)_4$; 533(2), 590(2) and 742(2) nm for $K_3Nd_3(BO_3)_4$; 405(2) and 473(2) nm for $K_3Sm_3(BO_3)_4$; 483(2) nm for $K_3Tb_3(BO_3)_4$; 419(2), 453(2), 537(2) and 640(2) nm for $K_3Ho_3(BO_3)_4$; 487(2), 523(2) and 651(2) nm for $K_3Er_3(BO_3)_4$. Samples $K_3RE_3(BO_3)_4$ for RE = Eu, Gd, Yb, Lu do not contain significantly intense absorptions above 400 nm, which contribute to their colourlessness in daylight. As such, beside the fundamental absorption, the characteristic electronic transition of RE^{3+} cations are labelled respectively. To determine the type and width of the bandgap, a combination of the Tauc method analysing $[F(R)*hv]^{1/n}$ with $n = 2$ for indirect and $n = 0.5$ for direct bandgap transitions and the DASF method by evaluating the derivative transition peak to obtain the absolute value of the bandgap energy (**figure 5d**) were used. The combined approach implies that each member of the $K_3Er_3(BO_3)_4$ series exhibits indirect bandgaps of 4.71(1), 5.28(1), 5.51(1) and 4.45(3) eV for Pr-, Gd-, Tm- and Yb-analogues, respectively. Direct bandgaps of 5.74(3), 4.99(1), 3.82(1), 5.41(1), 5.86(4), 5.99(1), 6.02(1) and 6.09(2) eV are observed for Nd-, Sm-, Eu-, Tb-, Dy-, Ho-, Er-, Lu-analogues, respectively. These values are comparable to those of the other rare-earth sesquioxides [49], but significantly lower than that of the well-known β -BaB₂O₄, LiB₃O₅ and KBe₂BO₃F₂ NLO borate crystals [50].

Vibrational spectra

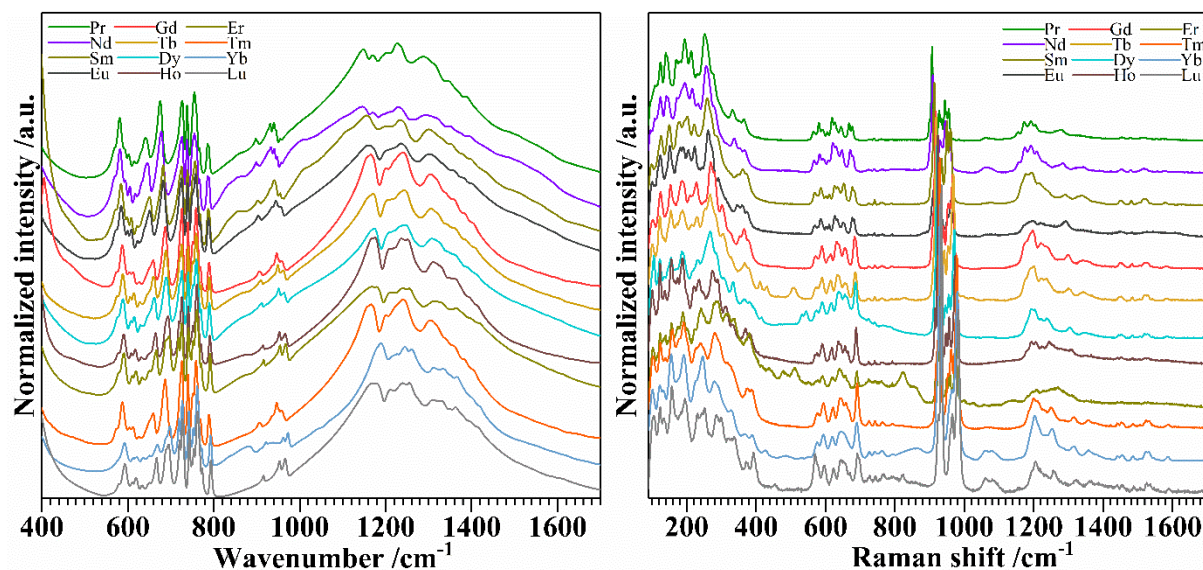


Figure 6: Fourier transform infrared (left) and Raman (right) spectra of $K_3RE_3(BO_3)_4$ (Pr, Nd, Sm-Lu).

FTIR spectra of $K_3RE_3(BO_3)_4$ (RE = Pr, Nd, Sm-Lu) are given in **figure 6**. Generally, all absorption bands in the IR spectra from 400 and 1700 cm^{-1} can be assigned to the trigonal planar BO_3 groups [51-53]. The pronounced broad absorption bands between 1000 to 1600 cm^{-1} originate from the B-O asymmetric stretching (ν_3) of the BO_3 groups. The vibrational regions from 600 to 700 cm^{-1} and from 700 to 800 cm^{-1} correspond to in-plane bending mode (ν_4) and out-of-plane bending mode (ν_2), respectively. Several medium absorption peaks centering between 850 cm^{-1} and 900 cm^{-1} can be assigned to the symmetric stretching modes (ν_1) of the BO_3 groups. Notably, the ν_1 mode of the ideal BO_3 group (D_{3h}) is theoretically infrared inactive due to the invariability of the molecular dipole moment. In contrast, the ν_1 modes in $K_3RE_3(BO_3)_4$ are infrared activate since the symmetry of BO_3 group is lower to the C_{2v} or C_s point group. Such distortion from the ideal geometry of BO_3 groups fits well to the results of the structural features observed by X-ray diffraction. The Raman spectra in the region of 90 to

1800 cm^{-1} are also shown (**figure 6b**). Below the 400 cm^{-1} region is dominantly contributed by the stretching modes of RE–O bonds and K–O bonds; the complex lattice vibrations at this region can be explicitly distinguished [51-53] from the rest of the spectral intensity. The most intensive peaks in the spectra located around between 900 and 980 cm^{-1} fit well to the stretching vibrations (ν_1 modes) of BO_3 groups which are formally Raman active. Alike FTIR spectra, the Raman shifts from 1000 to 1600 cm^{-1} can be ascribed to the BO_3 asymmetric stretching vibrations (ν_3 modes), while those bands observed in the regions of 560 – 700 cm^{-1} and 700 - 800 cm^{-1} arise from ν_4 and ν_2 modes, respectively. The vibrational features of BO_3 groups observed in the Raman spectra are in good agreement with the FTIR spectra. Beside the vibrational features appeared in the FTIR and Raman spectra, extra bands elsewhere can be assigned either to REBO_3 impurity (if any) or to 4f-electronic transitions.

4. Conclusion

A series of novel rare-earth borate compounds $\text{K}_3\text{RE}_3(\text{BO}_3)_4$ (RE = Pr, Nd, Sm - Lu) are obtained by solid state syntheses and spontaneous crystallization from a high-temperature flux. Combined X-ray single crystal and powder diffraction reveal the monoclinic space group $P2_1/c$ for $\text{K}_3\text{RE}_3(\text{BO}_3)_4$ (RE=Sm-Lu) and triclinic space group $P\bar{1}$ for $\text{K}_3\text{RE}_3(\text{BO}_3)_4$ (RE=Pr, Nd). The lattice parameters of $\text{K}_3\text{RE}_3(\text{BO}_3)_4$ determined by Rietveld refinement using the powder X-ray diffraction are found to comply with the lanthanide contraction. A thorough crystal structural analysis reveals that $\text{K}_3\text{RE}_3(\text{BO}_3)_4$ (RE = Pr, Nd) can be considered as pseudo-monoclinic archetypes of $\text{Rb}_3\text{La}_3(\text{BO}_3)_4$ and $\text{K}_3\text{RE}_3(\text{BO}_3)_4$ (RE = Sm - Lu) viewed as one-dimensional superstructures of $\text{Rb}_3\text{La}_3(\text{BO}_3)_4$ along the **b**-axis. However, all family members

are structurally distinct from the hexagonal-open-framework such as in $\text{Na}_3\text{Y}_3(\text{BO}_3)_4$. The results allowed to reveal a morphotropic series for alkali rare-earth borates based on the cationic size effects.

Acknowledgement

PYC gratefully thanks the Chinese Scholarship Council (CSC) for the financial support. The University of Bremen is cordially acknowledged for the technical and administrative supports. The authors thank the Deutsche Forschungsgemeinschaft (DFG) for financial supports for large scientific instruments INST 144/458-1 FUGG used for this project.

Compliance with Ethical Standards:

Conflict of Interest: The authors declare that they have no conflict of interest.

Reference

- [1] R. P. Rao, D.J. Devine, RE-activated lanthanide phosphate phosphors for PDP applications, *J. Lumin.*, 87-89 (2000) 1260-1263.
- [2] R. P. Rao, Tb^{3+} activated green phosphors for plasma display panel applications, *J. Electrochem. Soc.*, 150 (2003) H165-H171..
- [3] L. Zhang, C. Pédrini, C. Madej, C. Dujardin, J.C. Geon, B. Moine, I. Kamenskikh, A. Belsky, D.A. Shaw, M.A. MacDonald, P. Mesnard, C. Fouassier, J.C. Van't Spijker, C.W .E. Van Eijk, Fast fluorescence and scintillation properties of cerium and praseodymium doped lutetium orthoborates, *Radiat. Eff. Defects Solids*, 150 (1999) 47-52.
- [4] Z.-J. Zhang, T.-T. Jin, M.-M. Xu, Q.-Z. Huang, M.-R. Li, J.-T. Zhao, Low-Temperature Vaterite-Type $LuBO_3$, a Vacancy-Stabilized Phase Synthesized at High Temperature, *Inorg. Chem.*, 54 (2015) 969-975.
- [5] L. Gheorghe, M. Greculeasa, A. Broasca, F. Voicu, G. Stanciu, K. N. Belikov, E.Y. Bryleva, O. Gaiduk, Incongruent Melting $La_xY_ySc_{4-x-y}(BO_3)_4$: LYSB Nonlinear Optical Crystal Grown by the Czochralski Method, *ACS Appl. Mater. Interfaces*, 11 (2019) 20987-20994.
- [6] G. Aka, E. Reino, P. Loiseau, D. Vivien, B. Ferrand, L. Fulbert, D. Pelenc, G. Lucas-Leclin, P. Georges, $Ca_4REO(BO_3)_3$ crystals for green and blue microchip laser generation: from crystal growth to laser and nonlinear optical properties, *Opt.Mater.*, 26 (2004) 431-436.
- [7] G. Zou, Z. Ma, K. Wu, N. Ye, Cadmium-rare earth oxyborates $Cd_4ReO(BO_3)_3$ (Re = Y, Gd, Lu): congruently melting compounds with large SHG responses, *J. Mater. Chem.*, 22 (2012) 19911-19918.
- [8] D. Rytz, A. Gross, S. Vernay, V. Wesemann, $YAl_3(BO_3)_4$: a novel NLO crystal for frequency conversion to UV wavelengths, *Proc. SPIE, Solid State Lasers and Amplifiers III* (2008), 6998
- [9] Y. Yue, Y. Zhu, Y. Zhao, H. Tu, Z. Hu, Growth and Nonlinear Optical Properties of $GdAl_3(BO_3)_4$ in a Flux without Molybdate, *Cryst. Growth Des*, 16 (2016) 347-350.
- [10] S. H. Fang, H. Liu, L.X. Huang, N. Ye, Growth and optical properties of nonlinear $LuAl_3(BO_3)_4$ crystals, *Opt. Express*, 21 (2013) 16415-16423.
- [11] M. Mutailipu, Z. Xie, X. Su, M. Zhang, Y. Wang, Z. Yang, M. Janjua, S. Pan, Chemical Cosubstitution-Oriented Design of Rare-Earth Borates as Potential Ultraviolet Nonlinear Optical Materials, *J. Am. Chem. Soc.*, 139 (2017) 18397-18405.
- [12] Z. Xie, M. Mutailipu, G. He, G. Han, Y. Wang, Z. Yang, M. Zhang, S. Pan, A Series of Rare-Earth Borates $K_7MRE_2B_{15}O_{30}$ (M = Zn, Cd, Pb; RE = Sc, Y, Gd, Lu) with Large Second Harmonic Generation Responses, *Chem. Mater.*, 30 (2018) 2414-2423.
- [13] K. N. Gorbachenya, V. E. Kisel, A. S. Yasukevich, V. V. Maltsev, N. I. Leonyuk, N.V. Kuleshov, Highly efficient continuous-wave diode-pumped Er, Yb:GdAl₃(BO₃)₄ laser, *Opt. Lett.*, 38 (2013) 2446-2448.
- [14] A. Broasca, L. Gheorghe, M. Greculeasa, F. Voicu, G. Stanciu, S. Hau, C. Gheorghe, G. Croitoru, N. Pavel, Czochralski Growth and Characterization of Pure and Yb-Doped $La_xY_ySc_4$

$x-y(\text{BO}_3)_4$ Nonlinear and Laser Crystal, *Laser Applications Conference, Opt. Soc. Am.*, **2019**, pp. JM5A. 40.

[15] P. Dekker, J. M. Dawes, J. A. Piper, Y. Liu, J. Wang, 1.1 W CW self-frequency-doubled diode-pumped Yb:YAl₃(BO₃)₄ laser, *Opt. Comm.*, 195 (**2001**) 431-436.

[16] D. Z. Lu, Q. N. Fang, X. S. Yu, X. K. Han, J. Y. Wang, H. H. Yu, H. J. Zhang, Power scaling of the self-frequency-doubled quasi-two-level Yb:YCOB laser with a 30% slope efficiency, *Optics Letters*, 44 (**2019**) 5157-5160.

[17] R. K. Li, C. C. Wu, M. J. Xia, LiCaTb₅(BO₃)₆: A new magneto-optical crystal promising as Faraday rotator, *Opt. Mater.*, 62 (**2016**) 452-457.

[18] R. Li, Enhancing the Magnetocaloric Effect of a Paramagnet to above Liquid Hydrogen Temperature, *Energy Technol.*, 7 (**2019**) 1801070.

[19] G. K. Abdullaev, K.S. Mamedov, I. R. Amiraslanov, A.I. Magerramov, Crystal structure of lithium praseodymium orthoborate Li₃Pr₂(BO₃)₃, *J. Struct. Chem.*, 18 (**1977**) 331-333.

[20] B. Sebastian, H. Hubert, Synthesis and structural characterization of Li₃Y(BO₃)₂, *Z. Naturforsch., B*, 72 (**2017**) 153-158.

[21] V. Jubera, P. Gravereau, J. P. Chaminade, Crystal structure of the new borate Li₃Gd(BO₃)₂. Comparison with the homologous Na₃Ln(BO₃)₂ (Ln: La, Nd) compounds, *Solid State Sci.*, 3 (**2001**) 469-475.

[22] J. Mascetti, M. Vlasse, C. Fouassier, The crystal chemistry of the new rare-earth sodium borates Na₃Ln(BO₃)₂ (Ln = La, Nd), *J. Solid State Chem.*, 39 (**1981**) 288-293.

[23] Y. Zhang, X.L. Chen, J. K. Liang, T. Xu, Synthesis and structural study of new rare earth sodium borates Na₃Ln(BO₃)₂ (Ln=Y, Gd), *J. Alloys Compd.*, 333 (**2002**) 72-75.

[24] Z. Wang, H. Li, G. Cai, Z. Jin, Synthesis, crystal structure, and thermal stability of new borates Na₃REB₂O₆ (RE = Pr, Sm, Eu), *Powder Diffr.* 31 (**2016**) 110-117.

[25] F. Shan, L. Kang, G. Zhang, J. Yao, Z. Lin, M. Xia, X. Zhang, Y. Fu, Y. Wu, Na₃Y₃(BO₃)₄: a new noncentrosymmetric borate with an open-framework structure, *Dalton Trans.*, 45 (**2016**) 7205-7208.

[26] J. H. Gao, R. K. Li, Potassium rich rare earth (RE) borates K₃RE(BO₃)₂, *Solid State Sci.*, 10 (**2008**) 26-30.

[27] S. Zhao, G. Zhang, J. Yao, Y. Wu, K₃YB₆O₁₂: A new nonlinear optical crystal with a short UV cutoff edge, *Mater. Res. Bull.*, 47 (**2012**) 3810-3813.

[28] J. H. Gao, R. K. Li, Preparation, structure and luminescent properties of a new potassium yttrium borate K₃Y₃(BO₃)₄, *Mate. Res. Bull.*, 43 (**2008**) 882-888.

[29] V.V. Atuchin, A.K. Subanakov, A.S. Aleksandrovsky, B.G. Bazarov, J. G. Bazarova, S.G. Dorzhieva, T. A. Gavrilova, A.S. Krylov, M.S. Molokeev, A.S. Oreshonkov, A.M. Pugachev, Y.L. Tushinova, A.P. Yelissev, Exploration of structural, thermal, vibrational and spectroscopic properties of new noncentrosymmetric double borate Rb₃NdB₆O₁₂, *Adv. Powder Technol.*, 28 (**2017**) 1309-1315.

- [30] A. K. Subanakov, E.V. Kovtunets, B.G. Bazarov, S.G. Dorzhieva, J.G. Bazarova, New double holmium borates: $\text{Rb}_3\text{HoB}_6\text{O}_{12}$ and $\text{Rb}_3\text{Ho}_2\text{B}_3\text{O}_9$, *Solid State Sci*, 105 (2020) 106231.
- [31] V.V. Atuchin, A.K. Subanakov, A.S. Aleksandrovsky, B.G. Bazarov, J.G. Bazarova, T.A. Gavrilova, A.S. Krylov, M.S. Molokeyev, A.S. Oreshonkov, S.Y. Stefanovich, Structural and spectroscopic properties of new noncentrosymmetric self-activated borate $\text{Rb}_3\text{EuB}_6\text{O}_{12}$ with B_5O_{10} units, *Mater. Design*, 140 (2018) 488-494.
- [32] J. H. Gao, M.S. Zheng, Synthesis and Crystal Structure of a Rubidium Lanthanum Borate $\text{Rb}_3\text{La}_3(\text{BO}_3)_4$, *Chin. J. Struct.Chem.*, 28 (2009) 82-86.
- [33] G. Sheldrick, SHELXT - Integrated space-group and crystal-structure determination, *Acta Crystallogr. A*, 71 (2015) 3-8.
- [34] C. B. Hubschle, G.M. Sheldrick, B. Dittrich, ShelXle: a Qt graphical user interface for SHELXL, *J. Appl. Crystallogr.*, 44 (2011) 1281-1284.
- [35] A. Spek, Single-crystal structure validation with the program PLATON, *J. Appl. Crystallogr.*, 36 (2003) 7-13.
- [36] J. Rodriguez-Carvajal, T. Roisnel, WinPLOTR: A windows tool for powder diffraction pattern analysis, *Mater. Sci. Forum, Proceedings of the Seventh European Powder Diffraction Conference*, Barcelona, Spain, 2000, pp. 378-381.
- [37] P. Kubelka, Ein Beitrag zur Optik der Farbanstriche, *Z. Tech. Phys.*, 12 (1931) 593-601.
- [38] J. Tauc, R. Grigorovici, A. Vancu, Optical properties and electronic structure of amorphous germanium, *Phys. Status Solidi B*, 15 (1966) 627-637.
- [39] D. Souri, Z. E. Tahan, A new method for the determination of optical band gap and the nature of optical transitions in semiconductors, *Appl. Phys. B*, 119 (2015) 273-279.
- [40] A. Kirsch, M. M. Murshed, M. Schowalter, A. Rosenauer, T. M. Gesing, Nanoparticle precursor into polycrystalline $\text{Bi}_2\text{Fe}_4\text{O}_9$: an evolutionary investigation of structural, morphological, optical, and vibrational properties, *J. Phys. Chem. C*, 120 (2016) 18831-18840.
- [41] A. Kirsch, M. M. Murshed, F. J. Litterst, T. M. Gesing, Structural, spectroscopic, and thermoanalytic studies on $\text{Bi}_2\text{Fe}_4\text{O}_9$: tunable properties driven by nano-and poly-crystalline states, *J. Phys. Chem. C*, 123 (2019) 3161-3171.
- [42] R. Shannon, Revised effective ionic radii and systematic studies of interatomic distances in halides and chalcogenides, *Acta Crystallogr. A*, 32 (1976) 751-767.
- [43] Y. Q. Jia, Crystal radii and effective ionic radii of the rare earth ions, *J. Solid State Chem.*, 95 (1991) 184-187.
- [44] J. H. Lin, M. Z. Su, K. Wurst, E. Schweda, The Structure of $\text{La}_{26}(\text{BO}_3)_8\text{O}_{27}$: A structure with a distorted fluorite type arrangement of atoms, *J. Solid State Chem.*, 126 (1996) 287-291.
- [45] S. Noirault, S. Célrier, O. Joubert, M.T. Caldes, Y. Piffard, Effects of Water Uptake on the Inherently Oxygen-Deficient Compounds $\text{Ln}_{26}\text{O}_{27}\square(\text{BO}_3)_8$ ($\text{Ln} = \text{La}, \text{Nd}$), *Inorg. Chem.*, 46 (2007) 9961-9967.
- [46] S. Noirault, S. Célrier, O. Joubert, M.T. Caldes, Y. Piffard, Incorporation of Water and

fast proton conduction in the inherently oxygen-deficient compound $\text{La}_{26}\text{O}_{27}\square(\text{BO}_3)_8$, 19 (2007) 867-870.

[47] G.H. Dieke, H. M. Crosswhite, The Spectra of the Doubly and Triply Ionized Rare Earths, *Appl. Opt.*, 2 (1963) 675-686.

[48] W. T. Carnall, P. R. Fields, K. Rajnak, Electronic Energy Levels in the Trivalent Lanthanide Aquo Ions. I. Pr^{3+} , Nd^{3+} , Pm^{3+} , Sm^{3+} , Dy^{3+} , Ho^{3+} , Er^{3+} , and Tm^{3+} , *J. Chem. Phys.*, 49 (1968) 4424-4442.

[49] A. V. Prokofiev, A. I. Shelykh, B. T. Melekh, Periodicity in the band gap variation of Ln_2X_3 ($\text{X} = \text{O}, \text{S}, \text{Se}$) in the lanthanide series, *J. Alloys Compd.*, 242 (1996) 41-44.

[50] R. He, H. Huang, L. Kang, W. Yao, X. Jiang, Z. Lin, J. Qin, C. Chen, Bandgaps in the deep ultraviolet borate crystals: Prediction and improvement, *Appl. Phys. Lett.*, 102 (2013) 231904.

[51] A. Haberer, R. Kaindl, H. Huppertz, Synthesis and Crystal Structure of the Praseodymium Orthoborate λ - PrBO_3 , *Z. Naturforsch., B*, 65 (2010) 1206.

[52] K. Nakamoto, Infrared and Raman Spectra of Inorganic and Coordination Compounds, *Handbook of Vibrational Spectroscopy* (2006).

[53] C. Tao, C. Wu, M. Xia, R. Li, $\text{Li}_2\text{Ca}_5\text{Tb}(\text{BO}_3)_5$: An orthoborate with large spherical hollow cages, *Opt. Mater.*, 96 (2019) 109358.

Supporting Information

Synthesis and crystal structures of novel alkali rare-earth orthoborates $\text{K}_3\text{RE}_3(\text{BO}_3)_4$ (RE = Pr, Nd, Sm - Lu)

Pengyun Chen¹, M. Mangir Murshed^{1,2*}, Thorsten M. Gesing^{1,2}

¹University of Bremen, Institute of Inorganic Chemistry and Crystallography, Faculty of Biology and Chemistry, Leobener Straße 7, D-28359 Bremen, Germany

²University of Bremen, MAPEX Center for Materials and Processes, Bibliothekstraße 1, D-28359 Bremen, Germany

*Corresponding author: e-mail address: murshed@uni-bremen.de, phone: +49 (0)421 218 63144, fax: +49 421 218 63145.

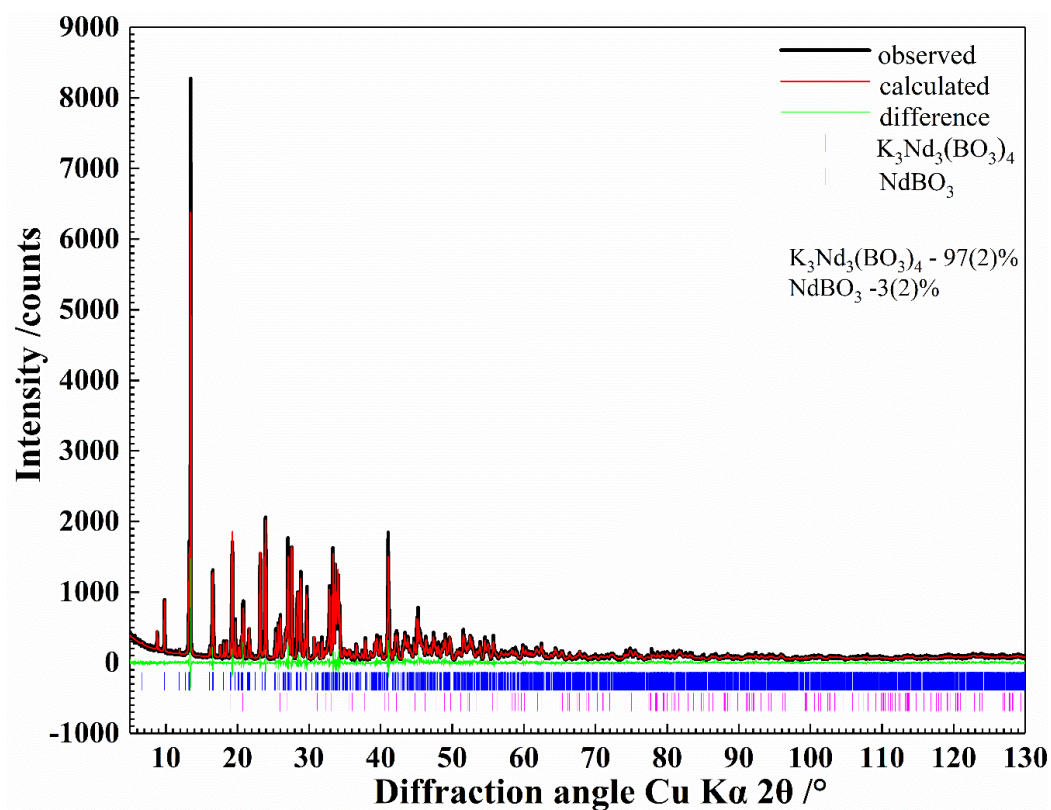


Figure S1: X-ray powder data Rietveld plot of $\text{K}_3\text{Nd}_3(\text{BO}_3)_4$.

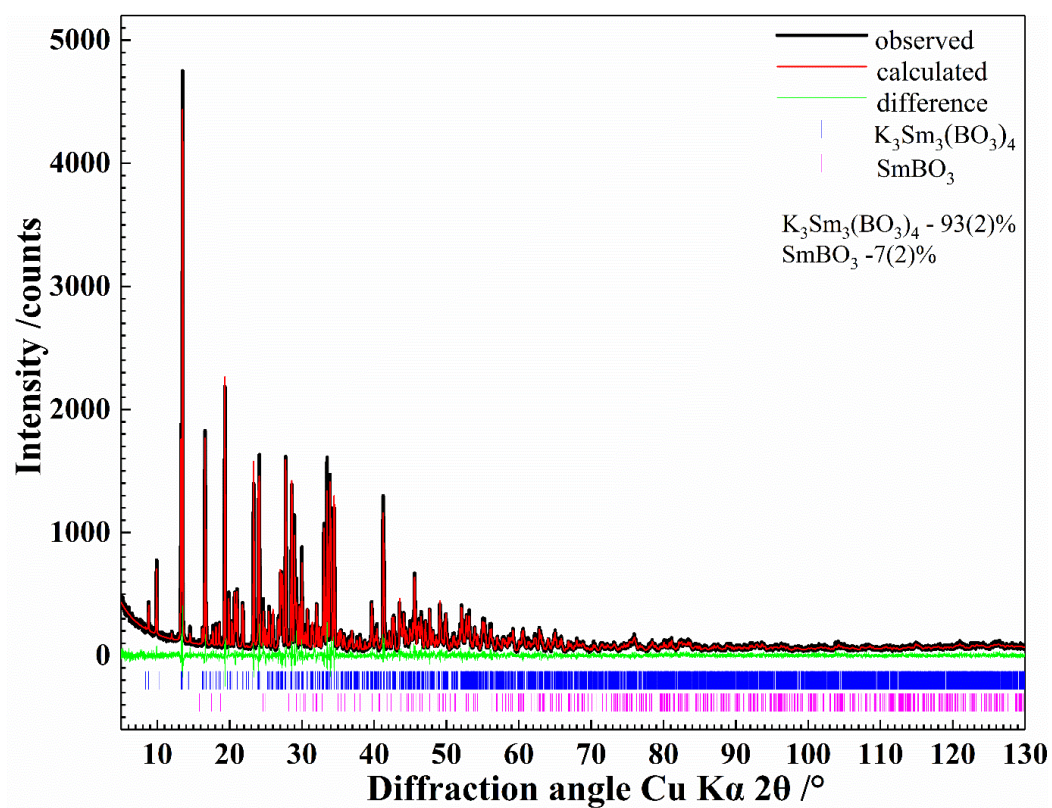


Figure S2: X-ray powder data Rietveld plot of $\text{K}_3\text{Sm}_3(\text{BO}_3)_4$.

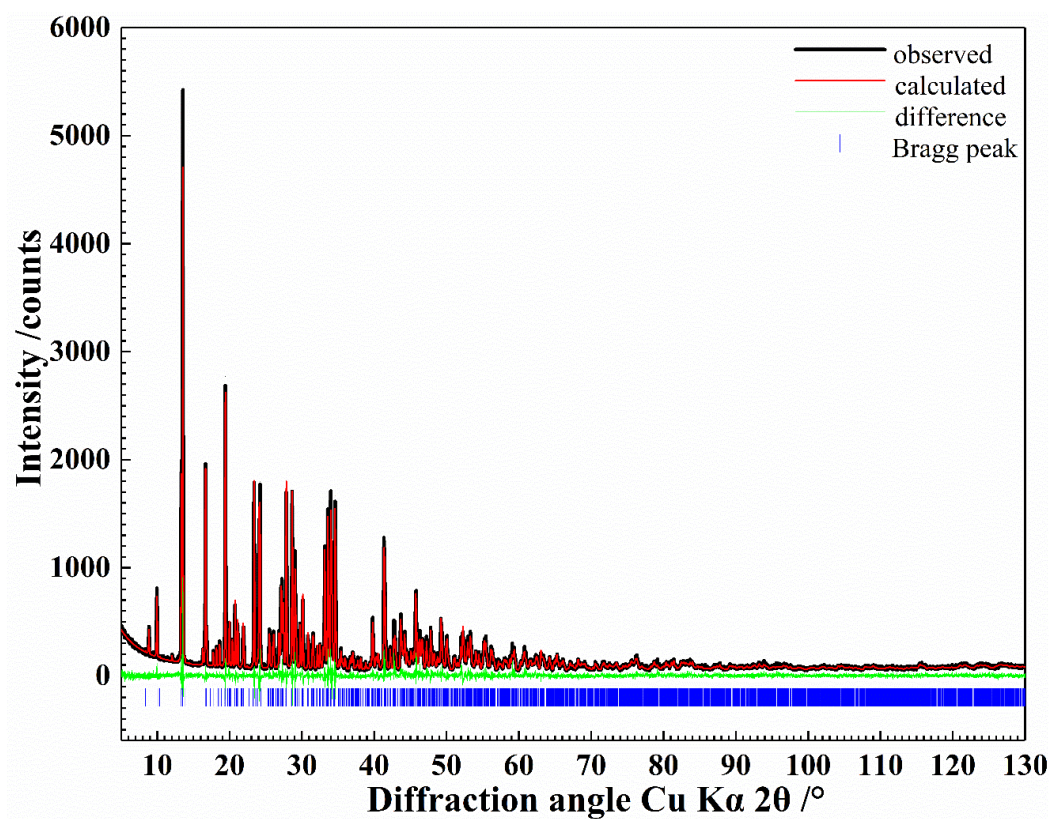


Figure S3: X-ray powder data Rietveld plot of $\text{K}_3\text{Eu}_3(\text{BO}_3)_4$.

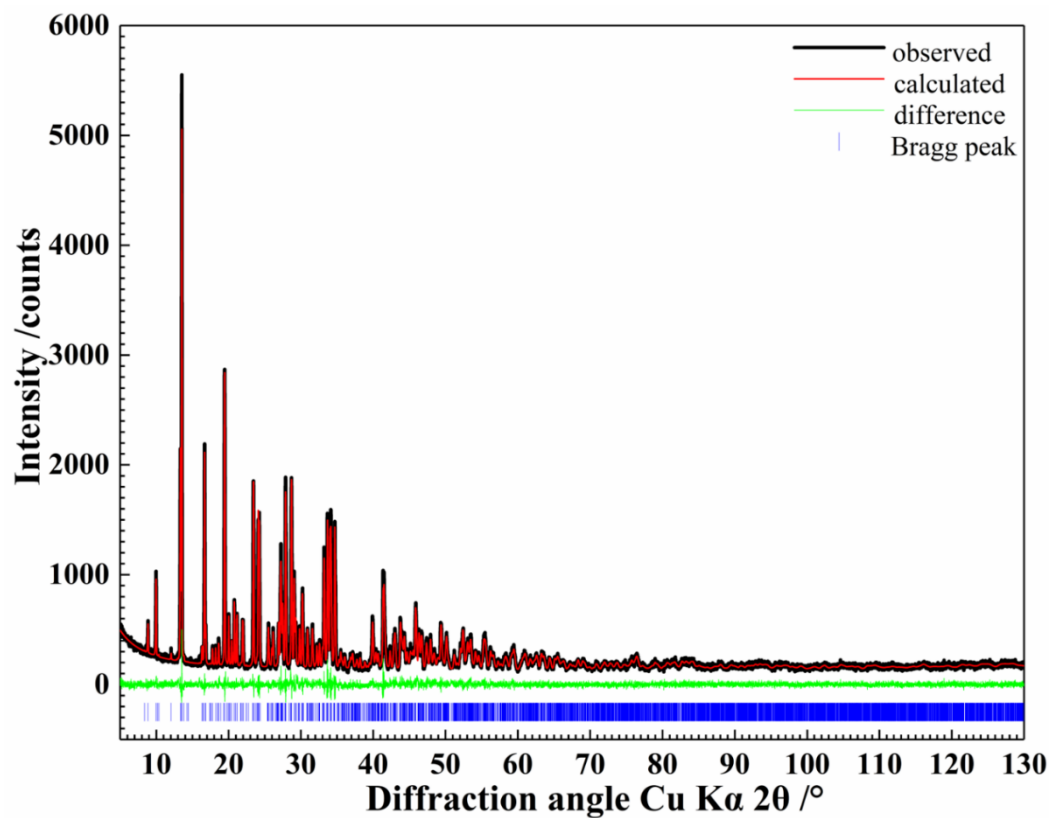


Figure S4: X-ray powder data Rietveld plot of $\text{K}_3\text{Gd}_3(\text{BO}_3)_4$.

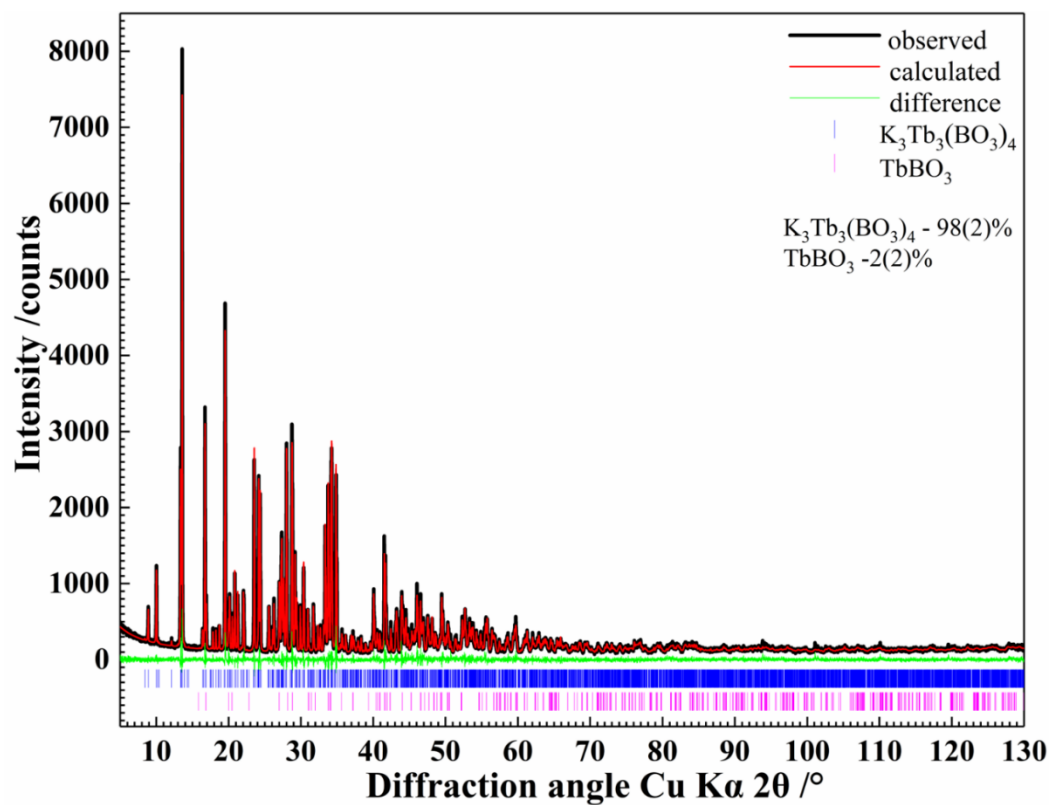


Figure S5: X-ray powder data Rietveld plot of $\text{K}_3\text{Tb}_3(\text{BO}_3)_4$.

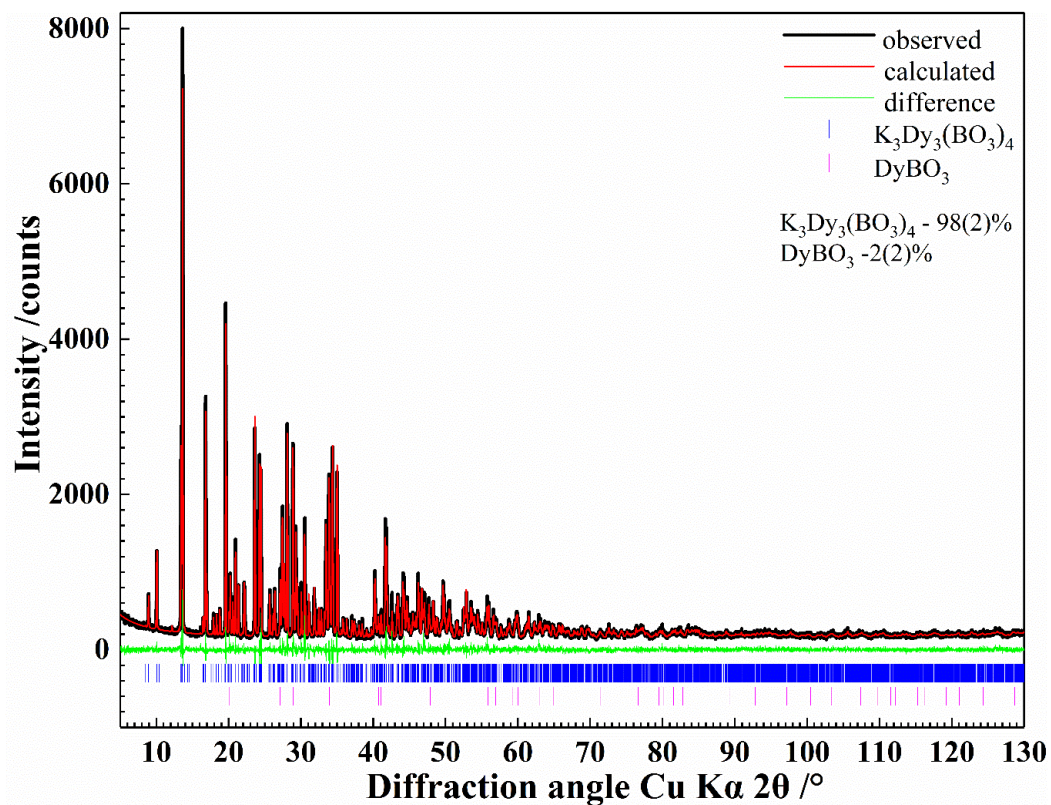


Figure S6: X-ray powder data Rietveld plot of $\text{K}_3\text{Dy}_3(\text{BO}_3)_4$.

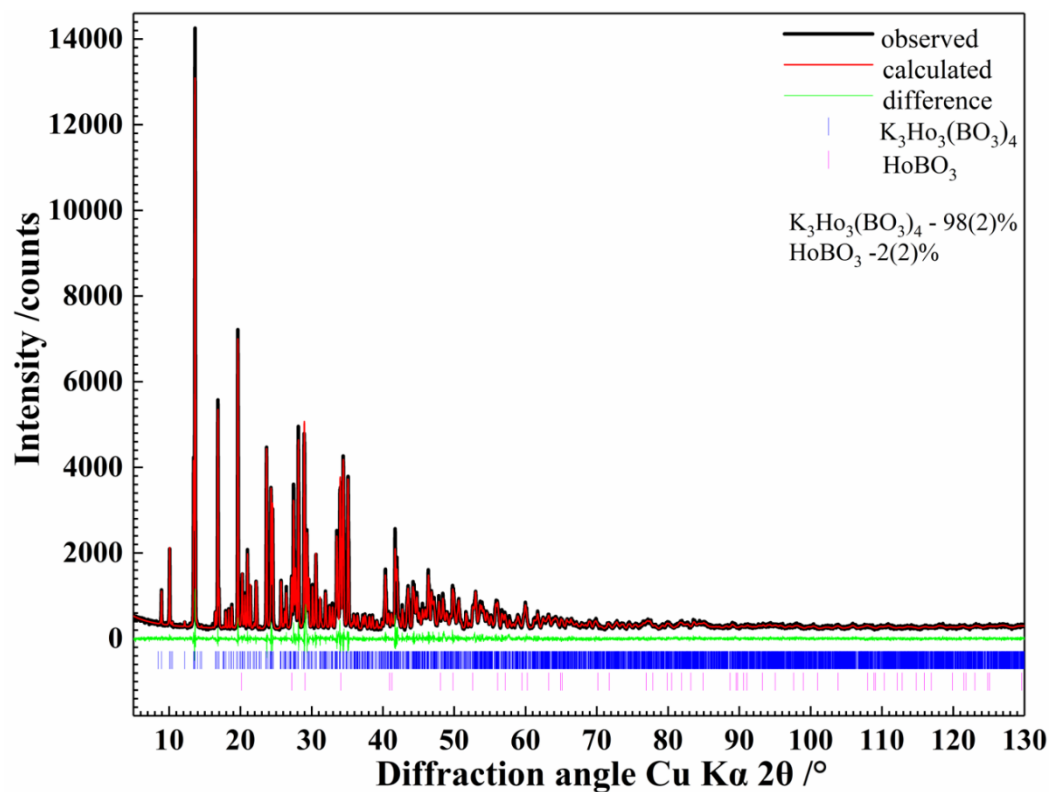


Figure S7: X-ray powder data Rietveld plot of $\text{K}_3\text{Ho}_3(\text{BO}_3)_4$.

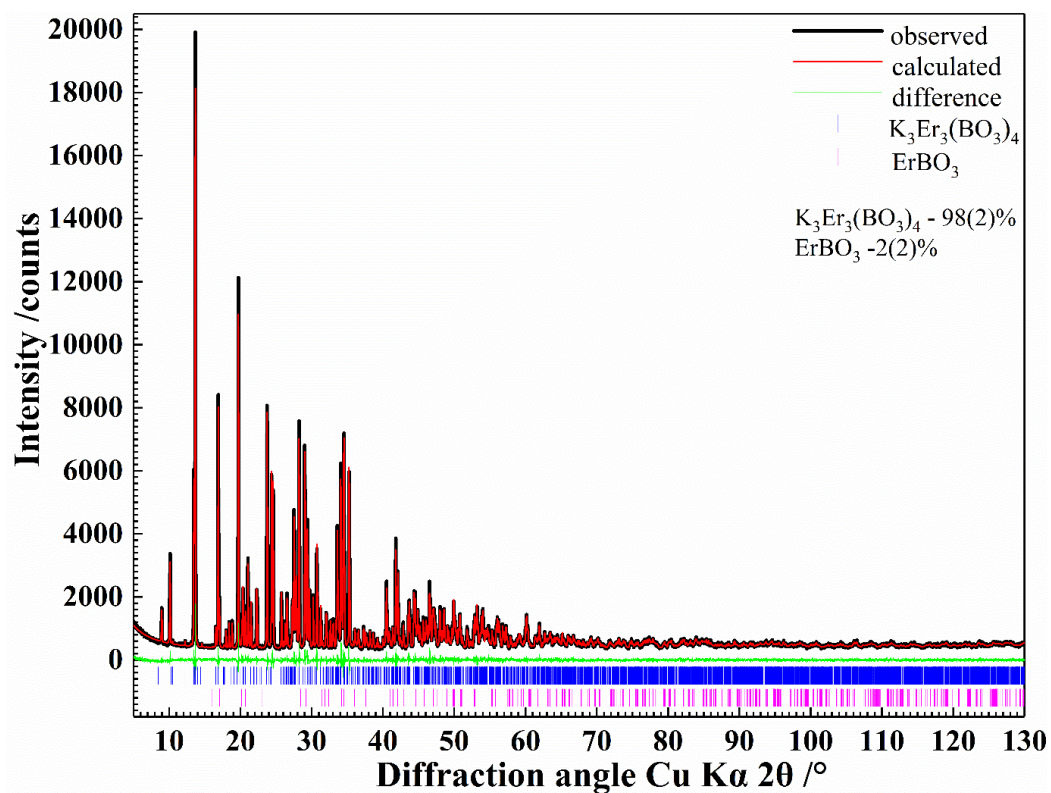


Figure S8: X-ray powder data Rietveld plot of $\text{K}_3\text{Er}_3(\text{BO}_3)_4$.

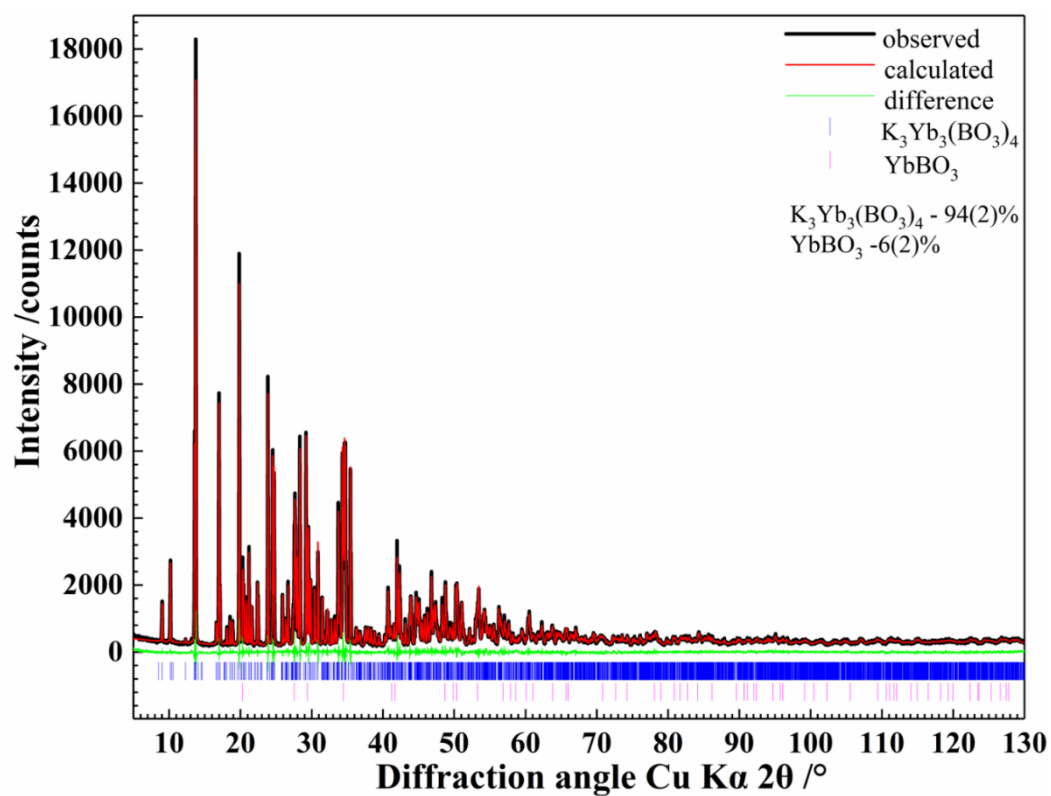


Figure S9: X-ray powder data Rietveld plot of $K_3Yb_3(BO_3)_4$.

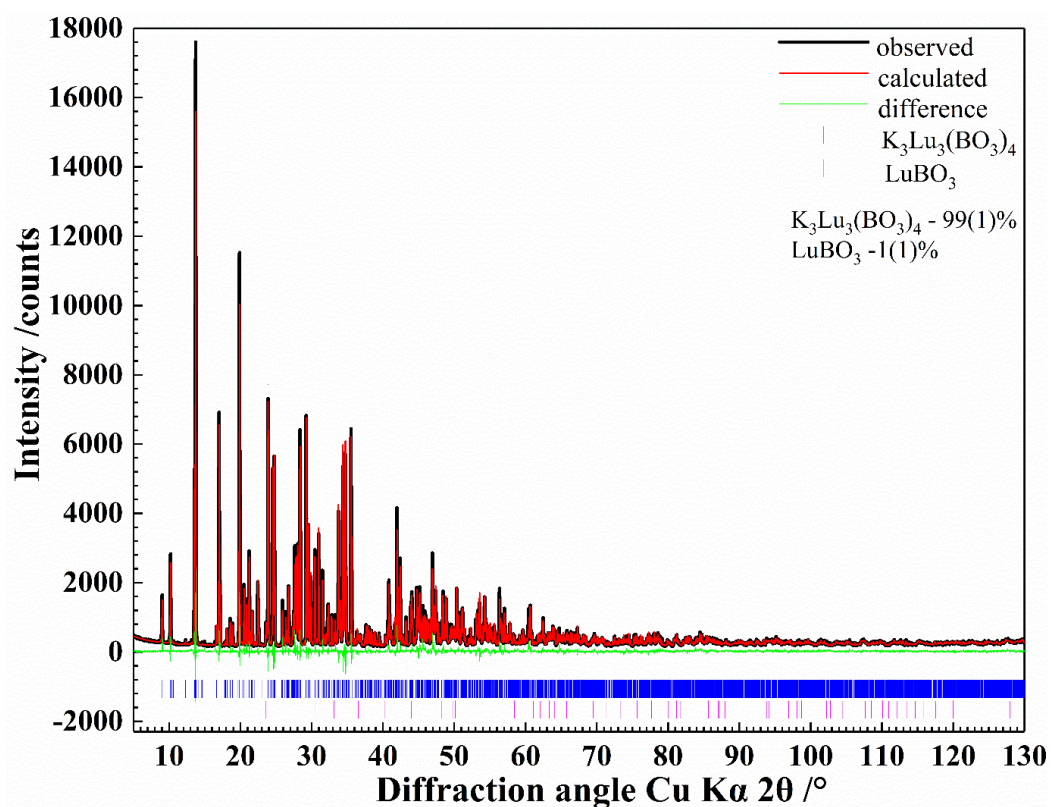


Figure S10: X-ray powder data Rietveld plot of $K_3Lu_3(BO_3)_4$.

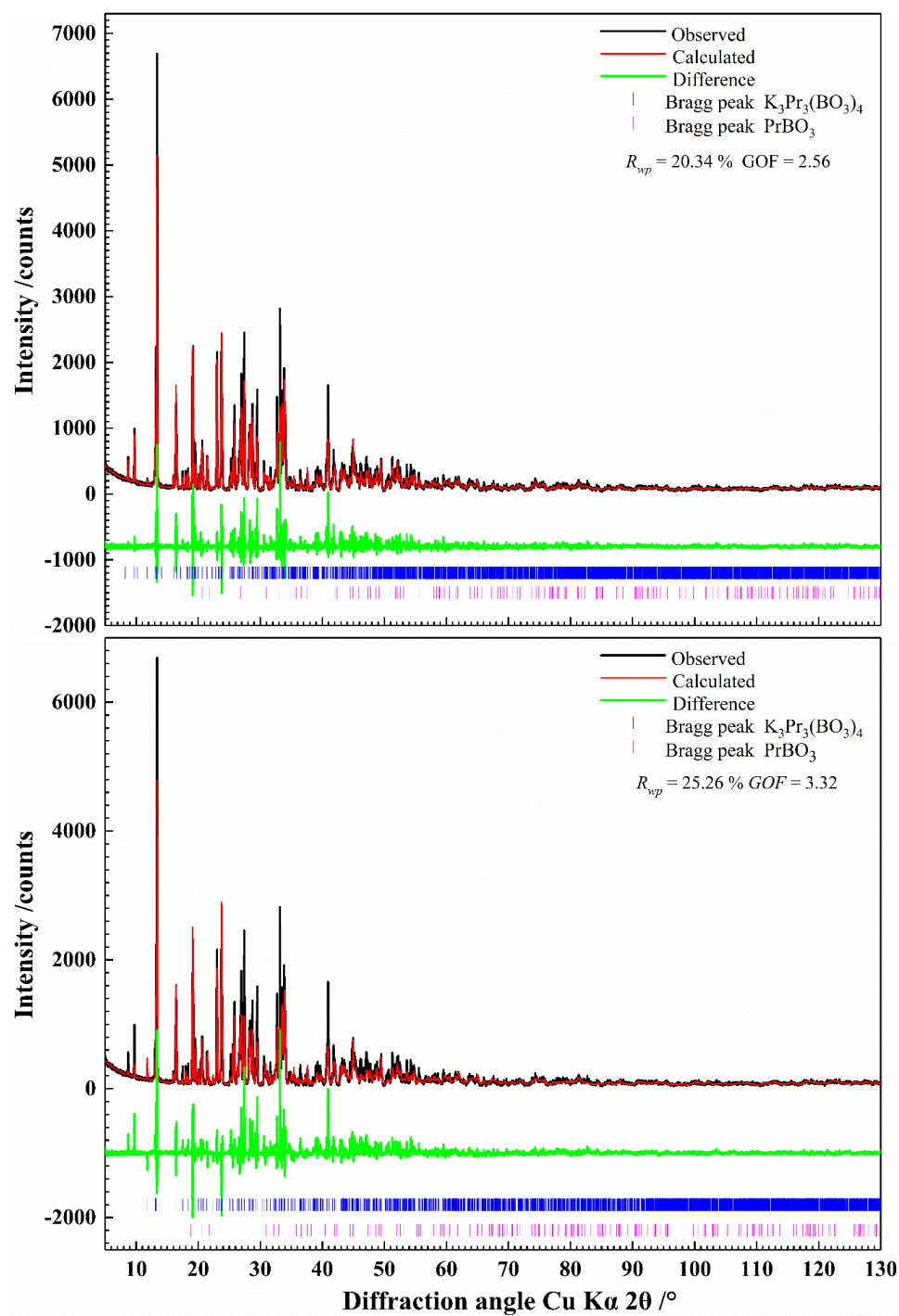


Figure S11: X-ray powder data Rietveld plots of $\text{K}_3\text{Pr}_3(\text{BO}_3)_4$ with the starting models of the space group $P2_1/c$ (top) and $P2/c$ (bottom).

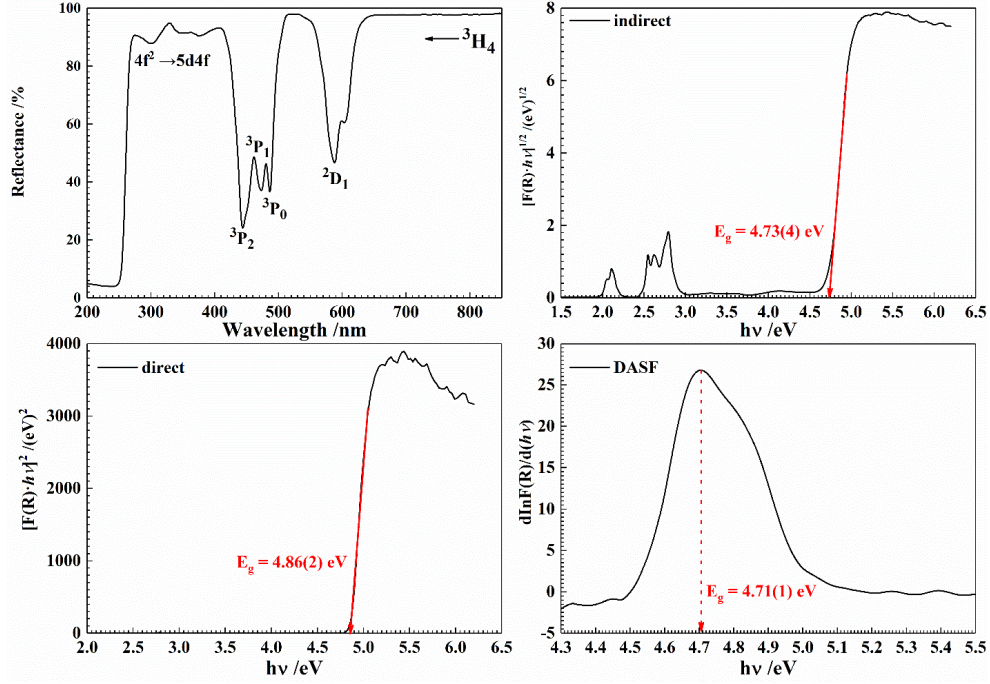


Figure S12: Diffuse reflectance spectrum of $\text{K}_3\text{Pr}_3(\text{BO}_3)_4$ (top left), Tauc plots for indirect (bottom left) and direct (top right) optical transitions, and DASF plot (bottom right).

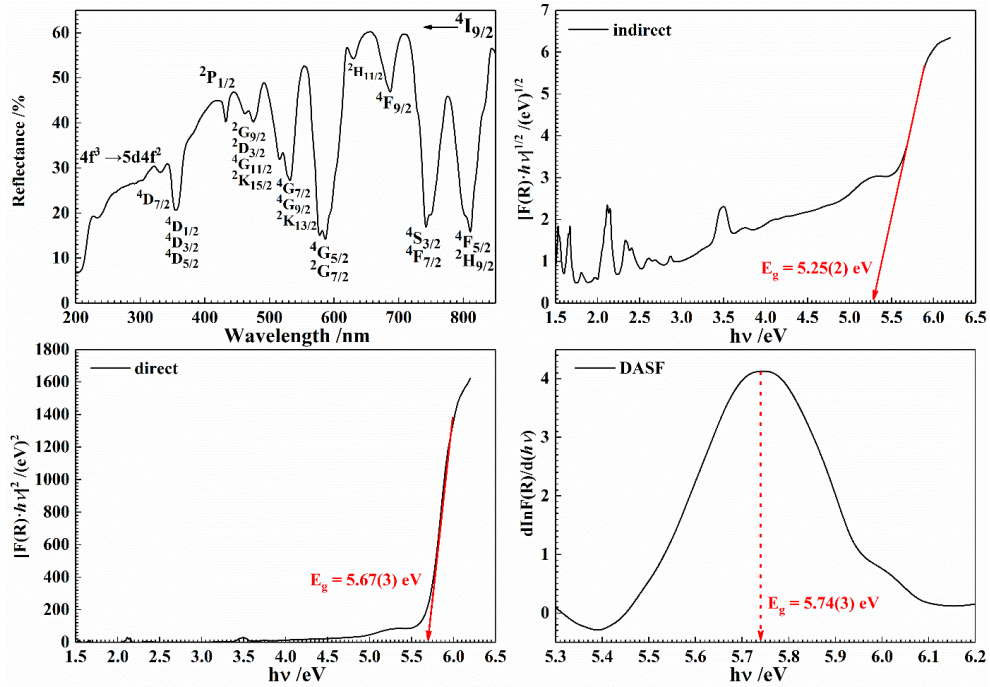


Figure S13: Diffuse reflectance spectrum of $\text{K}_3\text{Nd}_3(\text{BO}_3)_4$ (top left), Tauc plots for indirect (bottom left) and direct (top right) optical transitions, and DASF plot (bottom right).

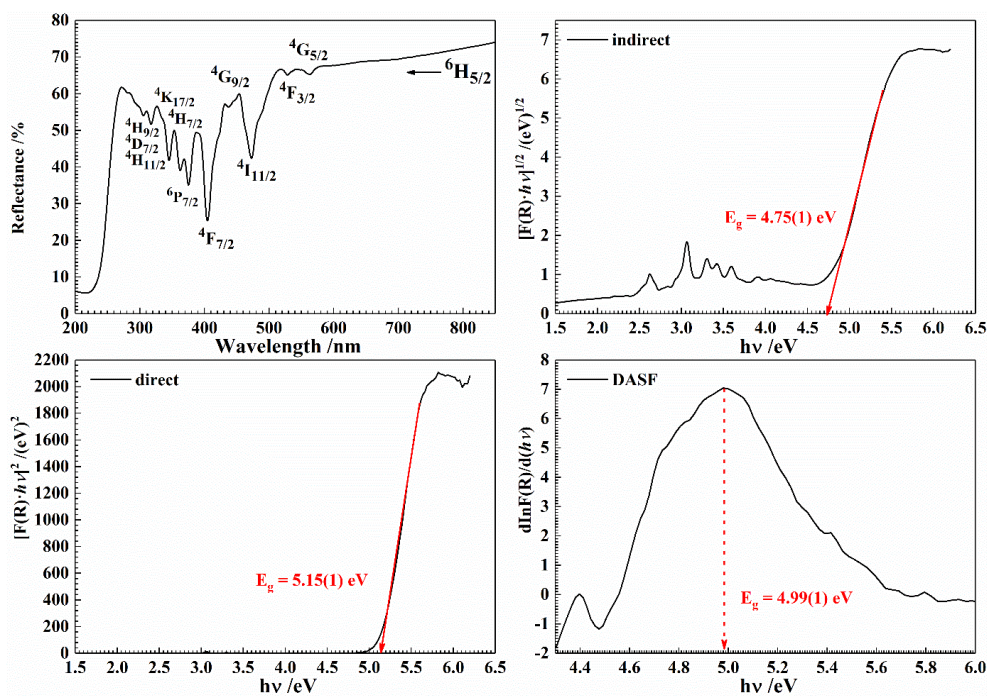


Figure S14: Diffuse reflectance spectrum of $\text{K}_3\text{Sm}_3(\text{BO}_3)_4$ (top left), Tauc plots for indirect (bottom left) and direct (top right) optical transitions, and DASf plot (bottom right).

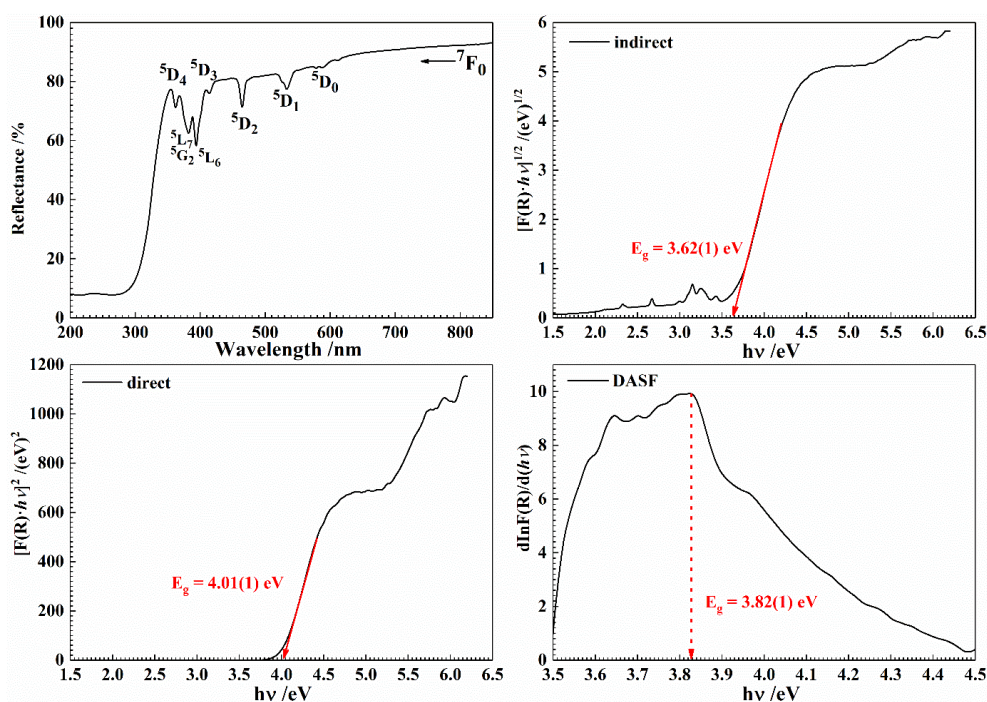


Figure S15: Diffuse reflectance spectrum of $\text{K}_3\text{Eu}_3(\text{BO}_3)_4$ (top left), Tauc plots for indirect (bottom left) and direct (top right) optical transitions, and DASf plot (bottom right).

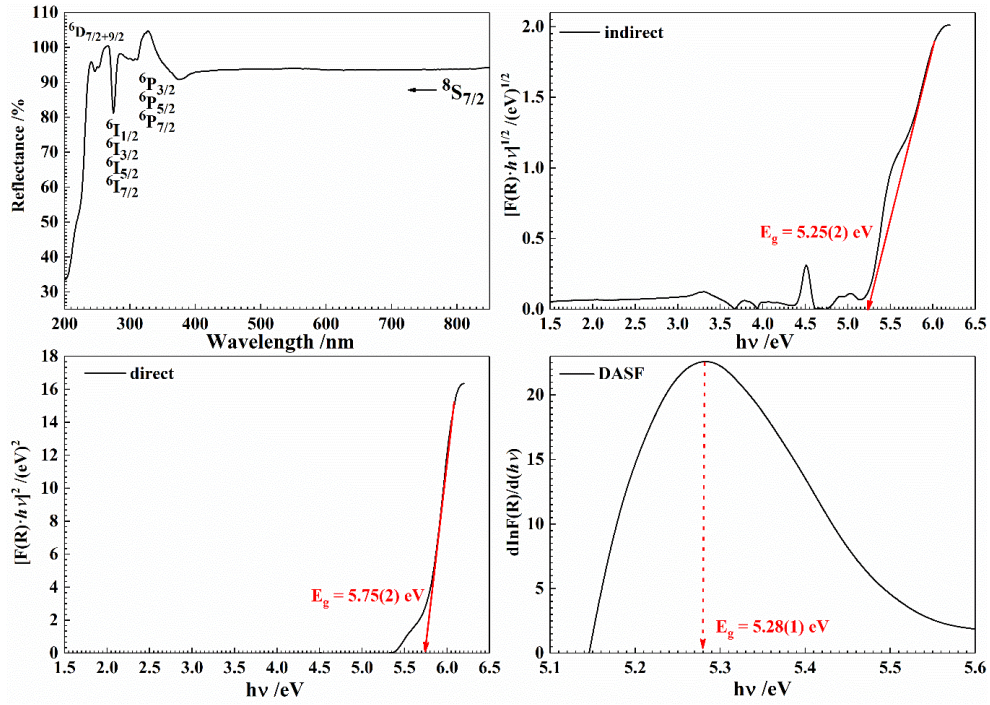


Figure S16: Diffuse reflectance spectrum of $\text{K}_3\text{Gd}_3(\text{BO}_3)_4$ (top left), Tauc plots for indirect (bottom left) and direct (top right) optical transitions, and DASF plot (bottom right).

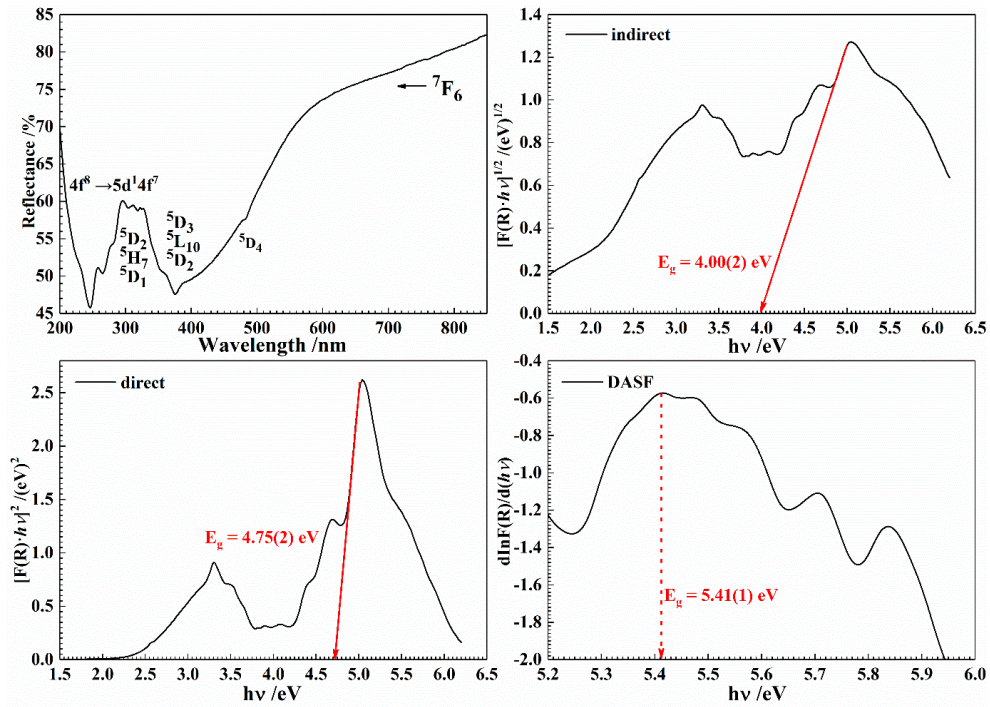


Figure S17: Diffuse reflectance spectrum of $\text{K}_3\text{Tb}_3(\text{BO}_3)_4$ (top left), Tauc plots for indirect (bottom left) and direct (top right) optical transitions, and DASF plot (bottom right).

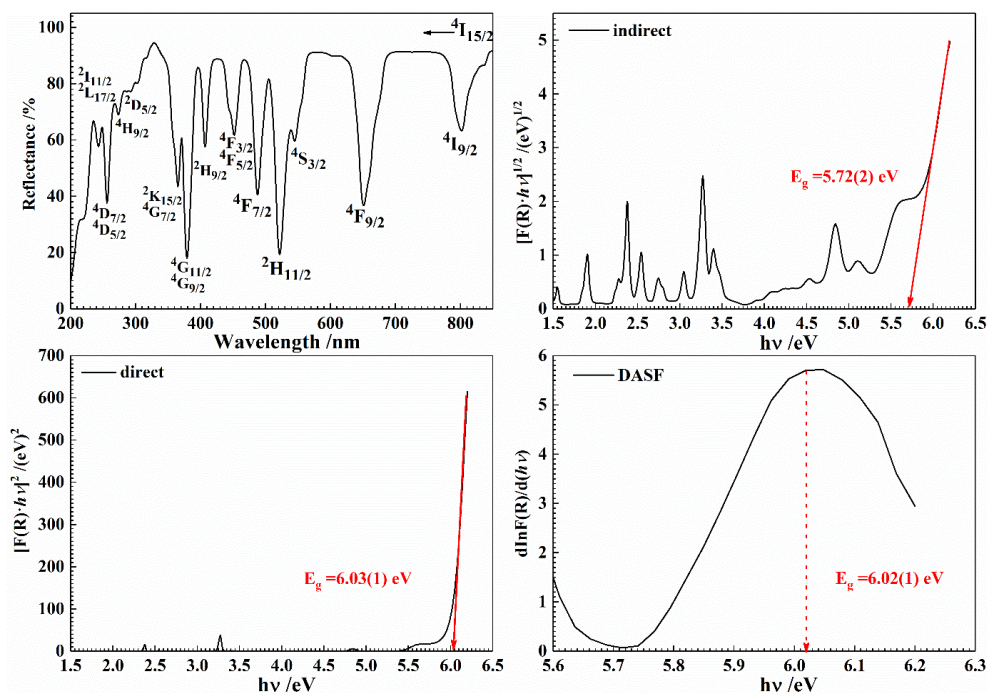


Figure S20: Diffuse reflectance spectrum of $\text{K}_3\text{Er}_3(\text{BO}_3)_4$ (top left), Tauc plots for indirect (bottom left) and direct (top right) optical transitions, and DASF plot (bottom right).

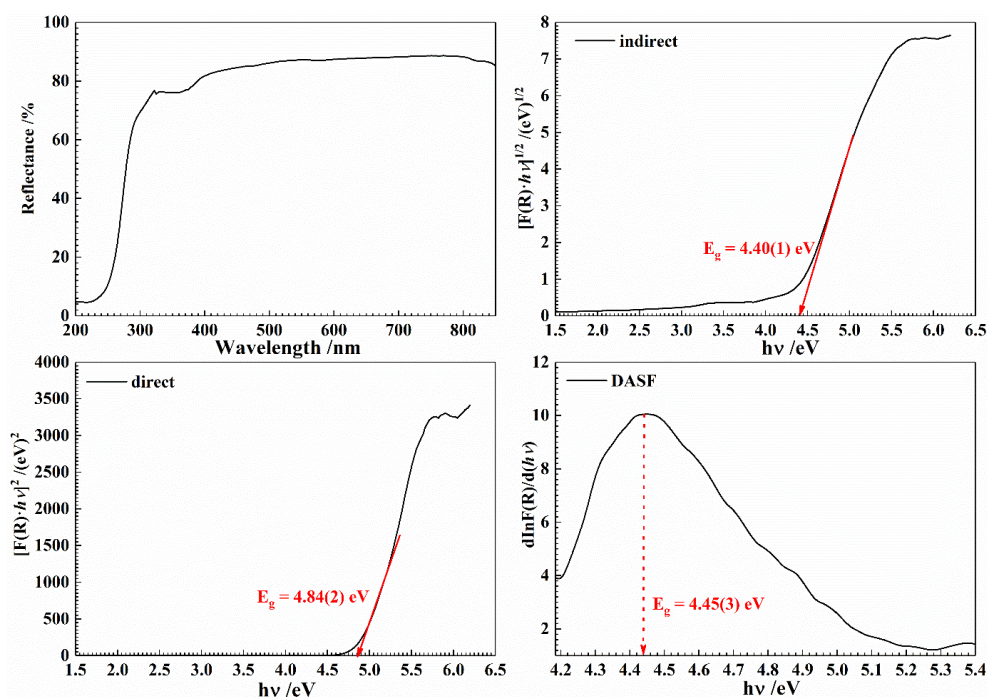


Figure S21: Diffuse reflectance spectrum of $\text{K}_3\text{Yb}_3(\text{BO}_3)_4$ (top left), Tauc plots for indirect (bottom left) and direct (top right) optical transitions, and DASF plot (bottom right).

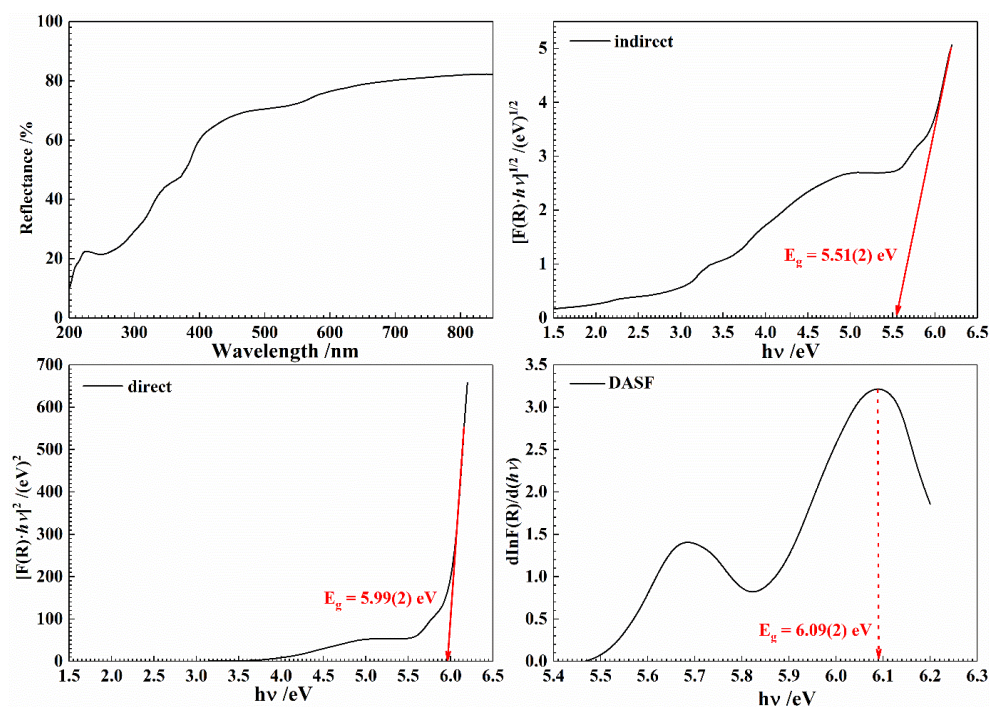


Figure S22: Diffuse reflectance spectrum of $K_3Lu_3(BO_3)_4$ (top left), Tauc plots for indirect (bottom left) and direct (top right) optical transitions, and DASF plot (bottom right).

Chapter 5

Synthesis and characterization of $\text{K}_2\text{Pr}_2\text{O}(\text{BO}_3)_2$: structural, spectroscopic and thermogravimetric investigations of a novel potassium praseodymium oxoborate structure-type

Pengyun Chen¹, M. Mangir Murshed^{1,2*}, Thorsten M. Gesing^{1,2}

¹University of Bremen, Institute of Inorganic Chemistry and Crystallography, Leobener Straße 7, D-28359 Bremen, Germany

²University of Bremen, MAPEX Center for Materials and Processes, Bibliothekstraße 1, D-28359 Bremen, Germany

*Corresponding author: e-mail address: murshed@uni-bremen.de, phone: +49 (0)421 218 63144, fax: +49 421 218 63145.

Abstract

Single crystal and polycrystalline powder samples of a new potassium praseodymium oxoborate $\text{K}_2\text{Pr}_2\text{O}(\text{BO}_3)_2$ were prepared by high-temperature solid-state methods. The crystal structure obtained from single-crystal X-ray diffraction data was confirmed by powder X-ray data Rietveld refinement ($P2_1/c$, $a = 1135.00(3)$ pm, $b = 660.64(2)$ pm, $c = 1072.03(3)$ pm, $\beta = 117.128(2)^\circ$, $V = 715.41(3) \times 10^6 \text{ pm}^3$). The bond-valence sum of the central cation for $\text{KO}_{6/7}$, PrO_9 and BO_3 coordination lies close to the respective empirical value. Both Fourier-transform infrared (FTIR) and Raman spectroscopy demonstrated the vibrational features of the isolated BO_3 planar group. The diffuse UV/Vis reflectance spectra showed fundamental absorption edge at 4.49(1) eV obtained from the combined approach using Tauc and derivation of absorption spectrum fitting (DASF) methods. The greenish color of the sample was identified originating from $4f-4f$ -electron transitions. The thermal stability was investigated by using simultaneous thermogravimetric analysis (TGA) and differential scanning calorimeter (DSC). The decomposed products $\text{Pr}_{26}\text{O}_{27}(\text{BO}_3)_8$ (90(2) wt.%) and Pr_6O_{11} (10(2) wt.%) were confirmed by powder X-ray diffraction data analysis, complementary to the weight-loss during the heating process. Since Pr^{3+} cation is known to show interesting photoluminescence property this novel compound may be a prospective candidate as phosphor.

Keywords: Potassium praseodymium borate, Crystal structure, Vibrational property, Optical property, Thermal stability

1. Introduction

Inorganic rare-earth borates have received intensive interests owing to their wide range of applications in nonlinear optics (NLO), laser hosts and photoluminescence materials [1-3]. Among the most attractive features of borate crystals, the key characteristics are their transparency in the wide range from mid-infrared to deep-ultraviolet [4], high optical damage threshold [5] and suitable physico-chemical stability [6]. Hitherto, $\text{Na}_3\text{La}_9\text{O}_3(\text{BO}_3)_8$ [7], $\text{La}_2\text{CaB}_{10}\text{O}_{19}$ [8], and $\text{YAl}_3(\text{BO}_3)_4$ [9] have been widely used as NLO crystals for second harmonic generation (SHG). Since the ionic radii of the rare-earth elements are close to each other, these rare-earth borates are favorable to host optical active cations such as Ce^{3+} , Nd^{3+} and Yb^{3+} [10]. Therefore, the rare-earth borates can further serve as an array of functional materials in optics: $\text{Ce}^{3+}:\text{Li}_6\text{Y}(\text{BO}_3)_3$ [11] as scintillator materials for neutron detection, $\text{Nd}^{3+}:\text{YAl}_3(\text{BO}_3)_4$ [12] as crystals for green laser emission, and $\text{Yb}^{3+}:\text{LiGd}_6\text{O}_5(\text{BO}_3)_3$ [13] as ultrashort-pulse lasers. Rare-earth orthoborate YBO_3 doped with Eu^{3+} and Tb^{3+} [14] are appropriate phosphors in plasma-display panels due to their high luminous efficacy and thermally stable luminescence yield.

Recently, Pr^{3+} cation-doping materials have drawn an intense research attention due to their promising applications in white-light emitting diodes [15-17]. The Pr^{3+} cation is able to release rich fluorescence spectral lines in the red, orange, green, and blue regions, which originate from the electronic transition between the 4f inner-shell configurations. For instance, in the alkali-metal borates steady and high-efficiency red emission have been detected in $\text{Pr}^{3+}:\text{KSr}_4(\text{BO}_3)_3$ powder [18], $\text{Pr}^{3+}:\text{Na}_3\text{La}_9\text{O}_3(\text{BO}_3)_8$ crystal [19] and Pr^{3+} doped lithium borate glasses [20] when activated by blue or ultraviolet light due to $^3\text{P}_0 \rightarrow ^3\text{H}_6$ and $^1\text{D}_2 \rightarrow ^3\text{H}_4$ transitions. Despite much

works on Pr^{3+} -doped borates, purely praseodymium borates have not been extensively studied. In search of novel rare-earth borate compounds the present investigation focus on $\text{A}_2\text{O}-\text{Pr}_2\text{O}_3-\text{B}_2\text{O}_3$ (A = alkali metal) quasi-ternary systems and their crystal-, chemico-physical properties. To the best of our knowledge, only $\text{Li}_3\text{Pr}_2(\text{BO}_3)_3$ [21], $\text{LiPr}_6\text{O}_5(\text{BO}_3)_3$ [22], $\text{Na}_3\text{Pr}(\text{BO}_3)_2$ [23] and $\text{K}_9\text{Li}_3\text{Pr}_3(\text{BO}_3)_7$ [24] were reported in these ternary systems. The alkali-metal praseodymium borate $\text{K}_2\text{Pr}_2\text{O}(\text{BO}_3)_2$ has been found to be a new member of the $\text{K}_2\text{La}_2(\text{BO}_3)_2\text{O}$ family [25]. The report particularly emphasizes on the synthesis, crystal structure, vibrational, optical and thermal properties of $\text{K}_2\text{Pr}_2\text{O}(\text{BO}_3)_2$.

2. Experimental

2.1. Synthesis

Single crystals of $\text{K}_2\text{Pr}_2\text{O}(\text{BO}_3)_2$ were obtained by means of the flux-assisted solid state reaction method. The starting materials K_2CO_3 , PrO_2 and H_3BO_3 with a molar ratio of 1.5: 2: 3, respectively, were thoroughly ground in an agate mortar, and put into a platinum crucible. The mixture of the starting chemicals can be regarded as the target product $\text{K}_2\text{Pr}_2\text{O}(\text{BO}_3)_2$ together with the assisted-flux KBO_2 in the molar ratio of 1:1. The crucible was heated up to 1173 K in a muffle furnace with a heating rate of 100 K/h and maintained at that temperature for 12 h. Afterward, the crucible was cooled down to room temperature with a cooling rate of 300 K/h. The obtained $\text{K}_2\text{Pr}_2\text{O}(\text{BO}_3)_2$ was found as greenish, chunk-shaped, air and water-resistant single crystals.

Polycrystalline samples of $\text{K}_2\text{Pr}_2\text{O}(\text{BO}_3)_2$ were prepared using a solid-state synthesis method in a platinum crucible. First, a stoichiometric batch of intimately mixed K_2CO_3 , PrO_2 and

H₃BO₃ (analytical grade) was heated at 773 K for 12 h to completely decompose K₂CO₃ and H₃BO₃. The resulting samples were then ground in agate mortar and heated further at 1123 K for 48 h. A 10 % excess molar ratio of K₂CO₃ was added into the samples during the sintering process to compensate the evaporation of potassium. The mixtures were repeatedly heated at 1123 K with intermediate grindings until their powder X-ray diffraction pattern confirms a pure phase.

2.2. X-ray single crystal diffraction

The small crystals of K₂Pr₂O(BO₃)₂ were isolated by mechanical fragmentation and picked using a polarization microscope. Single-crystal diffraction data were collected on a Bruker D8-Venture diffractometer in Kappa geometry with MoK α radiation ($\lambda_{K\alpha} = 71.0747(6)$ pm) at 297(2) K. A numerical absorption correction was applied to the intensity data sets. The systematic extinctions and $|E^2-1|$ statistics suggested the monoclinic space group $P2_1/c$; therefore the structure determination of K₂Pr₂O(BO₃)₂ was performed in this space group. The structure was finely solved via the intrinsic phasing method and successfully refined on F² by full-matrix least-square methods with the ShelxT and Shelxle program packages [26, 27]. All atoms were refined with anisotropic displacement parameters and the final difference Fourier synthesis did not reveal any significant residual electron density. All relevant details of the data collection and the refinement are listed in **table 1**, atomic coordinates and displacement parameters in **table 2** and the bond valence sums (BVSs) in **table 3**.

Further details of the crystal structure information can be obtained from FIZ Karlsruhe, 76344 Eggenstein Leopoldshafen, Germany (fax: +49-7247-808-666; e-mail: [152](mailto:crysdata@fiz-</p></div><div data-bbox=)

karlsruhe.de) on quoting the deposition number CSD-1978814.

Table 1. Crystal structure determination of $\text{K}_2\text{Pr}_2\text{O}(\text{BO}_3)_2$ in the space group $P2_1/c$ (No.14) from single crystal and powder X-ray diffraction data.

Crystals	Single	Powder
<i>Dimension/μm^3 /$L_{\text{Vol}}(\text{IB})/\text{nm}$</i>	$93 \times 66 \times 52$	249(8)
<i>a/pm</i>	1133.77(3)	1135.00(3)
<i>b/pm</i>	660.47(2)	660.64(2)
<i>c/pm</i>	1071.30(3)	1072.03(3)
<i>$\beta/^\circ$</i>	117.07(1)	117.13(1)
<i>Z</i>	4	4
Temperature/K	297(2)	300(2)
Diffractometer	Bruker D8 Venture	Panalytical X'Pert Pro
Wavelength/pm	71.0747(6)	154.1866(1)
Absorption coefficient/ mm^{-1}	14.638	113.568(6)
Absorption correction method	Numerical	
<i>F(000)/e^-</i>	888	888
<i>$\theta / 2\theta$ range/$^\circ$</i>	2.017-46.021	5-130
Range in <i>hkl</i>	$-22 \leq h \leq 20,$	$0 \leq h \leq 13,$
	$-12 \leq k \leq 13,$	$0 \leq k \leq 7$
	$-20 \leq l \leq 21$	$-12 \leq l \leq 11$
Reflections collected	64145	1230
Data/restraints/parameters	6129/0/119	7480/8/54
Goodness-of-fit on F^2	1.043	1.92
<i>R₁/wR₂</i> (all data)	0.0401/0.0438	$R_{\text{wp}} = 0.07786$

2.3. X-ray powder diffraction

The powder X-ray diffraction (PXRD) pattern was recorded on a Panalytical X'Pert Pro

powder diffractometer using Bragg-Brentano geometry with $\text{CuK}_{\alpha 1,2}$ ($\lambda_{\text{K}\alpha 1} = 154.05929(5)$ pm, $\lambda_{\text{K}\alpha 2} = 154.4414(2)$ pm) radiation. The measurement was carried out at ambient condition in a range between 5° and $130^\circ 2\theta$ with a step size of 0.0167° and a data collection time of 30 s/step. The fundamental parameter approach, where the fundamental parameters were fitted against a LaB_6 standard material, was applied for the Rietveld refinement using “Diffrac^{Plus} Topas 6” software (Bruker AXS GmbH, Karlsruhe, Germany). The starting lattice parameters and atomic coordinates were taken from the results of the single crystal structure determination.

2.4. UV/Vis spectroscopy

The UV/Vis diffuse reflectance measurement was collected from 200 nm to 850 nm with a step of 1 nm on a UV-2700 spectrophotometer (Shimadzu, Japan) equipped with an ISR-2600 plus two-detector integrating sphere (Pike Technologies, USA). The baseline correction was carried out against BaSO_4 powder.

2.5. Vibration spectroscopy

The Fourier transform infrared (FTIR) spectrum was recorded on a Bruker IFS66v/S spectrometer using the standard KBr method between 370 cm^{-1} and 4000 cm^{-1} . KBr pellets consist of 2 mg sample mixed with 200 mg KBr (sample) and 200 mg KBr (reference), pressed at 100 kN, forming disks of 12 mm in diameter.

Temperature-dependent Raman spectra were recorded on a LabRam ARAMIS (Horiba Jobin Yvon) Micro-Raman spectrometer equipped with a laser working at 785 nm and less than 5 mW.

The use of a 50x long working distance objective (Olympus) with a numerical aperture of 0.55

provides a focus spot of about 2 μm diameter when closing the confocal hole to 200 μm . Raman spectra were collected in the range 85 cm^{-1} to 1700 cm^{-1} with a spectral resolution of approximately 1.2 cm^{-1} using a grating of 1800 grooves/mm and a thermoelectrically cooled CCD detector (Synapse, 1024 x 256 pixels). The spectral positions were calibrated against the Raman mode of Si before and after the sample measurements. The position of the Si peak was repeatedly measured against the Rayleigh line (0.0 cm^{-1}) yielding a value of $520.7 \pm 0.1 \text{ cm}^{-1}$. The linearity of the spectrometer was calibrated against the emission lines of a neon lamp. For the low-temperature measurements, a pressed pellet of powder sample was placed on a Linkam cooling stage (THMS600) attached to a pump (LNP95 Cooling Pump) that provides a continuous flow of liquid nitrogen. The measurements were carried out between 78 K and 300 K. A ramp rate of 5 K/min and a holding time of 5 min were followed to properly equilibrate the temperature. For the spectrum at ambient condition the baseline was corrected and fitted with Pseudo-Voigt lineshape. account.

2.6. Thermal analysis

Simultaneous thermogravimetric analysis/differential scanning calorimetry (TGA/DSC) measurements were performed on TGA/DSC 3⁺ STAR^c system of Mettler Toledo. The sample was measured with a heating rate of 10 K/min and a continuous N_2 flow of 20 mL/min from 300 K to 1473 K. Afterward, the data were normalized to their respective mass. Approximately 16.159 mg of $\text{K}_2\text{Pr}_2\text{O}(\text{BO}_3)_2$ was measured relative to an empty corundum crucible as the reference. A drift correction was applied based on empty crucible data.

Table 2: Crystal structural data of $\text{K}_2\text{Pr}_2\text{O}(\text{BO}_3)_2$. The isotropic ($B_{\text{iso}}/10^4 \times \text{pm}^2$) and equivalent isotropic ($U_{\text{eq}}/10^4 \times \text{pm}^2$) atomic displacement parameters are obtained from powder X-ray and single crystal X-ray diffraction data analysis, respectively.

Atom	Wyckoff	SOF	x	y	z	U_{eq}	B_{iso}
Pr1	4e	1	0.51850(2)	0.04466(2)	0.31939(2)	49.0(2)	-
			0.5184(3)	0.0452(4)	0.3202(3)	-	0.46(5) ^a
Pr2	4e	1	0.32360(2)	0.41647(2)	0.41561(2)	56.3(2)	-
			0.3230(3)	0.4159(4)	0.4162(3)	-	0.46(5) ^a
K1	4e	1	0.03193(5)	0.06011(7)	0.26414(5)	129.9(8)	-
			0.0320(9)	0.0569(15)	0.2666(10)	-	0.55(18) ^b
K2	4e	1	0.11866(5)	0.74422(8)	0.05575(5)	137.7(3)	-
			0.1200(9)	0.7564(15)	0.0596(12)	-	0.55(18) ^b
B1	4e	1	0.6946(2)	0.3446(3)	0.1441(2)	67(3)	-
			0.6946 ^d	0.3446 ^d	0.1441 ^d	-	0.529 ^d
B2	4e	1	0.1978(2)	0.2469(3)	0.0897(2)	73(3)	-
			0.1978 ^d	0.2469 ^d	0.0897 ^d	-	0.576 ^d
O1	4e	1	0.79983(15)	0.2513(2)	0.14046(17)	103(3)	-
			0.808(3)	0.258(5)	0.144(3)	-	1.5(3) ^c
O2	4e	1	0.12430(16)	0.3490(3)	0.46490(17)	114(3)	-
			0.128(3)	0.327(4)	0.482(3)	-	1.5(3) ^c
O3	4e	1	0.14560(16)	0.3469(3)	0.16568(17)	119(3)	-
			0.154(2)	0.363(4)	0.169(3)	-	1.5(3) ^c
O4	4e	1	0.63161(15)	0.2468(2)	0.21263(17)	90(3)	-
			0.622(3)	0.267(4)	0.221(3)	-	1.5(3) ^c
O5	4e	1	0.52705(15)	0.3776(2)	0.40277(16)	77(2)	-
			0.528(3)	0.395(4)	0.419(3)	-	1.5(3) ^c
O6	4e	1	0.33651(15)	0.2428(2)	0.13950(17)	97(3)	-
			0.346(3)	0.233(4)	0.142(3)	-	1.5(3) ^c
O7	4e	1	0.35215(16)	0.0341(2)	0.41402(17)	92(3)	-
			0.361(2)	0.010(4)	0.402(3)	-	1.5(3) ^c

^{a,b,c} values with the same letters were constrained to each other during the refinements.

^d these values were fixed during the refinement. U_{ij} tensors can be obtained from CSD-1978814.

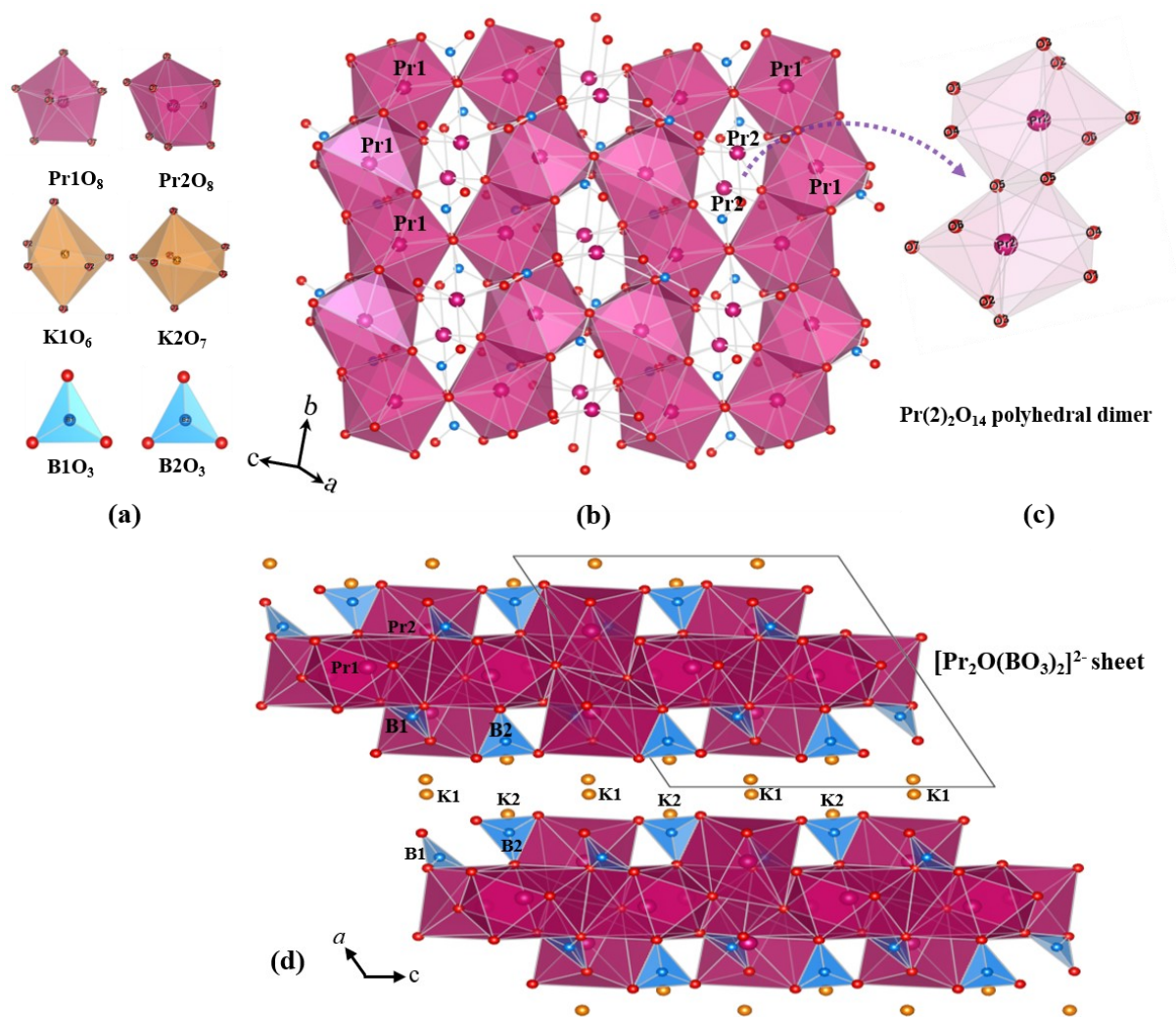


Figure 1. Crystal structure of $\text{K}_2\text{Pr}_2\text{O}(\text{BO}_3)_2$, showing polyhedral structural units (a) connectivity of Pr(1)O_8 dodecahedra (b), $\text{Pr(2)}_2\text{O}_{14}$ polyhedral dimer (c), and view of the structure of $\text{K}_2\text{Pr}_2\text{O}(\text{BO}_3)_2$ along the b -axis (d).

3. Results and discussion

3.1. Crystal structure of $\text{K}_2\text{Pr}_2\text{O}(\text{BO}_3)_2$

$\text{K}_2\text{Pr}_2\text{O}(\text{BO}_3)_2$ crystallizes in a new structure type in the monoclinic space group $P2_1/c$ (no. 14) with lattice parameters of $a = 1133.77(3)$ pm, $b = 660.47(2)$ pm, $c = 1071.30(3)$ pm, $\beta = 117.072(1)^\circ$, and $Z = 4$. The structural building units of $\text{K}_2\text{Pr}_2\text{O}(\text{BO}_3)_2$, as shown in **figure 1**, can be regarded as PrO_8 dodecahedra, KO_6 octahedra and KO_7 pentagonal bipyramid together

with isolated trigonal planar BO_3 groups. Both Pr(1) and Pr(2) form distorted PrO_8 dodecahedra, where the Pr–O bond lengths vary from 235.9(2) pm to 260.1(2) pm in Pr(1)O_8 , and from 234.6(2) to 274.6(2) pm in Pr(2)O_8 . The Pr(1)O_8 dodecahedra are axially connected with its neighbors via sharing two triangular faces to construct an infinite zig-zag chain along the **b**-axis (**Fig. 1b**). These zig-zag chains are further joined together by edge-sharing to form infinite two dimensional $\text{Pr(1)O}_{(3+3+2)/2}$ layers with elongated hexagonal voids in the *bc*-plane. Such a 2D REO_n layer with “honeycomb-like” voids was also found in other rare-earth borates, for instance, in $\text{Na}_3\text{La}_2(\text{BO}_3)_3$ [28]. By contrast, two Pr(2)O_8 dodecahedra share their O(5)-O(5) edge to construct $\text{Pr(2)}_2\text{O}_{14}$ dimers that fill into those “honeycomb-like” voids (**Fig. 1c**). It is interesting to mention that O(5), the isolated oxygen anion in $\text{K}_2\text{Pr}_2\text{O}(\text{BO}_3)_2$, connects only to Pr-atoms and plays an important role in the formation of a $\text{Pr(2)}_2\text{O}_{14}$ dimer. Therefore, $[\text{Pr}_2\text{O}(\text{BO}_3)_2]^{2-}$ sheets are composed of $\text{Pr(1)O}_{(3+3+2)/2}$ layers, $\text{Pr(2)}_2\text{O}_{14}$ dimers, isolated B(1) O_3 and B(2) O_3 planar groups via corner and edge sharing in the *ac*-plane. Two adjacent $[\text{Pr}_2\text{O}(\text{BO}_3)_2]^{2-}$ sheets in the structure are regulated by the inversion center (**Fig. 1d**). Two types of potassium K(1) and K(2) are found to occupy the inter-sheet space and separate the $[\text{Pr}_2\text{O}(\text{BO}_3)_2]^{2-}$ sheets along the **a**-axis. Similar stacking modes were also observed in other layered alkali-metal rare-earth borates such as $\text{K}_9\text{Li}_3\text{Nd}_3(\text{BO}_3)_9$ [24] and $\text{Rb}_2\text{LiNd}(\text{BO}_3)_2$ [24]. K(1) is six-fold coordinated to form a distorted K(1)O_6 octahedron while K(2) connects to seven oxygens in exhibition of a distorted pentagonal bipyramid K(2)O_7 . The K–O distances range from 265.9(2) to 282.4(2) pm with mean values of 273.6 (2) pm and 282.3 (2) pm for K(1)O_6 and K(2)O_7 polyhedra, respectively. These values fit well with the sum of the ionic radii of oxygen and potassium in six-fold and seven-fold coordination [29].

In the unit cell, both B(1) and B(2) atoms are three-coordinated to oxygen atoms, forming isolated planar BO_3 groups. The B-O distances range from 134.2(5) to 141.0(6) pm with an averaged bond length of 137.0(3) pm for B(1)O_3 and 137.9(3) pm for B(2)O_3 , respectively. These values are in agreement with those of other alkali-metal rare-earth borate-containing isolated BO_3 groups, for instance 137.1 pm in $\text{K}_3\text{Sm}(\text{BO}_3)_2$ [30], 137.4 pm in $\text{Li}_3\text{K}_3\text{Y}_7(\text{BO}_3)_9$ [31] and 137.6 pm in $\text{K}_9\text{Li}_3\text{Nd}_3(\text{BO}_3)_7$ [24]. The bond valence sums (BVS) calculation was performed for $\text{K}_2\text{Pr}_2\text{O}(\text{BO}_3)_2$ using the Bondstr software of the FullProf suite [32], which are listed in **table 3**. The structural BVSs of the atoms correspond well with the formal integer charge of the respective atoms. To confirm the single crystal structure of its bulk representative as well the purity of the as-synthesized $\text{K}_2\text{Pr}_2\text{O}(\text{BO}_3)_2$ polycrystalline powder sample, X-ray powder data Rietveld refinements were performed. The corresponding Rietveld plot is shown in **figure 2**. The metric parameters ($a = 1135.00(3)$ pm, $b = 660.641(15)$ pm, $c = 1072.03(3)$ pm, $\beta = 117.128(2)^\circ$ and $V = 715.41(3) \times 10^6 \text{ pm}^3$) are in excellent agreement with those obtained from the single crystal structure determination (**Tab. 1 & 2**).

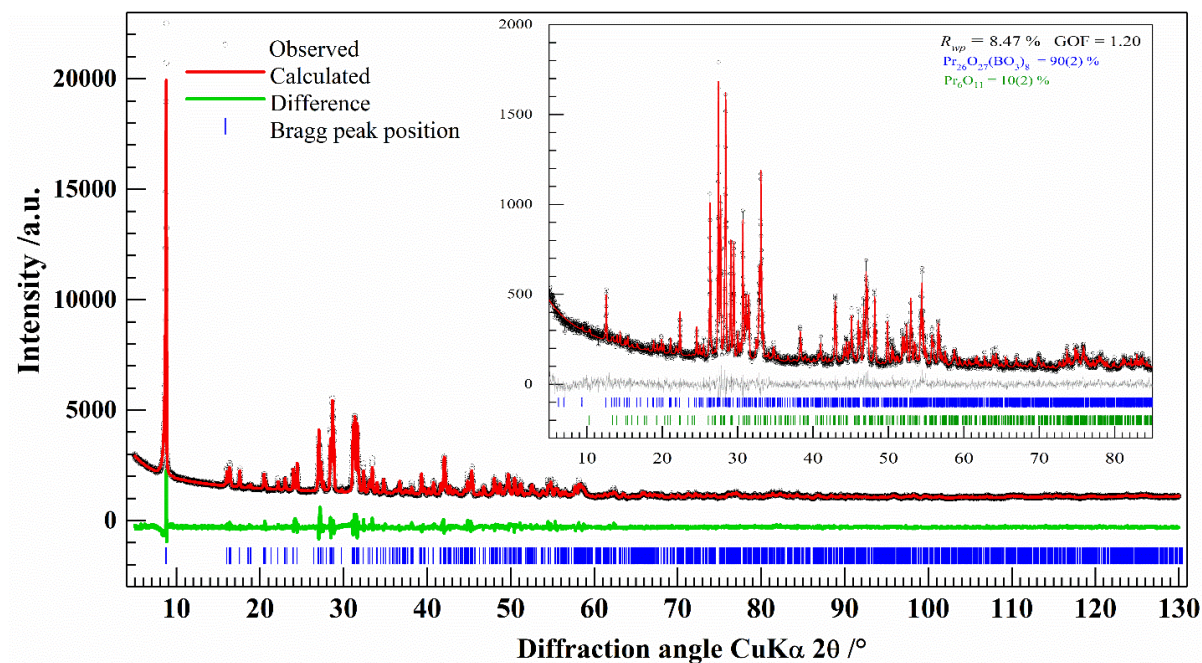


Figure 2. X-ray powder data Rietveld plots of $\text{K}_2\text{Pr}_2\text{O}(\text{BO}_3)_2$ and of the decomposition products as inset.

Table 3. Interatomic bond distance /pm and bond valence (BV /v.u.) and bond valence sum (BVS /v.u.) of the PrO₈, KO_{6,7} and BO₃ polyhedra in K₂Pr₂O(BO₃)₂.

Bond	Bond length	BV	Bond	Bond length	BV
Pr1O ₈			Pr2O ₈		
Pr1-O5	235.9(2)	0.551(2)	Pr2-O5	234.6(2)	0.570(2)
Pr1-O5	245.6(2)	0.424(2)	Pr2-O5	238.6(2)	0.511(3)
Pr1-O6	246.3(2)	0.416(1)	Pr2-O1	253.9(2)	0.339(1)
Pr1-O4	246.4(2)	0.415(2)	Pr2-O7	254.7(2)	0.331(1)
Pr1-O6	249.3(2)	0.384(2)	Pr2-O3	255.6(2)	0.323(1)
Pr1-O7	251.6(2)	0.360(2)	Pr2-O6	256.2(2)	0.318(2)
Pr1-O4	252.0(2)	0.356(1)	Pr2-O2	258.25(2)	0.301(2)
Pr1-O7	260.1(2)	0.286(1)	Pr2-O4	274.6(2)	0.193(1)
BVS(Pr1)		3.190(5)	BVS(Pr2)		2.886(5)
K1O ₆			K2O ₇		
K1-O1	265.9(2)	0.241(1)	K2-O1	265.4(2)	0.244(1)
K1-O1	266.5(2)	0.237(1)	K2-O2	275.0 (2)	0.188(1)
K1-O2	267.3(2)	0.232(1)	K2-O4	278.91(2)	0.169(1)
K1-O2	270.4(2)	0.213(1)	K2-O3	283.51(2)	0.149(1)
K1-O3	275.7(2)	0.185(1)	K2-O2	286.8(2)	0.137(1)
K1-O3	282.4(2)	0.154(1)	K2-O3	291.5(2)	0.121(0)
			K2-O1	295.1(2)	0.109(1)
BVS(K1)		1.261(1)	BVS(K2)		1.118(1)
B1O ₃			B2O ₃		
B1-O1	135.9(3)	1.033(8)	B2-O2	136.7(3)	1.011(7)
B1-O7	139.1(3)	0.948(6)	B2-O3	137.3(3)	0.992(9)
B1-O4	139.3(3)	0.939(8)	B2-O6	141.3(3)	0.894(7)
BVS(B1)		2.920(13)	BVS(B2)		2.897(13)

3.2. UV/Vis spectrum

The UV/Vis reflectance spectrum of $\text{K}_2\text{Pr}_2\text{O}(\text{BO}_3)_2$ in the range of 200 nm - 850 nm is shown in **figure 3**. The optical absorption in the visible range accounts for the green color of $\text{K}_2\text{Pr}_2\text{O}(\text{BO}_3)_2$ and also corresponds well to the presence of Pr^{3+} cation. All visible absorption bands in $\text{K}_2\text{Pr}_2\text{O}(\text{BO}_3)_2$ result from the inner-shell $4f^2$ -configuration electronic transitions from the ground state ($^3\text{H}_4$) to various excited states. According to the energy level scheme proposed by Dieke and Crosswhite [33], these bands from 400 nm to 520 nm can be assigned, respectively to $^3\text{H}_4 \rightarrow ^3\text{P}_2$, $^3\text{P}_1$, and $^3\text{P}_0$, while the band in the range of 550 nm - 650 nm ascribed to $^3\text{H}_4 \rightarrow ^1\text{D}_2$. Of particular notes, we clearly observe the Stark splitting of $^3\text{P}_2$, $^3\text{P}_1$, and $^3\text{P}_0$ and $^1\text{D}_2$ multiplets, which may help calculate the crystal field levels of Pr^{3+} cation in $\text{K}_2\text{Pr}_2\text{O}(\text{BO}_3)_2$. The monotonic drop of the reflectance between 290 nm to 270 nm (**Fig. 3**) corresponds to the valence-to-conduction-band absorption edge. The Kubelka-Munk function [34] treatment followed by the Tauc method [35] are often used to estimate the corresponding bandgap energy by finding the intercept of the abscissa from the following relations:

$$F(R) = \frac{(1 - R)^2}{2R}$$

$$F(R)(h\nu) = B(h\nu - E_g)^n$$

where R is the reflectance (%) in the UV/Vis spectra, h the Planck's constant, ν the frequency of light, E_g the bandgap in eV, and n -the type of optical transition. That is, $n = 2$ for an indirect transition (plotted as $[F(R) \cdot (h\nu)]^{1/2}$ vs. $h\nu$) and $n = 1/2$ for a direct transition (plotted as $[F(R) \cdot (h\nu)]^2$ vs. $h\nu$). The intercepts of the abscissa (**Fig. 3**) demonstrate bandgap values of 4.40(1) eV and 4.50(1) eV for an indirect and direct transition, respectively. These bandgap values of $\text{K}_2\text{Pr}_2\text{O}(\text{BO}_3)_2$ are smaller than those of 4.96 eV for $\lambda\text{-PrBO}_3$ [36] and 6.32 eV for

Rb₂LiLaB₂O₆ [37]. Recently, the DASF method was proposed by Souri et al. [38] for thin films to calculate the bandgap energies without any presumption of the nature of the transition. Notably, the DASF method can also be expressed as follows proposed by Kirsch et al. [39, 40] for powder samples:

$$\frac{d\ln F(R)}{dh\nu} = \frac{n}{h\nu - E_g}$$

The obtained bandgap of 4.49(1) eV using the DASF method is similar to the determined bandgap of 4.50(1) eV for a direct transition within the estimated uncertainty. Therefore, the combined approach suggests a direct bandgap transition for K₂Pr₂O(BO₃)₂.

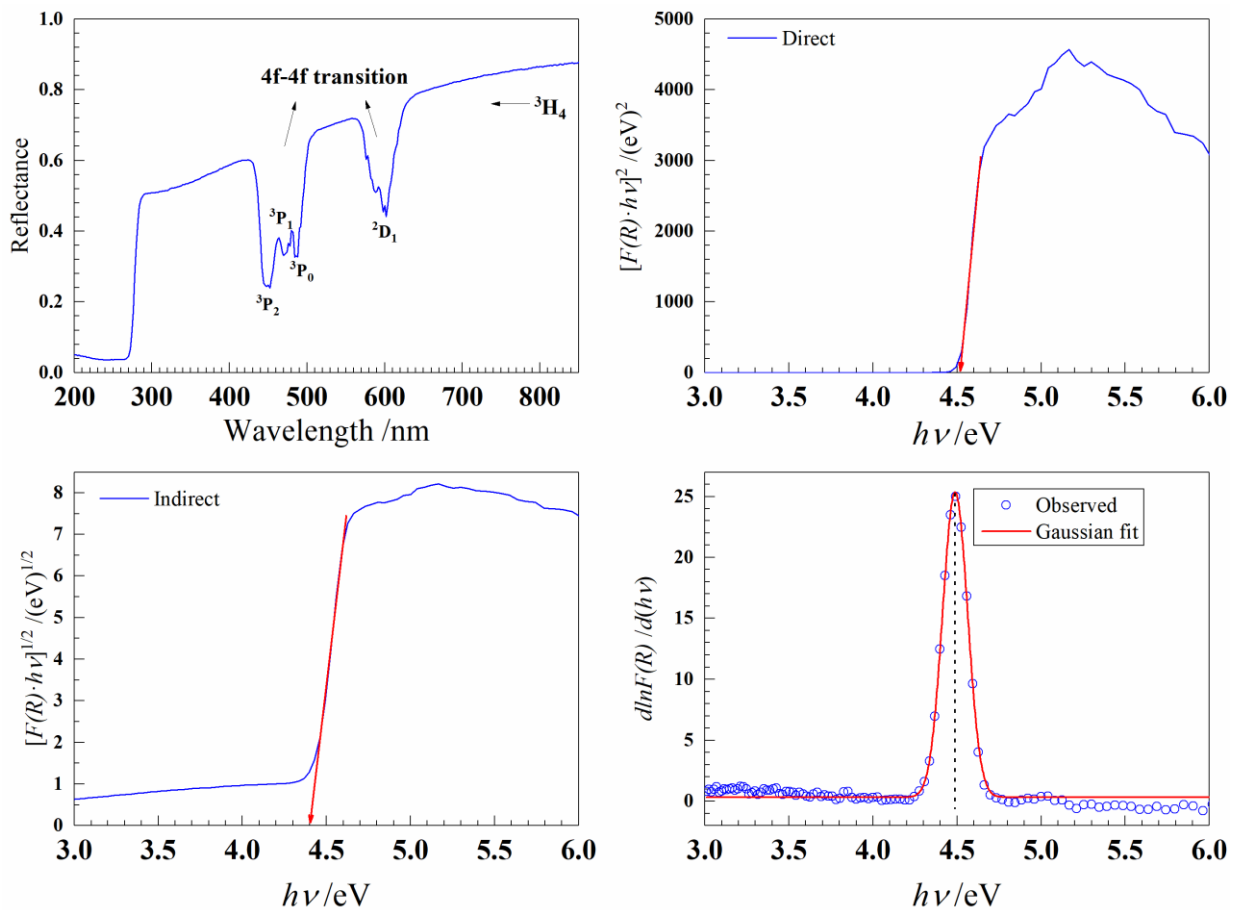


Figure 3. Reflectance spectrum of K₂Pr₂O(BO₃)₂ (top left), Tauc plots for indirect (bottom left) and direct (top right) optical transitions, and DASF plot (bottom right).

3.3. FTIR and Raman spectra

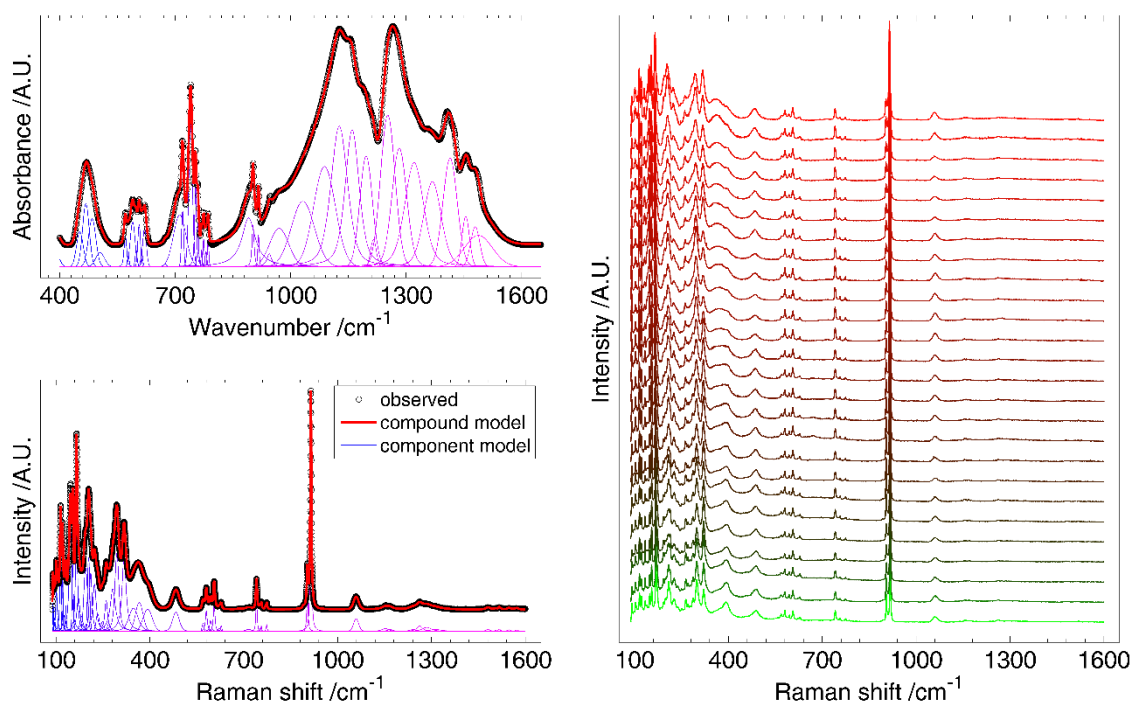


Figure 4. FTIR (left top) and Raman (left bottom) spectra of $\text{K}_2\text{Pr}_2\text{O}(\text{BO}_3)_2$ at ambient condition along with fitted compound and component models. Temperature-dependent Raman spectra (right); temperature increases upward from 78 K to 300 K.

The observed FTIR and Raman spectra along with the fitted compound and component models are shown in **figure 4**. Since the crystal structure of $\text{K}_2\text{Pr}_2\text{O}(\text{BO}_3)_2$ adopts $P2_1/c$ space group, factor group analysis predicts 156 vibrational modes at the zone center ($39A_g + 39A_u + 39B_g + 39B_u$), where 75 modes ($38A_u + 37B_u$) are IR active, 78 modes ($39A_g + 39B_g$) are Raman active and 3 are acoustic modes ($A_u + 2B_u$). To fit the observed IR spectrum, it requires 41 bands. The bands between 400 and 550 cm^{-1} can be attributed to bending of Pr-O, which was explicitly characterized in other praseodymium oxides [41, 42]. The bands between 600 cm^{-1} and 1600 cm^{-1} owing to vibration of planar BO_3^{3-} groups, can be categorized into four different types [37, 43, 44]: the in-plane bending (ν_4 ; 550 - 700 cm^{-1}), out-of-plane bending (ν_2 ; 740

cm^{-1} - 780 cm^{-1}) of BO_3 , B-O symmetric stretching (ν_1 ; $\sim 903\text{ cm}^{-1}$) and B-O asymmetric stretching (ν_3 ; 1000 cm^{-1} and 1500 cm^{-1}). Clearly, the ν_2 and ν_3 modes have much stronger absorption than that of ν_3 and ν_1 . Group analysis of an ideal planar BO_3 group possesses D_{3h} symmetry, where ν_2 and ν_3 are IR active, whereas the ν_1 is IR inactive. The clear appearance of ν_1 in the IR spectrum indicates that the BO_3 groups in $\text{K}_2\text{Pr}_2\text{O}(\text{BO}_3)_2$ are distorted from an ideal symmetry.

The observed Raman spectrum of $\text{K}_2\text{Pr}_2\text{O}(\text{BO}_3)_2$ at ambient condition could be fitted with **56 component** peaks (**Fig. 4**). Several intense bands below 550 cm^{-1} can be ascribed to the bending and stretching vibrations of K-O and Pr-O bonds as well as the lattice vibrations. The bands observed in the range of $600 - 700\text{ cm}^{-1}$ and $700 - 800\text{ cm}^{-1}$ correspond to the ν_4 and ν_2 modes, respectively. The most intense bands occur at 915 cm^{-1} resulting from the ν_1 mode. The symmetric stretching mode (ν_1) of BO_3^{3-} group is a strong Raman active vibration as known from other Pr^{3+} -containing orthoborates such as $\lambda\text{-PrBO}_3$ [37, 43, 44] and $\text{KCaPr}(\text{BO}_3)_2$ [45]. Above 1000 cm^{-1} , one peak locating at 1050 cm^{-1} and several border bands are found and can be ascribed to the ν_3 mode of BO_3^{3-} groups. Of notes, the Raman spectrum also clearly confirms the vibrational features of BO_3 and PrO_x groups in $\text{K}_2\text{Pr}_2\text{O}(\text{BO}_3)_2$. The temperature-dependent Raman spectra of $\text{K}_2\text{Pr}_2\text{O}(\text{BO}_3)_2$ from 83 K to 298 K (**Fig. 4**) show that the overall global quasi-harmonic change is not significant within the investigated low-temperature range. For instance, the intense band at $916.4(1)\text{ cm}^{-1}$ at 83 K shifts only to $914.5(1)\text{ cm}^{-1}$ at 298 K. Any phase transition driven by any optical soft-mode was not observed during the sample cooling from 298 K to 83 K. Extrapolation of the frequency of this mode down to 0 K suggests that the compound $\text{K}_2\text{Pr}_2\text{O}(\text{BO}_3)_2$ would be stable, a guideline for the phonon calculation using

density functional theory calculation.

3.4. Thermal analysis

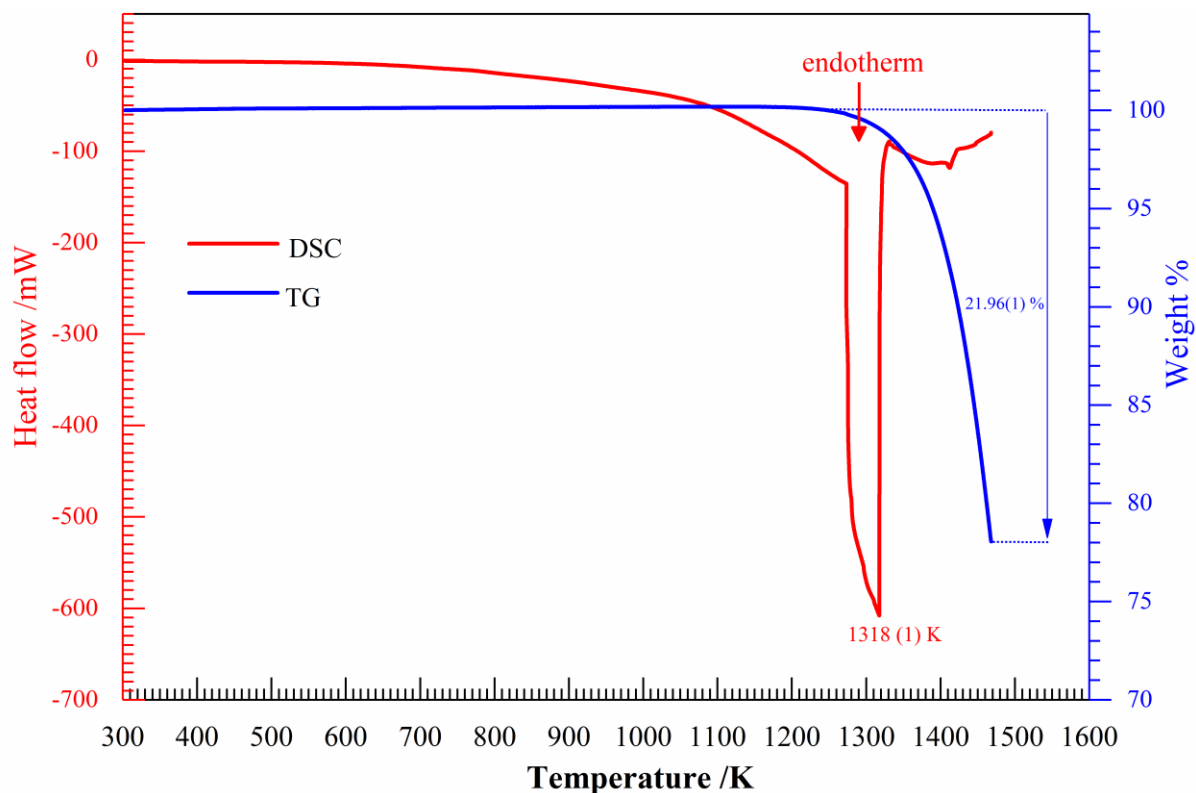


Figure 5. Thermogravimetry (TG) and differential scanning calorimetry (DSC) curves of $\text{K}_2\text{Pr}_2\text{O}(\text{BO}_3)_2$.

For the bulk single-crystal growth of inorganic compounds, determination of the melting point or the decomposition temperature is indispensable. The thermal behavior of $\text{K}_2\text{Pr}_2\text{O}(\text{BO}_3)_2$ was investigated by using simultaneous TGA and DSC methods. As shown in **figure 5**, the DSC curve demonstrates one sharp endothermic signal peak at 1318(1) K as well as one border and tiny peaks after 1400 K. The distinct endotherm in the range of 1273(3) K and 1330(3) K corresponds to melting or thermal decomposition. From the TG curve a weight-loss of 21.96(1) % is found to be at 1273(3) K. After the TGA /DSC experiment, X-ray powder data

Rietveld refinement (**inset Fig. 2**) demonstrates that the residual consists of $\text{Pr}_{26}\text{O}_{27}(\text{BO}_3)_8$ and Pr_6O_{11} phases. It is worthwhile to note that we used $\text{Nd}_{26}\text{O}_{27}(\text{BO}_3)_8$ [46] as the starting model and replaced Nd -atom with Pr-atom in the same Wyckoff position during the Rietveld refinement. For the obtained isotypic $\text{Pr}_{26}\text{O}_{27}(\text{BO}_3)_8$ lattice parameters of $a = 676.160(17)$ pm, $b = 1269.56(4)$ pm, $c = 1432.28(3)$ pm, $\alpha = 89.9979(17)^\circ$, $\beta = 99.9008(17)^\circ$, $\gamma = 89.9995(19)^\circ$ were calculated. From the distinct weight loss during the heating process one can safely assume that $\text{K}_2\text{Pr}_2\text{O}(\text{BO}_3)_2$ decomposes into $\text{Pr}_{26}\text{O}_{27}(\text{BO}_3)_8$, Pr_6O_{11} and potassium borates which eventually evaporates at the high-temperature regime. The TGA /DSC also confirms that $\text{K}_2\text{Pr}_2\text{O}(\text{BO}_3)_2$ possess an incongruent melting point, suggesting that the flux method would be necessary for the growth of its bulk crystal.

3.5 Magnetic Property

Plots of the magnetic susceptibility (χ) as well as reciprocal susceptibility (χ^{-1}) as a function of temperature at 100 oe field in the Zero Field Cooling (ZFC) and the Field cooling (FC) states for $\text{K}_2\text{Pr}_2\text{O}(\text{BO}_3)_2$ are given in Fig. 4. Above all, the magnetic susceptibilities for both ZFC and FC are observed to increase from 299 K to 2K without any suspicious bifurcation, implying that $\text{K}_2\text{Pr}_2\text{O}(\text{BO}_3)_2$ exhibits paramagnetism in this range. Thereby, Curie-Weiss law [47]

$$\chi^{-1} = \frac{T - \theta_{cw}}{C}, \quad C = \frac{\mu_{eff}^2}{8}$$

where T temperature, θ_{cw} the Weiss constant, C the Curie constant, μ_{eff} the effective magnetic moment, was applied to fit both the ZFC and FC reciprocal susceptibility plots, giving $\mu_{eff} = 3.32(1) \mu_B$ and $\theta_{cw} = -29.8(1)$ K for the ZFC as well as $\mu_{eff} = 3.33(1) \mu_B$ and $\theta_{cw} = -29.6(1)$ K for the FC, respectively. The negative Weiss temperatures indicate antiferromagnetic interactions between those Pr^{3+} cations. As is known to us, the free Pr^{3+} cation ion with a $4f^2$ electron

configuration is a non-Kramers ion in which a crystal field itself can resolve degeneracies to give a non-magnetic ground state [47]. As a result, the 3H_4 ground state of the Pr^{3+} cation (this state is also the ground state in the UV/VIS spectrum) split into three singlets and three doublets via the crystalline field, leading to the effective magnetic moment of $3.58(1) \mu_B$. The calculated values for both ZFC and FC are close to this expected value, further suggesting that $\text{K}_2\text{Pr}_2\text{O}(\text{BO}_3)_2$ is a Curie-Weiss magnet throughout the temperature range 2-300 K.

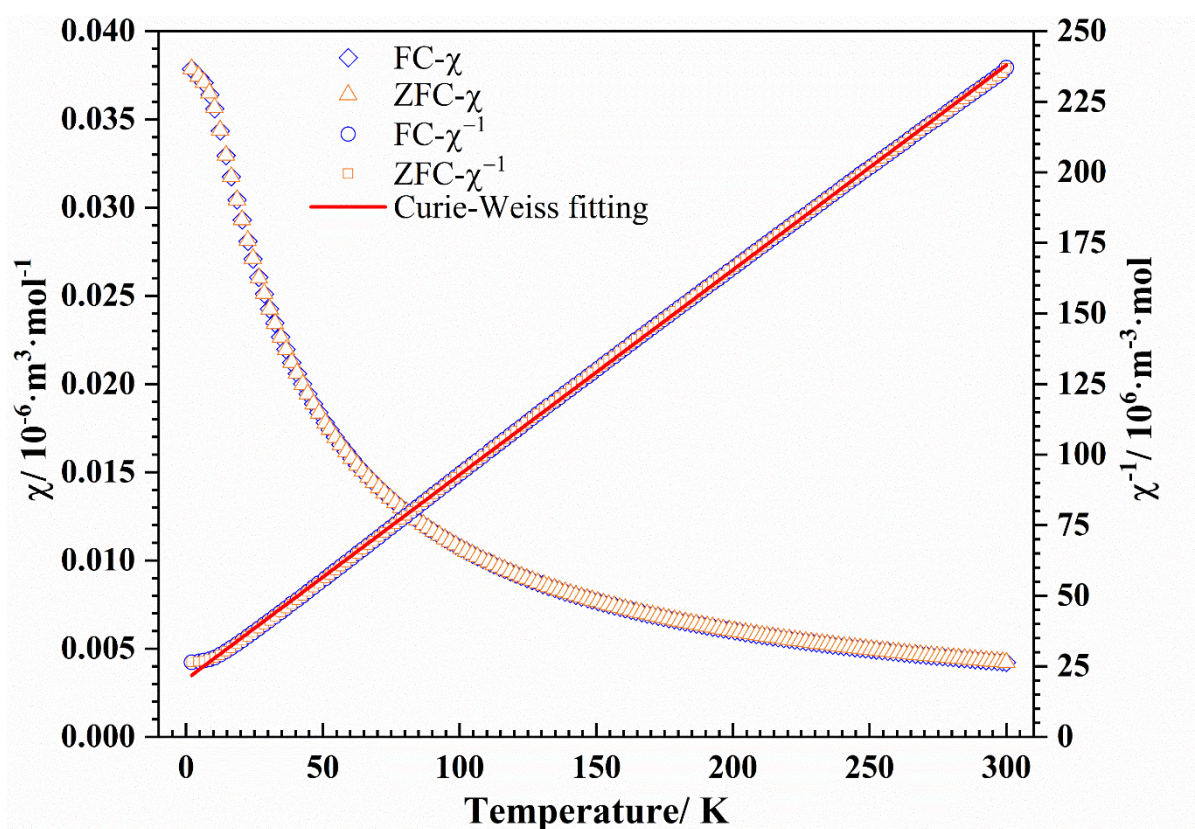


Figure 6. The temperature-dependent molar magnetic susceptibility and reciprocal susceptibility for $\text{K}_2\text{Pr}_2\text{O}(\text{BO}_3)_2$ measured in the Zero Field Cooling (ZFC) and the Field cooling (FC) states with applied fields of 100 oe

3.6 Structural comparison of $K_2RE_2O(BO_3)_2$ and $KREOCO_3$

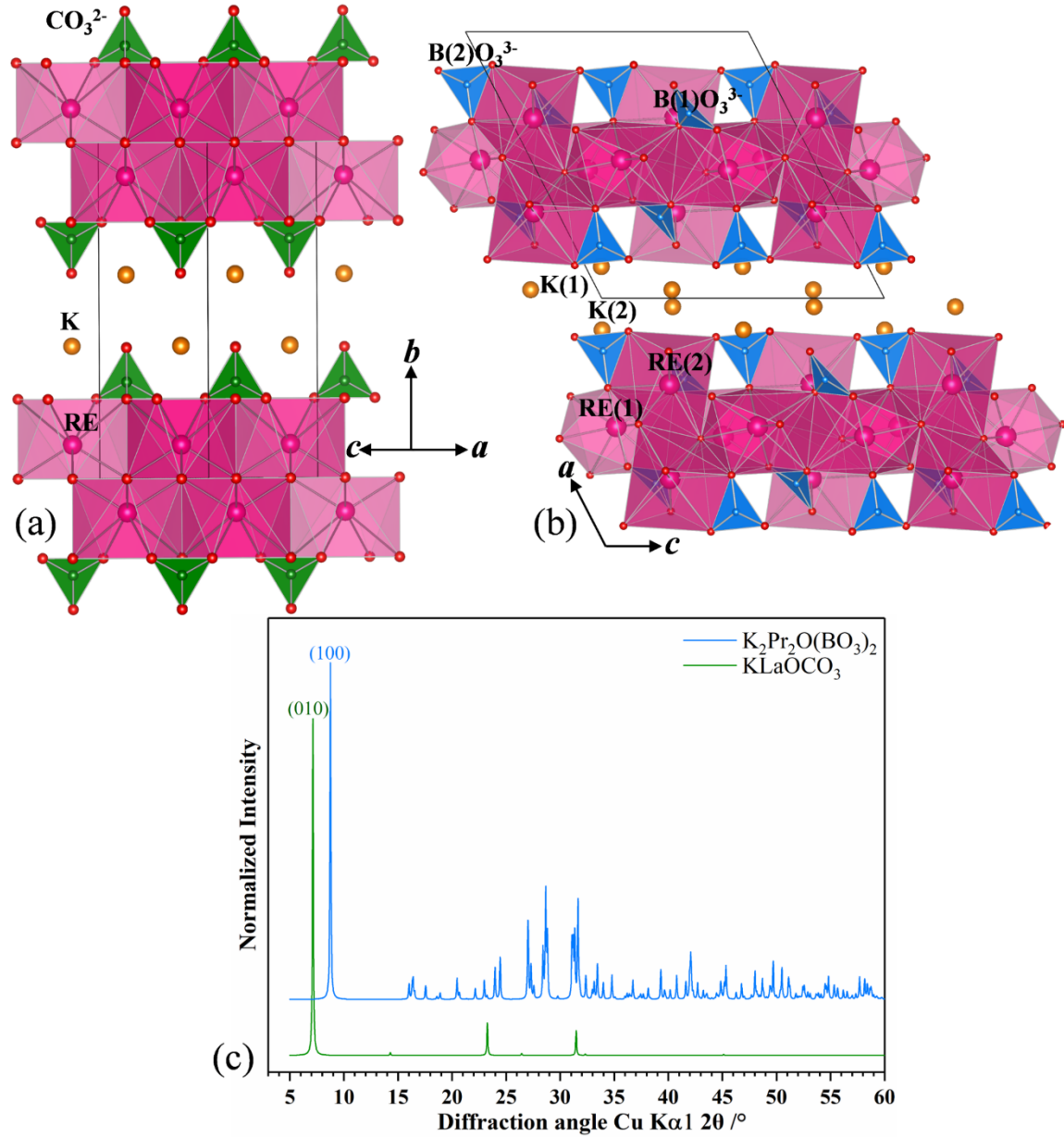


Figure 7. (a) crystal structure of $KREOCO_3$ viewed along the $[101]$ (b) crystal structure of $K_2RE_2O(BO_3)_2$ viewed along the $[010]$ (c) the simulated powder XRD patterns of $KLaOCO_3$ and $K_2Pr_2O(BO_3)_2$

In certain cases, the synthetic rare-earth orthoborates can be considered to originate from the natural carbonate minerals, such as β - $LuBO_3$ ($CaCO_3$ calcite) [48], $YCa_3(MnO)_3(BO_3)_4$ and $BiSr_3(YO)_3(BO_3)_4$ ($Ca_4Mn_3(BO_3)_3CO_3O_3$, gaudefroyite) [49-51], and $Ca_3La_3(BO_3)_5$

($\text{Na}_4\text{La}_2(\text{CO}_3)_5$ and $\text{Na}_2\text{Ca}_4(\text{CO}_3)_5$ Naburbankite) [52-53]. It is interesting to compare this potassium-containing rare-earth oxo-orthoborate $\text{K}_2\text{RE}_2\text{O}(\text{BO}_3)_2$ family [25] with the potassium-containing rare-earth oxo-carbonate KREOCO_3 i.e., $\text{K}_2\text{RE}_2\text{O}_2(\text{CO}_3)_2$ family [54-55].

One could see that $\text{K}_2\text{RE}_2\text{O}_2(\text{CO}_3)_2$ and $\text{K}_2\text{RE}_2\text{O}(\text{BO}_3)_2$ have a series of common features:

- 1) Both families characterize layered structures composed of infinite sheets of REO_n polyhedra and K^+ cations reside between the layers.
- 2) Anionic groups (CO_3^{2-} and BO_3^{3-}) in these two families are in the planar triangle geometry.
- 3) RE^{3+} cations are all eight-coordinated in these two structural types.
- 4) Both $\text{K}_2\text{RE}_2\text{O}_2(\text{CO}_3)_2$ and $\text{K}_2\text{RE}_2\text{O}(\text{BO}_3)_2$ can merely accommodate these light rare-earth elements with $\text{RE} = \text{La, Pr, Nd, Sm, Eu}$.
- 5) Both compounds exhibit pronounced preferred orientation along their stacking directions due to their layered nature and plate-like habitus.

On the other hand, the structural difference between KREOCO_3 and $\text{K}_2\text{RE}_2\text{O}(\text{BO}_3)_2$ also exists.

Above all, compared to $\text{K}_2\text{RE}_2\text{O}_2(\text{CO}_3)_2$ family in the monoclinic space group $P2_1/c$, KREOCO_3 crystallizes into a higher orthorhombic space group $Pcca$ with a pseudo-tetrahedral lattice parameter of $a = 567.93(3)$ pm, $b = 1238.41(3)$ pm, $c = 567.93(3)$ pm in the case of the La-member. As a result, the asymmetric unit of KREOCO_3 contains K^+ , RE^{3+} and CO_3^{2-} each unique. In contrast to the face-sharing REO_8 polyhedra in $\text{K}_2\text{RE}_2\text{O}(\text{BO}_3)_2$, the REO_8 polyhedra in KREOCO_3 only share common edges. Besides, the isolated oxygen anion in $\text{K}_2\text{RE}_2\text{O}(\text{BO}_3)_2$ connects only to RE^{3+} cations, whereas that one in KREOCO_3 does not connect to RE^{3+} at all. Thus, the actual ratio of RE: O in KREOCO_3 shifts to 1/3, making the REO_8 polyhedra arranged similar to that in REMnO_3 perovskite ($Pbnm$) [56]. In brief, understanding the structural

features of KREOCO_3 and $\text{K}_2\text{RE}_2\text{O}(\text{BO}_3)_2$ may provide helpful clues to the design and exploration of novel rare-earth borates derived from rare-earth carbonates, and vice versa.

4. Conclusion

The detailed structural, spectroscopic and thermal analysis reveal that the synthesized alkali metal praseodymium borate $\text{K}_2\text{Pr}_2\text{O}(\text{BO}_3)_2$ belongs to the new member of the $\text{K}_2\text{La}_2(\text{BO}_3)_2\text{O}$ family [25] providing also a new structure type. The crystal structure consists of 2D $[\text{Pr}_2\text{O}(\text{BO}_3)_2]^{2-}$ sheets and K^+ cations in a layered stacking along the **a**-axis. The greenish color stems from the electronic transitions from the ground state to various excited states within the $4f^2$ -configuration rather than from the fundamental absorption edge that lies in the UV-region. Since Pr^{3+} cation is of interest due to its photoluminescence property, $\text{K}_2\text{Pr}_2\text{O}(\text{BO}_3)_2$ may be a prospective red phosphor under the radiation of blue light [15-17]. Density functional theory (DFT) calculation would be necessary to distinguish the observed Raman and infrared bands between phonon at the zone-center and photoluminescence as well as for a fuller assignment of the modes. Given that $\text{K}_2\text{Pr}_2\text{O}(\text{BO}_3)_2$ is an incongruent melting compound, the bulk crystals may be grown via high-temperature flux method, which would help elucidate possible anisotropic properties.

Acknowledgement

PYC gratefully thanks the China Scholarship Council to carry out this work through a fellowship. PYC also acknowledges the supports from the University of Bremen.

Compliance with ethical standards

Conflict of interest: The authors declare that they have no conflict of interest.

Reference

- [1] M. Mutailipu, Z. Xie, X. Su, M. Zhang, Y. Wang, Z. Yang, M.R.S.A. Janjua, S. Pan, Chemical cosubstitution-oriented design of rare-earth borates as potential ultraviolet nonlinear optical materials, *J. Am. Chem. Soc.*, 139 (2017) 18397-18405.
- [2] A. Yoshida, A. Schmidt, V. Petrov, C. Fiebig, G. Erbert, J. Liu, H. Zhang, J. Wang, U. Griebner, Diode-pumped mode-locked Yb: YCOB laser generating 35 fs pulses, *Opt. Lett.*, 36 (2011) 4425-4427.
- [3] A. Kruopyte, R. Giraitis, R. Juskenas, D. Ensling, T. Jüstel, A. Katelnikovas, Luminescence and luminescence quenching of efficient GdB₅O₉: Eu³⁺ red phosphors, *J. Lumin.*, 192 (2017) 520-526.
- [4] W. Yao, R. He, X. Wang, Z. Lin, C.J. Chen, Analysis of Deep-UV Nonlinear Optical Borates: Approaching the End, *Adv. Opt. Mater.*, 2 (2014) 411-417.
- [5] R.A. Kumar, M. Arivanandhan, Y. Hayakawa, Recent advances in rare earth-based borate single crystals: Potential materials for nonlinear optical and laser applications, *Prog. Cryst. Growth Charact. Mater.*, 59 (2013) 113-132.
- [6] C. Chen, T. Sasaki, R. Li, Y. Wu, Z. Lin, Y. Mori, Z. Hu, J. Wang, G. Aka, M. Yoshimura, Nonlinear optical borate crystals: Principals and applications, John Wiley & Sons 2012.
- [7] A.H. Reshak, S. Auluck, I. Kityk, Optical susceptibilities of Na₃La₉O₃(BO₃)₈, ternary oxyborate nonlinear single crystal: theory and experiment, *J. Phys. Condens. Matter*, 20 (2008) 145209.
- [8] G. Wang, J. Lu, D. Cui, Z. Xu, Y. Wu, P. Fu, X. Guan, C. Chen, Efficient second harmonic generation in a new nonlinear La₂CaB₁₀O₁₉ crystal, *Opt. Commun.*, 209 (2002) 481-484.
- [9] D. Rytz, A. Gross, S. Vernay, V. Wesemann, YAl₃(BO₃)₄: a novel NLO crystal for frequency conversion to UV wavelengths, *Proc. SPIE 6998, Solid State Lasers and Amplifiers III*, 2008, 699814.
- [10] H.J. Eichler, J. Eichler, O. Lux, Lasers: basics, advances and applications. Springer, 2018.
- [11] J. Yin, J. Zhang, J. Wang, F. Du, R. Li, S. Pan, J. Pan, Growth and scintillation properties of Ce: Li₆Y(BO₃)₃ crystal enriched with ¹⁰B isotopes, *Radiat. Meas.*, 113 (2018) 20-24.
- [12] D. Jaque, J. Capmany, J. Garcia Solé, Red, green, and blue laser light from a single Nd: YAl₃(BO₃)₄ crystal based on laser oscillation at 1.3 μ m, *Appl. Phys. Lett.*, 75 (1999) 325-327.
- [13] V. Jubera, P. Veber, M. Chavoutier, A. Garcia, F. Adamietz, V. Rodriguez, J.-P. Chaminade, M. Velázquez, Crystal growth and optical characterizations of Yb³⁺-doped LiGd₆O₅(BO₃)₃ single crystal: a new promising laser material, *Cryst. Eng. Comm.*, 12 (2010) 355-357.
- [14] J. Dexpert-Ghys, R. Mauricot, B. Caillier, P. Guillot, T. Beaudette, G. Jia, P.A. Tanner, B.-M. Cheng, VUV excitation of YBO₃ and (Y, Gd)BO₃ phosphors doped with Eu³⁺ or Tb³⁺: comparison of efficiencies and effect of site-selectivity, *J. Phys. Chem. C*, 114 (2010) 6681-6689.
- [15] B. Han, Y. Dai, J. Zhang, X. Wang, W. Shi, H. Shi, NaLaMgWO₆:Pr³⁺: A novel blue-light excitable red-emitting phosphor for white light-emitting diodes, *J. Lumin.*, 196 (2018) 275-280.
- [16] L.Niu, Y. Zhou, C. Zhu, Z. He, X. Meng, Pr³⁺ doped oxyfluoride silicate glasses for LEDs

Ceram. Int., 45 (2019) 4108-4112.

[17] L. Marek, M. Sobczyk, Spectroscopic investigations of Pr^{3+} ions in $\text{Na}_2\text{O-La}_2\text{O}_3\text{-ZnO-TeO}_2$ glasses, *J. Non-Cryst. Solids*, 487 (2018) 96-103.

[18] S.-Z. Ma, W.-L. Feng, R. Chen, Z.-Q. Peng, $\text{KSr}_4(\text{BO}_3)_3\text{:Pr}^{3+}$: a new red-emitting phosphor for blue-pumped white light-emitting diodes, *J. Alloys Compd.*, 700 (2017) 49-53.

[19] X. Luo, F. Shan, T. Xu, X. Zhang, G. Zhang, Y. Wu, Growth and optical properties of Pr^{3+} doped $\text{Na}_3\text{La}_9\text{O}_3(\text{BO}_3)_8$ crystal, *J. Cryst. Growth*, 455 (2016) 1-5.

[20] D. Ramteke, H. Swart, R. Gedam, Spectroscopic properties of Pr^{3+} ions embedded in lithium borate glasses, *Physica B*, 480 (2016) 111-115.

[21] G. Abdullaev, K.S. Mamedov, I. Amiraslanov, A. Magerramov, Crystal structure of lithium praseodymium orthoborate $\text{Li}_3\text{Pr}_2(\text{BO}_3)_3$, *J. Struct. Chem.*, 18 (1977) 331-333.

[22] J.-P. Chaminade, P. Gravereau, V. Jubera, C. Fouassier, A New Family of Lithium Rare-Earth Oxyborates, $\text{LiLn}_6\text{O}_5(\text{BO}_3)_3$ ($\text{Ln} = \text{Pr-Tm}$): Crystal Structure of the Gadolinium Phase $\text{LiGd}_6\text{O}_5(\text{BO}_3)_3$, *J. Solid State Chem*, 146 (1999) 189-196.

[23] Z. Wang, H. Li, G. Cai, Z. Jin, Synthesis, crystal structure, and thermal stability of new borates $\text{Na}_3\text{REB}_2\text{O}_6$ ($\text{RE} = \text{Pr, Sm, Eu}$), *Powder Diffr.*, 31 (2016) 110-117.

[24] P. Chen, M. Xia, R. Li, Mixed Alkali Neodymium Orthoborates: $\text{K}_9\text{Li}_3\text{Nd}_3(\text{BO}_3)_7$ and $\text{A}_2\text{LiNd}(\text{BO}_3)_2$ ($\text{A} = \text{Rb, Cs}$), *Z. Anorg. Allg. Chem.*, 642 (2016) 424-430.

[25] Q. Zeng, R. Li, A new potassium rare earth oxyborate $\text{K}_2\text{La}_2(\text{BO}_3)_2\text{O}$, *Solid State Sci.*, 12 (2010) 2144-2147.

[26] G.M. Sheldrick, SHELXT—Integrated space-group and crystal-structure determination, *Acta Cryst. A*, 71 (2015) 3-8.

[27] C.B. Hübschle, G.M. Sheldrick, B. Dittrich, ShelXle: a Qt graphical user interface for SHELXL, *J. Appl. Crystallogr.*, 44 (2011) 1281-1284.

[28] G.C. Zhang, Y.G. Li, P.Z. Fu, S.L. Pan, F. Chang, Y.C. Wu, Crystal Structure of Sodium Lanthanum Borate $\text{Na}_3\text{La}_2(\text{BO}_3)_3$, *J. Synt. Cryst.*, 33 (2004) 490-495.

[29] R.D. Shannon, Revised effective ionic radii and systematic studies of interatomic distances in halides and chalcogenides, *Acta Crystallogr. A*, 32 (1976) 751-767.

[30] J. Gao, R. Li, Potassium rich rare earth (RE) borates $\text{K}_3\text{RE}(\text{BO}_3)_2$, *Solid State Sci.*, 10 (2008) 26-30.

[31] S. Bräuchle, H. Huppertz, Synthesis and structural characterization of $\text{Li}_3\text{K}_3\text{Y}_7(\text{BO}_3)_9$, *J. Solid State Chem*, 253 (2017) 242-248.

[32] T. Roisnel, J. Rodríguez-Carvajal, WinPLOTR: a windows tool for powder diffraction pattern analysis, Materials Science Forum, Transtec Publications; 1999, 2001, pp. 118-123.

[33] G.H. Dieke, H. Crosswhite, The spectra of the doubly and triply ionized rare earths, *Appl. Opt.*, 2 (1963) 675-686.

[34] P. Kubelka, F. Munk, Ein Beitrag zur Optik der Farbanstriche, *Z. Tech. Phys.*, 12 (1931) 593-601.

[35] J. Tauc, R. Grigorovici, A. Vancu, Optical properties and electronic structure of amorphous germanium, *Phys. Status Solidi B*, 15 (1966) 627-637.

[36] T.-T. Jin, Z.-J. Zhang, H. Zhang, J.-T. Zhao, Crystal structure, phase transition and optical properties of $\nu\text{-PrBO}_3$, *J. Inorg. Mater.*, 28 (2013) 1153-1157.

[37] D. Xu, F. Zhang, Y. Sun, Z. Yang, B. Lei, L. Liu, S. Pan, $\text{LiRb}_2\text{LaB}_2\text{O}_6$: a new rare-earth borate with a MOF-5-like topological structure and a short UV cut-off edge, *Dalton Trans.*, 46 (2017) 193-199.

[38] D. Souiri, Z.E. Tahan, A new method for the determination of optical band gap and the nature of optical transitions in semiconductors, *Appl. Phys. B*, 119 (2015) 273-279.

- [39] A. Kirsch, M.M. Murshed, M. Schowalter, A. Rosenauer, T.M. Gesing, Nanoparticle precursor into polycrystalline $\text{Bi}_2\text{Fe}_4\text{O}_9$: an evolutionary investigation of structural, morphological, optical, and vibrational properties, *J. Phys. Chem. C*, 120 (2016) 18831-18840.
- [40] A. Kirsch, M.M. Murshed, F.J. Litterst, T.M. Gesing, Structural, spectroscopic, and thermoanalytic studies on $\text{Bi}_2\text{Fe}_4\text{O}_9$: tunable properties driven by nano-and poly-crystalline states, *J. Phys. Chem. C*, 123 (2019) 3161-3171.
- [41] Z. Mo, Y. Sun, H. Chen, P. Zhang, D. Zuo, Y. Liu, H. Li, Preparation and characterization of a PMMA/Ce(OH)₃, Pr₂O₃/graphite nanosheet composite, *Polym.*, 46 (2005) 12670-12676.
- [42] S. Zinatloo-Ajabshir, M. Salavati-Niasari, Nanocrystalline Pr₆O₁₁: synthesis, characterization, optical and photocatalytic properties, *New J. Chem.*, 39 (2015) 3948-3955.
- [43] W. Steele, J. Decius, Infrared absorption of lanthanum, scandium, and indium borate and the force constants of borate ion, *J. Chem. Phys.*, 25 (1956) 1184-1188.
- [44] A. Haberer, R. Kaindl, H. Huppertz, Synthesis and crystal structure of the praseodymium orthoborate λ -PrBO₃, *Z. Naturforsch. B*, 65 (2010) 1206-1212.
- [45] A. Kuznetsov, K. Kokh, N. Kononova, V. Shevchenko, E. Kaneva, B. Uralbekov, V. Svetlichnyi, A.E. Kokh, Synthesis and growth of new rare earth borates KCaR(BO₃)₂ (R= La, Pr and Nd), *J. Solid State Chem.*, 282 (2020) 121091.
- [46] S. Noirault, S. Celerier, O. Joubert, M.T. Caldes, Y. Piffard, Effects of water uptake on the inherently oxygen-deficient compounds Ln₂₆O_{27□}(BO₃)₈ (Ln= La, Nd), *Inorg. Chem.*, 46 (2007) 9961-9967.
- [47] R. L. Carlin, *Magnetochemistry*, Springer, 1986
- [48] Levin, Ernest M., Robert S. Roth, and Jerry B. Martin, Polymorphism of ABO₃ type rare earth borates, *Am. Mineral.*, 46 (1961) 1030-1055.
- [49] R. K. Li, C. Greaves, YCa₃(MnO)₃(BO₃)₄: A manganese borate containing ferromagnetic chains on a kagomé lattice, *Phys. Rev. B*, 68 (2003) 172403
- [50] Gao, Jianhua, and Shuai Li, BiSr₃(YO)₃(BO₃)₄: a new gaufroyite-type rare-earth borate with moderate SHG response, *Inorg Chem.*, 51 (2012) 420-424.
- [51] R. K. Li, C. Greaves, One-dimensional ferromagnetism of gaufroyite Ca₄(MnO)₃(BO₃)₃CO₃, *Phys. Rev. B*, 70 (2004) 132411.
- [52] Zhou, T., Ye, N, Redetermination of tricalcium trilanthanum pentakis (orthoborate) from single-crystal data. *Acta Crystallogr. E*, 64 (2008), i37-i37
- [53] Rashchenko, Sergey V., Vladimir V. Bakakin, Anton F. Shatskiy, Pavel N. Gavryushkin, Yurii V. Seryotkin, and Konstantin D. Litasov, Noncentrosymmetric Na₂Ca₄(CO₃)₅ carbonate of “M₁₃M₂₃XY₃Z” structural type and affinity between borate and carbonate structures for design of new optical materials, *Cryst. Growth Des.* 17 (2017) 6079-6084
- [54] Günther, W., and R. Schöllhorn, Complete substitution of Cu/O layers in T-type oxocuprates by carbonate: The new series LnKO(CO₃), *Mater. Res. Bull.*, 30 (1995) 285-290.
- [55] Günther, W., W. Paulus, and R. Schöllhorn, stacking disorder in a layered carbonate phase: the structure of LaKOCO₃, *J. Phys. Chem. Solids*, 61 (2000) 1945-1953.
- [56] Z. Jiráček, J. Hejtmánek, K. Knížek, R. Sonntag, Structure and Properties of the Pr_{1-x}K_xMnO₃ perovskites (x = 0–0.15), *J. Solid State Chem.*, 132 (1997) 98-106

Summary and Outlook

Within the scope of this cumulative dissertation, several novel alkali-metal containing Rare-earth orthoborates were reported and extensively investigated:

1. Complementary X-ray Single-crystal and powder diffraction reveal that $\text{KLi}_2\text{RE}(\text{BO}_3)_2$ ($\text{RE} = \text{Dy, Ho, Er, Tm, Yb}$ and Y) crystallize isotypic in the $P2_1/n$ space group and represent a new, previously unreported structure type. $\text{KLi}_2\text{RE}(\text{BO}_3)_2$ phases are shown to possess a limited tolerance regarding the ionic radii of the incorporated rare-earth cations, as attempts to employ either larger (Eu^{3+} , Gd^{3+} and Tb^{3+}) or smaller (Lu^{3+} , Sc^{3+} and In^{3+}) radius cations did not result in the target phases. Moreover, trials to replace K^+ with larger alkali cations such as Rb^+ and Cs^+ did also not produce the desired compounds.

Given that $\text{KLi}_2\text{Y}(\text{BO}_3)_2$ has a high lithium and boron content and is of high transparency with no optical bandgap absorption in the visible range (insulator), investigations such as lithium-ion conductivity, photoluminescence and neutron scintillation etc. may be some attractive avenues for future investigations.

2. $\text{K}_3\text{RE}_3(\text{BO}_3)_4$ ($\text{RE} = \text{Pr, Nd, Sm, Eu, Gd, Tb, Dy, Ho, Er, Tm, Yb}$ and Lu) were obtained by solid state syntheses and spontaneous crystallization from a high-temperature flux. Combined X-ray single crystal and powder diffraction reveal the monoclinic space group $P2_1/c$ for $\text{K}_3\text{RE}_3(\text{BO}_3)_4$ ($\text{RE} = \text{Sm-Lu}$) and triclinic space group $P\bar{1}$ for $\text{K}_3\text{RE}_3(\text{BO}_3)_4$ ($\text{RE} = \text{Pr, Nd}$). The monoclinic and triclinic compounds are equivalent in terms of geometry and bonding and are related by symmetry lowering and doubling of the b -cell parameter. These materials are not to be confused with the hexagonal-open-framework compounds such as in $\text{Na}_3\text{Y}_3(\text{BO}_3)_4$, from which they are structurally distinct.

Attempts to obtain $\text{K}_3\text{La}_3(\text{BO}_3)_4$ and $\text{K}_3\text{Ce}_3(\text{BO}_3)_4$ were unsuccessful, indicating La^{3+} and Ce^{3+} are too large for the $\text{K}_3\text{RE}_3(\text{BO}_3)_4$ family. These results demonstrate a morphotropic series to exist for alkali rare-earth borates, based on the cationic size effect.

$\text{K}_3\text{Gd}_3(\text{BO}_3)_4$ and $\text{K}_3\text{Lu}_3(\text{BO}_3)_4$ co-doped by Eu^{3+} , Tb^{3+} , Ce^{3+} may be potential materials for white LED or scintillation. (Er^{3+} , Yb^{3+})-doped $\text{K}_3\text{Gd}_3(\text{BO}_3)_4$ and $\text{K}_3\text{Lu}_3(\text{BO}_3)_4$ could be interesting for up-conversion eye-safe emission. Due to the high gadolinium content, $\text{K}_3\text{Gd}_3(\text{BO}_3)_4$ is expected to exhibit a strong magnetocaloric effect.

3. The alkali metal praseodymium borate $\text{K}_2\text{Pr}_2\text{O}(\text{BO}_3)_2$ ($P2_1/c$) represents a new structure type in the $\text{K}_2\text{RE}_2(\text{BO}_3)_2\text{O}$ family. Its crystal structure consists of 2D $[\text{Pr}_2\text{O}(\text{BO}_3)_2]^{2-}$ sheets and K^+ cations stacked alternately along the **a**-axis. The $\text{K}_2\text{RE}_2(\text{BO}_3)_2\text{O}$ family is found to have many common features with the potassium-bearing rare-earth metal oxo-carbonates (KREOCO_3), which is also of a layered structure type.

Since the Pr^{3+} cation is of interest due to its photoluminescence properties, $\text{K}_2\text{Pr}_2\text{O}(\text{BO}_3)_2$ and $\text{K}_2\text{La}_{1-x}\text{Pr}_x\text{O}(\text{BO}_3)_2$ solid solution phases may serve as red phosphors or high-temperature sensors under blue light irradiation.

We hope that these novel alkali-metal containing Rare-earth orthoborates will enrich the crystal chemistry of the rare-earth and borate structures. The synthesis, property investigation and their structural comparison might prove beneficial in searching and designing novel rare-earth compounds for practical applications.

Zusammenfassung und Ausblick

Im Rahmen dieser kumulativen Dissertation wurde über mehrere neuartige alkalimetallhaltige Seltenerd-Orthoborate berichtet und diese ausführlich untersucht:

1. Komplementäre Röntgen-Einkristall- und Pulverdiffraktometrie zeigten, dass $\text{KLi}_2\text{RE}(\text{BO}_3)_2$ (RE= Dy, Ho, Er, Tm, Yb und Y) isotyp in der Raumgruppe $P2_1/n$ kristallisieren und einen neuen, bisher nicht berichteten Strukturtypen darstellen. Es hat sich gezeigt, dass $\text{KLi}_2\text{RE}(\text{BO}_3)_2$ -Phasen eine begrenzte Toleranz hinsichtlich der Ionenradien der inkorporierten Seltenerdkationen aufweisen, da Versuche, entweder Kationen mit größeren (Eu^{3+} , Gd^{3+} und Tb^{3+}) oder kleineren (Lu^{3+} , Sc^{3+} und In^{3+}) Ionenradien scheiterten. Darüber hinaus führten Versuche, K^+ durch größere Alkalikationen wie Rb^+ und Cs^+ zu ersetzen, ebenfalls nicht zu den gewünschten Zielverbindungen.

Angesichts der Tatsache, dass $\text{KLi}_2\text{Y}(\text{BO}_3)_2$ einen hohen Lithium- und Borgehalt aufweist und von hoher Transparenz, ohne optische Bandlückenabsorption im sichtbaren Bereich (Isolator) ist, könnten Untersuchungen wie Lithiumionenleitfähigkeit, Photolumineszenz und Neutronenszintillation usw. einige attraktive Ansätze für zukünftige Untersuchungen sein.

2. $\text{K}_3\text{RE}_3(\text{BO}_3)_4$ (RE = Pr, Nd, Sm, Eu, Gd, Tb, Dy, Ho, Er, Tm, Yb und Lu) wurden durch Festkörpersynthesen und spontane Kristallisation aus der Flussmittelschmelze erhalten. Kombinierte Röntgen-Einkristall- und Pulverdiffraktometrie weisen auf die monokline Raumgruppe $P2_1/c$ für $\text{K}_3\text{RE}_3(\text{BO}_3)_4$ (RE = Sm-Lu) und die triklinen Raumgruppe $P\bar{1}$ für $\text{K}_3\text{RE}_3(\text{BO}_3)_4$ (RE=Pr, Nd) hin. Die monoklinen und triklinen Verbindungen sind in Bezug auf Geometrie und chemische Bindungen äquivalent und stehen durch Symmetrieabsenkung und Verdoppelung des **b**-Zell-Parameters miteinander in Beziehung. Diese Verbindungen sind nicht zu verwechseln mit den hexagonalen, offenen Gerüstverbindungen wie beispielsweise $\text{Na}_3\text{Y}_3(\text{BO}_3)_4$, von denen sie sich strukturell stark unterscheiden.

Versuche, $\text{K}_3\text{La}_3(\text{BO}_3)_4$ und $\text{K}_3\text{Ce}_3(\text{BO}_3)_4$ zu erhalten blieben erfolglos, was darauf hindeutet, dass La^{3+} und Ce^{3+} für die $\text{K}_3\text{RE}_3(\text{BO}_3)_4$ -Familie zu groß sind. Diese Ergebnisse belegen eine morphotrope Reihe für Alkali-Seltenerdborate auf der Grundlage des kationischen Größeneffekts.

$\text{K}_3\text{Gd}_3(\text{BO}_3)_4$ und $\text{K}_3\text{Lu}_3(\text{BO}_3)_4$, kodotiert mit Eu^{3+} , Tb^{3+} , Ce^{3+} , könnten potenzielle Materialien für weiße LED oder Szintillatoren sein. (Er^{3+} , Yb^{3+})-dotiertes $\text{K}_3\text{Gd}_3(\text{BO}_3)_4$ und $\text{K}_3\text{Lu}_3(\text{BO}_3)_4$ könnten für augensichere Hochkonversions-Emission interessant sein. Zudem wird aufgrund des hohen Gadoliniumgehalts ein starker magnetokalorischer Effekt für $\text{K}_3\text{Gd}_3(\text{BO}_3)_4$ erwartet.

3. Das Alkalimetall-Praseodym-Borat $\text{K}_2\text{Pr}_2\text{O}(\text{BO}_3)_2$ ($P2_1/c$) stellt einen neuen Strukturtypen in der $\text{K}_2\text{RE}_2(\text{BO}_3)_2\text{O}$ -Familie dar. Seine Kristallstruktur besteht aus 2D $[\text{Pr}_2\text{O}(\text{BO}_3)_2]^{2-}$ Schichten welche mit Schichten von K^+ -Kationen abwechselnd entlang der **a**-Achse gestapelt sind. Es hat sich herausgestellt, dass die $\text{K}_2\text{RE}_2(\text{BO}_3)_2\text{O}$ -Familie viele Gemeinsamkeiten mit den kaliumhaltigen Seltenerdmetalloxocarbonaten (KREOCO_3) aufweist, welche ebenfalls Schichtstrukturverbindungen sind.

Da das Pr^{3+} -Kation aufgrund seiner Photolumineszenz-Eigenschaften von Interesse ist, sind $\text{K}_2\text{Pr}_2\text{O}(\text{BO}_3)_2$ und $\text{K}_2\text{La}_{1-x}\text{Pr}_x\text{O}(\text{BO}_3)_2$ -Mischungsreihen bei Bestrahlung mit blauem Licht potenziell als rote Leuchtstoffe oder Hochtemperatursensoren von Interesse.

Wir hoffen, dass diese neuartigen alkalimetallhaltigen Seltenerd-Orthoborate die Kristallchemie der Seltenerd- und Boratstrukturen bereichern werden. Die Synthese, die Untersuchung der Eigenschaften und ihr Strukturvergleich könnten sich bei der Suche und dem Entwurf neuer Seltenerdverbindungen für praktische Anwendungen als nützlich erweisen.

Appendix

The crystallographic data for

$\text{K}_{1.31(1)}\text{Li}_{1.69(1)}\text{Pr}_2(\text{BO}_3)_3$ (**Table A1**),

$\text{Na}_{2.86}\text{Gd}_{2.07}(\text{BO}_3)_3$ (**Table A2**),

$\text{Tl}_2\text{Pb}(\text{SO}_4)_2$ (**Table A3**)

with the corresponding atomic coordinates, equivalent isotropic displacement parameters (U_{eq} / pm^2), and bond valence sum (BVS /v.u.)

Table A1 $\text{K}_{1.31(1)}\text{Li}_{1.69(1)}\text{Pr}_2(\text{BO}_3)_3$, space group: $\text{Amm}2$, $a = 504.69(18)$ pm, $b = 1105.0(3)$ pm, $c = 733.92(14)$ pm,

$R_1 = 0.0138$ $wR_2 = 0.0300$ for all data, GooF=1.174, Flack parameter = 0.08(2)

Atoms	Wyckoff	x	y	z	U_{eq}	SOF	BVS
Pr1	4e	1/2	0.77852(2)	0.43667(4)	58.7(2)	1	3.099(4)
K1	2a	0	1/2	0.53616(15)	218.8(15)	1	0.855(1)
Li1	2b	1/2	1/2	0.2131(14)	185(13)	1	0.955(4)
K2 Li2	2a	0	0	0.5203(4)	199(9)	0.31(1) 0.69(1)	1.171(1)
B1	2b	0	0.6981(2)	0.2631(3)	96(3)	1	2.900(14)
B2	4d	1/2	0	0.2271(5)	79(4)	1	2.939(14)
O1	4d	0	0.8033(3)	0.3642(3)	209(4)	1	-2.105(12)
O2	8f	0.2399(2)	0.64329(11)	0.22242(18)	115.8(16)	1	-1.737(11)
O3	4e	1/2	0.89143(15)	0.1365(2)	133(3)	1	-2.023(5)
O4	2b	1/2	0	0.4169(3)	118(4)	1	-2.118(7)

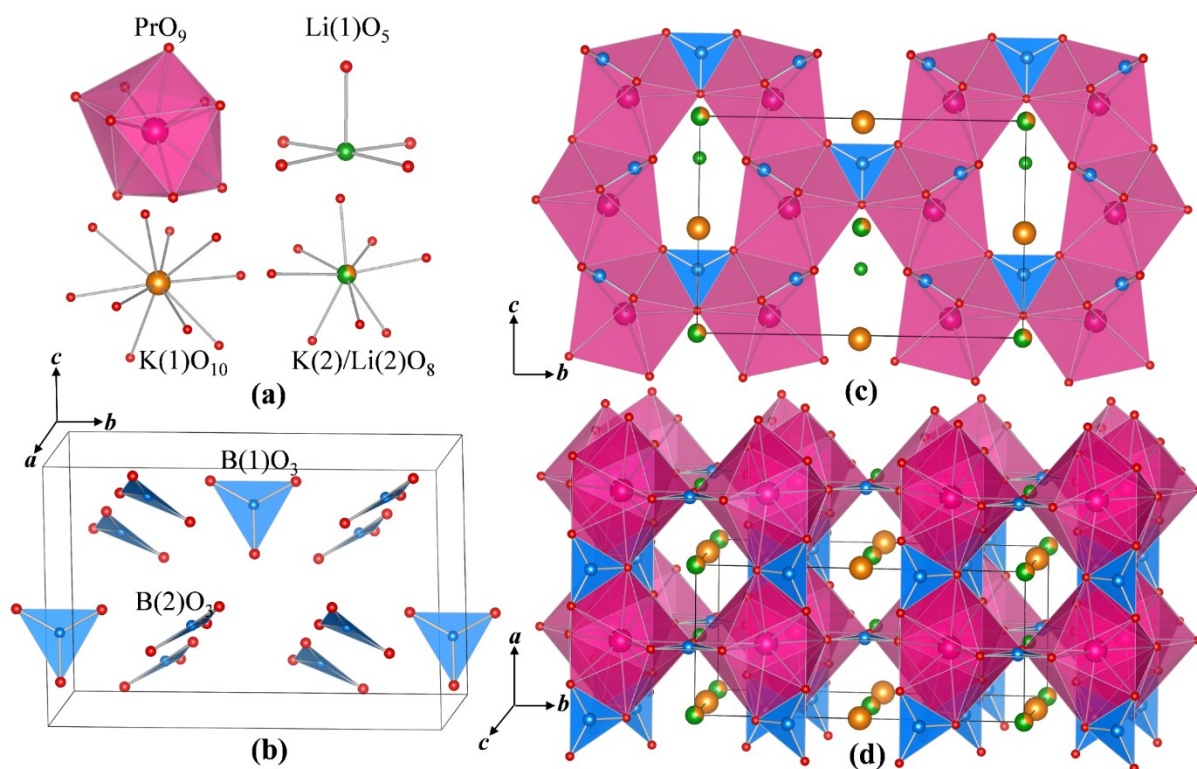


Figure A1 (a) coordination spheres of Pr^{3+} , Li^+ and K^+ cations; (b) the orientation of BO_3 groups in the unit cell; (c) the projection of the crystal structure along the a -direction, (d) the crystal structure viewed along the c -direction.

Table A2 $\text{Na}_{2.86}\text{Gd}_{2.07}(\text{BO}_3)_3$, space group: $\text{Amm}2$, $a = 504.69(18)$ pm, $b = 1105.0(3)$ pm, $c = 733.92(14)$ pm, $R_1 = 0.011$ $wR_2 = 0.0248$ for all data, $\text{Goof} = 1.183$, Flack parameter = 0.05(2)

Atoms	Wyckoff	x	y	z	U_{eq}	SOF	BVS
Gd1	4e	1/2	0.78777(2)	0.89751(3)	88.9(6)	1	3.07(1)
Na1	2a	0	1/2	0.5579(10)	630(30)	0.86	0.51 (1)
Na2	2b	1/2	1/2	0.2447(4)	154(5)	1	1.47(1)
Na3 Gd3	2a	0	0.5	0.9793(2)	94(5)	0.93(1) 0.07(1)	1.42(1)
B1	2b	0	0.7809(5)	0.7006(8)	142(8)	1	2.99(3)
B2	4d	1/2	1/2	0.2271(5)	107(9)	1	3.07(3)
O1	4d	0	0.6718(6)	0.7886(9)	432(15)	1	-1.82(3)
O2	8f	0.2370(4)	0.3383(2)	0.1654(4)	152(4)	1	-2.07(1)
O3	4e	1/2	0.6068(3)	0.5587(6)	343(12)	1	-2.13(2)
O4	2b	1/2	1/2	0.8542(9)	155(10)	1	-2.12(2)

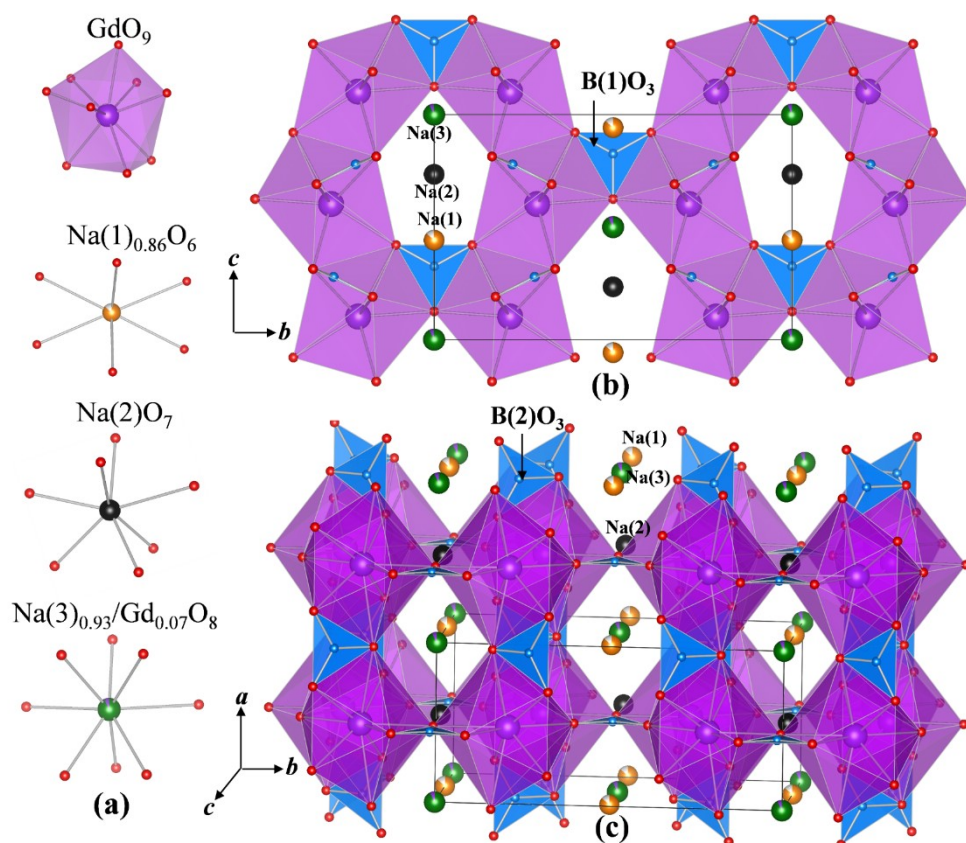


Figure A2 (a) coordination spheres of Gd^{3+} and Na^{+} cations; (b) the projection of the crystal structure along the a -direction, (c) the crystal structure viewed along the c -direction.

Table A3 $\text{Ti}_2\text{Pb}(\text{SO}_4)_2$, space group: $R\bar{3}m$, $a = 559.55(2)$ pm, $c = 22.1001(9)$ pm, $R_1 = 0.0224$ $wR_2 = 0.0497$ for all data, $\text{GooF} = 1.123$,

Atoms	Wyckoff	x	y	z	U_{eq}	BVS
Tl	$6c$	$1/3$	$2/3$	0.46244(2)	24.31(8)	1.967(3)
Pb	$3a$	0	$1/2$	0.5371(10)	26.63(9)	1.984(9)
S	$6c$	$1/2$	$1/2$	0.2447(4)	15.4(5)	5.985(24)
O1	$18h$	0.4766(3)	0.5234(3)	0.24795(13)	24.9(5)	-1.964(20)
O2	$6c$	$1/3$	$2/3$	0.3372(2)	38.8(8)	-1.967(3)

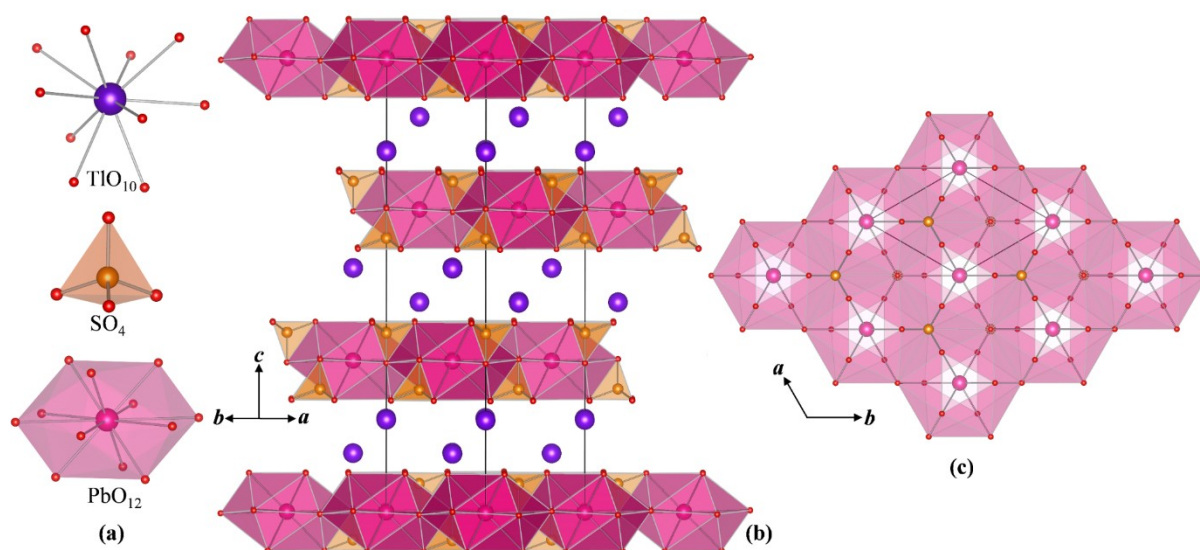


Figure A3 (a) coordination sphere of Tl^+ , S^{6+} and Pb^{2+} cations; (b) the layered crystal structure of $\text{Ti}_2\text{Pb}(\text{SO}_4)_2$, (c) the PbO_{12} layer embedded with SO_4 , viewed along the c -direction.

Curriculum Vitae

Pengyun Chen

Solid State and Crystallographic Chemistry,
Universität Bremen
Leobener Straße / NW2, D-28359 Bremen (Germany)
Email: pengyun@uni-bremen.de

Education

University of Bremen, Bremen, Germany
PhD student in Solid-state Chemistry and Crystallography, Supervisor: Prof. Dr. Thorsten M. Gesing

Beijing Center for Crystal Research and Development, Chinese Academy of Sciences (CAS), China
Master of Science in Inorganic Chemistry, Supervisor: Prof. R. K. Li

Beijing University of Chemical Technology (BUCT), Beijing, China
Bachelor of Science in Applied Chemistry

Publications during the stay in Prof. Thorsten M. Gesing's group

1. P. Chen, M. Murshed*, T. M. Gesing, Synthesis and characterization of $K_2Pr_2O(BO_3)_2$: structural, spectroscopic and thermogravimetric investigations of a novel potassium praseodymium oxoborate structure type, *Springer-Nat. Appl. Sci.*, **2020**, 747,
2. P. Chen, M. Murshed*, M. Fischer, T. Frederichs, T. M. Gesing, $KLi_2RE(BO_3)_2$ (RE = Dy, Ho, Er, Tm, Yb and Y): Structural, Spectroscopic, And Thermogravimetric Studies on a Series of Mixed-Alkali Rare-Earth Orthoborates, *Inorg. Chem.*, **2020**, 59, 18214–18224
3. P. Chen, M. Murshed*, T. M. Gesing, Synthesis and crystal structures of novel alkali rare-earth orthoborates: $K_3RE_3(BO_3)_4$ (RE = Pr, Nd, Sm-Lu), *J. Mater. Sci.*, **2021**, 56, 3639–3652.